Behavioural analysis of PEM fuel cell components and research of causal relationships between in-situ and ex-situ observed performances

El Mahdi Khetabi

université PARIS-SACLAY

Behavioural analysis of PEM fuel cell components and research of causal relationships between in-situ and ex-situ observed performances

Thèse de doctorat de l'Université Paris-Saclay

École doctorale n°575 : electrical, optical, bio : physics and engineering (EOBE)

Spécialité de doctorat : Génie électrique

Unité de recherche : SATIE UMR CNRS 8029

Référent : ENS Paris-Saclay

Thèse présentée et soutenue par visioconférence, le 1er avril 2021, par

El mahdi KHETABI

Composition du Jury

Pierre MILLET Professeur, Université Paris-Saclay	Président
Christophe TURPIN Directeur de recherche, Centre National de la Recherche Scientifique	Rapporteur
Olivier LOTTIN Professeur, Université de Lorraine	Rapporteur
Dietmar GERTEISEN Docteur, Fraunhofer Institute for Solar Energy Systems ISE (Allemagne)	Examinateur
Dominique CHAMORET Maître de conférences, Université de Technologie de Belfort-Montbéliard	Examinatrice
Nadia YOUSFI STEINER Professeure, Université de Franche-Comté	Examinatrice

Denis CANDUSSO Directeur de recherche, Université Gustave Eiffel	Directeur de thèse
Xavier FRANÇOIS Ingénieur de recherche, Université de Technologie de Belfort-Montbéliard	Co-Encadrant
Yann MEYER Professeur, Université Savoie Mont Blanc	Co-Directeur
Mehdi FERHAN Vice President Innovation, Engineering & Partnerships, Plastic Omnium	Invité

Thèse de doctorat

NNT : 2021UPAST044

Acknowledgements

Writing these lines marks the culmination of my PhD journey that I started in October 2017 at the Hydrogen Energy Platform in Belfort, and I feel lucky to have some amazing people by my side during this period. What I have attained in this PhD was made possible due to a combination of guidance, encouragement and support from my family, friends, colleagues, and supervisors.

First, I would like to express my sincere gratitude to my supervisor, Dr. Denis Candusso – research director at the *Université Gustave Eiffel*, for his valuable and constructive suggestions and enthusiastic encouragement all along this PhD journey. His willingness to give his time and scientific assistance so generously has been very much appreciated. Without his ongoing support, kindness and patience, this work would never have been the same. I would also like to express my deepest gratitude to my co-supervisors, Pr. Yann Meyer – Professor at the *Université Savoie Mont Blanc*, for his insightful comments, constructive feedback, and the invaluable scientific guidance all along my PhD journey, and Dr. Xavier François – Fuel-Cell System Research Engineer and facilities manager at the Hydrogen Energy Platform of the *Université de Technologie de Belfort-Montbéliard* (*UTBM*), for all the scientific discussions that we had, and for the time, and energy, that he dedicated to the installation and the maintenance of the experimental means employed in this thesis. I could not have asked for a more encouraging, motivated, and supportive team of supervisors to lead this PhD thesis project.

I would like to thank the jury members for accepting to evaluate my work, and for all the enriching discussions that we had during my PhD defence. Special thanks go to the two reviewers, Dr. Christophe Turpin and Pr. Olivier Lottin, for their valuable comments and suggestions to improve this manuscript. Also, I would like to thank my colleagues at *Fi Group* in Lille for helping me organise my PhD defence in the best conditions.

I am also grateful to the *Région Bourgogne-Franche-Comté* and the *Université Gustave Eiffel* (Former *IFSTTAR*) for funding this PhD thesis project. My sincere thanks go also to the *UTBM*, the *Fraunhofer Institute for Solar Energy Systems ISE*, and the *Plastic Omnium* company for their contributions to this PhD thesis.

Special words of gratitude go to my friends, from all around the world, who have always been a source of delight during this PhD journey. You made my PhD thesis a pleasant experience and I have enjoyed all the cheerful moments that we shared. To all my colleagues and friends in Belfort: you made my stay memorable, delightful (*Lancia*), and rewarding, so thanks to all of you, it has been a great experience.

My deep and sincere gratitude goes to my family for their love, encouragement, help and support. I am forever indebted to my mother and father for always encouraging me to explore new opportunities in life. This memorable journey would not have been possible without their invaluable support, and I dedicate this work to them. Their love has always been there with me no matter where on the planet I was.

Finally, my very distinctive thanks go to my lovely wife for supporting me throughout the years of my PhD thesis. I would not have been able to accomplish this work without your patience, love, and continuous encouragement. I will always remember your unfailing support and I am so thankful to have you in my life.

Abstract

Polymer Electrolyte Fuel Cells (PEFCs) have shown their potential for both mobile and stationary applications. Assembling the PEFC stacks requires an appropriate mechanical compression in order to achieve adequate contacts (i.e. mechanical, thermal, and electrical) between the fuel cell components and to ensure gas-tight operation. However, an excessive mechanical compression may worsen the fuel cell performance as a result of the reduction in the porosity and mass transport ability of the Gas Diffusion Layers (GDLs). The work presented in this thesis aims to investigate the effects of 12 levels of mechanical compression, ranging from 0.35 to 2 MPa, on the in-situ performance of a 225 cm^2 PEFC. The experimental investigations present the novelty of combining various characterisation techniques (i.e. polarisation measurement; Electrochemical Impedance Spectroscopy - EIS; local current/temperature and pressure distributions analysis; displacement measurement) while providing correlations with ex-situ results obtained within the MIREPOIx research project.

The results show that a mechanical compression up to 1.55 MPa improves the PEFC performance at all tested operating conditions. This finding was attributed to the dominant reduction of the ohmic resistance against the increase in mass transport resistance. The results also emphasise the fact that mechanical compression up to 1.55 MPa improves the distributions of current and temperature. This effect was attributed to the enhanced pressure distribution achieved with increasing mechanical compression. The results obtained in this thesis suggest that compressing the PEFC beyond a specified level (1.55 MPa) would not lead to any further improvement of the PEFC performance. It may even worsen this performance due to the increase in the mass transport resistance. Finally, valuable correlations between the results from in-situ and ex-situ characterisation techniques are provided and analysed throughout the thesis.

Keywords: Fuel cell; In-situ experimental characterisation; Mechanical compression.

Résumé

Les piles à combustible à membrane échangeuse de protons (sigle PEFC en anglais) ont déjà montré un potentiel important dans des applications mobiles et stationnaires. L'empilement des PEFCs (stack) nécessite, à l'assemblage, l'introduction d'une compression mécanique afin d'obtenir des contacts (mécaniques, thermiques, électriques) adéquats entre les composants et pour assurer une étanchéité vis-à-vis des réactifs. Cependant, une contrainte mécanique excessive peut détériorer les performances de la PEFC en réduisant notamment la porosité des couches de diffusion (GDLs) et leur capacité à transporter les espèces (réactifs et produits). Les travaux présentés dans cette thèse visent à étudier les effets d'une compression mécanique (variant de 0.35 à 2 MPa suivant 12 niveaux) sur les performances in-situ d'une PEFC à la surface active de 225 cm^2. Les travaux menés présentent la particularité de combiner plusieurs techniques de caractérisation et d'analyse (courbes de polarisation et Spectroscopie d'Impédance Électrochimique - SIE ; distributions locales de courant, de température et de pression ; mesures de déplacement mécanique) tout en fournissant des corrélations avec les résultats d'essais ex-situ obtenus dans le cadre du projet de recherche MIREPOIx.

Les observations réalisées ici indiquent qu'une compression mécanique allant jusqu'à 1.55 MPa améliore les performances électriques de la PEFC dans les conditions opératoires considérées. Ce résultat est attribué à la réduction dominante de la résistance ohmique par rapport à l'augmentation de la résistance au transport des espèces. Par ailleurs, l'augmentation de la compression mécanique homogénéise les répartitions des densités de courant et des températures jusqu'à 1.55 MPa. Cette homogénéisation est attribuée à une meilleure distribution de la pression mécanique obtenue avec la compression croissante. Les essais suggèrent que la compression de la PEFC au-delà d'un niveau spécifié (1.55 MPa) n'entraînerait pas d'amélioration significative des performances électriques. Elle pourrait même les détériorer en raison de l'augmentation de la résistance au transport des espèces. Enfin, des corrélations entre les résultats des techniques de caractérisation in-situ et ex-situ sont fournies et analysées tout au long de la thèse.

Mots clés : Pile à combustible ; Caractérisation expérimentale in-situ ; Compression mécanique.

Content

List of figures

List of tables

List of abbreviations

AC	Alternating current
AFC	Alkaline Fuel Cell
BEV	Battery Electric Vehicles
BPP	BiPolar Plate
CCUS	Carbon Capture, Use, and Storage
CHP	Cogeneration of Heat and Power
CL	Catalyst Layer
CT	Computed Thermography
DC	Direct Current
DMFC	Direct Methanol Fuel Cell
DoE	Departement of Energy
DOE	Design Of Experiment
ECSA	ElectroCatalyst Surface Area
EIS	Electrochemical Impedance Spectroscopy
FC	Fuel Cell
FCEV	Fuel Cell Electric Vehicles
FCH-JU	Fuel Cells and Hydrogen Joint Undertaking
FFP	Flow Field Plate
FRA	Frequency Response Analyser
GDL	Gas Diffusion Layer
HF	High Frequency
HOR	Hydrogen Oxidation Reaction
HRS	Hydrogen Refuelling Stations
IEA	International Energy Agency
LF	Low Frequency
LSR	Liquid Silicone Rubber
LVDT	Linear Variable Differential Transformer
MAST	Multi-Axial Simulation Table
MCFC	Molten Carbonate Fuel cell
MCU	Mechanical Compression Unit
MEA	Membrane Electrode Assembly
MIREPOIx	Study of the influence of internal MechanIcal compRession on the Electrical PerfOrmance of a PEFC
MPL	Micro Porous Layer
OCV	Open Circuit Voltage
ORR	Oxygen Reduction Reaction
PàC	Pile à Combustible
PAFC	Phosphoric Acid Fuel Cell
PBI	Polybenzimidazole
PEFC	Polymer Electrolyte Fuel Cell

PFSA	PerFluoroSulfonic Acid
Pt	Platinum
PTFE	PolyTetraFluoroEthylene
qCf	quickCONNECT fixture
RH	Relative Humidity
SD	Standard Deviation
SEM	Scanning Electron Microscopy
SOFC	Solid Oxide Fuel Cell

Introduction

Global population growth and evolutions in human society have been marked by a significant increase in energy use and a surging need in power production. Fossil fuels have ensured these energy requirements since the industrial revolution of the 18th century. However, the combustion of fossil fuels results in many adverse consequences. Some of these include severe air pollution that causes many health issues and reduces the quality of life, especially in densely populated urban areas. The political influence of countries with extensive fossil fuels reserves is also driving governments to develop solutions to be less dependent on these hydrocarbon deposits. All these issues are tailored towards developing new energy conversion systems that have low greenhouse gases emissions, that are energy-efficient, and that have abundant reserves of fuel. In this regard, fuel Cells (FCs) are now closer to fulfil energy requirements than ever as they can provide environmentally friendly energy conversion systems required for a long-awaited transition to a renewable energy powered world.

A fuel cell is an electrochemical device that converts the chemical energy of a fuel and an oxidant directly into electrical energy, heat and water through a redox electrochemical reaction. The reactants are stored in external reservoirs and should be continuously supplied to allow fuel cell operation. Most of the fuel is dihydrogen, which reacts with dioxygen (generally from ambient air) during the redox electrochemical reaction. The recent increasing concern in developing and commercialising fuel cells is driven by their numerous advantages; namely, their environmentally friendly by-products (e.g. water when pure dihydrogen is used) with virtually no greenhouse gases emissions, their quiet operation, since the fuel cell assembly does not include any moving parts, and their higher efficiency, typically 40–70%[1], which could further be improved when the generated heat is used for heating purposes.

There are different types of fuel cells that are distinguished by the electrolyte type, by the operating temperature, by the employed technology, or by the exchanged ions, and therefore the occurring electrochemical reactions [2]. Among different fuel cell types, Polymer Electrolyte Fuel Cells (PEFC) and Solid Electrolyte Fuel Cell (SOFC) have been considered as the technology offering a forthcoming commercialisation possibility, namely due to their lower cost per unit and their potential strategic markets [3]. PEFCs have particularly shown their potential for both mobile (e.g. automobile, aerospace, portable) and stationary applications (e.g. micro-cogeneration of heat and power, µ-CHP) due to their high efficiency, their reduced weight and their low operating temperature (usually between 60 and 80 °C for low-temperature PEFC [4]). Hence, attention will be turned to low-temperature PEFC technology for the rest of this manuscript.

This promising technology is, however, facing some obstacles towards its large commercialisation. First, in order to take part in the ecological transition, the dihydrogen used in fuel cells must be produced from a non-polluting source that, for instance, can be ideally

achieved via water electrolysis coupled with electricity generated from a renewable source. Then, dihydrogen[1] storage and delivery, which must be conducted in an energetically sober and economically viable and safe way. Finally, the durability, reliability, performance, robustness, material use, and cost-effectiveness of fuel cells must be optimised. Indeed, for the fuel cells to be competitive with other traditional energy conversion devices (e.g. internal combustion engines) that present mature technologies so far, a deep understanding of all the parameters affecting the fuel cell performance is of significant importance for the development of not only durable and high-performance fuel cells, but also cost-effective energy conversion systems. In this respect, academia and industrial researchers are placing their focus on various issues, including, among others:

- Development of the PEFC core components (e.g. electrolyte, electrodes, gas diffusion layers, bipolar plates) using fewer natural resources while ensuring a good level of efficiency.
- Optimisation of the PEFC operating parameters (e.g. pressure, temperature, humidification).
- Development of modelling and control strategies (e.g. multiphysics and multiscale modelling, energy management approaches).
- Study of the evolution of the PEFC performance over time (e.g. ageing, deterioration, reliability).
- Development of health management and prognostic methods (e.g. determination of the state-of-health, monitoring and analysis of the remaining useful life).
- Optimisation of the stack assembly (e.g. mechanical compression inside the stack, clamping modes, clamping pressure distribution). It is within this issue that the work presented in this thesis is conducted.

i. Objectives of the thesis

Fuel cell stacks require mechanical compression during the assembly process, which necessitates first an accurate control to ensure proper alignment of the stack's components. Then an appropriate assembly pressure is applied in order to achieve adequate contacts (i.e. mechanical, thermal, and electrical) between the fuel cell components and to ensure gas-tight operation. In fact, a PEFC is a multi-contact structure in which multi-physical phenomena are coupled. Interactions of these phenomena affect the performance of the fuel cell and its durability. It is therefore essential to thoroughly study the mechanical compression effects in order to better understand the complex interactions that are taking place at the PEFC's components level.

In a PEFC, two significant types of compression mechanisms take place. The first is due to external forces (e.g. the applied compression during the assembly process, shock and vibrations) and the second is caused by internal forces that are generated inside the fuel cell during its

[1] For the rest of this manuscript, dihydrogen will be referred to as "hydrogen" and dioxygen as "oxygen" wherever there is no ambiguity with the chemical elements with the same names.

operation (e.g. membrane hydration/dehydration, temperature variation, freeze/thaw cycles). In both cases, components within the fuel cell are subjected to compressive forces that may either improve or worsen the fuel cell performance.

It is well reckoned in the research community that mechanical compression is one of the main factors that affect the PEFC performance [5–7]. Although this compression plays a vital role to ensure efficient gas sealing along with optimised electrical and thermal conductivities during PEFCs operation, excessive mechanical compression may worsen the fuel cell performance. Some of the adverse effects of the mechanical compression (e.g. creation of hot spots) may even induce long term and irreversible performance losses, which in turn affects the durability of the PEFCs. It is therefore essential to strengthen the knowledge of the effects of mechanical stresses on the PEFC performance and durability; it is within this practical issue that the present work is conducted. The preeminent scientific objectives, among others, are:

- Deepen the understanding of the occurring phenomena inside the PEFC when subjected to mechanical stresses.
- Development of in-situ characterisation and analysis techniques to finely investigate the effects of mechanical compression on the PEFC performance.
- Deconvolution of the different loss sources of the PEFC performance in relation to mechanical compression.
- Provide correlations between in-situ and ex-situ characterisation results.

The overall goal is to investigate the effects of mechanical compression on PEFCs operating in real-life conditions. The conducted investigations are not only attempted to define solutions that can be used in laboratories, but rather to provide solutions applicable in industrial level through the development of selection criteria for an optimal choice of the PEFC components depending on the targeted application. The work presented in this thesis is a part of the **MIREPOIx** project described hereafter.

ii. Scope of the research project

Improving PEFC performance must involve a better understanding of the different mechanical interactions of the components within the fuel cell assembly. As a matter of fact, the effects of mechanical compression on an operating PEFC is not yet comprehensively covered by the scientific community [5], which is mainly due to the relatively recent interest of fuel cell developers to investigate mechanical issues that are stemmed from the need to deploy this technology on a larger scale. In this context, there are still many subjects to be addressed, especially in the correlations between in-situ and ex-situ investigations on the effects of mechanical stresses on the PEFC performance. It is within this framework that the project MIREPOix is conducted. MIREPOix is the acronym of Study of the influence of internal **M**echan**I**cal comp**R**ession on the **E**lectrical **P**erf**O**rmance of a PEFC. The main goal of this project is to study the effects of mechanical compression on the PEFC components by combining both electrical, electrochemical, and mechanical characterisation techniques and

modelling. One of the leading scientific challenges is to develop methods allowing the deconvolution of the different sources of the performance losses within the PEFC when it is subjected to mechanical stresses (e.g. contact resistance, mass transport resistance, pressure distribution, current density and temperature distributions). The work presented in this manuscript is conducted within the framework of development of new experimental procedures allowing a comprehensive understanding of the phenomena occurring in an operating PEFC when subjected to various mechanical stresses, namely in-situ characterisation techniques. Ex-situ investigations are carried out by another colleague, Khadidja BOUZIANE, as a part of her PhD thesis. The final aim, in the short-term, is to find relevant correlations between in-situ and ex-situ results.

Funding for this PhD thesis of the *Université Paris-Saclay* has been received from the *Région Bourgogne-Franche-Comté (France)* and the *Université Gustave Eiffel (Former IFSTTAR) (France)*. Other partners are invested in this project including the *Université de Technologie de Belfort Montbéliard (France)* where all the experimentations were conducted, and the *Fraunhofer Institute for Solar Energy Systems ISE (Germany).* The research carried out within the MIREPOix project has also interested the *Plastic Omnium* company.

iii. Overview of the manuscript

This thesis is divided into five chapters. Relevant in-situ / ex-situ correlations are emphasised throughout the manuscript. Also, conclusions and directions for future research are outlined in the different chapters of the manuscript. A brief description of the chapters is given below:

- **Chapter 1** A brief introduction to the background of the thesis is given in this chapter. The latest developments in fuel cell technology are also put forward.
- **Chapter 2** A comprehensive review of the previously published studies concerning the effects of mechanical comprehension on the PEFC performance is presented in this chapter. Critical analysis of the reported studies is given first, then promising routes for future studies are evoked.
- **Chapter 3** The developed experimental means for the work presented in this thesis are detailed; relevant technical information for the understanding of the employed experimental process is emphasised in this chapter.
- **Chapter 4** The impact of mechanical compression on the global PEFC performance is analysed and discussed in this chapter; The performance of a single-cell PEFC as a function of the assembly pressure is further investigated.
- **Chapter 5** An in-situ assessment of the mechanical compression and its impacts on the local phenomena taking place within the PEFC is detailed in this chapter. The impacts of mechanical compression on the current, temperature, and pressure distributions are investigated in this chapter.

The thesis is concluded by outlining the key contributions and by giving a number of proposed research activities to follow up on the work presented in this manuscript.

Chapter 1
Background

Fuel cells are nowadays extensively investigated by research teams for both mobile and stationary applications. This chapter aims to present the basic operating principle of PEFCs, their constituent components and their current state of development in different markets. This chapter begins with a brief overview of the history of fuel cells.

1 A brief history of fuel cells

The history of fuel cells is marked by a succession of periods of intensive research and incomplete abandonment. The concept of fuel cells was effectually demonstrated almost two centuries ago. After the age of early development, the principle of the fuel cell was published by the German-Swiss chemist Christian Friedrich Schönbein in the Philosophical Magazine in January 1839 [8]. Shortly afterwards, the British scientist William Robert Grove demonstrated the first fuel cell producing electricity from hydrogen and oxygen using platinum electrodes [9]. For many years, research on fuel cells had been going on, but without reaching the stage of applications.

Interest in fuel cells had lessened until the 1960s with the invention of PEFC by General Electric (GE) [10]. Many scientists and industrials started research on fuel cells, with the first applications in the military and space fields. NASA had first started research on fuel cell technology for the Gemini and Apollo programs [9]. However, cost issues and performance shortcomings had restricted fuel cells to limited applications, and fuel cells research was slowing down.

Problems related to global energy consumption have become increasingly acute since the 1970s with oil price shocks [11]. Fossil fuels have started being depleted while energy demand was increasing. During the 1990s, global warming issues commenced gaining ground and considerable research efforts were undertaken to make efficient use of renewables and to control the energy consumption better; this awareness rise was beneficial for fuel cells as they regained research interest and started being extensively investigated by research teams for stationary, transportation and portable applications. For the last 30 years, many technological barriers have been removed, and fuel cells are now closer than ever for large scale commercialisation.

2 Fuel cells basic principle

A fuel cell is an electrochemical device where the chemical energy of a fuel and an oxidant is converted directly into electrical energy and heat via an oxidation-reduction (redox) reaction. The fuel and the oxidant are supplied to the fuel cell under specified conditions of temperature, humidity, flow rate and pressure. The fuel cell produces electricity, heat and water as long as it is fuelled with chemical reactants (Figure 1.1). The reactants involved in the redox reaction are supplied permanently to the cell. The products formed as a result of the redox reaction are continuously removed.

Figure 1.1. Fuel cells' basic operating principle.

When it comes to fuel cells, it is often assumed that the fuel used is hydrogen or hydrogen-rich mix. This assumption is generally correct, though some fuel cells can also be operated using other fuels (e.g. methanol). In all cases, the operating principle remains the same and it is based on two electrochemical reactions. One occurs on the anode side where the fuel is oxidised (electrons released), the other takes place on the cathode side where the oxidant is reduced (electrons consumed). The electrical power generated by the fuel cell comes from the transfer of electrons from the anode to the cathode through an external load. The redox reaction is also characterised by the transfer of ions from one electrode to another through the electrolyte.

In fuel cells, the electrolyte, which is an ions conductor and an electrons insulator, determines the mode of operation of the fuel cell. The type of the electrolyte can have various forms and materials (e.g. polymer, alkaline, carbonate); therefore, different types of fuel cells exist today [2].

3 Fuel cell types

Fuel cells can be classified based on different aspects:

- The operating temperature, which distinguishes between high-temperature and low-temperature fuel cells.
- The type of the fuel (e.g. pure H_2, methanol).
- The liquid or solid state of the electrolyte.
- The pH of the electrolyte, which differentiates between alkaline and acid fuel cells, for which the mobile ions are anions and cations, respectively.

There are several types of fuel cells [2,12]; the most common ones are shortly presented hereunder:

- **AFC**s: Alkaline Fuel Cells operate at temperatures between 80 and 150 °C; the electrolyte is an aqueous solution of potassium hydroxide.
- **PEFC**s: Low-Temperature Polymer Electrolyte Fuel Cells operate at temperatures from 60 to 80 °C (LT-PEFCs); the electrolyte is a polymer membrane; the most commonly used materials are Nafion™-based. High-Temperature PEFC operate at temperature range 120-180 °C; the most promising membrane material is polybenzimidazole (PBI) doped with phosphoric acid [13]
- **DMFC**s: Direct Methanol Fuel Cells, the fuel is liquid methanol which reacts "directly" at the negative electrode. The operating temperature is in the range of 60 to 70 °C. The electrolyte is a membrane similar to that of PEFCs.
- **PAFC**s: Phosphoric Acid Fuel Cells operate at temperatures between 180 and 220 °C; the electrolyte is liquid phosphoric acid held in a porous matrix.
- **MCFC**s: Molten Carbonate Fuel cells operate at a temperature of around 650°C; the electrolyte is a eutectic mixture of lithium and potassium carbonates.
- **SOFC**s: Solid Oxide Fuel Cells operate at temperatures from 900 to 1100°C; the electrolyte is ceramic - Yttria-stabilised zirconia.

Each fuel cell type presents advantage and drawbacks depending on the nature of the electrolyte used, the operating temperature, and the cost per unit. These specifications make some fuel cell types more suitable for a specified application than another. The variety of fuel cell types is, therefore, a valuable advantage as it allows a wide range of applications.

In this manuscript, attention is turned to low-temperature PEFCs. This technology presents many advantages, including quick start-up time, low operating temperature, and a solid and compact structure. These advantages allow PEFC technology to be developed for various applications (e.g stationary, automotive, and portable). Their power range is extensive which allows this technology to contribute in a substantial part of the power generated by fuel cells worldwide, in 2019 the power generation by PEFCs attained 934.2 MW and it is expected to grow for the coming years [14]. Figure 1.2 shows the development of power generation per fuel cell type in the last five years.

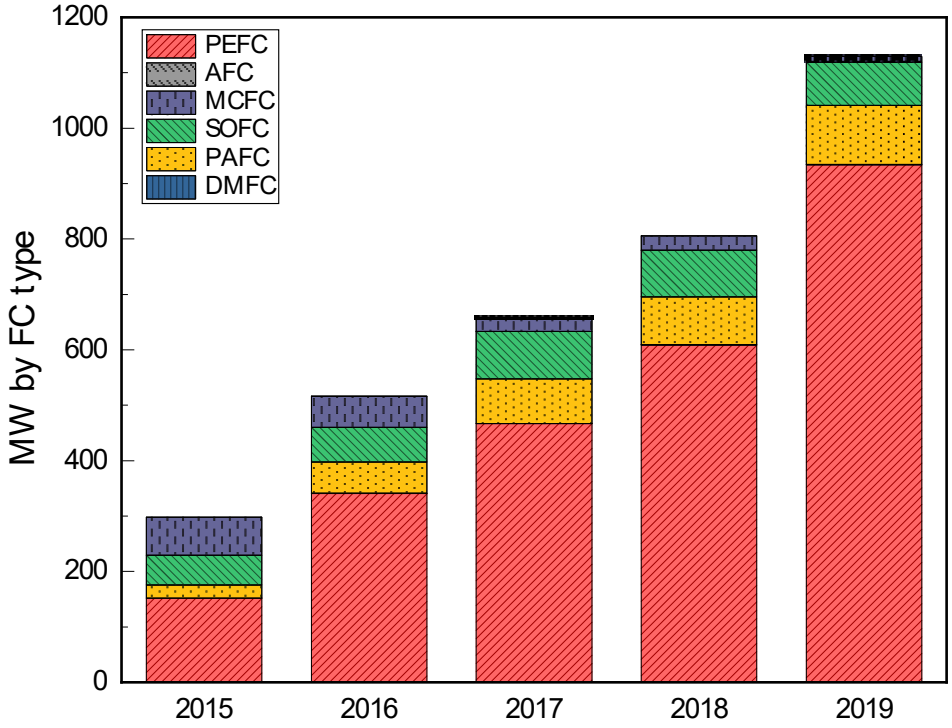

Figure 1.2. The development of power generation (MW) per fuel cell type from 2015 to 2019 [14].

PEFCs are nowadays undergoing rapid and significant development pushed by the willingness of fuel cell developers to offer, in the short run, an economically viable and reliable energy conversion solution. This technology, namely low-temperature PEFC, is further described in Section 6 of this chapter.

4 Hydrogen economy

Hydrogen is a chemical energy carrier that is versatile and might be used in a various range of applications. Over the coming decades, hydrogen economy would take a more prominent place in the ecological transition. One of the main reasons for this is that fuel cells can power a wide range of applications (e.g. mobile electronic devices, buildings, transportation). The following subsections provide some examples of fuel cells applications in three main sectors, namely stationary, portable, and transportation.

4.1 Stationary application

Fuel cells have significant potential in stationary applications, especially in the microgeneration of heat and power (µ-CHP) that offers many opportunities for fuel cells deployment in buildings. This technology can concurrently provide heat and electricity for a building; the operating principle is depicted in Figure 1.3. In 2019, the most significant part of fuel cell units shipment was for the stationary application, and this is mainly due to the Japanese ENE-

FARM programme delivering units for µ-CHP [14]. As a matter of fact, Japan leads the world in µ-CHP deployment, with over 235000 units installed in 2018 [15]. Similar projects are currently developed in Europe, namely the PACE project with some 2800 units to be installed by 2021 [16].

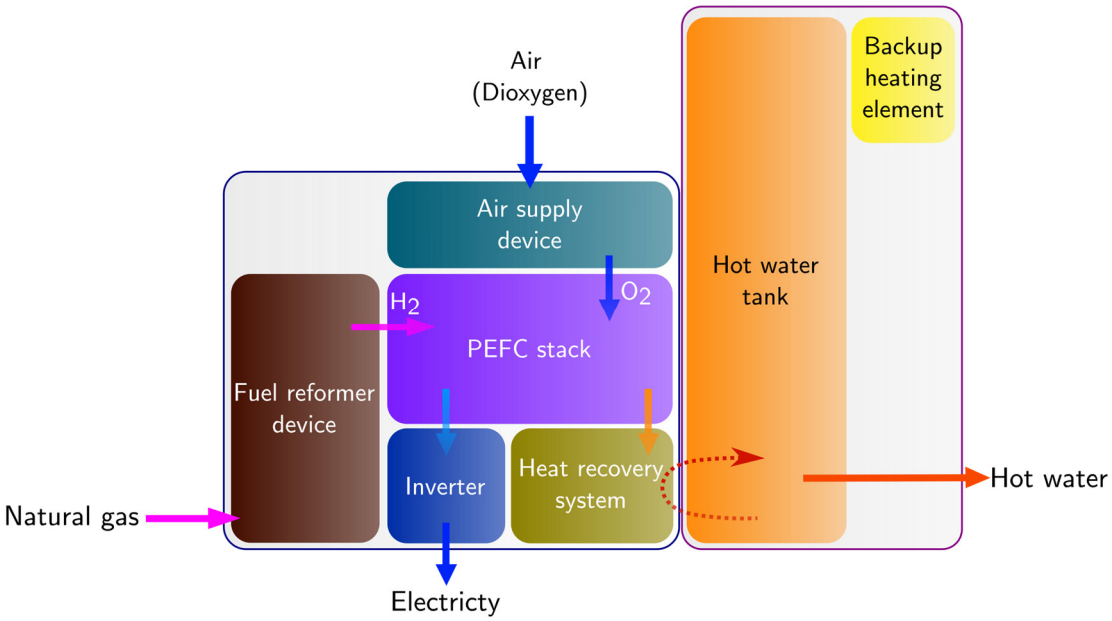

Figure 1.3. operating principle of a µ-CHP application using PEFC technology.

4.2 Portable market

The use of fuel cells in portable applications is quite encouraging as various portable devices may benefit from the reduced recharging time provided by fuel cells (e.g. mobile phones, laptops, cameras). Moreover, instant recharging via replacement or refiling of the fuel cartridge makes fuel cells favourable for nomad applications. In 2018, portable applications contributed to some 0.7 MW of worldwide fuel cells power generation [14]. The most significant contribution comes from SFC energy company [17] that has commercialised more than 41000 units based on PEFC and DMFC technologies, mainly for off-grid batteries recharging. Figure 1.4 depicts an example of fuel cell use in portable applications.

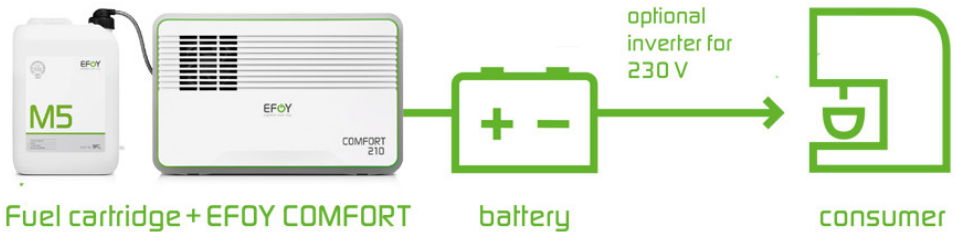

Figure 1.4. Example of DMFC portable application, EFOY COMFORT 105 W with a charge capacity of 210 Ah - Fuel cartridge M5 - 5 Litres [18].

4.3 Focus on the transportation sector

The transportation sector is at the centre of questions related to sustainable development. These questions arise from the fact that this sector is confronted with a paradox. On one side, the transport sector is essential for both the daily activities of individuals and the economic growth of countries. On the other hand, two main questions of its sustainability arise: the first is about its heavy dependence on fossil fuels as the primary source of energy supply, whereas the second is related to its relatively significant greenhouse gas emissions. Indeed, in 2018, the transport sector represented 8.1 Gt of CO_2 emissions, which represents 24% of global direct CO_2 emissions from fuel combustion, with 3.6 Gt of CO_2 (representing 44%) directly from passenger road vehicles [19]. Figure 1.5 depicts the transport sector CO_2 emissions by transport mode in 2018.

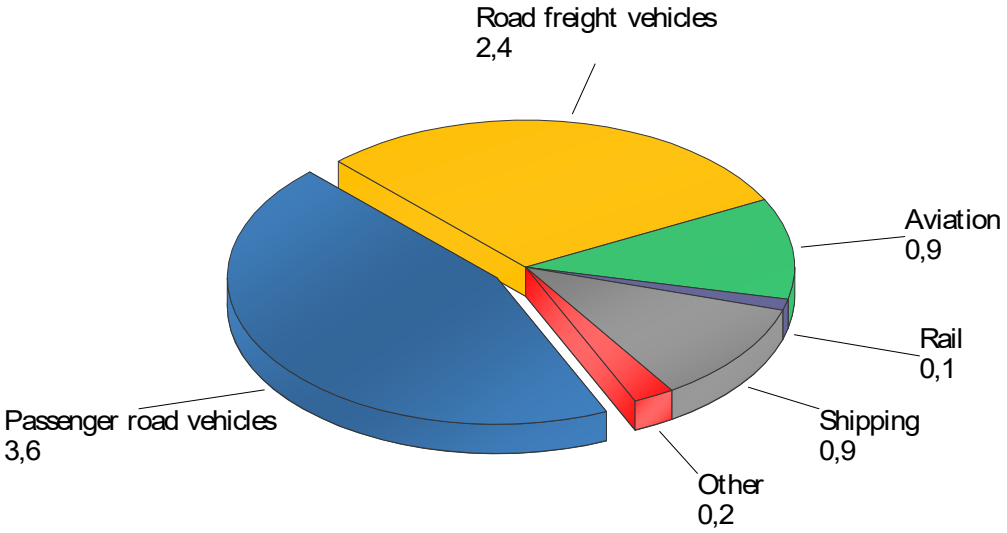

Figure 1.5. Transport sector CO_2 emissions (in Gt) by transport mode in 2018 [19].

In order to reduce both the transportation sector CO_2 emissions and its dependence on fossil fuels, decision-makers are seeking a sustainable transportation sector strategic orientation, which could be in part achieved through a hydrogen-based mobility.

4.3.1 Hydrogen mobility

Recent years have been marked by growth in interest amongst policymakers for hydrogen mobility and fuel cells deployment in virtually all the transportation modes (e.g. passenger cars, buses, trucks, trains, aircraft). Due to stricter environmental legislation, global transportation actors that are so far dependent on fossil fuels are seeking alternative technologies to stay competitive (in defensive and offensive ways) in the long-term run.

Passenger road vehicles are at the centre of the ecological transition to be carried out. This transportation mode is responsible for various environmental issues, and yet it remains an indispensable object for many activities. In the absence of an alternative, it is necessary to

rethink its energy source. In this context, Fuel Cell Electric Vehicles (FCEVs) would play a significant role in the ecological transition. FCEVs could reduce local air pollution as they provide zero tailpipe emissions. They can also reduce CO_2 emissions when a low carbon source is used to produce hydrogen. Moreover, at driving speed of 50 km/h, which is the maximum allowed speed in the majority of European cities, the efficiency of a fuel cell electric drive is twice as much as that of conventional internal combustion engines [20].

Battery Electric Vehicles (BEVs) will definitively play a significant role in future green transport as they present higher efficiency compared to FCEVs [21]. However, weight and recharge time are still their major disadvantages, especially as distances get longer and applications to become heavier. In fact, here where FCEVs enjoy advantages compared to BEVs, as the refuelling of the hydrogen reservoirs requires remarkably less time compared to batteries recharging time. Indeed, an FCEV requires approximatively 5 minutes to refill a 5 kg hydrogen reservoir, providing a range up to 500 km [22]. Actually, FCEVs running on hydrogen are complementary to BEVs; this is achieved through offering higher energy storage, which allows increasing the transported mass and autonomy. Several configurations are possible, ranging from FCEVs equipped with PEFCs with low power as range extenders to PEFCs capable of directly powering the vehicle engine. Figure 1.6 depicts the primary components of a passenger car FCEV.

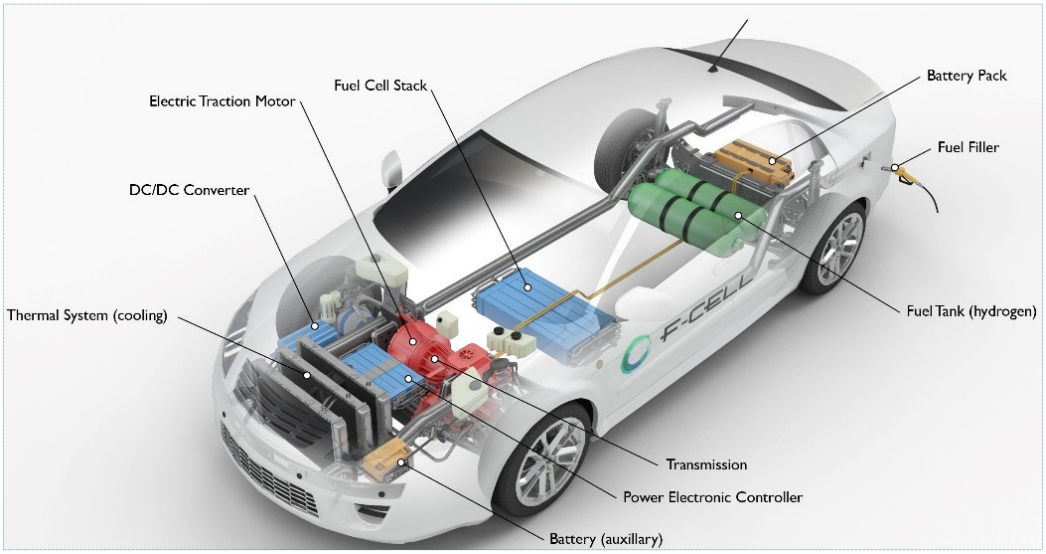

Figure 1.6. Key constituents of a passenger car FCEV [23].

Benefits are to come as fuel cells and hydrogen technology is getting more mainstream. For instance, Paris taxis Hype fleet, which is the world's first fleet of FCEVs taxis, counts 100 vehicles and aims to attain 10 000 FCEVs taxis by 2024 [24,25]. As a matter of fact, passenger cars represent the vast majority of FCEVs currently deployed in public roads. According to International Energy Agency (IEA), their number reached 11 200 in 2018, with more than half in the United States, followed by Japan and Republic of Korea. These numbers are still low but enthusiastic as they have augmented by 56% from 2017 to 2018 [11].

Up to 2019, passenger cars FCEVs are still majorly produced by Toyota (*Mirai* [22]) and Hyundai (e.g. *Nexo* [26]) with over two-thirds of fuel cell systems used in transportation were produced by these two automakers, with small participation of Honda and Daimler [14]. Enthusiastically, the leading FCEVs manufacturers are giving optimistic goals for the future, namely as Toyota aims to produce 30 000 FCEVs per annum starting from 2020 and Hyundai aims 70 0000 FCEVs per annum starting from 2030 [11].

The market penetration of FCEVs depends on the costs of fuel cells and onboard hydrogen storage as well as the construction and the utilisation of Hydrogen Refuelling Stations (HRS). For passenger cars, the challenge is to reduce the cost of the onboard hydrogen storage and fuel price which could finally make passenger cars FCEVs more attractive for ranges around 400-600 km, especially for nonurban users/fleets that prioritise long distances.

4.3.2 Hydrogen infrastructure

A good number of reliable HRS is needed to introduce more FCEVs into the market. Confidently, the number of HRS has been continuously growing recently, reaching 376 HRS worldwide by the end of 2018 [27]. These stations are located mainly in the first adoption regions, namely Japan (100 HRS), Germany (69 HRS) and United States (63 HRS). However, the low initial utilisation of HRS tends to rise hydrogen prices, and considerable work is still to be done to provide FCEVs users a comfortable use of their vehicles.

Finally, it has to be noted that around 70 Mt of pure hydrogen is produced per year, the majority of this pure hydrogen is used in oil refining and ammonia production (which is the basis of fertilisers). Only less than 0.7 % of hydrogen production comes from renewables or fossil fuels plants equipped with Carbon Capture, Use, and Storage (CCUS) [11], which shows that much work is still to be done to get to a "clean" ecological transition using hydrogen.

In order to get further into the problem of this thesis, it is necessary to present in more detail the operating principle of PEFCs. This technology dominated shipments by fuel cell type in 2019, either in power generation (more than 900 MW) or in the number of shipped units (44 000 units annually) [14]. The former is due to the development in the transportation sector, mainly the deployment in roads of the Toyota and Hyundai FCEVs [22,26], and the latter is due to the Japanese µ-CHP ENE-FARM project [15]. The following section aims to give a comprehensive understanding of the PEFCs and their main constituent components.

5 Low-Temperature Polymer Electrolyte Fuel Cells – LT-PEFCs

5.1 PEFC single-cell Operating principle

PEFCs have the basic structure that is common to all fuel cell technologies, namely the membrane electrode assembly (MEA) as shown in Figure 1.7.

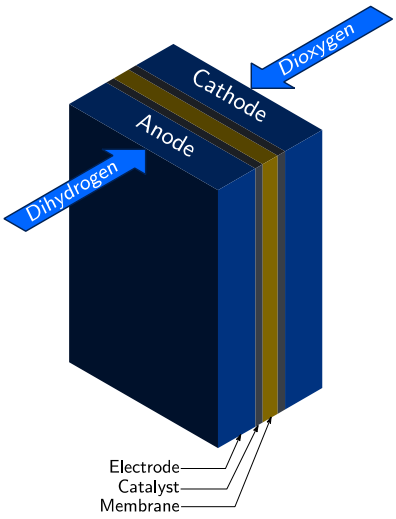

Figure 1.7. Membrane Electrode Assembly of a PEFC.

In a PEFC, hydrogen is used as a fuel and oxygen (commonly from ambient air) as an oxidant. The hydrogen is introduced at the anode where it is oxidised into electrons e^- and protons H^+ (1.1). The resulting H^+ protons pass through the electrolyte while the electrons e^- flow through an external circuit. Air (or less commonly pure oxygen) is introduced at the cathode, where the oxygen is reduced to water (1.2). In order to improve the kinetics of the electrodes' reactions, a catalyst layer made up of carbon agglomerates on which are deposited fine platinum particles is used. The overall redox reaction (1.3) corresponds to the reverse principle of water electrolysis.

Anode	$H_2\ (g) \rightarrow 2H^+(aq) + 2e^-$	(1.1)
Cathode	$\frac{1}{2}O_2(g) + 2H^+\ (aq) + 2e^- \rightarrow H_2O\ (l)$	(1.2)
Overall	$H_2\ (g) + \frac{1}{2}O_2(g) \rightarrow H_2O\ (l)$ + electrical energy + heat	(1.3)

The produced heat is generated as a result of: i) the transport of protons and electrons through the different fuel cell components, and ii) the oxygen reduction reaction at the cathode [28].

5.2 PEFC single cell structure

State-of-the-art PEFC is composed of different components, including cathode and anode catalyst layers (CLs), polymer electrolyte membrane (PEM), gas diffusion layers (GDLs), bipolar plates (BPPs), end plates, current collectors, gaskets, and commonly a thin layer referred as a microporous layer (MPL) located between the CL and the GDL, which is commonly considered as a part of the GDL. Figure 1.8 below depicts the operating principle and the core components of a single cell PEFC.

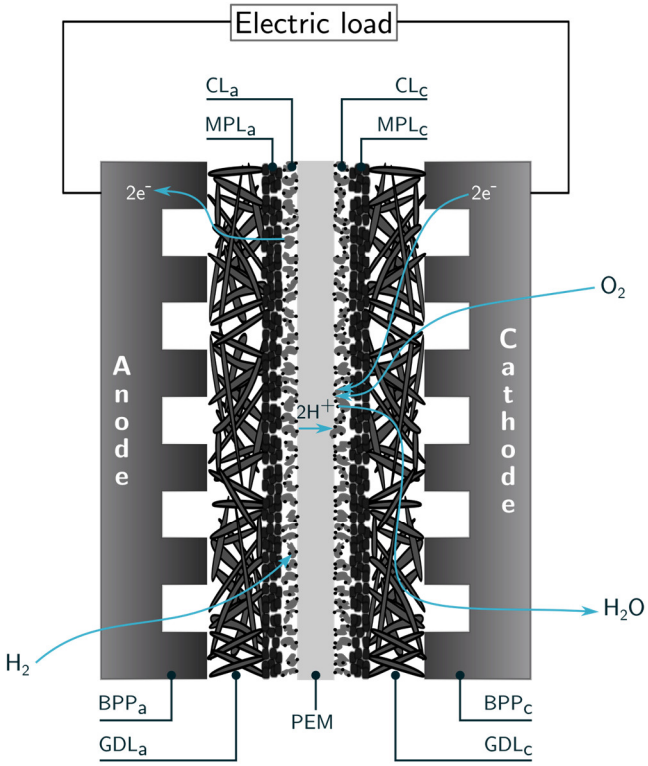

Figure 1.8. Typical single-cell PEFC components.

5.2.1 Membrane

The membrane is a thin layer (range [22 – 254 µm] [29]) that acts as an electrolyte; the most widely used is Nafion™ [30]. This material, when sufficiently hydrated, allows the conduction of H^+protons while preventing electrons and reactants from passing through it. The main characteristic of a membrane is its ionic conductivity, which is a function of its thickness and, especially, of its state of hydration. Insufficient hydration increases the ionic resistance of the membrane while excessive hydration reduces the catalytic activity by blocking the pores of the active area. It is, therefore, necessary to maintain a well-specified level of humidification to achieve optimal PEFC operation.

The membrane degradation can be classified into three main categories, namely thermal, chemical/electrochemical, and mechanical [31]. Among all, mechanical degradation is responsible for many early life failures due to cracks, perforation, pinholes, and tears formation [31]. These effects are mainly due to the swelling and shrinking of the membrane as a result of the change in its water content (i.e. membrane humidification). Humidification variations are mainly caused by changes in the operating parameters (e.g. flow rates, relative humidity of the inlet reactants, temperature, load current). Low water content shrinks the membrane and makes it fragile and brittle, whereas over humidification swells the membrane and generates stresses as the membrane is mechanically constrained between the electrodes [24]. The effects of membrane swelling/shrinking are described in more details in the following chapter.

5.2.2 Catalyst layers

The catalyst layers are the site of the electrochemical redox reaction. Their role is to speed up reactions, especially at low operating temperatures. Usually, Platinum is used for the cathode and Platinum/Ruthenium mixture for the anode. The catalyst is generally attached to fine carbon particles that are deposited on the membrane. The main drawback of these materials is the high price of the noble metals used; the objective is to reduce their quantities as much as possible. This could be achieved, for instance, by decreasing the particles size and improving the homogeneous dispersion on the catalyst support [32].

The catalyst layers are sensitive to chemical poisoning, especially by carbon monoxide (CO). In an operating PEFC, CO molecules adsorb on the surface of the platinum more easily than hydrogen and therefore block access for H_2 molecules. This sensitivity requires the reactants to be purified to an acceptable contaminants level, which explains the use of pure H_2 in PEFC. Corrosion of the catalyst layer carbon support is also a critical degradation factor. In fact, two modes are leading to carbon corrosion: i) fuel starvation caused by H_2 blockage and ii) start-up/shutdown cycles [33]. This degradation leads to i) a decrease in the conductive material of the catalyst layer (which in turn increases the internal resistance of the cell), and ii) a reduction of the active surface of the electrode.

Another notable degradation factor is the volume changes of water (namely due to freeze/thaw cycles) on the physical properties of the membrane/catalyst layer interface. This catalyst layer degradation is caused by mechanical stresses generated by ice expansion at sub-zero operating conditions. This effect is described in more details in the second chapter of this manuscript.

5.2.3 Gas diffusion layers

The GDLs are carbon-based porous materials (porosity reaching 70% to 85 % [34]), generally treated with a hydrophobic agent (e.g. polytetrafluoroethylene - PTFE), to improve its water-repellent characteristics. Metal-based GDLs are also currently developed [35,36]. However, carbon-based GDLs still represent the typical material of PEFC GDLs [37]. Therefore, the focus will be on the carbon-based GDLs for the rest of this manuscript.

Carbon-based GDLs play a vital role in the diffusion of reactant gases and the water management. In PEFCs, GDLs need to: (1) - provide pathways for reactant gases from the BPPs channels to the catalyst layers; (2) - provide pathways for product water from the catalyst layer to the BPPs channels; (3) - electrically connect the catalyst layers to the BPPs; (4) - conduct heat generated during the electrochemical reactions from the catalyst layers to the BPPs (which have means for heat removal); (5) - mechanically support the MEA; and (6) - homogenise the distribution of the reactants from the BPP channels to the CLs. In order to ensure these functions, the GDL must be: (1) - sufficiently porous to allow the flow of both reactant gases and product water (which have opposite flow directions); (2) - electrically and thermally conductive; and (3) - sufficiently rigid to support the MEA and at the same time flexible to maintain good interfacial contact with the adjacent components. The GDLs are

often coated with an MPL to reduce the contact resistance and the mass transport resistance, especially at high current densities [38], and mitigate water management issues [39–41]. Various GDL types have been reported in the literature, and each type has its specified characteristics. Figure 1.9 shows different types of carbon-based GDLs, namely carbon cloth, carbon paper, and felt/spaghetti paper [42].

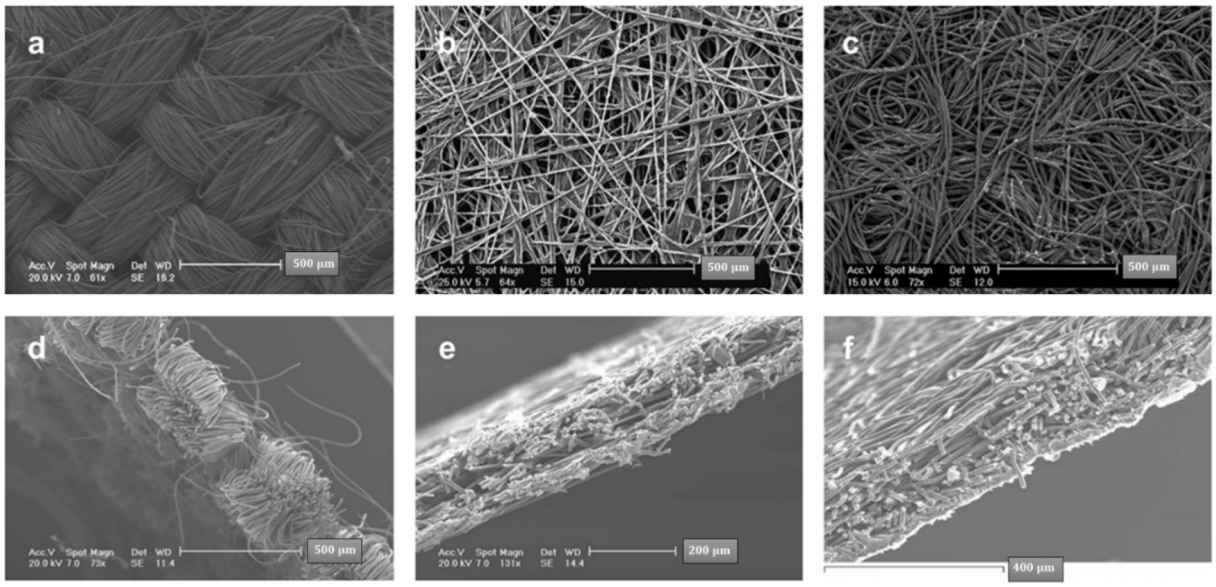

Figure 1.9. Different GDL materials a) & d) woven fibres in carbon cloth; b) & e) straight stretched fibres in carbon paper c) & f) felt fibres in carbon paper. Modified from [42].

Mechanical stresses cause the main degradation effects of the carbon-based GDLs, and these effects are further detailed in the following chapter of this manuscript.

5.2.4 Bipolar plates

Bipolar plates (BPPs) ensure reactants distribution on the MEA surface as well as electronic conduction so that electrons from the electrochemical reaction can flow from one cell to the other. BPPs also provide the mechanical strength to the stack; they also have the role of evacuating excess reactants and water produced by the redox reaction. Some BPPs also integrate PEFC temperature control by means of channels in which a heat-transfer fluid circulates.

Different shapes of BPPs are currently developed including, among others, parallel, serpentine, parallel-serpentine, and interdigitated designs. Figure 1.10 shows some of the typical configurations. The optimal choice of channels configuration is an essential parameter for uniform distribution of current density, efficient water management, and stable PEFC operation [43].

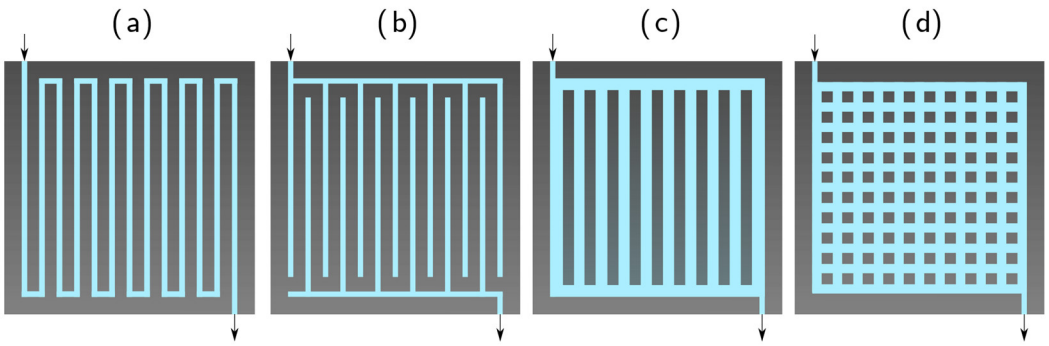

Figure 1.10. BPPs geometry design, (a) Serpentine design (b) Interdigitated design (c) Parallel design (d) Pin design.

BPPs are generally made by machining/moulding of high-density graphite. This material choice is stemmed from the excellent electrical and chemical properties (high corrosion resistance) of graphite material in the PEFCs' harsh operating conditions. However, graphite BPPs account for 80% and 40% of the total PEFC stack weight and cost, respectively [44]. This is caused by the costly and time-consuming process of the machining of gas channels in graphite BPPs. Recently, attention was turned to metallic bipolar plates as they offer superior mechanical properties (better shock resistance compared to graphite BPPs), better manufacturability (i.e. stamping and hydroforming), lower gas permeability and high electrical conductivity [44,45].

The main failure modes of the BPPs are originating from corrosion caused by the acid and humid conditions inside the fuel cell stack, especially in metallic BPPs. This effect can adversely impact the performance and durability of the PEFC [44]. Corrosion can also contaminate the membrane and may adversely affect the catalyst layer leading to performance loss and, in worst cases, premature failure of the stack. Mechanical stresses also affect the durability of the BPPs. In fact, BPPs are subjected to mechanical tightening forces to prevent reactants leaks and provide sufficient contact surface. Inhomogeneous tightening can cause deformation or cracks, especially in graphite BPPs. Theses defects are accentuated under severe environmental conditions (e.g. shocks and vibrations).

5.3 PEFC performance characteristics

A PEFC converts chemical energy into electrical energy. For standards conditions (@0.1 MPa and 25 °C), the open circuit voltage (OCV) can be given by [46]:

$$E_0 = \frac{-\Delta G_f}{n.F} \tag{1.4}$$

Where:

- ΔG_f is the Gibbs free energy of formation (kJ.mol^{-1}).
- F is the Faraday's constant (96 485 C.mol^{-1}).
- n is the number of electrons transferred for each molecule of hydrogen used (n=2 in PEFC).

The value of ΔG_f depends on the temperature and the form, liquid or gaseous, of the produced water. In PEFCs, if we assume that water is in the liquid form, then ΔG_f=-237 kJ.mol^{-1} (higher heating value – HHV of the consumed H_2). From (1.4) the ideal OCV at standard conditions is given by:

$$E_0 = \frac{237.2}{2 \times 96458} = 1.229 \text{ V} \tag{1.5}$$

5.3.1 The Nernst equation

The Nernst's equation integrates the changes in Gibbs free energy of formation with reactants pressure and temperature, that is when the fuel cell is not working at standard conditions:

$$E_{rev} = E_0 + \frac{RT}{2F} \ln\left(\frac{a_{H_2} . a_{O_2}^{\frac{1}{2}}}{a_{H_2O}}\right) \tag{1.6}$$

Where:

- E_{rev} is the reversible fuel cell voltage.
- T is the absolute temperature.
- R is the universal gas constant (8.314 J.K^{-1}.mol^{-1}).
- a is the activity of an ideal gas and might be expressed in terms of its partial pressure [46]:

$$a = \frac{P}{P^0}$$

Where P^0 is the standard pressure (0.1 MPa) and P is the partial pressure of the gas. Since the LT-PEFC operates under 100 °C, so that liquid water is produced, the activity of water can be set to 1 (a_{H_2O}=1). In this case, the Nernst's equation becomes:

$$E_{rev} = E_0 + \frac{RT}{2F} \ln\left(P_{H_2} . P_{O_2}^{\frac{1}{2}}\right) \tag{1.7}$$

The voltage given in (1.7) is the maximum theoretical voltage that could be obtained if the chemical energy of reactants is fully converted into electrical energy without any loss. This maximal possible fuel cell voltage is the reversible fuel cell voltage ($V_{rev}=E_{rev}$), which is achieved when the fuel cell operates under thermodynamically reversible conditions [47]. In practice, the output voltage of a fuel cell, at a specified current density (i_{FC}), is the difference between the reversible and the irreversible fuel cell voltage (V_{irrev}) (also called overpotential, polarisation, and voltage loss) and can be written as:

$$V(i_{FC})=V_{rev}-V_{irrev} \tag{1.8}$$

5.3.2 PEFC voltage losses

For given PEFC operating conditions (e.g. temperature, pressure, flow rate, humidification), the characteristics of the voltage/current density graph (i.e. the polarisation curve) results from different voltage loss sources, namely:

- **Fuel crossover and internal currents losses $\eta_{crossover}$:** these losses are related to the permeation of reactants through the membrane from both sides. Moreover, the membrane material is not completely insulator for the electric current, and therefore some amount of electrons flow will be taking place. As a result of these losses, the practical OCV is slightly less than 1 V and will always be lower than the theoretical voltage [48,49].
- **Activation losses η_{act}:** this type of losses is related to the slowness of the kinetics of the electrochemical reaction taking place on the surface of the electrodes. These losses are highly nonlinear, and they are higher at the cathode compared to the anode as the oxygen reduction reaction (ORR) is four to six times slower than the hydrogen oxidation reaction (HOR) [50].
- **Ohmic losses η_{Ω}:** this voltage drop reflects resistances to electrons e^- and protons H^+ flow. Losses related to electrons flow are located in the electron-conducting materials and their different interconnections (i.e. due to contact resistance). Losses due to proton transport are located in the membrane and the active area of the electrodes.
- **Mass transport losses η_{mass}:** also called concentration losses and arise from reactants concentration drop at the active area surfaces. These losses originate more importantly from the limitation in the diffusion of reactants and liquid water accumulation resulting in GDLs pores and BPPs channels blockage. This type of loss is more prominent on the cathode side, due to the relatively important production of liquid water compared to the anode side.

Combining all the presented voltage losses, the operating PEFC voltage can be written as:

$$V(i_{FC})=V_{rev}-\eta_{crossover}-\eta_{act}-\eta_{\Omega}-\eta_{mass} \tag{1.9}$$

Figure 1.11 shows a typical polarisation curve of a single cell PEFC with different sources of voltage loss.

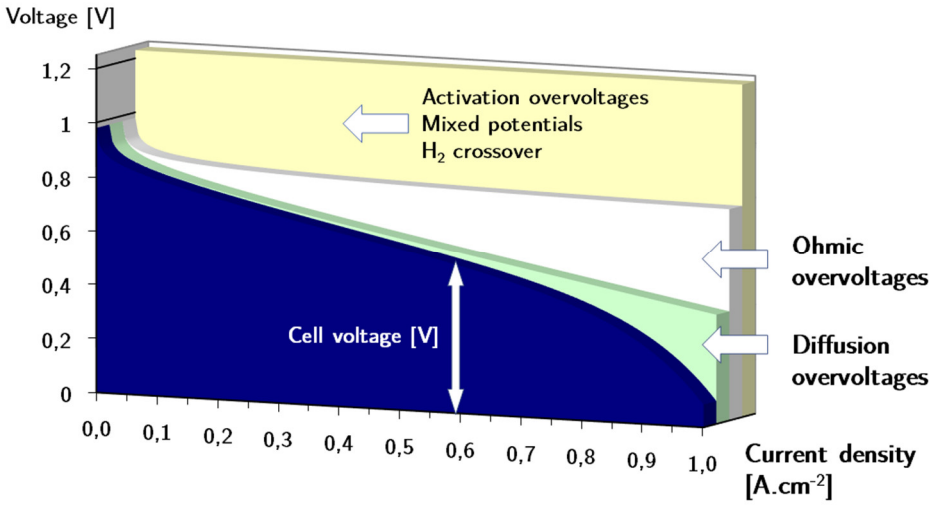

Figure 1.11. Typical PEFC polarisation curve showing the different sources of voltage loss.

5.4 PEFC system

Generally, the nominal voltage produced by a single cell PEFC is around 0.5 - 0.7 V at rated conditions of power generation [51]. In order to obtain a higher voltage, multiple cells are stacked together (i.e. electrically connected in series) forming a "PEFC stack" by way of mechanical fasteners (e.g. 370 cells in the Toyota Mirai [22]).

The fuel cell system is composed from the fuel cell stack and the auxiliary components needed for its operation, also called balance-of-plant. The auxiliaries ensure the supply and the conditioning of the reactant gases, the control of the fuel cell temperature, the evacuation of products and heat, the conversion of the electrical energy, and the management and control of the entire fuel cell system. Figure 1.12 depicts a real-life application of the PEFC system with the auxiliary components.

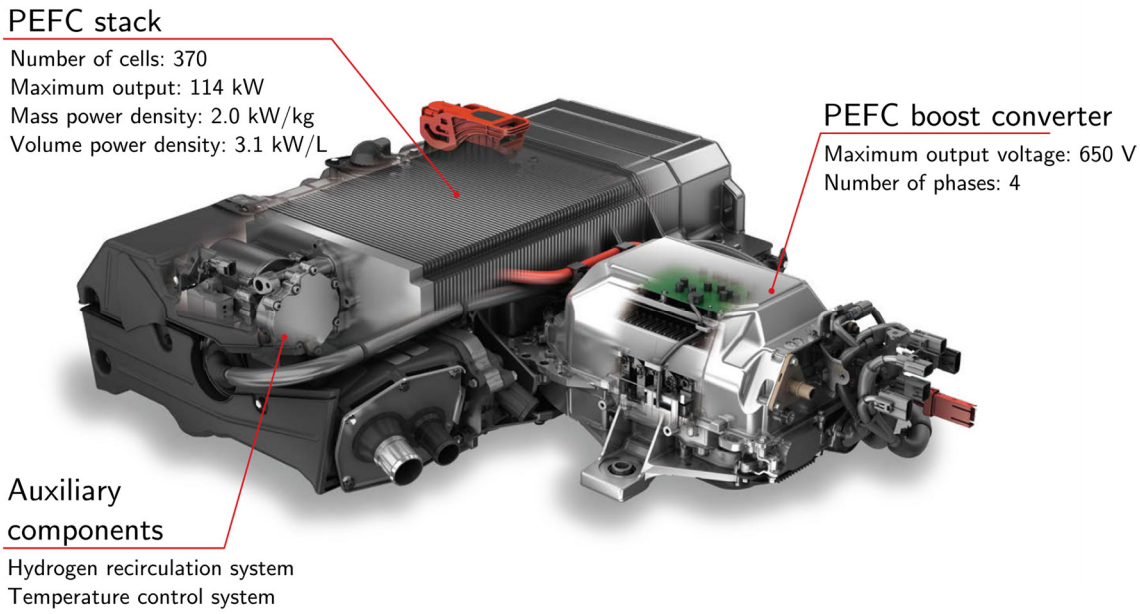

Figure 1.12. Toyota Mirai PEFC system [22].

5.5 PEFC stack assembly

For the PEFC to operate at useful voltage, the individual cells must be assembled in a stack, which requires means of mechanically connecting the cells to provide efficient current collection, reactants tightness and distribution. Traditionally, A PEFC stack consists of a series of single cells clamped firmly by various tie rods and bolts (i.e. point-load design). A typical PEFC stack configuration is depicted in figure 1.13.

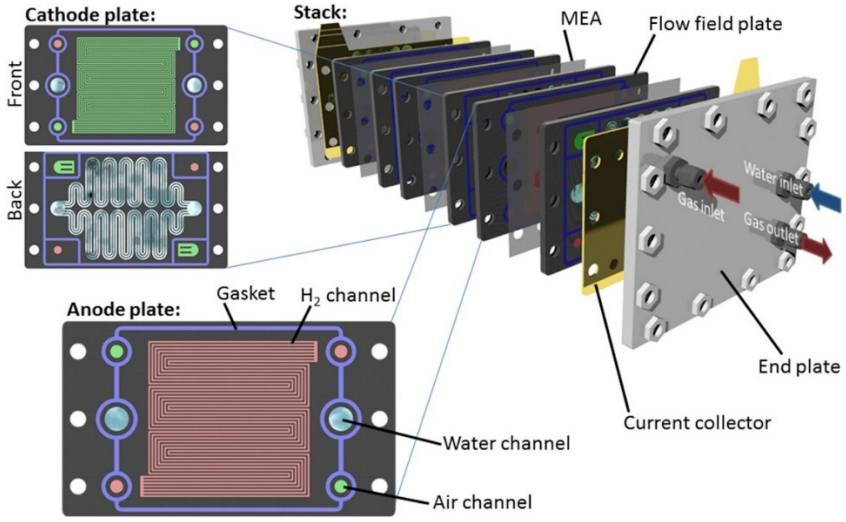

Figure 1.13. PEFC stack assembly comprising an exploded view (right side), cathode and anode BPPs showing gas and heat-transfer fluid channels (left side) [7].

The clamping force ensures both the sealing of the PEFC stack and the electrical conduction between its single cells' components. An excellent sealing is crucial for fuel cell operation as reactants leakage can reduce the power density of the fuel cell and lead, in worst cases, to hazardous situations. Also, the electrical resistance is inherent during the electrical conduction, leading to a loss of performance as previously described in the polarisation curve (Figure 1.11). Electrical resistance is not only due to the bulk resistance of the stack components, but also to the contact resistance at the interfaces between the components of the fuel cell. Therefore, the mechanical characteristics at the interfaces of the PEFC components must be studied in order to reduce the stack's ohmic resistance.

As well as good electric conductivity, the efficient gas supply is also crucial for optimal PEFC operation. It is necessary to uniformly supply the reactants for continuous operation of the PEFC. The reactants supply is achieved through engraved/embossed channels on the BPPs and also by the GDLs' pores. On the one hand, the shape, size, and configuration of the channels of the BPPs are crucial for the optimal feeding of the reactant gases. On the other hand, GDLs' porosity is essential for the transport and the homogenisation of the reactants (from BPPs to MEA) and products (from MEA to BPPs). As described previously, GDLs are made of carbon paper, with a high porosity to facilitate reactants and products transport. Also, at equivalent stress, GDLs deform more than any other component of the PEFC [52]. When the PEFC is subjected to mechanical stresses, the GDL porosity is reduced, which hinders the flow of reactants and liquid water, leading to a reduction in fuel cell performance. Therefore, a trade-off between the reduction in the ohmic resistance and the GDLs' porosity is to be found in order to optimise the PEFC performance.

6 Conclusion

The hydrogen economy has gained considerable development momentum in the last few decades and hydrogen might finally be put on its way to fulfil its long-term capabilities as a clean energy carrier. It may also help tackle energy conversion issues as it provides, in more ways than one, solutions to decarbonise many sectors. This enthusiastic vision is, however, conditioned by a hydrogen generation and distribution infrastructure based on renewables, which could finally reduce the reliance on fossil fuels. Such an asset is of paramount importance to reduce the energy dependency of countries with low, if any, reserves of fossil fuels.

Among various types of fuel cells, PEFCs are the most promising ones, especially in the transportation sector as a number of car manufacturers have started commercialising passenger cars based on this technology (FCEVs). However, a deep understanding of all the parameters affecting the fuel cell performance is of significant importance for the PEFCs to be competitive with other traditional energy conversion devices that present mature technologies so far.

One of the factors that affect the PEFC performance is the mechanical compression inside the stack. Although this compression plays a vital role to ensure efficient gas sealing along with optimised electrical and thermal conductivities during PEFCs operation, excessive mechanical

pressure may worsen the fuel cell performance through reducing the porosity and transport ability of PEFC components. It is therefore important to provide a comprehensive study on the performance of the PEFC when subjected to mechanical stresses to be able to enhance and optimise the PEFC performance, which brings us to the following chapter of this manuscript.

Chapter 2
Effects of mechanical compression on the performance of PEFCs

PEFC has been shown as a promising solution to decarbonise many sectors. In the last few years, significant efforts have been made to commercialise PEFC-based energy conversion systems on a larger scale. With this relatively recent trend to deploy fuel cells in a wide range of applications, production needs to be shifted from small-scale manufacturing to more established industrial processes. That led the research community to investigate aspects related with the mechanics of fuel cell stacks. In this context, mechanical stress inside the PEFC stack represents one of the main factors that affect the performance of the fuel cell. In a PEFC, two major types of compression mechanisms take place, the first is due to external forces (e.g. the applied compression during the assembly process), and the second is caused by internal forces that are generated inside the fuel cell during its operation (e.g. membrane hydration/dehydration, temperature variation, freeze/thaw cycles). In both cases, components within the fuel cell are subjected to compressive forces that may either improve or worsen the fuel cell performance. Figure 2.1 represents the compression sources associated with each fuel cell component.

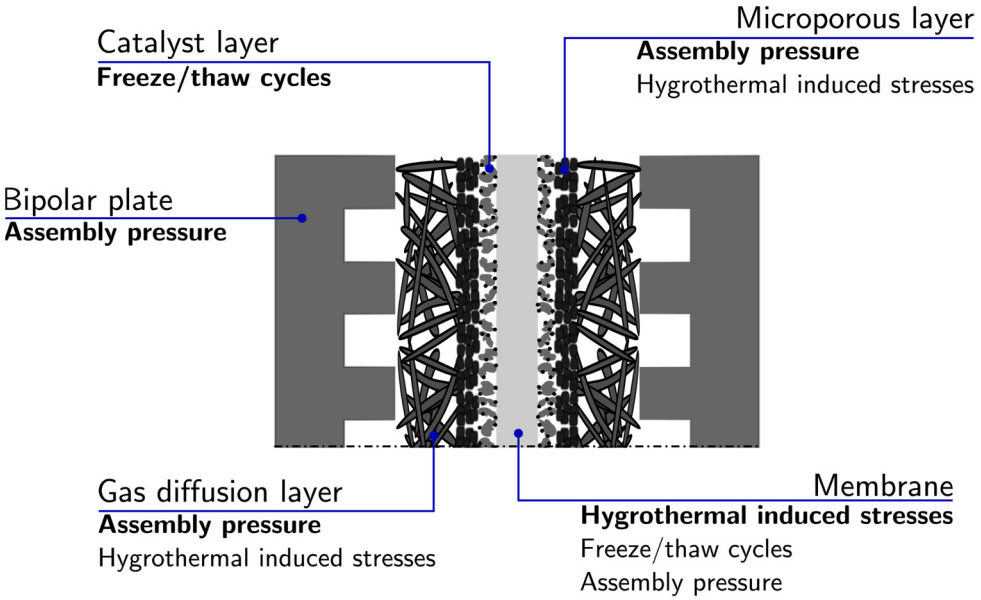

Figure 2.1. Different effects of mechanical compression on a PEFC; in bold the most important effects on each component.

Fuel cell stacks require mechanical compression during the assembly process to ensure both good electrical and thermal conductivities, between the stack components, and gas-tight operations. The clamping pressure influences not only the protonic and electronic conductivity but also the porosity of the gas diffusion layers (GDLs). Recently, intensive research studies have focused on the GDLs due to the strong relation between their compressibility and the performance of the PEFCs. In fact, excessive clamping pressure can lead to a decrease in contact resistance but also to a decrease in the porosity of the GDL, which reduces the supply of reactants gases to the CLs and hinders excess water from being removed.

Assembling a fuel cell stack requires first an accurate control to ensure proper alignment of the stack's individual components, then an appropriate assembly pressure is applied in order to achieve adequate contact between the fuel cell components and to ensure gas-tight operation. In order to prevent hazardous situations, sealing gaskets are generally inserted between the MEA and the bipolar plates to ensure that no gas leakage (between the fuel cell and its external environment) occurs during the fuel cell operations. Various investigations have been reported in the literature to assess compression characteristics during the assembly process, either by simulations using numerical models [53,54] or experimental investigations using piezoresistive arrays [55,56] or pressure-sensitive thin films [57,58]. However, each fuel cell component has its unique characteristics, especially the GDLs. Thus, the assembly pressure depends on these characteristics, which makes it challenging to propose a recommended assembly pressure value for PEFCs.

In order to assess the effects of assembly pressure on fuel cell performance, several characterisation techniques have been used in the literature. Two main types of characterisation are currently employed: (1) - ex-situ, where the individual components are characterised externally to the fuel cell, (2) - and in-situ, where the components are characterised within a fuel cell operating in real-life conditions. Through employing these characterisation techniques, a number of researchers working on the characterisation of PEFCs are placing their focus on some particular issues: (1) - GDL electro-physical properties [59–61]; (2) - mass transport limitations [62–64]; (3) - durability [65–67]; (4) - water transport visualisation techniques [68–70]; and (5) - pressure distribution [55–58]. Due to the complexity of the occurring phenomena, PEFCs must be diagnosed using suitable techniques that allow both the evaluation of all the presented issues and the separation of their respective impacts on the overall fuel cell performance.

Until now, numerous characterisation techniques have been reported in the literature to assess the fuel cell performance. A number of reviews focusing on the characterisation techniques for PEFCs have already been reported. Wu et al. [71] presented a review of the diagnostic tools employed in PEFC using electrochemical techniques. Arvay et al. [72] reported a review of the characterisation techniques for GDLs used in PEFCs. Their study focused on the essential properties of GDL, i.e. thermal and electrical conductivity, porosity, pore size, gas permeability, and wettability. The authors regrouped a set of tools used for the evaluation of GDLs by the use of in-situ and ex-situ characterisation techniques and concluded that the employment of

both in-situ and ex-situ techniques is of significant importance towards developing high-performance GDLs.

Whilst a number of studies in the literature have focused on the ex-situ characterisation techniques to investigate the effect of mechanical compression on the fuel cell performance [73–76], others employed both ex-situ and in-situ techniques with less focus on the latter [77,78]. Some review studies have also been reported in the literature so far [6,7,79]. In all these studies, it was well recognised that mechanical stress is one of the main factors that affect PEFC performance. In a recent review on the effect of mechanical compression and dimensional change analysis on PEFC components [7], a special attention has been attributed to the GDLs, and a range of dedicated characterisation methods have been presented. In their manuscript, Millichamp et al. [7] provided a good state-of-the-art review regarding these issues, with an important focus on ex-situ characterisation techniques. A number of clamping methods described in the academic and patent literatures has also been presented. However, no direct conclusion was drawn since there were no comparative studies on the different clamping procedures [7]. In another study, Dafalla and Jiang [6] reported a comprehensive review of the mechanical stresses and their related effects on structural properties of PEFC components and performances. The authors reviewed different sources of stress within the cell and their respective impacts on its performance deterioration as well as the induced structural damage of the fuel cell components. The report concluded that a comprehensive understanding of the combined realistic effects of mechanical stresses might be of major influence on the enhancement of fuel cell performance.

Thus far, to the best of our knowledge, no review focusing principally on the effects of mechanical compression on PEFCs operating in real-life condition, that is to say on in-situ characterisation techniques, has been reported in the literature. The effects of the generated stresses within an operating fuel cell evaluated by the use of in-situ characterisation technique have not been reviewed so far, even though they might be a key issue towards the improvement of the fuel cell performance. In this regard, the objectives of this chapter are to identify and review studies tailored towards the investigation of these effects, to provide a comprehensive overview of the experimental in-situ characterisation techniques and to suggest promising routes for more advanced PEFCs characterisation techniques. Based on this review, a summary of the progress made in the investigated field and an outlook for future works are then put forward. The review presented in this chapter was first published in the *Journal of Power Sources – Elsevier*. The present chapter is, therefore, an extended and updated version of the previously published paper [5].

1 Sources of mechanical stress and their respective impacts

A fuel cell operated in real-life conditions is subjected to many stresses, originating either from internal or external sources. In this section, compression mechanisms and their respective effects are presented.

It has to be mentioned that in all the following sections of this chapter, and for comparison purposes, compression data are preferentially provided in MPa units (which equals to 1 $N.mm^{-2}$). However, in a number of the studies reported in the literature, this information has not been provided or cannot be determined. In these cases, other compression data (e.g. clamping torque, compression ratio) are given.

1.1 Assembly pressure

One of the significant sources of mechanical stresses within the fuel cell components is the clamping pressure. These induced stresses are generated during the final operation of the assembly process of the fuel cell stack. Although mechanical compression must be evenly applied onto the fuel cell stack to prevent gas leakage during the fuel cell operation, excessive compression was shown to cause permanent damage to the fuel cell components [52,80,81]. Compared to other fuel cell components, the GDL is considered to be the component most subjected to structural deformation under compressive loads due to its soft and brittle structure [52,82]. Mason et al. [81] presented a study on the effect of GDL compression on PEFC performance. It was observed that higher compression not only leads to deformation of carbon fibres, but also to an increasing number of high-stress regions between intersecting fibres that causes fibre crushing. Moreover, GDLs can deform differently under the applied compression. Under the channels, the GDL intrudes in the void spaces creating a phenomenon referred to as 'tenting'. Whereas under the ribs, the GDL is compressed to the gasket thickness [83] and the carbon fibres are crushed. This leads to a decrease in the porosity of the GDL that, in turn, increases the mass transport resistance of the fuel cell stack. This resulting loss in the ability to supply the reactant gases to the catalyst layers may induce reactants starvation and could also hinder liquid water from being removed causing flooding [84]. The Scanning Electron Microscopy (SEM) images shown in Figure 2.2 depict the compression effect on a carbon paper GDL, with the two regions of compressed and uncompressed material, under the ribs and the channels, respectively. The rib area is visible from the zone (b), where broken and compacted carbon fibres can be seen. The compression of GDL fibres not only decreases the porosity of the GDL material but also enlargens internal fibre connections leading to a decrease in the contact resistance. This latter effect will be discussed in more detail in the next sections.

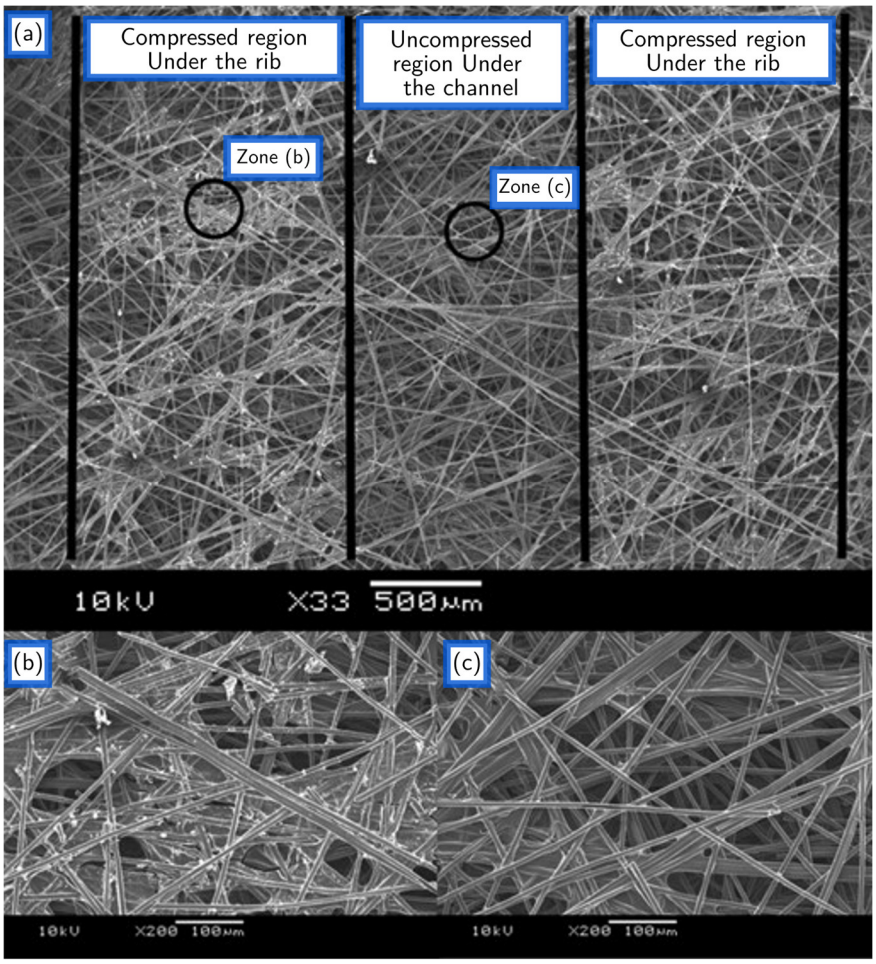

Figure 2.2. SEM image of a GDL carbon paper under mechanical compression of 2,5 MPa depicting: (a) the impression of the BPP ribs and channels, (b) broken and compacted fibres under the rib, and (c) uncompressed zone under the channels [81].

Khajeh-Hosseini-Dalasm et al. [85] carried out a study on the effects of mechanical compression on a TGP-H-120 Toray paper GDL using the high-resolution X-ray Computed Thermography (CT) technique. Under a compression of 3 MPa, a 16% reduction in the average porosity was observed between the region under the rib and the zone under the channels. In addition, a significant GDL penetration into the channel was seen as the compression increased, namely 28, 61 and 132 µm were measured under compression of 1, 2 and 3 MPa, respectively. In line with [85], Kandlikar et al. [80] investigated the effects of GDL intrusion into the gas channels of the BPP. The authors reported that as the compression was applied, a part of the GDL protruded into the channels, leading to a partial blockage of the gas channels. Furthermore, it was observed that this intrusion was not uniform for all the gas channels; some significant intrusions were witnessed within the channels located at the edges of the BPPs. This effect was explained by the location of the assembly bolts that were located at the edges of the used PEFC fixture.

1.1.1 Electrochemical characterisation techniques

Electrochemical techniques have been widely employed for in-situ investigations on the effects of mechanical stresses on PEFC performance. Thus far, two usual methods have been typically reported in the literature covering this area, namely polarisation curves and electrochemical impedance spectroscopy (EIS). The former has the advantage of being simpler to implement and use. However, the quantity of information related to fuel cell physical behaviour and performance is relatively limited. Whereas the latter is more complex to employ, but gives further insights on the evaluation of the fuel cell performance, especially as it allows a better deconvolution of the different loss sources within the fuel cell. For further details on the electrochemical techniques used for PEFCs, the reader can refer to the state-of-the-art study conducted by Wu et al. [71]. These authors addressed a comprehensive review of the electrochemical tools used for the diagnosis of PEFCs, with a focus on EIS and polarisation curve records.

Polarisation measurement is a standard performance characterisation technique for either single cells or fuel cell stacks. A polarisation curve is a plot of the fuel cell voltage as a function of the load current density (or load current) measured at specified operating conditions. Polarisation curves analyses have been widely employed in the literature to study the effects of mechanical compression on the fuel cell performance. This technique was initially employed by Ge et al. [86], these authors reported an early use of a fuel cell test fixture allowing in-situ investigations on the effects of mechanical compression on the fuel cell performance. The compression process consisted of a compression plate acting on one fuel cell endplate. The authors used a single cell with two GDLs (ELAT carbon cloth and Toray carbon fibre paper). It was shown that mechanical compression has a limited impact on fuel cell performance at low current densities (below 0.8 $A.cm^{-2}$). However, the effect of mechanical compression was more pronounced when the cell was operated at high current densities for both carbon cloth and carbon paper GDLs. This effect was found to be more dominant in the case of the carbon fibre paper GDL (Toray). Figure 2.3 shows the polarisation curves for the carbon cloth GDL for different compression ratios. It can be seen that, at low current densities, the fuel cell performance increased first with increasing the compression ratio (from 40 to 45%), then decreased at high current densities, at which lower compression ratio (14%) gave the best fuel cell performance. Therefore, an optimal compression ratio exists at which the fuel cell reaches its maximum performance. However, this latter was not reported in this study since compression ratios below 14% were not attainable, as the sealing of the fuel cell used could not be ensured at compression ratios lower than this value.

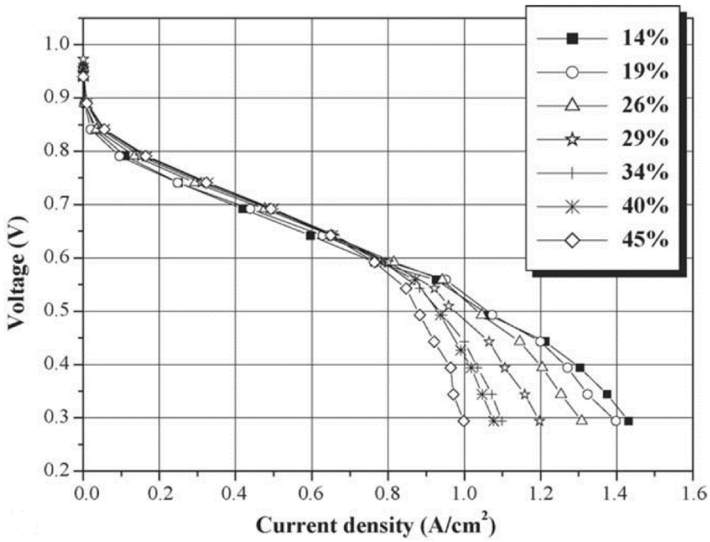

Figure 2.3. Polarisation curves for carbon cloth GDL at different compression ratios, at a cell temperature of 65°C, with cathode and anode flow rates of 1200 sccm and 2200 sccm, respectively, with cathode and anode humidifiers temperatures of 80°C [86].

Senthil Velan et al. [87] investigated three carbon cloth GDLs with three compression ratios of 16.6, 22.2, and 30.55%, along with a pristine GDL. It was shown that the GDL with a compression ratio of 30.55% showed the worst performance in the high current density region. This finding was attributed to the fact that mechanical compression narrows down the pore size of the GDL and thus hinders reactant from reaching the CL. Moreover, it was reported that higher compressive loads might worsen the water management capability of the fuel cell. According to this study, a 16.6 % compression ratio gave the best performance at fuel cell voltages of 0.15 V and 0.6 V. This finding was attributed to the better pore distribution and the reduced ohmic resistance achieved at this compressive load. Similar results were reported in [88] and [89] for a self-humidifying and air-breathing PEFC.

The EIS characterisation technique is based on applying a harmonic perturbation, i.e. a small AC current or voltage of known amplitude and frequency, to an operating fuel cell and measuring the amplitude and the phase response in a wide range of frequencies. A Frequency Response Analyser (FRA) and an electronic load are employed to perform the EIS technique. Some impedance spectra are calculated, and Nyquist diagrams are generally used to plot the spectra of the response. For further details on the study of PEFCs through EIS, the reader can refer to the review study dedicated to the EIS characterisation technique and proposed by Rezaei Niya and Hoorfar [90]. Mason et al. [52] carried out a study on the effect of mechanical compression on the PEFC performance using the EIS technique. Their experimental setup consisted of a commercially available cell compression unit (Pragma Industries SAS, France), allowing two operating modes, namely controlled compression and controlled displacement with resolutions of 0.01 MPa and 1 µm, respectively. The analysis of the effect of compression on individual loss mechanisms was carried out using EIS measurements (Figure. 2.4 (a)). The authors reported that as the compression increased, the high-frequency intercept of the impedance spectra with the real axis decreased. This was explained exclusively by the reduction in the contact resistance between the GDL and BPP as it was assumed that there was no change in the protonic resistance of the membrane. Furthermore, it was observed that, simultaneously with the decrease in contact resistance, the charge transfer and mass limitation arcs increased in size. These changes were reported to be solely due to the increase in mass transport resistance. Similar results were reported in [38,91,92]. Figure 2.4 (b) represents the evolution of the contact resistance and mass transport resistance as a function of the applied compression [52]. The non-linear change in the contact resistance with respect to the applied compression reported in this study agrees well with previously published work [76] using mainly ex-situ techniques to determine the electrical contact resistance between BPP and GDL materials. Throughout the range of compression, the increase in mass transport resistance was seen to be much higher than the decrease in contact resistance; therefore, the optimum compression point was reported to be the minimum compression that ensures gas sealing and, concurrently, maximum fuel cell performance.

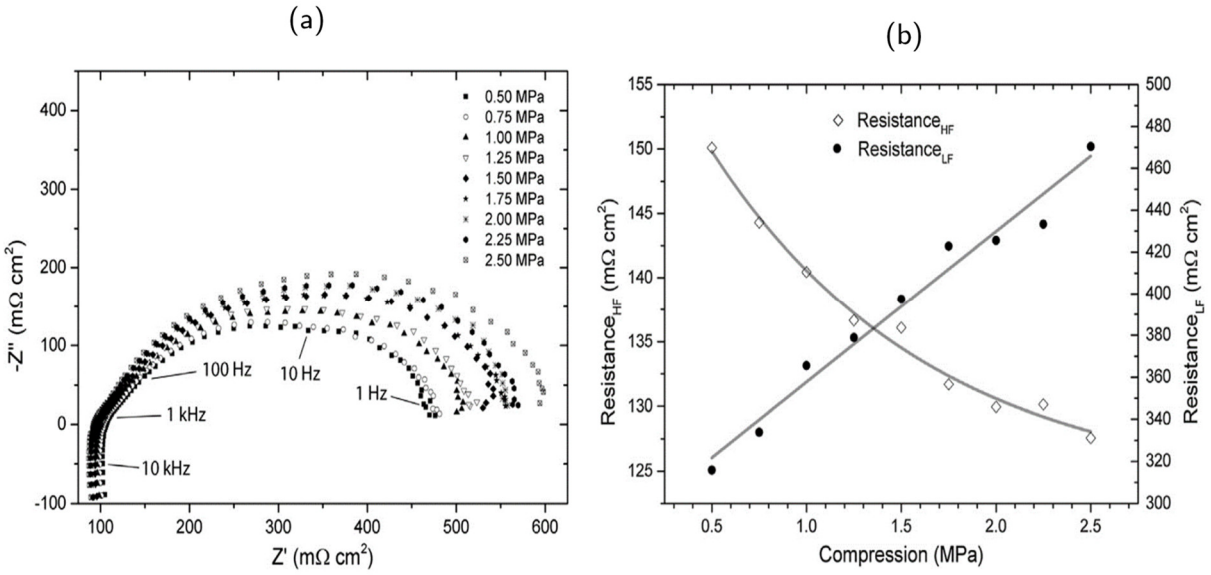

Figure 2.4. (a) EIS plots of a PEFC under a mechanical compression ranging from 0.5 to 2.5 MPa, (b) Relationship between the high and the low-frequency resistances ($Resistance_{HF}$ and $Resistance_{LF}$) as a function of the compression (data from (a)) $Resistance_{HF}$ and $Resistance_{LF}$ are proxies for the contact resistance and the mass transport resistance, respectively [52].

Wen et al. [58] presented a study on the effects of the mechanical clamping pressure on both a single cell and a 10-cell PEFC stack. The authors reported that, for either the single cell or the 10-cell stack, a maximum power density was achieved at higher clamping torque. In line with [58], Yim et al. [93] investigated two stacks (5-cell PEFC) with different GDL compression ratios of 15% and 30%. It was observed that the stack with a high compression ratio presented a better performance, for all current ranges, compared to the stack with a low compression ratio. This was attributed to the dominance of the decrease in the contact resistance against the increase in mass transport resistance as the applied compression increases.

Ous and Arcoumanis [94] employed a fuel cell compression unit allowing the application of compressive loads from 0.8 to 5 MPa through changing the clamping torque of a central screw. The used PEFC consisted of a single cell with a Toray H-060 GDL. The authors reported that increasing the compression from 0 to 2 MPa improved the fuel cell performance, with more considerable improvement in the ohmic region compared to the mass transport one. However, as the compression exceeded 5 MPa, the fuel cell performance declined drastically. This result was attributed to two main factors: i) the deflection of the plates in the compression unit, leading to an increase in the internal resistance of the fuel cell, and ii) the decrease in the GDL porosity as the compression loads become more important. Chang et al. [95] investigated a single cell with three GDL types (Sigracet® 10BA, 25BA, and 35BA). The assembly pressure was applied using a test fixture allowing the compression to be applied through a push rod driven by a pneumatic cylinder. For the three GDLs used, it was found that the peak power density reached its maximum at a compression of 3 MPa. The authors reported that higher

compression loads (over 3 MPa) resulted in a decrease in fuel cell performance. This finding was explained by some ex-situ measured changes in the GDL's electro-physical properties (gas permeability, water contact angle and in-plane electrical resistivity) as the compression exceeded 3 MPa. Similar results were reported in [77,82,96] where a trade-off between the contact resistance and the mass transport resistance was found to give the best fuel cell performance.

A range of studies has been conducted on the effects of assembly pressure through employing both polarisation measurements and EIS technique. Some authors emphasised that higher clamping pressure gives best PEFC performance whereas others reported that minimal clamping pressure, which ensures gas tight operation, needs to be considered for PEFCs. However, most of the studies suggested optimal clamping pressure that gives a trade-off between the reduction in the ohmic resistance and the mass transport resistance after GDL deformation to be most desirable towards achieving high PEFC performance. Nonetheless, the lack of cohesion in the reported studies (clamping methods, operating conditions, PEFC components) makes it hardly possible to draw general conclusions regarding optimal clamping pressure.

1.1.2 Assembly pressure distribution

Various research teams investigated the mechanical pressure distribution in PEFCs. In addition to the assembly pressure, the clamping configuration (e.g. the number of clamping bolts and their positions with respect to the cell geometry) may drastically affect the fuel cell performance. Different PEFC assembly configurations have been reported in the literature. For instance, the point-load design has received much attention [54,58,94,97]. In this design, bolt configuration and clamping torque are considered as the most important factors that affect the uniformity of the pressure distribution within the fuel cell components. A well-developed clamping design will minimise the interfacial contact resistance, homogenise the pressure distribution, and ensure gas-tight operation. These combined effects lead to the enhancement of the PEFC performance. Indeed, it was reported in [88] that homogeneous pressure distribution could improve the maximum power density of the PEFC by about 12% compared to an inhomogeneous one. In fact, uneven pressure distribution may worsen fuel cell performance or even permanently damage its components, e.g. through the creation of hot spots [91,92] which have detrimental effects on the fuel cell durability.

Up to now, two techniques have been reported in the literature to investigate the pressure distribution in PEFCs, namely the pressure-sensitive thin films and the piezoresistive mapping sensors. Although the investigations on pressure distribution using pressure-sensitive films have been used in off-line fuel cells (non-operating PEFCs) so far, this technique still provides valuable information regarding the pressure distribution across the fuel cell components. The analysis of the pressure distribution using this technique is based on the principle that as the mechanical compression is applied, microcapsules contained in the pressure-sensitive film are broken, and a colour-forming material is released and absorbed by the thin film. The released

colour intensity indicates the degree of the applied compression: the higher the mechanical compression, the more intense the colour. Since pressure-sensitive films have small thicknesses (lower than 200 µm for all compression ranges [98]) compared to the thicknesses of GDLs and the gaskets (e.g. 0.5 mm thickness of the gasket compared to 90 µm for the pressure-sensitive film in [58]), it was reported that pressure-sensitive films have a negligible effect on the internal compression distribution [58]. Thus far, their use to investigate pressure distribution across PEFC components remains suitable.

Wen et al. [58] experimentally investigated the effect of different combinations of clamping torque and bolt configuration on the performance and the pressure distribution of a single cell and 10-cell PEFC stack. The authors reported that for both single cell and a 10-cell stack, the pressure distribution uniformity and the maximum power density was improved as the number of bolts and the clamping torque was increased. This finding was explained by the changes of the electrical contact resistance and the GDL porosity under the effect of mechanical compression, meaning that the pressure uniformity was improved and consequently reduced the ohmic resistance of the PEFC, especially the contact resistance, and thus increased the maximum power density. These results are in good agreement with the findings reported in [93,96].

De la Cruz et al. [57] measured the stress distribution in a PEFC stack. The effect of the membrane swelling was investigated by soaking the MEA in liquid water. Afterwards, the MEA was assembled between two pressure-sensitive films in a single cell test fixture with fixed clamping pressure. It was shown that the pressure distribution in the MEA increased from the centre to the edges. Therefore, the edges of the membrane underwent the highest mechanical stresses. The report concluded that using special materials to dissipate high-stress concentration at the edges could be an alternative solution to mitigate the inhomogeneous pressure distribution issue.

Bates et al. [99] experimentally investigated the pressure distribution on the GDLs in a 16 cell PEFC stack using various clamping pressures (from 0.5 to 2.5 MPa) and clamping durations. Through a visual analysis of the compressed pressure-sensitive films, higher stress regions were observed at the edges compared to the centre of the GDL used. The authors also reported that preloading might be of significant impact on the pressure distribution. It was shown that increasing the duration of a load applied at the centre of the endplates resulted in a significant increase in the pressure applied to the GDL. The study concluded that applying a load at the centre of the endplate for a given duration before operating the fuel cell might have some beneficial impacts on fuel cell performance. Indeed, it allows materials to be settled and the load to be distributed more uniformly over the surface of the stack components. As a matter of fact, fuel cells may be subjected to hundreds of thousands of load cycles during their operational lifetime [100]. With this regard, some authors have already investigated the effects of cyclic loading on the PEFC performance and components properties [76,101,102], it was shown in [76] that the total through-plane resistance of a GDL Sigracet® 24AA decreased upon increasing loading/unloading cycles up to the third cycle, with the first cycle showing the

highest decrease up to 50%. Similar results were also reported in [101] where cyclic loading/unloading was shown to decrease the total resistance of a GDL Sigracet® 34BC up to the eighth cycle, with the highest decrease of about 30% occurring during the first cycle.

Peng et al. [35] investigated the effect of clamping pressure on the distribution of local current densities. They reported that mechanical compression homogenises the current density distribution and therefore improves the PEFC performance. The authors reported that higher current flows through regions with larger contact pressure, and that the current density is low in the regions with reduced contact pressure. Gatto et al. [56] investigated the effects of assembly pressure and gasket materials on PEFC performance and mechanical pressure distribution. The authors employed a pressure mapping sensor (TEKSCAN #5076, USA [103]) that had a pressure resolution of about 10 kPa. A single cell PEFC with a carbon cloth GDL was used. The mechanical compression was applied through varying the clamping torque on the assembly bolts, ranging from 7 to 13 N.m. With regard to the pressure distribution, it was reported that as the clamping torque increased, the clamping plates of the assembly fixture were deformed, leading to uneven pressure distribution. The centre of the GDL was reported to be less loaded (descending below 0.7 MPa) compared to its edges. The pressure concentration on the edges was shown to rise upon increasing the clamping torque until it reached the saturation level of the sensor used (over 10 MPa in some regions starting from a clamping torque of 7 N.m). Similar results were reported in [55]. Figure 2.5 depicts the experimental measurements that were carried out using the pressure mapping sensor for different clamping torques. The authors in [56] also emphasised that the gasket material and thickness affect the pressure distribution, for the same assembly pressure, and thus may influence the performance of the PEFC; this latter is in good agreement with results reported in [104,105].

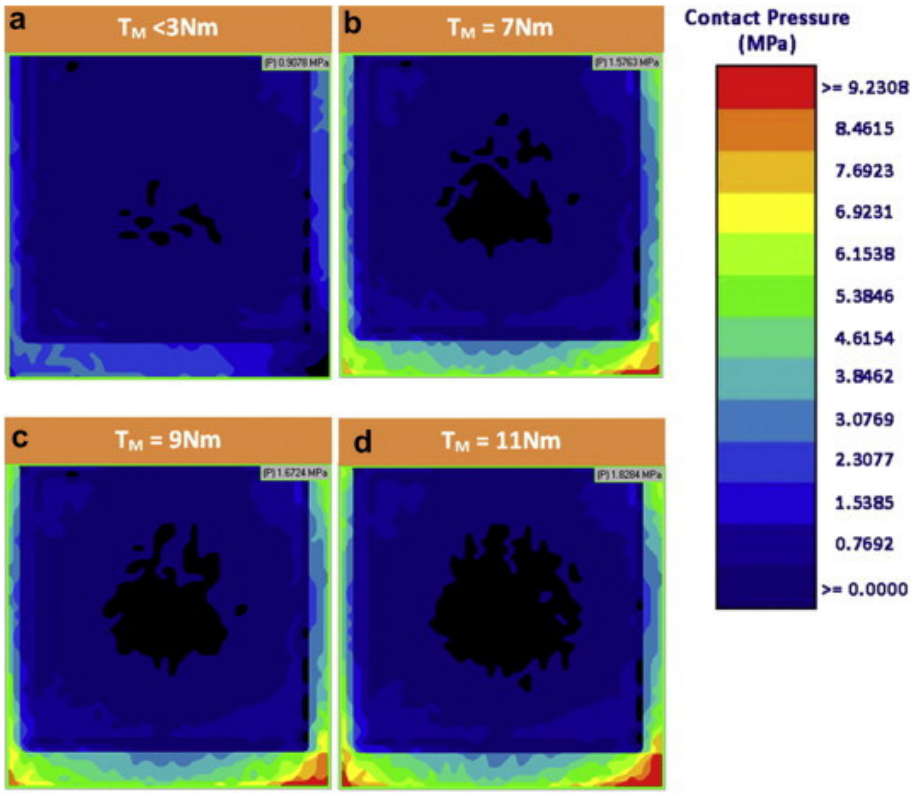

Figure 2.5. Pressure maps measured in a PEFC single cell with an active area of 25 cm^2, at clamping torques of (a) <3, (b) 7, (c) 9 and (d) 11 N.m, black spots correspond to the regions where the compression descends below the range of measurement of the sensor (< 0.7 MPA) [56].

In summary, the reported studies in the literature emphasise that the PEFC clamping process using typical fasteners induce an inhomogeneous pressure distribution across the fuel cell components. Moreover, it has been well proven that the inhomogeneity increases upon increasing the clamping torque (i.e. higher stress regions on the edges compared to the centre that remains with less compressive load). Therefore, developing new compression methods is of paramount importance in order to reduce the detrimental effects of inhomogeneous pressure distribution on the PEFC performance. Some clamping mechanisms aiming to homogenise the pressure distribution in PEFC stacks have already been reported in the patent literature, e.g. compression retention systems using: external springs [106,107], compliant strapping [108], overlapping sheets [109]. With this regard, Millichamp et al. addressed a range of compression assembly procedures (Figure 2.6) reported in the patent literature [7]. However, studies focusing on the comparison of the reported assembly procedures are still lacking in the literature [7]. This is owing to the fact that almost all the reported studies focused on the pressure distribution in PEFC using the traditional assembly procedure (point-load design using typical fasteners: bolts and nuts). Therefore, future investigations in this area could propose some novel optimised clamping methods by including technical comparisons of the compression retention systems reported in the patent literature.

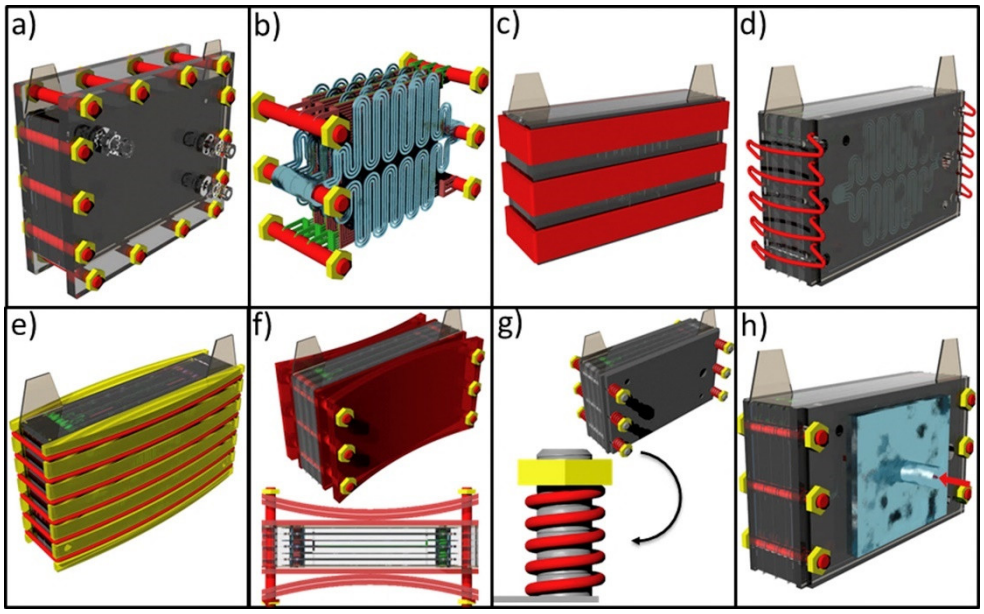

Figure 2.6. Clamping mechanisms for fuel cell stacks (a) point-load design, (b) tie rods through gas/water manifolds, (c) bands, (d) crimps, (e) straps/curved endplates, (f) leaf-spring, (g) point-load design with springs, (h) dynamic fluid compression plate [7].

1.2 Vibration

Although fuel cell assemblies are not a source of induced vibrations due to their compact structure with no moving parts (unlike internal combustion engines), fuel cells are subjected to vibrations caused by the sometimes-harsh external environments they are operated in (e.g. transportation sector and portable applications). The frequency of these vibrations may vary depending on the application. For automobile applications, it was assessed that the fuel cell experiences vibrations within the frequency range of 8-16 Hz due to the oscillations of the vehicle wheels and axles along with the non-uniform nature of the road [110,111]. The effects of vibration on PEFCs have already been investigated in the literature. These effects were assessed under: i) harmonic [112–114], ii) random [115,116], and iii) real-world vibrations [117–121]. The reader can refer to the review study reported by Haji Hosseinloo and Ehteshami [122] for more details on the effects of shock and vibration on PEFC performance and component degradation.

In this study, the reported work related to the effects of real-world induced vibrations on PEFC performance will be discussed. These studies were carried out by investigating the fuel cell performance either during or after the fuel cell operation by means of: i) mounting the fuel cell directly on its final application; ii) placing devices that measure the real multi-directional excitations (e.g. accelerometers) on the final application and then reproducing the same vibration conditions (from an excitation spectrum) in the laboratory using vibrating platforms. Bétournay et al. [123] reported one of the first studies related to this issue. These authors examined the effects of underground mining conditions on fuel cell performance and physical

degradation of the fuel cell stack. Vibration tests were carried out over a period of 49 h. The results showed that there was neither physical damage nor significant decrease in the fuel cell performance after exposing the fuel cell to vibration/shock during underground driving conditions. Rajalakshmi et al. [116] evaluated the effects of simulated vibrations on the performance and the mechanical integrity of a PEFC stack that was subjected to swept-sine and random excitations for a duration of one and a half hours. Their results showed no significant decrease in the PEFC performance and no changes in individual cell voltages. This latter was attributed to the fact that contact resistance had not increased after the vibration tests.

Hou and co-workers reported a series of experimental studies with regard to the effects of long-term vibrations on fuel cell performance in light-duty vehicles [117–121]. In all the five reported studies, real-world vibrations were first measured on a fuel cell mounted in a vehicle, which was, in turn, mounted on a road simulation test bench (MAST - Multi-axial Simulation Table). This system allows the simulation of realistic real-world vibrations of a driving vehicle on real-world roads. Afterwards, the measured excitation spectra were applied to the fuel cell using a six-degrees-of-freedom vibrating platform. During the vibration tests, the fuel cell stack was not in operation; nonetheless, the fuel cell stack was moved to a PEFC test bench within regular periods in order to assess the performance as a function of the progression of the vibration tests. In their earliest study, Hou et al. [117] investigated the effects of vibration on electrical insulation and gas-leakage. After a 150 h vibration test, the hydrogen leakage rate was reported to increase by 50%, whereas the insulation resistance of the stack was shown to decrease by 17.5%. They also reported an increase of the ohmic resistance by 55.8% in [118].

In a later study, Hou et al. [119] extended their earlier investigation to examine the cell's steady-state efficiency undergoing a 160 h vibration test. The authors reported a decrease of 20% and 5.4% in the fuel cell steady-state efficiency and the maximum efficiency point, respectively. Moreover, a decrease of 30.7% in hydrogen use was recorded after the vibration test. This was explained by the appearance of pinholes on the membrane caused by the vibration conditions. In another study, Hou et al. [120] examined the effects of vibration on the performance of a PEFC using the EIS technique. The vibration tests were carried out over 200 h. The authors reported an average rise in the ohmic resistance of 0.0357 % per hour. This growth corresponds roughly to a 7.14% increase in the ohmic resistance over the 200 h test duration. Recently, Hou et al. [121] revised the findings reported in their earlier investigations [117–120] and conducted a study with a more developed characterisation process. The test duration was extended to 250 h. Concurrently, the time intervals separating the performance tests were shortened. After the vibration tests, the anode hydrogen leakage rate increased to reach 1.7 times its initial value. In addition, the rated voltage and the OCV dropped by 3.6% and 0.9%, respectively. Furthermore, the ohmic resistance was shown to increase by 5.4% after vibration tests. The performance degradation was attributed to the increase in the ohmic resistance and the mass transport limitation at high current densities.

Liquid water transport under vibration was investigated in [124] using a transparent cell. Visual inspection of water transport under vibration showed that vibration (a frequency of 20 Hz and an amplitude of 4 mm) could facilitate evacuating liquid water as it reduces water adherence to the surface of the fuel cell components. Therefore, operating the fuel cell under specific vibration conditions might be beneficial for water management within the fuel cell; this issue was reported earlier by Palan and co-workers [125,126]. In their first investigation on this topic, Palan and Shepard [125] studied the feasibility of the use of vibrational and acoustical methods to enhance water management of the fuel cell assembly through atomisation of the condensed water droplets in either the BPPs gas channels or the MEA. The authors employed numerical simulation and showed that the proposed methods might achieve the required acceleration levels (250 g) to atomise a water droplet having a radius of 2 mm. The report concluded that the proposed method was feasible via an appropriate choice of the source strength and the frequency of the excitation. In their second study, Palan et al. [126] theoretically investigated the use of vibrational and acoustical methods to enhance the performance of a PEFC by improving the water removal capacity of the fuel cell components. It was shown that a displacement amplitude of 1 µm on a vibrating BPP could evoke water droplets movement. This might be achieved by the implementation of surface acoustic waves with a minimal parasitic power consumption of 21 mW. This finding seems to be a promising route to mitigate PEFC water management issues. Indeed, recent studies carried out by Ma and co-workers [127–130] investigated the potential use of the piezoelectric polymer electrolyte fuel cells (PZT-PEFCs).

In these novel PZT-PEFCs, the piezoelectric actuators are placed on the cathode channels allowing the operation of an air-breathing PEFC by forcing the air into the channels and, at the same time, pumping out water during the compression phase of the PZT device. In their last study [130], the PZT device was stated to require a power of 0.64 W for a PEFC stack with an optimal power of 4.5 W and a 60 Hz functioning frequency. This novel technique was shown to mitigate cathode flooding effects and enhance the performance of air-breathing fuel cells. However, the proposed techniques in [127–130] are only dedicated to air-breathing PEFCs, which are generally suitable for low power portable applications [131–133]. Therefore, new numerical models development and experimental investigations should be carried out to validate the proposed methods in [125,126] for fuel cells operating with air compressors and humidifiers, which are more likely used in high power PEFC applications.

In summary, a number of research teams have studied the effects of vibration-induced stresses on the PEFC performance and component degradation. Some studies concluded that vibration had beneficial impacts on fuel cell performance, whereas others reported that vibrations worsened fuel cell performance. Even though recent studies seem to be more representative of real-world vibration and with more developed characterisation techniques, the results regarding the effects of vibration are still inconclusive. Further experimental investigations could include: i) implementation of in-situ water visualisation techniques to assess the effects of vibration, either detrimental or beneficial, on the fuel cell performance and ii) ex-situ investigations on

the degradation of the fuel cell components (e.g. SEM, synchrotron X-ray) to further explain the evolution in performance caused by the changes in the electro-physical properties of the fuel cell components. Thus far, to our knowledge, protection means of the fuel cell under vibration conditions have not been reported in the literature; namely, no academic publication was found on the topic. Therefore, future studies on the effects of vibration on fuel cell performance should include vibration protection systems for fuel cells.

1.3 Freeze/thaw cycles

According to the US Department of Energy (DoE) technical targets for fuel cell power systems [134], fuel cells must be able to start and operate at environmental conditions at which ambient temperature may drop below 0 °C. Operating at such subfreezing temperatures leads to ice formation. In fact, as water freezes, its volume expands. This expansion creates uneven stresses within the fuel cell stack that may damage the fuel cell components (e.g. GDL broken fibres [135], cracks, delamination and Pt particle migration [136]). In addition, as water thaws, its volume diminishes, and the created stresses vanish. These Freeze/Thaw (F/T) cycles may damage the fuel cell components and lead to a decrease in the fuel cell performance. The effects of subfreezing conditions, on either the fuel cell performance or its individual components, have already been covered in literature [136–141]. Hou et al. [140] employed the EIS technique to investigate the effects of residual water on a PEFC operating at repetitive sub-zero conditions (-10 °C). It was reported that the ohmic resistance remains unchanged after eight freezing cycles regardless of the amount of residual water. In contrast, mass transport resistance was shown to be highly dependent on the amount of residual water. In line with [140], Alink et al. [137] investigated the effects of subfreezing operating conditions (varying between -40°C and 100°C) on both the PEFC performance and the physical properties of its components. In this study, the performance of two stacks with different initial states (i.e. dry and wet) was investigated. It was shown that after repeated F/T cycles (62 F/T and 120 F/T cycles for the wet and dry state, respectively), only a small performance degradation was witnessed for the fuel cell with an initial dry state, especially at high current densities, whereas the fuel cell with a wet initial state showed major performance degradation. This was explained by less efficient water management resulting in more prominent flooding effects. Moreover, a decrease in the electrocatalyst surface area (ECSA) and an increase in the porosity were observed for both stacks. These effects were more marked for the F/T cycles applied to the stack with a wet initial state.

Alink et al. [137] also reported that only a small water content freezes inside the membrane, whereas most of the water freezes in the electrodes causing cavities and micro-cracks. The authors concluded that removing water from the cell before freezing would be helpful to mitigate performance degradation caused by repeated F/T cycles. The authors also reported that compression of GDLs and MEAs restrains the formation of severe cracks and electrode material detachment. Furthermore, designing the fuel cell components with more flexible materials would tolerate volume expansion caused by ice formation and thus prevent physical deterioration of the stack components caused by the induced stresses. This proposition is in

good agreement with the results reported by Lee et al. [141] where MEAs were prepared in-house by distributing catalyst ink over the electrolyte. By comparing commercial MEAs with some in-house prepared ones, the latter showed no significant structural changes caused by the water/ice formation. This was attributed to the good membrane-CL interfacial properties resulting from directly spraying the catalyst ink onto the membrane. The authors concluded that the F/T degradation is caused by the initial component microstructure, which is in turn related to the process of fabrication of the fuel cell components.

Guo and Qi [138] investigated the effect of F/T cycles (between -30°C and 20°C) on the physical properties of the MEA. For a fully hydrated membrane, physical damage in the CL was observed, namely catalyst domain segregation and cracks formation, in conjunction with a loss in the ECSA. Moreover, the authors reported that the volume expansion created by water freezing might induce considerable stress in the assembled PEFCs. The report concluded that lowering the water content in the membrane could mitigate the MEA damage caused by F/T cycles. Lee et al. [139] studied the effect of MPL on the PEFC degradation caused by F/T cycles (between -15°C and 70°C). The authors compared the performance degradation in an MPL-coated GDL and an uncoated one. For both GDLs, the performance degradation was observed as the number of F/T cycles was increased. The authors reported that the MPL-coated GDL showed an earlier degradation in the CL compared to the uncoated one. This was attributed to the fact that when the fuel cell operation is stopped, using an MPL keeps more water in the membrane and the CL. This leads to ice formation and thus volume expansion, which may, in turn, lead to a compression induced stresses.

Gavello et al. [136] examined the effects of repetitive freezing conditions on a single cell PEFC. SEM images analysis showed a limited number of broken fibres, cracks and delamination areas, which may be attributed to the induced mechanical stress caused by the freeze/thaw cycles taking place within the fuel cell components. Furthermore, a substantial migration of Pt particles from the CL to the membrane was observed, which could be a reason for the performance degradation due to the ice formation within the MEA. This finding is in contrast with the results of [137] where it was reported that due to ice formation, few Pt particles detach from the CL, pass through the GDL, and are finally transported via the exhaust gases. Thus, further investigations of this issue still need to be carried out.

From the reported studies, it was proven that the degradation related to F/T cycles is caused by water volume expansion, decrease in the ECSA, and Pt particles migration. However, no study has reported the induced compression value caused by operating the fuel cell at subfreezing conditions. Knowing such a value would be of major importance to help modellers to accurately predict the F/T-induced stresses.

1.4 Hygrothermal-induced stresses

Fuel cells are subjected to external and internal temperature variations, which may lead to the development of expansion forces within the fuel cell components. Heat management is of

paramount importance for PEFCs since they repel roughly 50 to 70% of chemical energy contained in the hydrogen in the form of heat [142]. Internal heat generation may come from different processes: i) the ohmic resistance losses, ii) entropic heat of reactions, and iii) irreversible heat of electrochemical reactions [143]. These heat generation processes present approximately 10%, 55%, and 35% of the overall amount of the released heat, respectively [143]. Fuel cells are also subjected to temperature variations from their external environments, with portable and transportation fuel cell applications more likely to be operated at temperatures ranging from higher to sub-zero levels. These temperature variations add up to the induced stresses within the fuel cell and depend on the different thermal expansion coefficients of the fuel cell components and the fuel cell assembly system.

Chen et al. [144] reported a study on the effects of PEFC temperature variation on the GDLs under different compressive loads. The authors investigated three operating temperature, namely 25, 60, and 90 °C, and a compression range up to 10 MPa. It was found that temperature decreases the stiffness of the tested GDLs, resulting in more displacement as a function of mechanical compression of the GDL tested at 90°C compared to the ones tested 25 and 60°C. Khandelwal and Mench [145] measured the thermal through-plane conductivity and contact resistance of different fuel cell components. The authors reported that the thermal conductivity of the GDL decreases with increasing temperature. This latter may have detrimental effects as the GDLs play an important role in conducting temperature from the membrane and CLs to the BPPs that have means for heat removal. Correlation between GDL compression and thermal contact resistance was also emphasised by the authors in [145]. It was reported that the thermal contact resistance between the GDL and an aluminium bronze material dropped from 6.7×10^{-4} to 2.0×10^{-4} m^2KW^{-1} as the compression increased from 0.4 to 2.2 MPa. Cui et al. [146] reported a study on the degradation of polymer gaskets used in PEFCs. In this study, liquid silicone rubber (LSR) was investigated as a sealing gasket material. It was shown that during the temperature change, the thermal contraction and expansion of the LSR cause nearly all of the stress variation. In addition, the temperature history was shown to have a significant correlation with the stiffness variation of the LSR material. In another study, Lai et al. [147] investigated the effects of cycling on the mechanical properties of a Nafion® NR-111 membrane. Among several results, the authors reported crack formation caused by the resulting stress as the membrane was subjected to in-situ cycling experiments between dry and wet conditions. The induced cracks led to gas crossover and thus fuel cell performance degradation. This effect was shown to be less pronounced as the membrane was subjected to shorter humidity fluctuations.

With regard to the stresses caused by the hydration state of the membrane, Mason et al. [148] reported some important compression and thickness changes caused by the MEA hydration. It was shown that flooding conditions increase the membrane hydration resulting in an increase of the stress across the MEA. The authors concluded that the generated stresses from repetitive hydration cycles, e.g. due to start-up and shutdown procedures, could lead to long-term degradation of the fuel cell performance. In line with [148], de la Cruz et al. [57] reported an increase of 22% of the mass of a fully hydrated MEA compared to a dry one. This was explained

in terms of water retention of the membrane. It was also reported that excess water could expand the membrane by 10%-15% in all directions [57]. Given that the membrane is constrained by the adjacent fuel cell components, the membrane expansion leads to the appearance of a creeping effect in the areas beneath the channels. This expansion is presumed to push the GDL inside the channels and could lead to mechanical failures of the membrane. The authors also reported that the constrained membrane showed a reduced water uptake, which may have a detrimental effect on its ionic conductivity.

Generated stresses caused by the membrane swelling received significant attention in the literature. However, no experimental mechanical measures of these stresses have been reported so far. Quantifying these stresses might be of major importance, especially for model development. In contrast, little has been done concerning the temperature-induced stresses of the other cell components. This might be due to the negligible thermal expansion of materials caused by either internal or external temperature variations.

Table 2.1 highlights relevant conclusions regarding the effects of mechanical stresses on the PEFC components properties.

Mechanical stress sources	Effects on components properties	Ref.
Clamping pressure	GDL carbon fibre crushing.	[81]
	Reduction in the porosity of the GDL.	[81,85,87,94]
	Reduction in the electrical contact resistance between the cell components (generally between the GDL and the BPP).	[38,52,81,91–93]
	GDL protrusion into the BPPs' channels.	[80,81,85]
	Reduction in the water management capability.	[87]
	Increase in the mass transport resistance.	[38,52,91,92]
	High stress regions located at the edges compared to the centre of the GDL (point-load assembly design).	[55–58,99]
	Decrease in the GDL's thermal contact resistance.	[145]
Vibration	Unchanged electrical contact resistance.	[116]
	Increase in the hydrogen leakage rate.	[117,121]
	Increase in the ohmic resistance (electronic, ionic and contact resistance).	[118,120,121]
	Decrease in the hydrogen use.	[119]
	Decrease in the stack electrical insulation.	[117]
	Improvement in the excess liquid water evacuation.	[125–130]
Freeze/thaw cycles	Unchanged ohmic resistance.	[140]
	Reduction in the electrocatalyst surface area (ECSA).	[137,138]
	Increase in the porosity of the electrode.	[137]
	Appearance of cavities and micro-cracks on the electrodes.	[136–138]
	Migration of Pt particles from the CL to the membrane.	[136]
	Migration of Pt particles from the CL to the exhaust gases.	[137]
Hygrothermal-induced stresses	Decrease in the thermal conductivity of the GDL upon increasing temperature.	[145]
	Membrane crack formation caused by cycling experiments between dry and wet conditions.	[147]
	Decrease in GDL stiffness with increasing temperature.	[144]

Table 2.1. Relevant conclusions regarding the effects of mechanical stresses on the PEFC components properties.

As shown in this section, various compression mechanisms take place in operating PEFCs and may affect their performance. In order to understand these effects, especially on the GDL, the following section aims to give an overview of the intrinsic characteristics of the GDL that may affect its electro-physical characteristics with respect to the applied mechanical compression.

2 Effects of mechanical compression on the GDL characteristics

The electro-physical properties of the GDL are highly influenced by mechanical compression, as the GDL was reported to be the component most subjected to structural deformation under mechanical compression [52]. Thus far, different aspects were investigated by researchers focusing on the in-situ investigations of the effects of mechanical compression on GDL properties. Under this section, the effects of mechanical compression on the following GDL characteristics are reported: MPL coating, PTFE loading, and the induced effects on the water management within the GDL.

2.1 MPL coating

The GDL substrate is often coated with a microporous layer (MPL) either on one side, which is generally the catalyst layer side, or on both sides of the GDL, also called double-side MPL coating [149]. The MPL is fabricated from carbon particles and hydrophobic agent (typically PTFE). Coating GDLs with MPL aims to improve the GDL electro-physical characteristics by reducing the contact resistance and by enhancing the water transport and removal capacity of the PEFCs [39–41]. MPL also improves the membrane humidification as it enhances its water retention by keeping water within the membrane.

Sadeghifar [76] studied the effect of MPL coating on the GDL electrical conductivity. Among several findings, it was shown that the MPL coating significantly decreases the electrical conductivity of the MPL-coated GDLs since the MPL electrical conductivity is much lower than the GDL's one (conductivity of carbon black is lower in comparison with carbon fibres [76]). The difference between the GDL and the MPL conductivities was seen to increase upon increasing compression. This latter was attributed to the fact that GDL conductivity increases with increasing compression, whereas MPL conductivity reaches a plateau at high compression levels. It was also shown that MPL coating significantly increases the contact resistance between the GDL and the BPP. In contrast with [76], Ismail et al. [60] measured the electrical contact resistance as a function of the clamping pressure for both uncoated (Sigracet® 10BA) and MPL-coated GDLs (Sigracet® 10BC and 10BE). The electrical contact resistance was shown to be lower for the MPL-coated GDLs compared to the uncoated GDL. These findings were explained by the presence of more conductive carbon particles in the MPL compared to the GDL substrate. The reduction in the contact resistance between the MPL-coated GDLs and the BPPs was also attributed to the compressible nature of the MPLs that favours them

to occupy the gaps that exist in the surface of the BPPs and thus enlarges the surface contact between the BPP and the GDL.

Regarding the effect of MPL coating on fuel cells operating in real-life conditions and under different compressive loads, Dotelli et al. [38] investigated the effect of compression on three carbon cloth GDLs. Two of the GDL substrates were coated by MPL. The compression ratio of the cell, i.e. the ratio of the operating thickness of the GDL to its original thickness, was set at either 30% or 50%. The ohmic resistance was shown to decrease in the uncoated GDL upon increasing compression ratio, whereas it stayed unchanged in the other two MPL coated GDLs. At a compression ratio of 50%, the uncoated GDL showed the worst performance compared to the other MPL-coated GDLs. In addition, the MPL-coated GDLs showed higher power density compared to the uncoated one as the reduction in the mass transport resistance (due to the MPL coating) had a more pronounced effect on the performance than the reduction in the ohmic resistance.

2.2 GDL hydrophobic content

The GDL is typically treated with PTFE to improve its water-repellent properties. However, the PTFE conductivity was reported to be several times lower than that of the carbon fibres [76]. This low conductivity may affect the overall electrical conductivity of the PTFE-treated GDLs. Ismail et al. [60] measured the in-plane electrical conductivity of a number of untreated and PTFE-treated GDLs. The authors reported that the in-plane conductivity remains almost unchanged regardless of the PTFE loading. This was explained by the structure of carbon fibres that remains unaffected upon adding PTFE particles. The through-plane resistance was shown to increase with increasing PTFE content. This effect was attributed to the electrically insulating nature of the PTFE particles. These findings agree well with results reported in [76]. PTFE loading was also reported to affect the thermal conductivity of the GDLs. A decrease by a factor of two in the through-plane thermal conductivity was reported by Khandelwal and Mench [145] from their measurements of treated (20wt% PTFE) and untreated GDLs.

Tötzke et al. [150] conducted a study on the influence of hydrophobic treatment on the structure of compressed GDLs (Freudenberg H2315 with different PTFE loadings). It was reported that PTFE loading reduces the GDL penetration into the gas channels by improving the stiffness of the GDL substrate and enhancing the shape of the GDL as smoother surfaces of PTFE-treated GDLs, compared to untreated ones, were witnessed when the mechanical compression was applied. This latter might be beneficial to mitigate water management issues since the protruded fibre endings in the case of untreated GDLs (Figure 2.7 (A)) could form a potential barrier for water droplets removal and thus lead to water accumulation in the gas channels. Figure 2.7 (D) depicts the effect of PTFE loading on the GDL penetration into the gas channels with respect to the applied mechanical compression. It can be seen that PTFE loading decreases the penetration depth of the fibres leading to less deformation of the investigated GDLs. Comparable protrusion behaviour of T20A and T10A was attributed to similar PTFE loading on the upper regions of the GDLs used.

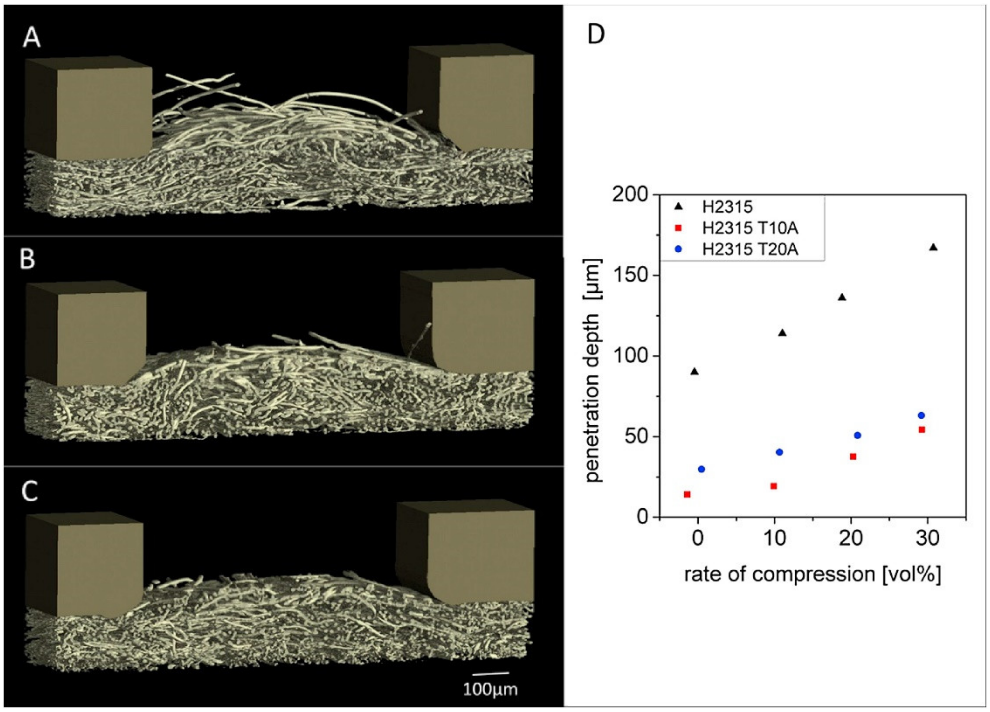

Figure 2.7. 3D-view of the compressed sample at a compression ratio of 30%: (A) H2315 (0 wt% PTFE); (B) H2315 T10A (10 wt% PTFE); (C) H2315 T20A (20 wt% PTFE). (D) GDL penetration into the gas channel as a function of the applied compression [150].

Dotelli et al. [38] studied the effect of MPL's PTFE loading on the fuel cell performance with respect to the applied mechanical compression, by comparing two MPLs with different PTFE contents (40% and 12%) and under different compression ratios (30% and 50%). The results obtained from the analysis of power and polarisation curves showed that PTFE content within the MPL has a minor impact on fuel cell performance. However, this impact became more noticeable at high current densities where the MPL with high hydrophobic content (40% PTFE) showed better performance compared to the MPL with low hydrophobic content (12% PTFE). These results were attributed to the fact that high PTFE content results in higher hydrophobicity, which helps to evacuate the excess water produced at the cathode CL at high current densities. The authors concluded that MPL hydrophobicity improves fuel cell performance by reducing the mass transport resistance at high current densities. In line with [38], Ferreira et al. [151] reported that MEAs with PTFE-treated GDLs showed a better performance than the ones with untreated GDLs. This was attributed to the fact that GDL hydrophobic treatment provided an enhanced overall water management capability within the fuel cell.

In a recent study carried out by Biesdorf et al. [152], the authors investigated the effects of the hydrophobic coating on the mass transport resistance in an operating PEFC. GDLs were subjected to a 25% compression ratio. It was found that among different PTFE loadings, the cell with the highest amount of PTFE showed the lowest amount of water accumulation; in

contrast, high mass transport losses were detected in fuel cells with high PTFE content. Hence, it was concluded that high mass transport losses are not always associated with a higher amount of water accumulation. This was explained by different morphologies of water accumulation. Namely, in hydrophobic GDLs, water accumulates in the form of droplets leading to restricted areas for reactants transport; whereas in GDLs with lower PTFE content, water accumulates in the form of films, allowing more paths for reactant gases to reach the CL. Water management within the GDL will be addressed in more detail in the following section.

In summary, the electro-physical characteristics of GDLs have a significant impact on the performance of the fuel cell when it is subjected to mechanical stresses. Two main factors were analysed in this chapter, namely the MPL coating and the PTFE loading, as these factors present a considerable part of the reported studies in the literature so far. Correlations between GDL characteristics and PEFC performance with regard to the applied mechanical stresses have been reported in the literature [77,104,105]. Nevertheless, future studies combining both in-situ and ex-situ characterisation techniques could investigate the effects of the variation in the electrophysical properties of the GDL on the PEFC performance as a function of the applied mechanical compression. The objective of such studies could be the research of the relationship between in-situ and ex-situ observed performance of the GDLs, which represents one of the main goals of our study.

Table 2.2 highlights relevant conclusions regarding the effects of the MPL coating and hydrophobic content treatments on the GDL electro-physical characteristics.

GDL treatments	Effects on the GDL electro-physical characteristics	Ref.
MPL coating	Reduction in the electrical conductivity of the MPL-coated GDLs. Increase in the electrical contact resistance between the GDL and the BPP.	[76]
	Reduction in the mass transport resistance of the MPL-coated GDLs.	[38]
	Larger surface contact between the BPP and the GDL. Reduction in the electrical contact resistance between the GDL and the BPP.	[60]
	Stagnation of MPL-coated GDLs' electrical resistance upon increasing mechanical compression.	[60,76]
Hydrophobic agent	Unchanged GDL's electrical in-plane conductivity regardless of the PTFE loading.	[60]
	Increase in the electrical through-plane resistance with increasing PTFE content.	[60,76]
	Increase in the mass transport resistance with high PTFE content.	[152]
	Reduction in the GDL penetration into the gas channels by improving the stiffness of the GDL substrate.	[150]
	Reduction in the mass transport resistance at high current densities due to the improved water evacuation.	[38,151]
	Decrease in the GDL's through-plane thermal conductivity.	[145]

Table 2.2. Summary of relevant conclusions regarding the effects of the MPL coating and hydrophobic content on the GDL electro-physical characteristics.

2.3 Water management

PEFC water management has been widely covered in the literature due to its strong association with fuel cell performance. In fact, in order to ensure a good ionic conductivity of the electrolyte, the membrane (perfluorosulfonic acid, PFSA) needs to be sufficiently hydrated. In PEFCs, water might be provided through the anode and/or cathode stream gases to hydrate the electrolyte, at least for stacks with power levels higher than 1 kW. However, excess water may cause electrode flooding. The latter occurs when the rate of liquid water accumulation outpaces the rate of water removal. Under these conditions, GDL pores get clogged, and reactant gases do not reach the CLs leading to an increase in mass transport losses and therefore to a decrease in fuel cell performance caused by reactant starvation. These effects are more pronounced when mechanical compression is applied, leading to a reduction in the porosity of GDL [153].

Liquid water is more apparent at the cathode side where it is generated as a product of the cell reaction on the cathode CL. Moreover, the transport of hydrogen protons through the membrane accompanies the transport of water molecules from the anode to the cathode side in a phenomenon commonly referred to as electroosmotic drag [154,155]. The latter also increases the water content on the cathode side. In addition, the electroosmotic drag and the

water production at the cathode side create a concentration gradient that leads to the transport of a portion of water from the cathode to the anode side via back diffusion through the membrane [155,156]. The water transport mechanisms in PEFCs have been comprehensively reviewed in [154]. The accumulated water at the cathode of a PEFC is generally removed from the fuel cell via the gas stream at the cathode flow channels [154]. Besides the fact that water accumulation may cause flooding, the protonic conductivity of PFSA membranes was reported to be highly dependent on its water uptake [157]. Therefore, a dynamic balance of water is needed in order to achieve effective water removal along with a proper hydration state of the membrane [154].

Cha et al. [158] carried out a study on the effects of assembly pressure on both the PEFC performance and its water management using the EIS technique. Their apparatus consisted of a single cell with a Toray TGP-H-120 GDL. The compression process was carried out through varying the clamping torque on the bolts of the fuel cell assembly. It was shown that the ohmic resistance decreased as the clamping torque increased, which was attributed to the decrease in the contact resistance and also to the increase in the membrane hydration on the anode side. The latter was explained by the reduction of the porosity and the permeability of the GDL as the assembly pressure increased leading to a higher back-diffusion water transport mechanism (from the cathode to the anode side) and therefore uniform membrane hydration. It was also seen that as the current density increased, the ohmic resistance decreased, which was reported to be due to better membrane hydration caused by the increase in water generation on the cathode side. However, excessive compression was reported to increase the mass transport resistance that was attributed to water accumulation on the cathode side, leading to flooding conditions. The report concluded that the fuel cell assembly pressure needs to be optimised in agreement with the water content in the PEFC.

Mason et al. [148] investigated the effects of flooding on the dimensional changes of the MEA. They reported that as flooding occurred, the membrane thickness increased leading to the appearance of higher stresses, which in turn had detrimental effects on the GDL (e.g. carbon fibres crushing). The report concluded that flooding effects might lead to long-term performance degradation. In this regard, the development of in-situ water visualisation techniques plays a major role in the assessment of water management capacity of the PEFCs. Various visualisation techniques have been reported in the literature, e.g. neutron imaging, X-ray microtomography, electron microscopy, and fluorescence microscopy. For more details on the water visualisation techniques, the reader shall be referred to the review study reported by Bazylak [159]. Even though numerous studies have been conducted on the water management issue, little has been done on the effect of mechanical compression on water management in operating PEFCs. Bazylak et al. [160] reported a study on the effect of compression on liquid water management. The authors used an ex-situ apparatus allowing visualisation of liquid water based on fluorescence microscopy. The GDL used (Toray TGP-H-060) was placed under an optically transparent clamping plate with a clamping pressure of 1.5 MPa. The authors reported that the compressed regions of the GDL present preferential pathways for water transport and break-through. This finding, which is in contrast with the expected behaviour of

the water transport within the GDL, was reported to be due to the loss of hydrophobicity in the compressed regions of the GDL. In the study reported by Bazylak et al. [160], SEM images showed that compression causes carbon fibres and PTFE coating breakage, which was reported to lead to the degradation of the hydrophobic content in the compressed regions of the GDL used. This effect, in turn, favours the water accumulation in the regions beneath the ribs compared to the regions beneath the channels where the hydrophobic agents are less impacted by mechanical compression. The authors in [160] concluded that the reported water transport behaviour might be beneficial for PEFC performance since the liquid water can be located in the GDL regions under the ribs where water accumulation is less critical than in the regions under the channels (e.g. possible creation of diffusion barriers leading to reactants starvation). Similar results were also reported in a study carried out by Ince et al. [161]. The authors experimentally investigated the water distribution using thermographic and synchrotron X-ray imaging. They employed a water injection point method where liquid water was injected directly beneath the MPL before reaching the GDL substrate. Two GDL samples were investigated in this study: i) Sigracet® 29BC with a compression ratio of 11%, and ii) Sigracet® 25BC with a compression ratio of 21%, referred to as the uncompressed and the compressed GDL samples, respectively. It was observed that the pore saturation of the compressed GDL was higher than the one of the uncompressed GDL in both the MPL and the GDL substrate. Furthermore, water transport in the in-plane direction of the compressed GDL was higher compared to the uncompressed GDL. These results indicate that compression promotes in-plane water transport in the compressed regions of the GDL [162].

Zenyuk et al. [163] employed the X-ray computed thermography technique to investigate water distribution in GDLs with different compression ratios of 15%, 35%, and 47%. The GDL used was a carbon paper Sigracet® 10BA. The authors reported that the porosity of the GDLs is higher under the channels compared to the porosity under the ribs. In contrast to the results reported in [160,164], liquid water was shown to flow through the higher porosity pathways, indicating that areas beneath the channels present preferential pathways for water transport within the GDL. Moreover, it was shown that as the compression increases, the size of water agglomeration decreases and form small clusters located mostly underneath the channels. The study concluded that future improvements of fuel cell design might include GDLs with modulated porosity, which would enhance water removal capacity by directing liquid water through desired porosity pathways.

With regard to in-situ water visualisation studies, Manke et al. [165] investigated the water transport and evolution in an operating PEFC by means of high-resolution synchrotron X-ray radiography. It was shown that liquid water clusters are located in the areas beneath the channels in an operating PEFC. Hartnig et al. [164] carried out a study on the transport of liquid water in operating PEFCs using high-resolution synchrotron X-ray radiography. Their test apparatus consisted of a single channel PEFC with a Sigracet® 10BB GDL. Figure 2.8 shows the through-plane observation of initial spots of liquid water. It can be seen that liquid

water clusters under the ribs are higher compared to the ones under the channels, which is in good agreement with the ex-situ results reported in [160].

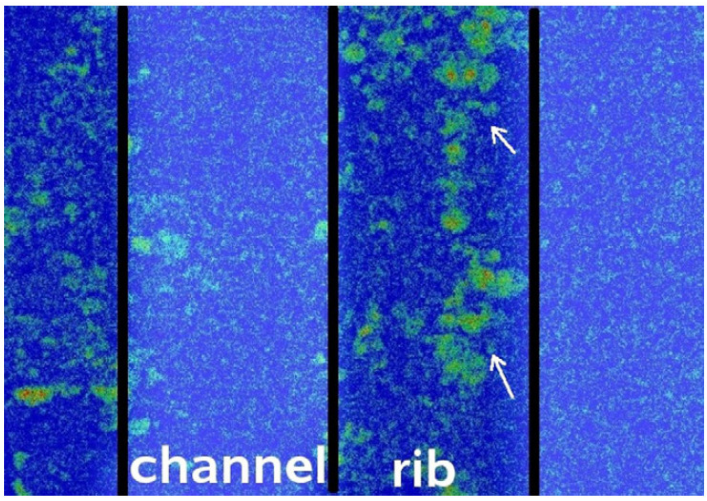

Figure 2.8. Spots of liquid water accumulation beneath the rib of the BPP (bright spots). From [164].

Water management is one of the major issues affecting the PEFCs' mechanical behaviour and electrical performance. In order to investigate the effect of mechanical compression on water management, in-situ and ex-situ characterisation techniques, with more focus on the latter, have been employed by a number of research teams. Many authors reported some causal relationships between water management issues and the applied mechanical compression. Preferential pathways for water transport in the GDLs under mechanical compression are still a subject of debate; some studies reported that water is preferentially transported in the compressed regions underneath the ribs [160,164] whereas others claimed preferential pathways in the areas beneath the channels [163]. Therefore, the results regarding this subject are still inconclusive. Moreover, although a number of in-situ water visualisation techniques exist, as have been employed by different authors using synchrotron X-ray radiography [164,165] and neutron imaging [166–168], to our knowledge, the use of these techniques to conduct specific investigations about the effects of mechanical compression on water management in an operating PEFC is still limited. The use of such techniques would be of major importance in order to validate some previous assumptions regarding the impacts of mechanical compression on the water management capacity of operating PEFCs [169].

3 Conclusion and future prospects

Through the application of in-situ characterisation techniques, valuable information regarding the effects of mechanical compression on the performance of operating PEFCs has been widely reported in the literature. In this regard, a literature-based analysis has been carried out in this chapter in order to give a comprehensive overview on the previously published studies on

the effects of mechanical compression and their respective impacts on the fuel cell performance and component properties. First, both internal and external mechanical compression mechanisms, along with their respective impacts, were presented. Then, the effects of mechanical compression on GDL properties and its water management were analysed. Finally, a summary of the studies focusing on the in-situ characterisation of the effects of mechanical compression on PEFC performance by way of electrochemical and mechanical techniques was provided (see Appendix B). From this literature review, the following conclusions can be drawn:

- The development of new compression methods, devices, and materials, allowing homogeneous pressure distribution and dissipating the pressure concentration on the edges of the PEFC components is needed in order to mitigate the detrimental impacts of mechanical compression on the PEFC performance.
- Although extended studies have been conducted on water management and in-situ liquid water visualisation techniques, dedicated investigations on the effect of mechanical compression by the use of in-situ water visualisation technique are still needed in the literature. Using such techniques would help either validating or disapproving various hypothesis and conclusions reported in the literature. Thus, proper implementation of in-situ water visualisation techniques in mechanical compression studies seems to be necessary for further investigations on the effects of mechanical compression on water management in PEFCs.
- Both pressure-sensitive and piezoresistive films have been used to assess the generated mechanical stresses under the assembly pressure. However, these techniques allow the investigation of pressure distribution in off-line fuel cells (i.e. not in operation). Therefore, reports on new techniques that allow measuring the generated stresses during PEFC operations still lack in the literature, e.g. smart composite structures with embedded mechanical stress measurement devices. The development of such new tools would be of major benefit for the understanding of stresses generated during PEFC operations, and it could be of significant help for the development of enhanced PEFC multi-physical models.
- Real-world vibration tests were carried out on PEFCs mounted on either vibrating platforms or real vehicles. However, the investigated fuel cells were usually not in operation during vibration, and the performance tests were carried out on steady test benches either after vibration tests or at regular periods during tests. It would be interesting to investigate the effects of real-world vibration on fuel cell performance using real-time procedures. The use of such characterisation procedures would help to assess the variations of the PEFC performance while undergoing real-world vibration conditions, which is more representative of the real-life operating PEFCs.
- Freeze/thaw cycles related performance degradation was attributed to the water volume expansion and Pt particles migration. However, no study has measured the induced compression value caused by freezing conditions so far. Knowing such values would be of significant importance to help modellers to accurately determine the F/T-induced stresses.

- Various researchers have investigated the issue of optimal PEFC assembly pressure. Though in most of the cases, incohesive clamping parameters were used, e.g. cell compression procedures, cell operating conditions, single-cell, fuel cell stacks, and components. Therefore, this lack of cohesion makes it difficult, if not impossible, to draw a conclusion concerning the optimal assembly pressure. Moreover, the research of optimal clamping pressure was only related to the performance of the fuel cell without considering the clamping process; therefore, studies combining both clamping mechanisms and optimal clamping pressure are lacking in the literature. In order to optimise the PEFC performance, future investigations may include the research of both optimal clamping pressure and its adequate clamping mechanism as a function of the final application of the fuel cell since the mechanical stresses may differ from one application to another (e.g. stationary, portable, and transportation).
- With regard to the pressure distribution across the fuel cell stack components, it has been well recognised that, for a typical fuel cell assembly method (namely point-load designs with bolts and nuts), the pressure distribution concentrates on the edges of the fuel cell components whereas the centre receives much lower clamping load. In order to reduce this inhomogeneity, new techniques allowing the mitigation of the effects related to this issue have already been reported in the patent literature. However, no comparative studies have been carried out to investigate these techniques even though it may have a significant impact on the enhancement of fuel cell performance. Thus, it would be interesting for future studies to investigate the advantages and drawbacks of different compression retention systems reported in the patent literature.
- Although some studies have combined both in-situ and ex-situ characterisation techniques in order to investigate the effects of mechanical compression, causal relationships between in-situ and ex-situ observed performance are still needed in the literature. Therefore, there is still a large area to explore in order to deepen our understanding of the effect of mechanical compression on the PEFCs performance by combining both in-situ and ex-situ characterisation techniques. Indeed, this present one of the main objectives of this thesis, results related to the in-situ/ex-situ correlations will be given in chapters 4 and 5 of this thesis.

Before going into the analysis of the experimental results of our work, it appears essential to start first with the presentation of the experimental means employed during this thesis, which lets us introduce the following chapter of this manuscript focusing mainly on the development of dedicated PEFC experimental means for in-situ coupled mechanical/electrical investigations.

Chapter 3
Development of dedicated PEFC experimental means for combined mechanical/electrical in-situ investigations

In-situ investigations of the effects of mechanical compression on the performance of the PEFC necessitate first the development of adapted test facilities. In the case of this thesis, the development of the experimental means was the first task to be conducted since we have special specifications that are intended to be as close as possible to real-life operating PEFCs (e.g. components properties, active area size). This chapter, therefore, deals with our contribution to the development of dedicated hydrogen test facilities for the fuel cell platform of Belfort. In fact, this task presents an important part of the work of this manuscript. Firstly, the developed fuel cell test bench is described. Then, the different steps of the instrumentation of the cell compression unit are explained. This chapter ends with a repeatability study of the mechanical compression and displacement measurements. It has to be mentioned that this chapter details the developed experimental means; the experimental results are given in chapter 4 of this thesis.

Before going into the presentation of the developed experimental means, it seems opportune to start with a brief introduction of the context in which this thesis was carried out.

1 The fuel cell platform

The work presented in this thesis was fully carried out in the fuel cell platform located in Techn'hom, which is a 110-hectare site located in Belfort with more than a hundred industrial and engineering companies and 7000 employees. The fuel cell platform is managed by the UTBM in close collaboration with the hosted structures. It regroups facilities dedicated to research and development for hydrogen and fuel cell systems. These facilities are used by personnel from different institutions (e.g. UBFC, CNRS, Univ. Gustave Eiffel) and companies (e.g. H2SYS). They account for nearly 3500 m^2 for 115 hosted personnel, composed of permanent members (e.g. full and associate professors, researchers, engineers, administrative staff) and other temporary members (e.g. PhD graduate students, postdocs, teaching and research assistants - ATER).

The fuel cell platform includes two areas of around 450 m² dedicated to the testing of hydrogen and fuel cell systems, with some specific facilities:

- Climate chamber (-45°C → +130°C).
- Vibrating table (250 kg, max acceleration 3g, max sine force 35 600 N).
- Fuel cell auxiliaries test facilities (e.g. DC/DC converters, actuators).
- Hydrogen suppressor up to 350 bars for H_2 vehicles refilling.
- Metal hydride characterisation (PCT samples, reservoirs).
- On-site hydrogen electrolyser (1 $Nm^3.h^{-1}$).
- Fuel cell test benches (< 1 kW up to 120 kW).

These test facilities, along with the rest of the installations of the fuel cell platform, are prepared for hydrogen experimentations in complete safety standards (e.g. ATEX zones, dinitrogen inerting, continuous ventilation). The platform is securely supplied by a technical gas storage and distribution facility located next to the building. Hydrogen is stored at 200 bars and depressurised to 10 bars before being distributed to the platform.

2 Presentation of the developed experimental means

In order to experimentally investigate the effects of mechanical compression on the PEFC performance, a specially designed test equipment was developed during this thesis. Figure 3.1 depicts the main parts of the developed apparatus.

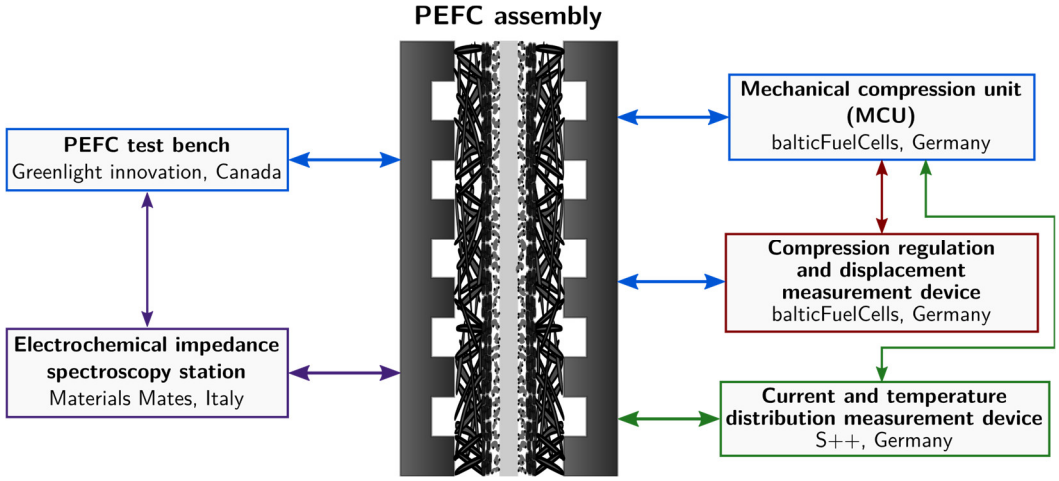

Figure 3.1. General description of the developed experimental means.

This apparatus allows combined electrical and mechanical characterisations of a single cell PEFC subjected to various operation conditions and mechanical compression, and it includes:

- **PEFC test bench:** control and monitoring of the reactant gases, cell temperature, electronic load.

- **Mechanical Compression Unit (MCU):** application of controlled mechanical compression to a PEFC single cell assembly with an active area of 225 cm^2.
- **Current and temperature distribution measurement device:** simultaneous measurements of the distributions of current and temperature.
- **Compression regulation and displacement measurement device:** regulation of the compression applied and measurement of the displacement in thickness of the single cell PEFC (measurement resolution in the order of microns) as a function of the operating conditions.
- **Electrochemical Impedance Spectroscopy (EIS) station:** specific electronic load and Frequency Response Analyser for EIS records.

In the following subsections, more details are given on each part of the equipment developed during this thesis.

2.1 PEFC test bench

The PEFC test bench, in its early development phase, consisted of a 660W fuel test bench (LS600 from PRAGMA Industries [170], France) associated to a FCW2500T [171] recirculating cooler (JULABO, Germany) for temperature control of the fuel cell. This early version of the test bench was originally installed during Khadidja BOUZIANE's master internship and during the first year of this PhD thesis. This test bench was constrained by a number of technological limitations, mainly due to the insufficient maximum current of the electronic load (i.e. 132 A) leading to a maximum current density of 0.58 $A.cm^{-2}$ for our PEFC with 225 cm^2 active area, which is not truly representative of the real conditions related to the transport application, along with a limited instrumentation and control possibilities. In 2018, the 3M® company (Beauchamp site, which we truly acknowledge) donated to the UTBM a 1.5 kW test bench (G7805 from Greenlight Innovation® [172], Canada) allowing to reach a maximum current of 500 A, which allows to reach a current density of 2.22 $A.cm^{-2}$ for our fuel cell. Significant work was carried out to get this new test bench operational in the fuel cell platform in Belfort. Firstly, we connected the test bench to our test platform (fluid arrivals and electrical connections). We then connected our mechanical compression unit to this bench. This test bench allows all the measurements necessary for the monitoring and the control of the PEFC (e.g. cell voltage, flows, and pressures, temperatures). The test bench is controlled using a dedicated control and automation software developed by Greenlight Innovation® (i.e. HyWARE II™).

The G7805 test bench is composed of three main parts. The first one includes the complete gas conditioning system, namely gas flows, temperatures and pressure controls, and gas humidification subsystem. The second part includes a DSLV1520 electronic load (Höcherl & Hackl [173], Germany), and the electronic management system. Finally, the third part is made of the peripherals necessary for the temperature control of the PEFC, namely the cooling/heating circuit and its equipment. A simplified functional block diagram of the test bench is depicted in figure 3.2 and technical specifications of the equipment are given in

Appendix C. We will give hereafter a brief description of the fuel, oxidant, and temperature control circuits.

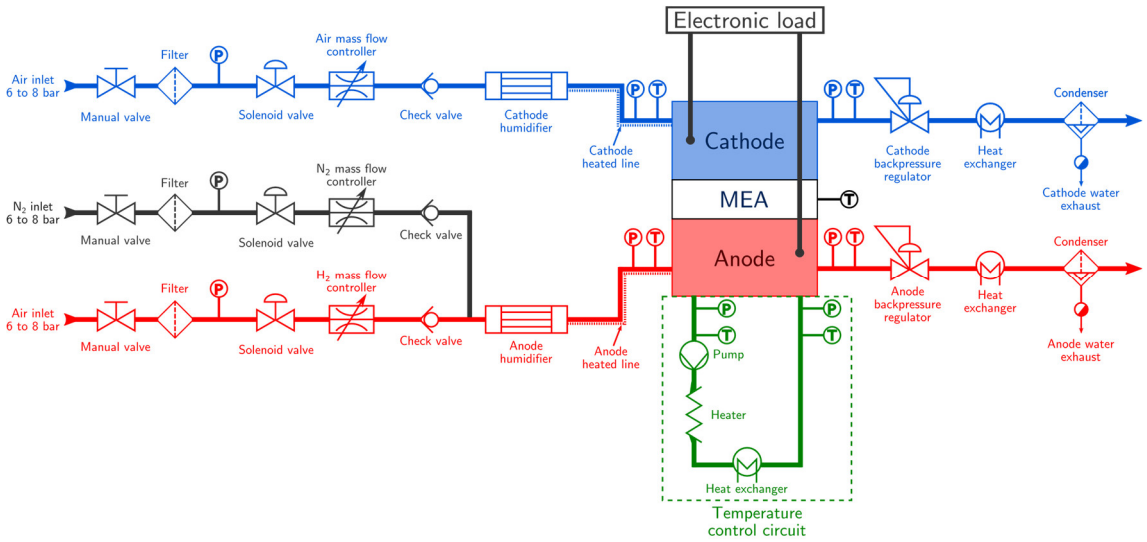

Figure 3.2. Simplified functional block diagram of the Greenlight™ G7805 test bench.

2.1.1 Fuel circuit

As mentioned earlier, the hydrogen is stored at 200 bars in high-pressure tanks located outside of the fuel cell platform. The test bench is fed by the fuel cell platform facilities, which deliver a pressure of about 8-10 bars. The hydrogen pressure is, therefore, regulated a first time, prior to the fuel cell, at the exit of the platform distribution circuit. A mass flow controller is used to control the hydrogen flow in the fuel circuit. Another mass flow controller can be used in order to control the flow of nitrogen to be possibly injected into the hydrogen stream (used mainly for the inerting of the hydrogen line). The hydrogen humidification process is based on deionised water steam injection into the gas feeding the PEFC. The pressure and temperature of the reactants are measured at the inlet of the PEFC. Upstream of the PEFC, the hydrogen temperature is kept constant using flexible heated lines that ensure the connection between the hydrogen circuit of the test bench and the PEFC. At the fuel cell outlet, the temperature and pressure are measured again. A backpressure valve located at the outlet of the fuel cell regulates the pressure measured at the PEFC gas inlets. Finally, a condenser allows the evacuation of the water contained in the anode exhaust gases.

2.1.2 Oxidant circuit

The air supply is ensured by a compressor system located in a technical room inside the fuel cell platform. Air mass flow is measured upstream to the PEFC. Air temperatures and pressures are measured at fuel cell inlet and outlet. The air humidification process is also based on the principle of deionised water vapour injection into the air stream of the fuel cell. The rest of the air circuit is quite similar to that of hydrogen as shown in figure 3.2.

2.1.3 Temperature control circuit

Deionised water is used in the test bench as a cooling medium of the PEFC. The conductivity of the cooling medium is continuously measured by a conductivity meter to ensure low electrical conductivity of the deionised water. The cooling medium is circulated by a pump in a controlled flow mode. In our experimentations, the outlet temperature of the PEFC cooling medium is considered as representative of the PEFC temperature. The temperature control is conducted through the variation of the heater temperature and/or the flow rate of the cold water, provided from the fuel cell platform facilities, passing through the heat exchanger.

2.2 Mechanical compression unit (MCU)

A custom-built Mechanical Compression Unit (MCU), quickCONNECT fixture FC225 (batlticFuelCells [174], Germany), was specially designed for our test requirements. The MCU comes with four pneumatic cylinders that are capable of exerting a continuously adjustable mechanical compression (up to 2.15 MPa) on a single-cell PEFC (active area of 225 cm^2). The rapid fixing module (i.e. quickCONNECT fixture - qCf) allows precise assembly of the cell components (flow field plates, gas diffusion layer, membrane electrode assembly) in a relatively straightforward and fast manner. figure 3.3 and figure 3.4 depict the MCU and its operating principle.

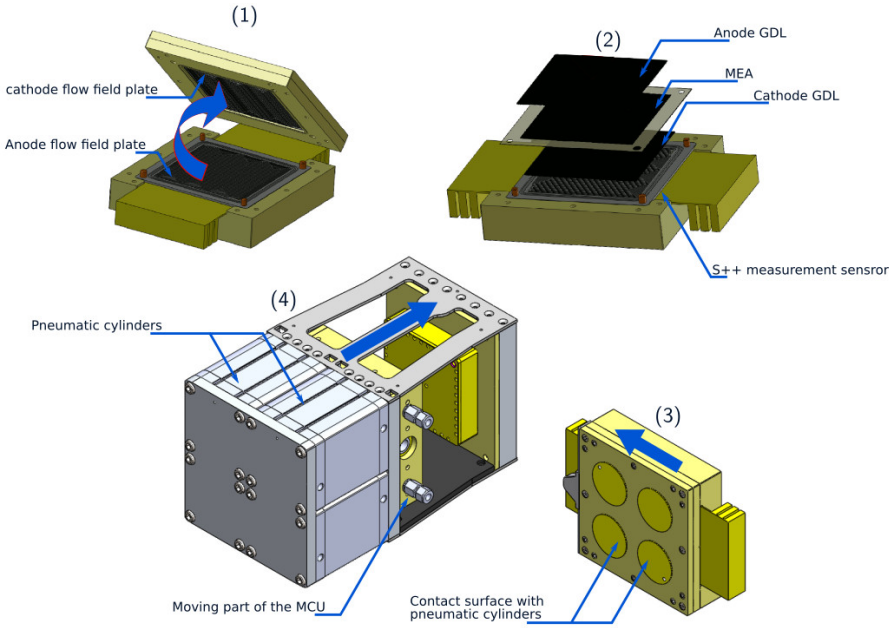

Figure 3.3. Mechanical compression unit: (1) opening of the qCf, (2) assembly of the PEFC components, (3) placement of the qCf, (4) application of the mechanical assembly compression by the four pneumatic cylinders (images courtesy of balticFuelCells GmbH, Germany).

In order to get a thorough understanding of the effects of mechanical compression on PEFC performance, the MCU was instrumented and equipped with: i) proportional pressure regulator that allows the regulation of the mechanical compression with a dynamic resolution of 0.02 MPa; ii) displacement sensor with a dynamic resolution of 1 µm; and iii) sensor for measuring the distributions of the current and the temperature (S++®, Germany), with 441 and 49 current and temperature measuring points respectively. More details about these instrumentations are given in the following subsections. This cell fixture was developed to allow accurate and repeatable characterisation of the fuel cell components under different operating conditions and assembly pressure. A repeatability study is, therefore, provided at the end of this chapter.

2.2.1 Mechanical compression regulation system

A proportional pressure regulator (FESTO [175], Germany) was used to accurately control and measure the pressure inside the four pneumatic cylinders. The characteristics of this device are given in table 3.1.

Characteristic	**Value**
Pressure regulation range	0.1 - 10 bars
Operating medium	Nitrogen
Linearity error	2 % Full scale
Repetition accuracy	0.5 % Full scale

Table 3.1. Main characteristics of the proportional pressure regulator.

The force per unit area (in $N.mm^{-2}$ or MPa) of the fuel cell is calculated from the pressure inside the pneumatic cylinders along with the backpressure inside the PEFC components (i.e. FFPs channels) regulated at the anode and the cathode compartments. These pressures apply forces that have opposite directions.

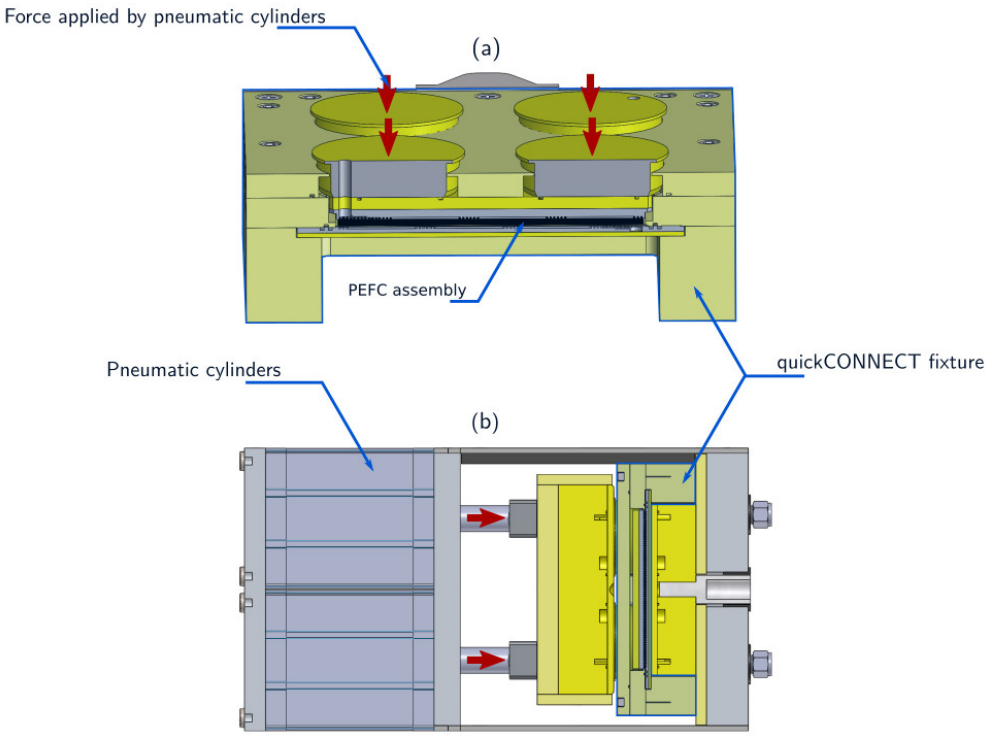

Figure 3.4. Compression process of the MCU: (a) uncompressed qCf, (b) compressed qCf (images courtesy of balticFuelCells GmbH, Germany).

The manufacturer of the MCU (i.e. balticFuelCells) considers the area of the four pneumatic cylinders and the area of the flow field channels to be equivalent to the areas of two cylinders with radiuses of R=125 mm and r=70 mm, respectively. Therefore, the force per unit area of the PEFC can be calculated using equation 3.1:

$$P_{MPa}=\pi\frac{R^2p_{cyl}-r^2p_{bp}}{A}\times10^{-1} \tag{3.1}$$

Where:

$\mathbf{P_{MPa}}$	[MPa]	the pressure per unit area of the PEFC.
$\mathbf{p_{cyl}}$	[bar]	the pressure in the pneumatic cylinders, measured from the outlet of the proportional pressure regulator.
$\mathbf{p_{bp}}$	[bar]	the backpressure of the PEFC, measured from the backpressure regulators of the test bench.
A	[mm^2]	the active area of the fuel cell.

Figure 3.5 shows the force per unit area as a function of the pressure in the pneumatic cylinders, in the case of a backpressure value of 0.5 barg, which will be the standard value that will be used later in our experimental investigations.

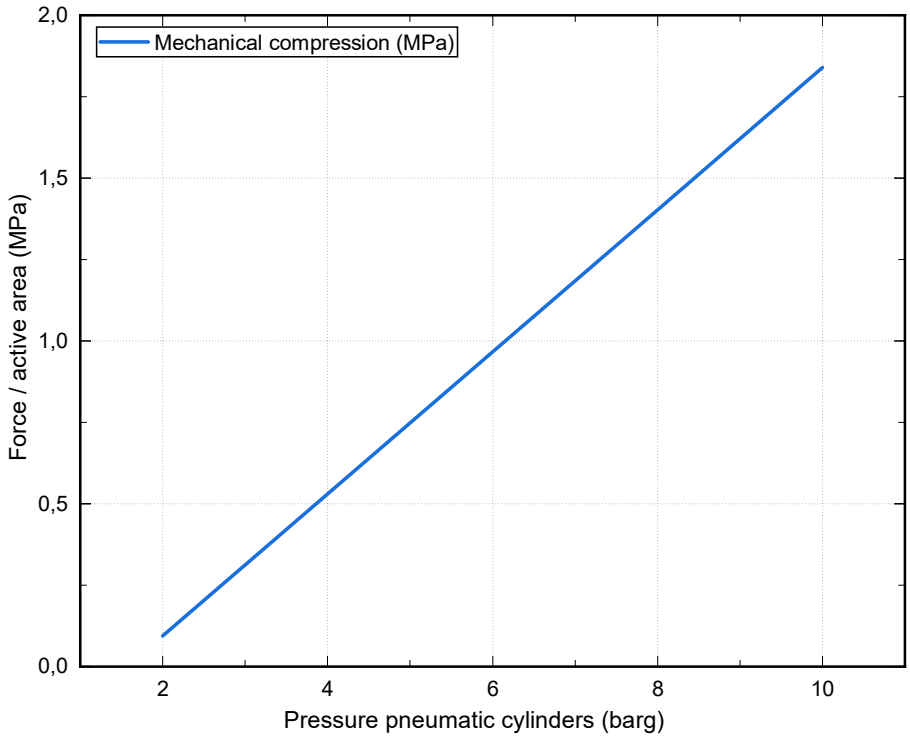

Figure 3.5. Force per unit area (in N.mm^{-2} or MPa) as a function of the pressure in the pneumatic cylinder with a backpressure value of 0.5 barg.

For the rest of this manuscript, mechanical compression will be given in force per unit area (MPa) of the fuel cell.

2.2.2 Mechanical displacement measurement device

The mechanical displacement measurement sensor is used for displacement and/or position measurements. This sensor allows accurate displacement measurement of the moving part of the MCU relatively to the fixed one. This sensor employs the principle of the linear variable differential transformer (LVDT), which is one of the most accurate and reliable mechanical displacement sensors type available. The advantage of this LVDT-based sensor is that there is no electrical contact across the displacement sensing elements, allowing it to have an excellent resolution (see table 3.2).

In our application, the displacement sensor allows the measurement of the variation of the fuel cell thickness associated with the changes in the operating conditions (applied mechanical compression, load current, fuel cell temperature, physical parameters related to reactants conditioning). The sensor used in our test apparatus is a spring returned D6/01000A [176] (RDP Group, UK), and its main characteristics are listed in table 3.2.

Characteristic	Value
Range	±1 mm
Linearity error	±0.5 % Full scale
Dynamic resolution	1 µm

Table 3.2. Main characteristics of the displacement sensor.

Figure 3.6. shows the location of the displacement sensor in the MCU. A repeatability study of the displacement measurement is provided at the end of this chapter.

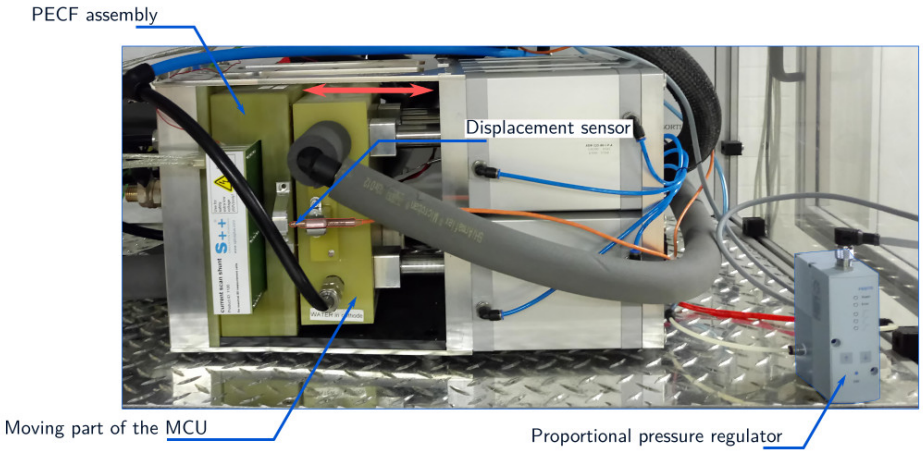

Figure 3.6. Position of the displacement sensor on the MCU.

2.3 Local currents and temperatures measurement

Along with the electrochemical measurements of the PEFC performance, the distributions of the current and the temperature were studied in this thesis. The purpose is to investigate the local phenomena occurring within the PEFC components when subjected to mechanical stresses. The system used is a current scan shunt [177] (S++® Simulation Services, Germany) that allows measurements of local current densities and temperatures. The device used has been specifically designed for our 225 cm^2 PEFC with 21×21 and 7×7 points (or segments) for local current densities and temperatures measurements, respectively.

The sensor of the segments has a thickness of 700 µm and uses a low ohmic shunt resistor for local current density measurements, and it is directly connected to the anode flow field of the PEFC assembly. The sensor is made from a special copper layer with gold plated contact segments in order to prevent corrosion and to have a low electrical contact resistance with the flow field plates; the operating principle of the local currents and temperatures measurements is described in figure 3.7. The left side is connected to the anode flow field plate while the right side is connected to the current collector side of the MCU.

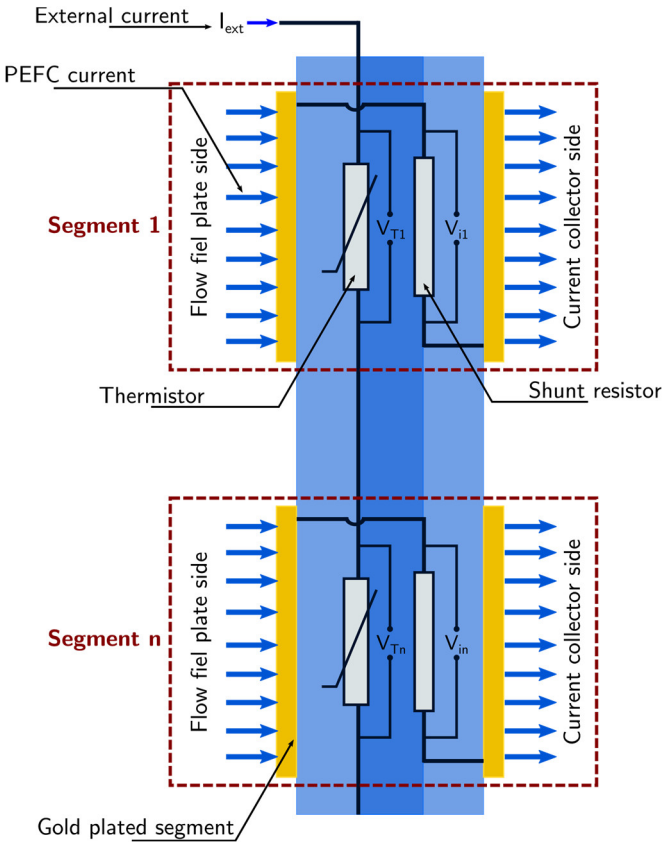

Figure 3.7. The measurement principle of the local currents and temperatures device.

The current measurement zone is divided into 441 insulated segments, each segment has an area of 1.96 cm^2. Figure 3.8 depicts the segments of the measurement device. The local currents collected by the segments flow through the shunt resistors. The current of the segment is obtained by measuring the voltage drop across the shunt resistor with a maximum reading measurement error of 1%. An automated calibration process is conducted during each experimentation in order to compensate the variation in the measured resistance due to the temperature coefficient related to the resistance of the copper layer.

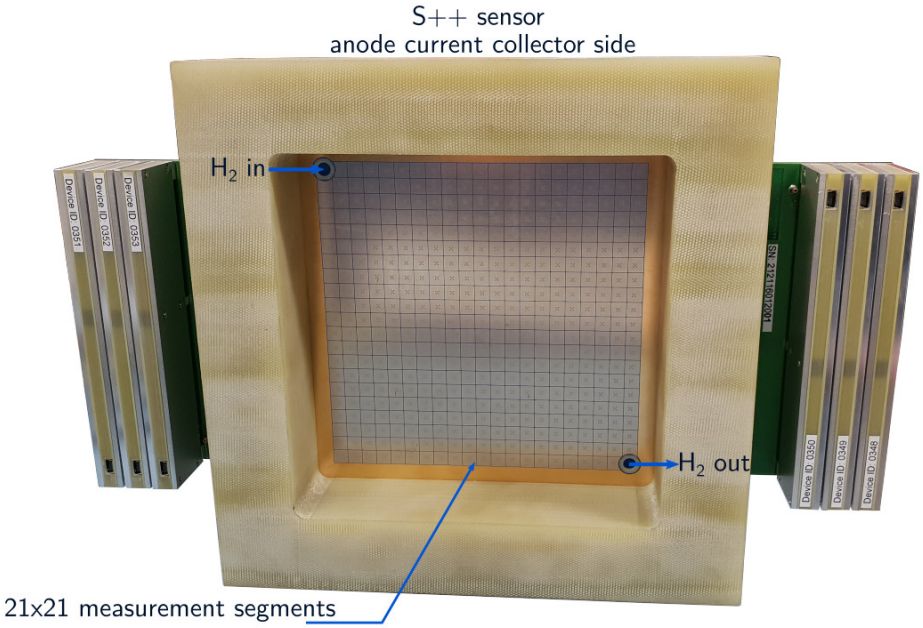

Figure 3.8. Anode current collector side of the S++® sensor

With regards to the temperature distribution, the local temperatures are measured in 49 segments. Each segment has an area of 4.6 cm^2. The measurement principle is based on voltage drop measurement in a series of thermally controlled resistors (i.e. thermistors) as depicted in figure 3.7. The current scan shunt can operate at temperatures up to 100°C with a resolution of 0.1°C.

2.4 Electrochemical impedance spectroscopy station

Th EIS station comprises different modules: a power unit of 1.5 kW (0-50V) reversible in current (±50A), a one-channel master frequency analyser for the fuel cell sack voltage, and a 12-channel frequency analyser for the single cell voltages of the fuel cell. This instrument will be mainly used for EIS analysis in our single cell PEFC. Figure 3.9 depicts the apparatus developed for this thesis.

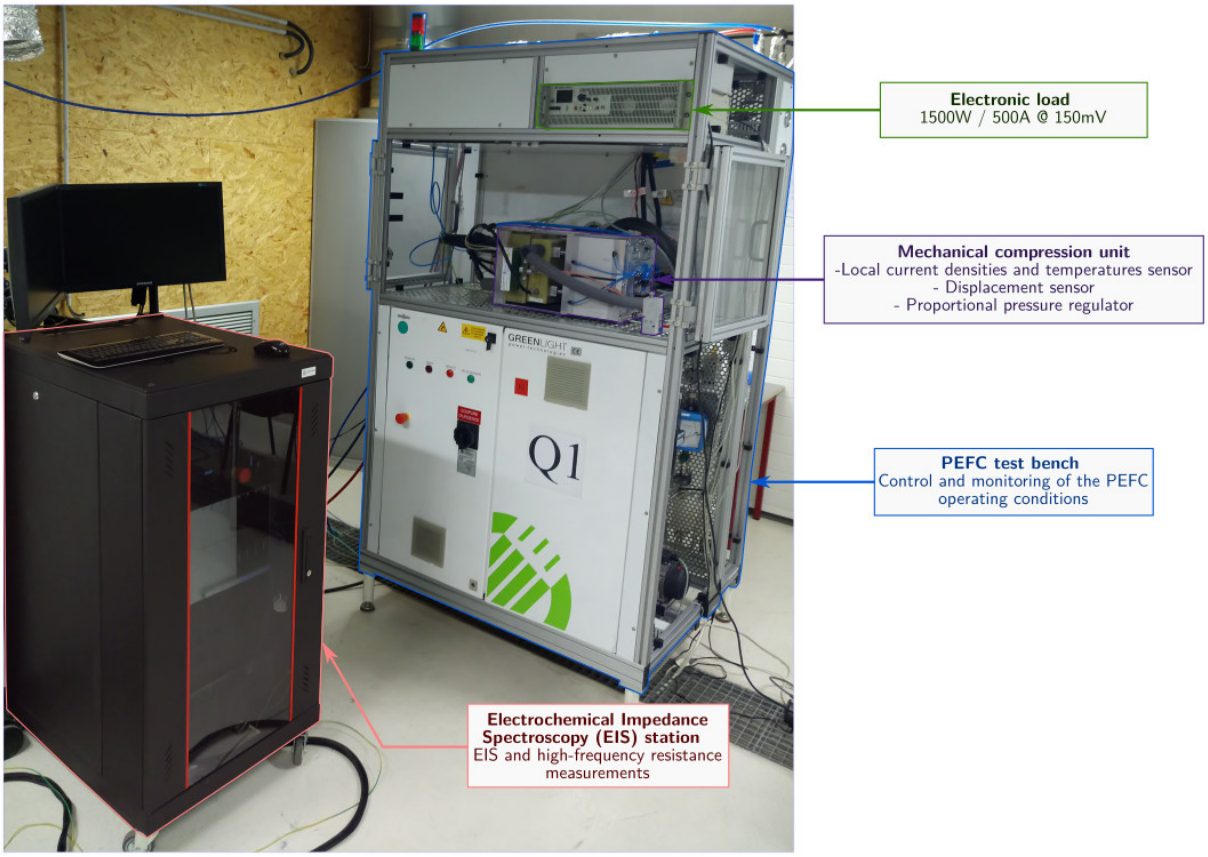

Figure 3.9. Image of the experimental means developed in the framework of this thesis

Through the development of the experimental means shown in figure 3.9. valuable results regarding the effects of mechanical compression on PEFC performance will be given in chapter 4. As a matter of fact, the reliability of these results is conditioned by good repeatability of the mechanical compression and displacement measurements. A repeatability study is, therefore, provided in the following section.

3 Repeatability study of the displacement measurements

Repeatability refers to the variation in repeated measurements due to the measuring instrument. It is, by definition, the variation observed in the measured value when the same operator measures the same subject several times, using the same instrumentation, under identical conditions over a short period of time, over which the measured value is considered constant [178]. In the case of our study, it is important to start first with a repeatability study of the compression and displacement measurements before going into experimental investigations. The goal is to ensure that the mechanical compression and displacement measurements are quite repetitive. With this regard, the aim of this section is to study the

repeatability of the compression and displacement measurements under a set of anode and cathode backpressures and a number of mechanical compression assembly values.

For all the experimentation in this study, a single cell PEFC was investigated using i) three-layer Membrane Electrode Assembly (MEA) with 225 cm^2 active area and a Nafion® XL membrane; ii) Sigracet® 38BC GDL; iii) Parallel serpentine (12 parallel channels) flow fields with channel and land width of 1 and 0.96 mm, respectively. More details about the investigated PEFC components will be given later in chapter 4 as the aim of this chapter is to study the repeatability of the compression and displacement measurements of the MCU, and not to study the performance of the PEFC, which is the objective of the following chapter.

3.1 Experimental protocol

In this study, five different backpressure levels were investigated, namely atmospheric pressure (atm), 12.5 kPa, 25 kPa, 50 kPa, and 100 kPa. At each backpressure level, three cycles of mechanical compression were applied to the PEFC assembly ranging from 0.35 MPa to 2 MPa with steps of 0.15 MPa each 10 seconds. Figure 3.10 depicts the mechanical compression cycles applied to the PEFC. It has to be mentioned that the PEFC used has been subjected to hundreds of mechanical compression cycles before conducting this repeatability study. Therefore, the break-in and the first cycle compression effects are not considered in this study.

It can be seen from figure 3.10 that the repeatability of the compression measurement is quite good, as the standard deviation of these three mechanical compression cycles was almost zero. Therefore, in this chapter, the focus will be mainly put on the repeatability study of the mechanical displacement measurements.

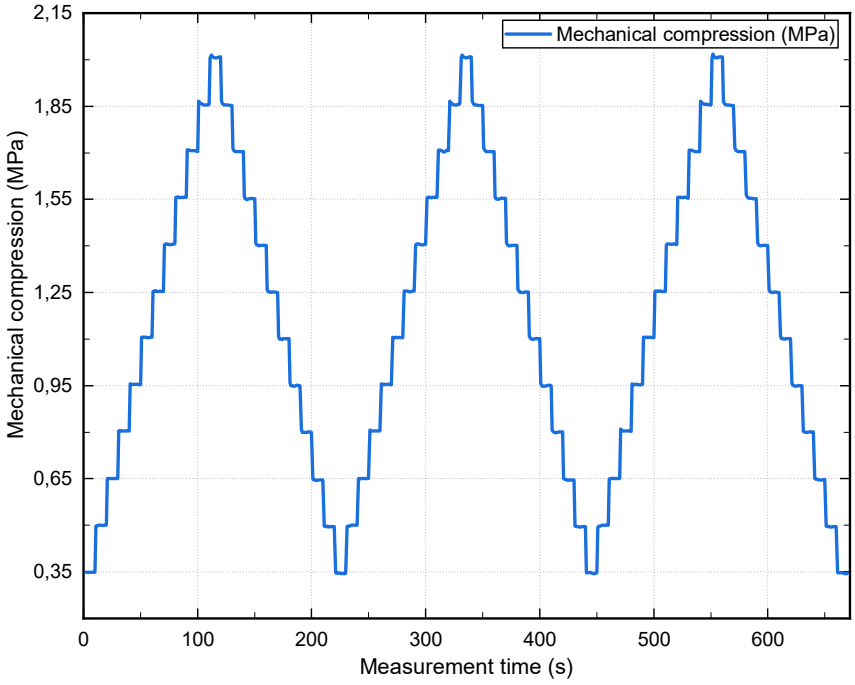

Figure 3.10. Mechanical compression cycles applied to the PEFC for repeatability study.

In order to reduce the effects of the variation of temperature and humidity on the displacement measurements, all tests were conducted offline (nonoperating PEFC) and under ambient temperature (i.e. 21°C and 54%RH), which was considered to be constant during the test period. Nitrogen was used in the anode at a flowrate of 3 Nl.min^{-1} and air in the cathode at a flowrate of 6 Nl.min^{-1}. The experimental procedure is depicted in figure 3.11.

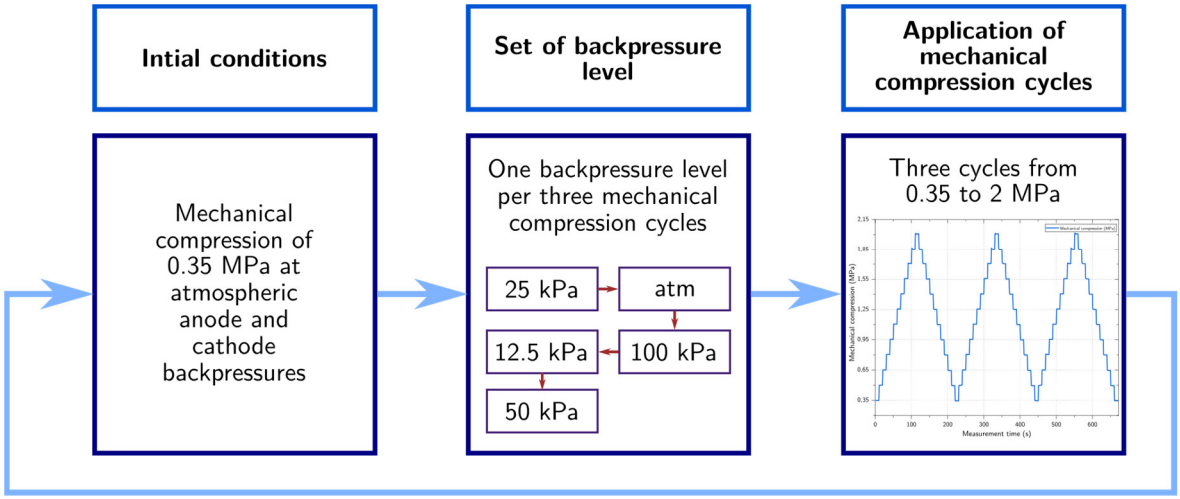

Figure 3.11. Experimental procedure for the repeatability study of the displacement measurements.

This experimental procedure gives displacement measurement of 12 levels of mechanical compression per half cycle, with three cycles per test, and with three tests repeated for every backpressure level. The backpressures were applied thusly: 25 kPa → atm → 100 kPa → 12.5 kPa → 50 kPa. Before conducting the first test (i.e. 25 kPa), an anterior conditioning cycle was conducted at atmospheric pressure. Results at 50 kPa and 100 kPa will be discussed in this section. Nonetheless, the results of other backpressure levels, namely atm, 12.5 kPa, 25 kPa will be given in Appendix D.

3.2 Displacement measurements at 50 kPa

The repeatability study was conducted at 50 kPa backpressure at both anode and cathode. Figure 3.12 shows the displacement measurement for three tests. Three mechanical compression cycles, as shown in figure 3.10, were applied for each test.

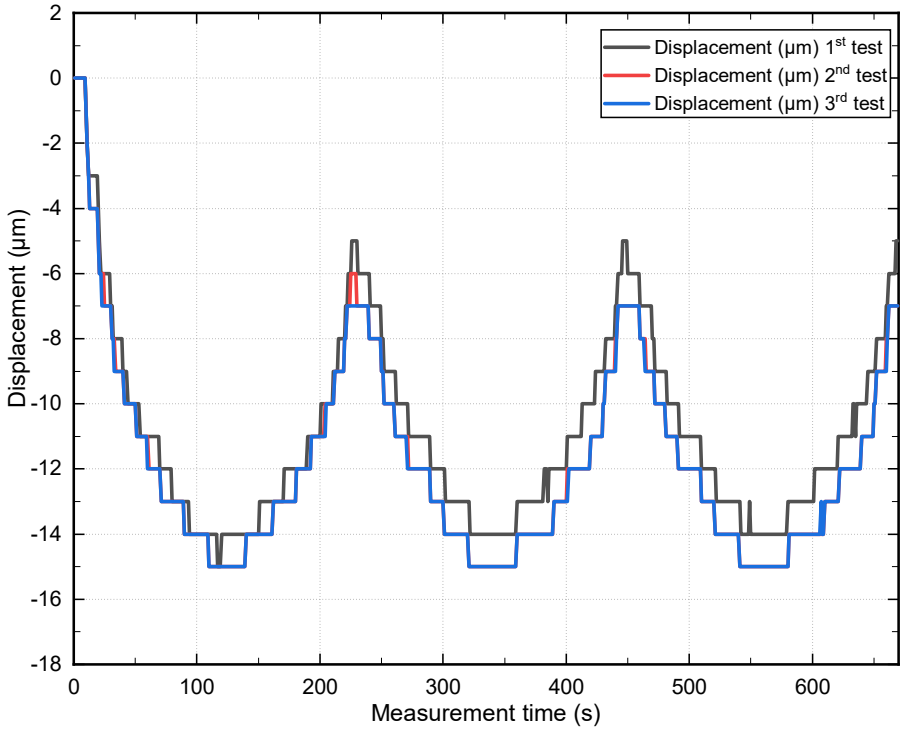

Figure 3.12. Displacement measurements of three tests at 50 kPa backpressure.

The standard deviation was calculated for every level of mechanical compression of the three tests. In order to quantify the repeatability error, the average and median values of all the calculated standard deviations are given.

It can be seen from figure 3.12 that measurements from the second and third tests are almost equal. The average standard deviation between the three tests is 0.54 µm and the median is 0.58 µm. These values are thoroughly low, and therefore prove a good repeatability of the displacement measurements.

The maximum displacement shown in figure 3.12 is 15 µm. This value was achieved between 1.7 MPa and 1.85 MPa, which means that increasing mechanical compression beyond 1.85 MPa would not lead to additional displacement of the components of the mechanical compression unit.

The measured displacement at the end of the first cycle is 6 µm for the first and the second tests and 7 µm for the third test. These same displacement values were also measured at the end of the second and third cycles for all three tests. Meaning that in order to attain a repetitive displacement measurement, this initial offset (measured at the end of the first cycle) has to be deducted from the rest of the measurements. This method will be discussed later in this section.

3.3 Displacement measurements at 100 kPa

The displacement measurements were conducted at 100 kPa backpressure at both anode and cathode. Figure 3.13 depicts the displacement measurements for three tests; three mechanical compression cycles were conducted for each test.

It can be seen from figure 3.13 that all the three tests gave virtually the same results. The calculations of the average and the median of standard deviation give 0.03 µm and 0 µm respectively. These results confirm the good repeatability of both the displacement measurements and the process of mechanical compression application.

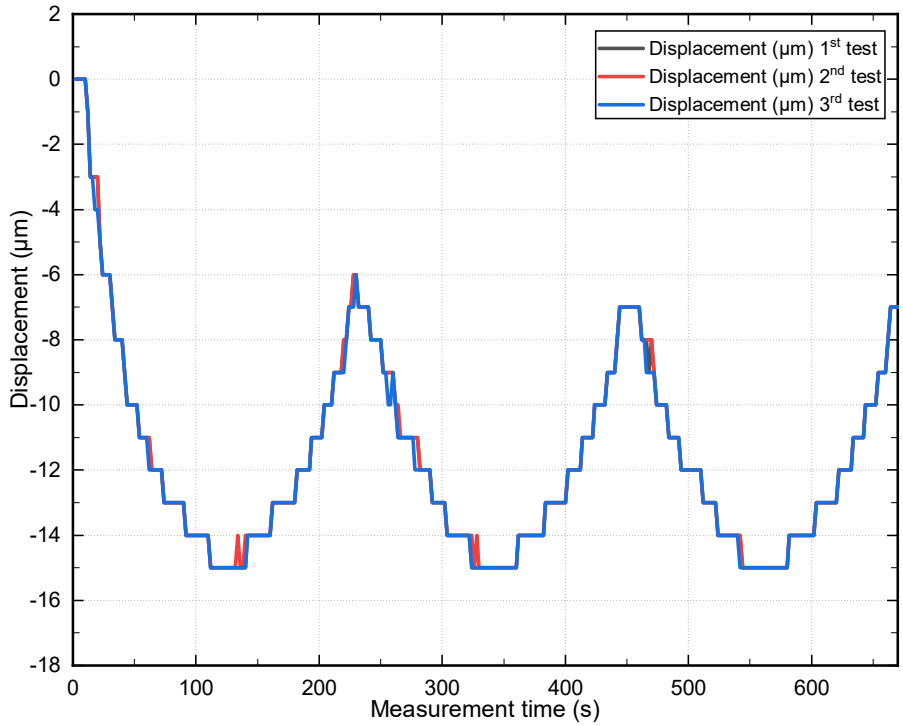

Figure 3.13. Displacement measurements of three tests at 100 kPa backpressure.

The maximum displacement in figure 3.13 was measured between 1.85 MPa and 2 MPa, which means that compression beyond 1.85 MPa would not result in any additional displacement of the components of the cell compression unit. These results are in good agreement with the results of the tests conducted at 50 kPa backpressure.

The displacement measured at the end of the first cycle is 7 µm for all the three tests. The same value was measured at the end of the second and third cycles. These results suggest that, in order to attain repeatable displacement measurements, this value must be deducted from measurements of the second and third cycles in order to get a standardised displacement measurement, which could be achieved using the offset deduction method as described hereafter.

3.4 Offset deduction method

The displacement measurement at the end of the first cycle was 7 µm for the three tests shown in figure 3.12. However, for other tests with the same backpressure of 100 kPa, as well as for other backpressures (i.e. atm, 12.5 kPa, and 25 kPa), this value varied from 2 to 8 µm, meaning that in order to get repeatable measurements, this first cycle offset needs to be deducted from the rest of the measured values starting from the second cycle. An offset deduction method is therefore proposed, where the first cycle is considered as a conditioning cycle needed for the initial positioning of the cell compression unit. Hereunder the proposed method:

i. Measurement of the displacement value (in µm) at mechanical compression of 0.35 MPa at the end of the first cycle (i.e. first cycle offset).
ii. Deduction of the first cycle offset value from all the measured values of the same test. The calculated displacement values will be referred to as standardised displacement.

For validation purposes, the proposed offset deduction method was employed using the experimental procedure described in figure 3.11 for nine tests at 100 kPa backpressure. Figure 3.14. depicts the obtained displacement measurements.

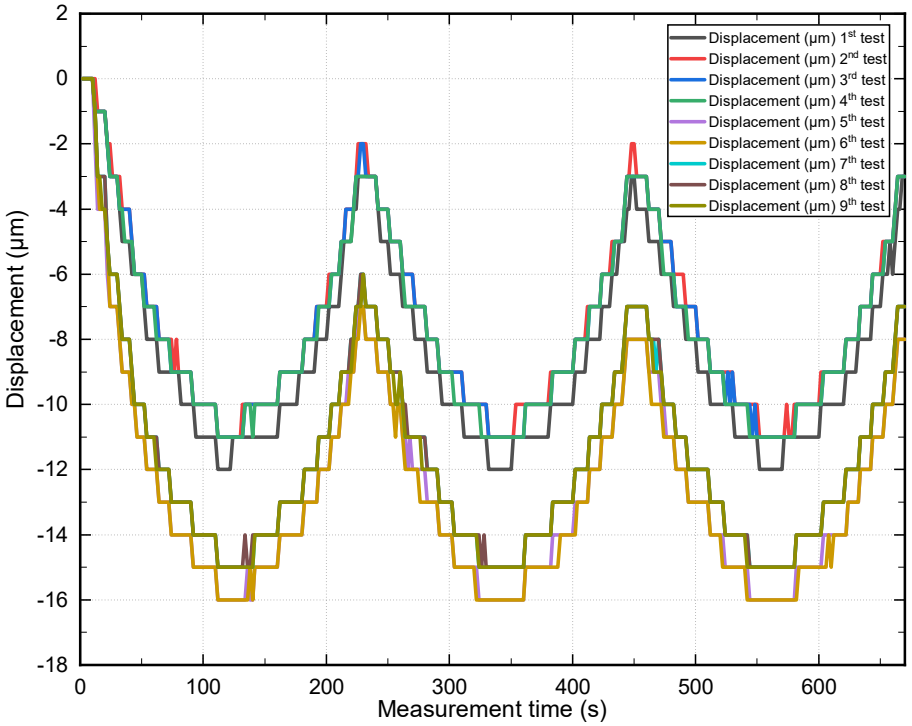

Figure 3.14. Displacement measurement for nine tests at 100 kPa backpressure.

It can be observed from figure 3.14 that the displacement measured at the end of the first cycle (i.e. first cycle offset) varied between 2 µm and 8 µm. The offset deduction method consists of deducting the first cycle offset from measurements in all other cycles of the same test. Figure 3.15 shows the results of this method.

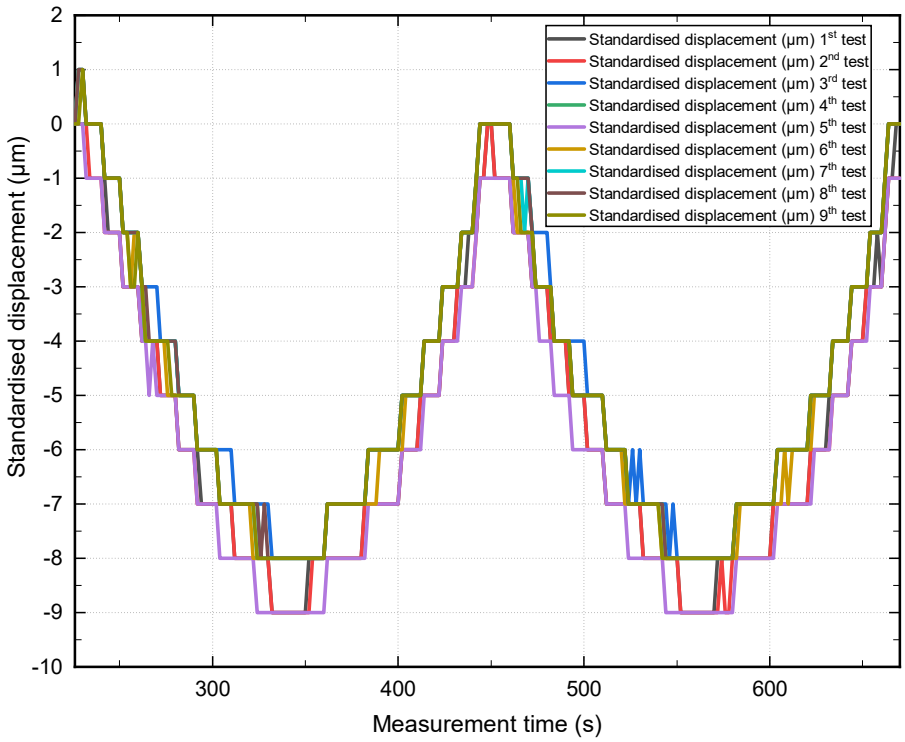

Figure 3.15. Standardised displacement measurements at 100 kPa – 9 test measurements.

The standard deviation was calculated for every standardised displacement value shown in figure 3.15. The average value of the standard deviations is 0.48 µm and the median value is 0.5 µm. These results represent lower values compared to the resolution of the displacement sensor of 1µm. For better readability, figure 3.16 shows the distribution of the calculated standard deviations as a function of mechanical compression.

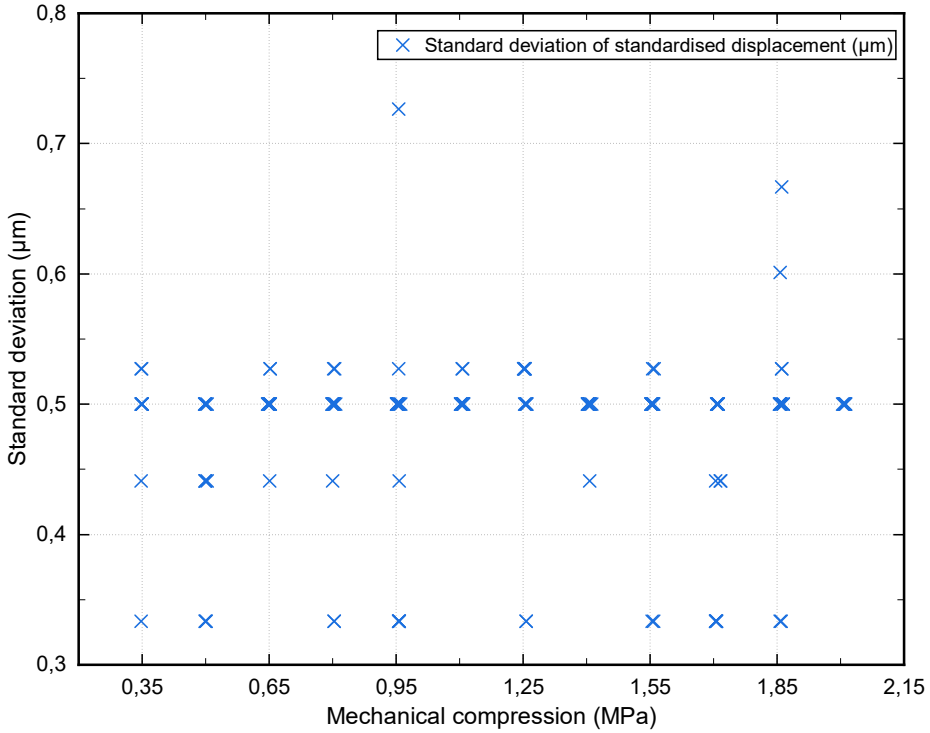

Figure 3.16. Calculated standard deviations as a function of mechanical compression (data from figure 3.15).

It can be concluded from figure 3.16 that the results of the offset deduction method are quite repeatable, and that the displacement measurements are substantially the same regardless of the displacement value of the first cycle offset.

4 Conclusion

This chapter detailed the experimental means developed in the framework of this thesis. The results presented here constituted a significant part of the work carried out during this thesis. First, the test bench used for the control and monitoring of the PEFC operating conditions was described, then the operating principle of the mechanical compression unit was given, including the proportional pressure regulator, the displacement sensor, and the current and temperature distributions' measurement system. Finally, a repeatability study of the mechanical compression and displacement measurement was conducted. Conclusions can be summarised as follows:

- The repeatability of the displacement measurements is good as the maximum average and median standard deviation, for all tested backpressure values, is about 0.58 µm and 0.6 µm, respectively. These values are lower than the measurement resolution of the displacement sensor of 1 µm.

- The repeatability of the mechanical compression measurements is excellent, as the calculated standard deviations from three mechanical compression cycles were insignificant (i.e. almost zero).
- Starting from the second cycle, the maximum displacement is achieved between 1.85 and 2 MPa, meaning that increasing the mechanical compression would not lead to further displacement of the compression unit components (including the PEFC). Besides, the displacement rate is about 1 µm for every 0.15 MPa.
- The first cycle displacement offset was measured between 2 and 8 µm, however, these values should not be taken as references. This suggests that the method of the first cycle offset deduction should be applied in order to get repeatable displacement measurements.
- Through employing the first cycle offset deduction method, the maximum displacement was measured between 7 µm and 9 µm.

From the results of this chapter, it was shown that the compression and displacement measurement are quite repeatable, especially when using the offset deduction method for displacement measurements. In fact, fuel cells may be subjected to hundreds of thousands of load cycles during their lifetime [100]. Also, the subject of the first cycle offset, or preloading the PEFC, was already discussed in the literature. Some authors reported that applying a compressive load before operating the PEFC would result in improved performance [76,101,102]. Indeed, it allows materials to be settled and the mechanical compression to be distributed more uniformly over the surface of the stack components. Therefore, for all the experimental results reported in the following chapters, and in order to get a repeatable mechanical compression, displacement and PEFC performance measurements, the offset deduction method will be systematically applied before conducting experimental investigations.

Chapter 4
Mechanical compression and its impact on the global performance of the PEFC

We showed in chapter 2, through the literature review, that mechanical compression is a major factor that impacts the PEFC performance. In order to investigate this effect, different characterisation techniques have been reported by the research community in this field and can be divided into two main categories, namely ex-situ, where the PEFC components are characterised outside the fuel cell assembly, and in-situ, where components are investigated within a PEFC operating under real-life conditions. Considering the complexity of the phenomena occurring within the PEFC, combining these two characterisation techniques is of paramount importance in order to evaluate the effects of mechanical compression and deconvolute their specific impacts on the overall performance of the PEFC. The objective of this chapter is, therefore, to investigate the effects of mechanical compression on the PEFC performance through: i) the use of in-situ characterisation techniques and ii) finding correlations with ex-situ results conducted within the framework of the research project of this thesis (i.e. MIREPOIx project).

This chapter aims to provide a thorough understanding of how mechanical compression quantitively affects PEFC performance. Investigations are conducted by combining polarisation measurements analysis, cell voltage monitoring, and electrochemical impedance spectroscopy (EIS). These investigations are realised using three different experimental procedures that represent, as close as possible, the operating conditions of the fuel cell during its lifelong operation. In order to finely investigate these effects, 12 levels of mechanical compression are considered in this study, ranging from 0.35 MPa to 2 MPa with steps of 0.15 MPa. The analysis provided in this chapter gives insight into the enhancement of PEFCs performance through optimising the assembly pressure and provides guidelines for researchers and industrials to further understand the effects of mechanical compression in order to optimise the PEFC performance.

This chapter proceeds as follows: we first present the constituent components of the PEFC used. We then present the experimental procedures employed in our investigations. Following that, we analyse the results obtained and provide quantitative results regarding mechanical compression impacts on the phenomena occurring within the PEFC. Correlations with ex-situ results are given throughout the chapter.

1 Presentation of the investigated PEFC components

The PEFC assembly was conducted using quickCONNECT fixture (balticFuelCells [174], Germany), which is a PEFC test fixture that allows rapid assembly/disassembly of a single cell PEFC. The operating principle and its constituent components are described in chapter 3. This section aims to provide details of the PEFC components employed in this study.

1.1 Membrane Electrode Assembly (MEA)

A three-layer Membrane Electrode Assembly (MEA) with a 225 cm^2 active area was used in this study. This MEA contains CLs with 0.2 and 0.4 mg $Pt.cm^{-2}$ at the anode and cathode sides, respectively. The membrane is a Nafion™ XL, which is based on a reinforced and chemically stabilised perfluoro sulfonic acid (PFSA) polytetrafluoroethylene (PTFE) copolymer. The reinforcement enhances the membrane physical properties [179,180]. Table 4.1 regroups the main characteristics of the Nafion™ XL membrane.

Characteristic	**Unit**	**Value**
Thickness [1]	µm	27.5
Area weight [1]	$g.m^{-2}$	55
Conductivity [2]	$mS.cm^{-1}$	Through-plane: >50.5
		In-plane: >72.0
Hydrogen Crossover [3]	$mL.min^{-1}.cm^{-2}$	<0.015

Table 4.1. characteristics of the Nafion XL membrane.

[1] Measurements taken for a membrane conditioned at 23 °C and 50% RH

[2] Conductivity measured at 23 °C and 100% RH

[3] Hydrogen crossover measured at 65 °C and 100% RH.

The choice of the MEA is based on the enhanced performance of the Nafion™ XL membrane and also the Pt loading that is comparable to what is actually found real-life operating PEFC used, for instance, in transportation applications [181].

1.2 Gas Diffusion layer (GDL)

The GDL used is a Sigracet® 38 BC (SGL Carbon [182], Germany), which is a non-woven carbon paper, MPL-coated, and PTFE-treated GDL. The Sigracet® 38 BC is considered as a low porosity GDL compared to other types (e.g. Sigracet® 39 BC [183]) and it is, therefore, more suited for operating conditions below 50%RH [183]. The specific characteristics of the GDL used are given in table 4.2.

Characteristic	Unit	Value
PTFE load of carbon substrate	%	5 ± 1
Porosity	%	46 – 47
PTFE content of MPL	%	23
Area weight	g m^{-2}	125
Thickness	µm	325
Gas permeability	10^{-12} m^2	7 - 8
Thermal conductivity	W m^{-1} K^{-1}	0.35

Table 4.2. Characteristics of Sigracet® 38 BC GDL [183].

1.3 Flow field plates (FFPs)

Graphite flow field plates (grade FU 4369 HT) were used in our experimentation (from Schunk [184], Germany). Figure 4.1 shows the FFPs used at the cathode and anode sides. These FFPs consist of a parallel serpentine (12 parallel channels) design with channel and land width of 1 and 0.96 mm, respectively. The main characteristics of the FFPs used are given in table 4.3.

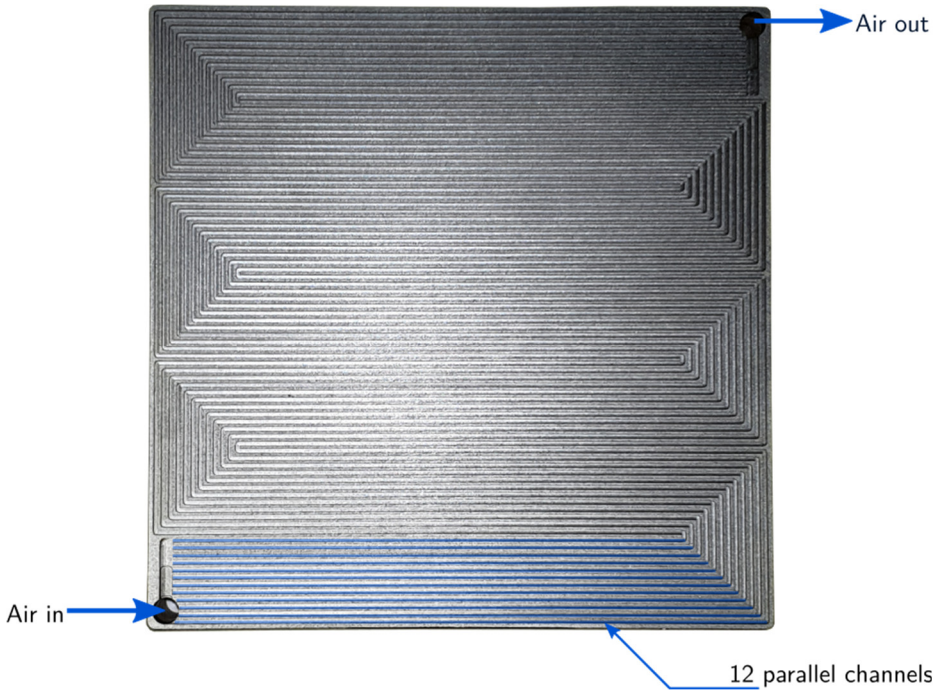

Figure 4.1. Image of the FFPs used in this study.

Characteristic	Unit	Value
Bulk density	g cm^{-3}	1.90
Compressive strength	MPa	50
Flexural strength	MPa	40
Thickness	mm	1.3 (channel depth 0.5)
Thermal conductivity	W m^{-1} K^{-1}	55

Table 4.3. Characteristics of the flow field plates - Schunk FU 4369 HT.

2 Experimental design

Before going into the details of the experimental campaign conducted in this study, it seems important to specify firstly the operations conducted prior to the electrochemical tests, namely the leak test and the break-in procedures.

2.1 Leak test

Leak tests were conducted following the harmonised test protocols for PEFC testing in single-cell configuration for automotive applications proposed by the European Fuel Cells and Hydrogen Joint Undertaking (FCH-JU) [185]. The goal was to ensure that the gas tightness, of the PEFC components and test apparatus, remains below leak rate thresholds recommended by the FCH-JU before conducting experimental investigations. This test was conducted through measuring the leak rate, represented by the pressure decrease in cathode and anode compartments, at a mechanical assembly pressure of 0.35 MPa. This latter was considered to be the minimum mechanical compression value that ensures the gas-tight operation of the PEFC. Results showed that the leak rates were 1.2 and 1 mbar.min^{-1} at the cathode and anode compartments, respectively. These leak rate values are far below the acceptance criterion defined in [185] which considers that the PEFC and the test bench are gas-tight when the leak rate is lower than 3 mbar min^{-1}.

2.2 Break-in procedures

Break-in procedures are typically applied to a newly assembled fuel cell and have a lifelong effect on the PEFC materials and performance, they are also likely to have a permanent bias of the test results when inappropriate break-in procedure is conducted during the early life of the fuel cell [186]. In our study, two types of break-in procedures were conducted, namely electrochemical and mechanical procedures, which are described hereafter.

2.2.1 Electrochemical break-in procedure

The PEFC used in our study was assembled in-house and no break-in procedure was recommended by the MEA provider. Therefore, the break-in procedure was conducted following an adapted protocol from the harmonised PEFC testing for automotive applications, recommended by the European FCH-JU [185]. This procedure mainly consists of varying the electronic load as well as the operating conditions of the fuel cell while monitoring the fluctuation of the fuel cell voltage. The aim was to bring the PEFC components' materials to a steady level of performance for posterior testing.

The recommended stability criterion that marks the end of the break-in procedure depends on the PEFC voltage fluctuation and it is considered satisfied when it is lower than ±5 mV at the end of the break-in protocol. This criterion was accomplished in our break-in protocol (which lasted about 6 hours) since during the last 30 minutes the PEFC voltage was fluctuating at less than ±5 mV.

2.2.2 Mechanical break-in procedure

In order to exclude the effects of the first mechanical compression cycles on the PEFC performance [76,102], a break-in protocol was conducted following an in-house developed procedure that consists of applying hundreds of compression cycles, ranging from 0.35 MPa to 2 MPa, prior to the experimental investigations described hereafter.

2.3 PEFC conditioning and operating conditions

2.3.1 Operating conditions

The PEFC was operated under Air/H_2 at fixed cathode and anode flowrates, which resulted in better stability of the cell voltage compared to fixed stoichiometry. In fact, the cell voltage stability is necessary in order to be able to observe the impacts of mechanical load changes (which lead to small voltage variations). Indeed, using stoichiometric control of our PEFC single cell resulted in a highly unstable performance in all the current densities range. This is attributed to fact that the test bench (i.e. Greenlight G7805, see chapter 3 for more details) was more likely developed for testing short PEFC stacks (max power of 1.5 kW) and rather not single cell with low flowrates, namely at low current densities, where even small changes in flow rate provoke lasting deviations in the PEFC performance. Moreover, even with a lower power test bench, the coupled regulation of the mass flow regulator/backpressure valve may lead to variations in the fuel cell voltage that could hinder the observations of the impacts of mechanical compression on the fuel cell performance. Therefore, the PEFC was operated at constant flowrates that are optimal for a current density of 0.9 A cm^{-2} for the rest of this study.

The reactants were supplied in flow-through mode at anode and cathode backpressures of 50 kPa. Hydrogen and air were used as reactants in co-flow mode, and this choice was motivated by a better current density distribution of the co-flow mode compared to counter-flow mode

considering our operating conditions. The hydrogen was provided by a gas producer and distributor (Messer, France [187]) with a 5.0 quality (i.e. composition of $H_2 > 99{,}999\%$).

It has to be mentioned that several experimental investigations were conducted prior to the experimental design presented in this section. The goal was to ascertain the optimal operating conditions for our PEFC components. The determined operating conditions deduced from the aforementioned experimental investigations were held constant, and only the operating conditions allowing to investigate the effects of mechanical compression on the PEFC performance were varied in our study. Table 4.4 presents the operating conditions that are considered optimal for our PEFC. These conditions were maintained constant throughout the experimental investigation presented in this thesis.

Factor	**Value**
H_2 flow rate	2.4 $Nl.min^{-1}$
Air flow rate	19.1 $Nl.min^{-1}$
Cell operating temperature	60 °C
Cathode backpressure	50 kPa
Anode backpressure	50 kPa

Table 4.4. Fixed operating conditions of the used PEFC.

2.3.2 PEFC conditioning

The purpose of the PEFC conditioning protocol is to ensure that the operating conditions presented in table 4.4 are maintained constant and that the cell voltage is sufficiently stable before conducting our experimental investigations. This conditioning protocol is depicted in figure 4.2.

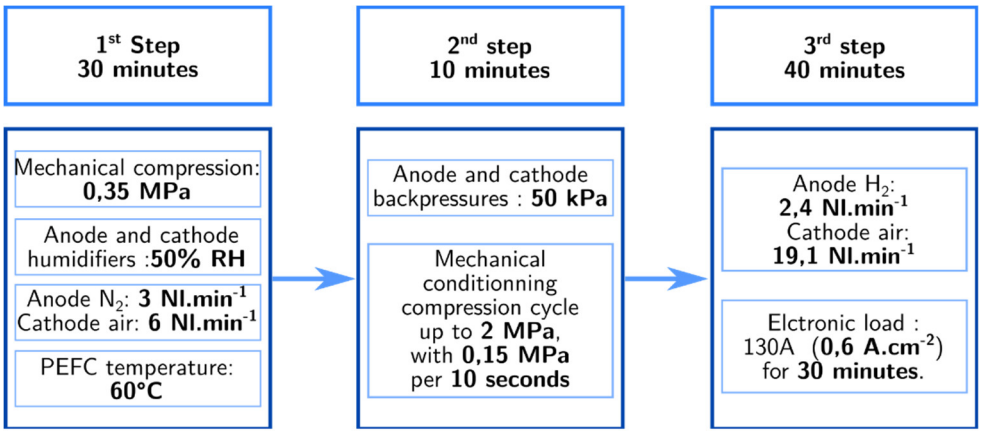

Figure 4.2. PEFC conditioning protocol.

The conditioning protocol was considered as achieved when the voltage stability criterion, which is in our study defined based on the voltage fluctuation over the last 30 minutes, is lower than ± 5 mV. This conditioning protocol was systematically applied before each experimental investigation reported in this thesis.

At the end of each experimentation, a shut-down protocol is conducted, which consists of inerting the PEFC with dinitrogen while reducing the cell temperature to ambient temperature under mechanical compression of 0.35 MPa.

2.4 Investigated parameters range

Real-life operating PEFCs, especially in the transportation and portable applications, must provide stable performance over a wide range of operating conditions (e.g. pressure, temperature, shocks and vibrations). Given the fact that the operating conditions provided in table 4.4 were kept constant, we have been particularly interested in this thesis in the variation of three operating conditions, namely mechanical compression, reactants relative humidity, and current density. Hence, twelve levels of mechanical compression, ranging from 0.35 MPa to 2 MPa with 0.15 MPa increments, were applied to the PEFC. These mechanical compression levels were studied at current densities of 0.6 $A.cm^{-2}$ and 0.9 $A.cm^{-2}$, which are representative of regions where the ohmic and mass transport losses have relatively important values and will be referred to as medium and high current density, respectively. Finally, the tests were conducted under cathode and anode reactants humidification of 50%RH and 100%RH. In fact, the GDL provider (i.e. SGL Carbon) indicated that the Sigracet® 38 BC used in our study operates best at relative humidity less than or equal to 50%RH. As a part of the investigations intended to determine the optimal operating condition of the PEFC components, we concluded that the optimal humidification of the reactants is 50%RH. Therefore, this value is used for the majority of the experimentations reported in this thesis. However, a 100%RH was also used to further investigate the effect of water flooding on the PEFC performance when subjected to mechanical compression. During all the experimentations, the relative humidity was changed simultaneously at the anode and cathode sides. Henceforth, whenever the relative humidification is mentioned, it concurrently refers to the cathode and anode sides.

2.5 Mechanical compression protocols

In this study, we have investigated two mechanical compression profiles as depicted in figure 4.3. The first, shown in figure 4.3 (a), represents a complete mechanical compression cycle, from 0.35 MPa to 2 MPa, and from 2 MPa back to 0.35 MPa, with steps of 0.15 MPa per 300 seconds. The duration of the mechanical compression levels was chosen to allow materials to be settled and performance to be stabilised before going from one mechanical compression to another. The objective of using this profile (figure 4.3 (a)) is to finely investigate the effect of the increase and also the decrease of the mechanical stress inside the fuel cell. From a real-life perspective, this mechanical compression protocol is representative of the mechanical stresses that can gradually be created and vanished inside the PEFC, namely the mechanical stresses

generated during the PEFC assembly process, freeze/thaw cycles, and hygrothermal stresses generated as a result of the swelling/shrinking of the membrane. The second profile, depicted in figure 4.3 (b), is intended to reproduce randomised mechanical compression levels in order to minimise the effects of material memory, and therefore to reduce the impacts of gradual water accumulation with increasing mechanical compression. In fact, as mechanical compression gradually increases, GDLs' pores get clogged and GDLs' fibres intrude into the FFPs channels leading the worsening of the water management capability of the PEFC. This latter effect leads to a progressive creation of water clusters within the PEFC components.

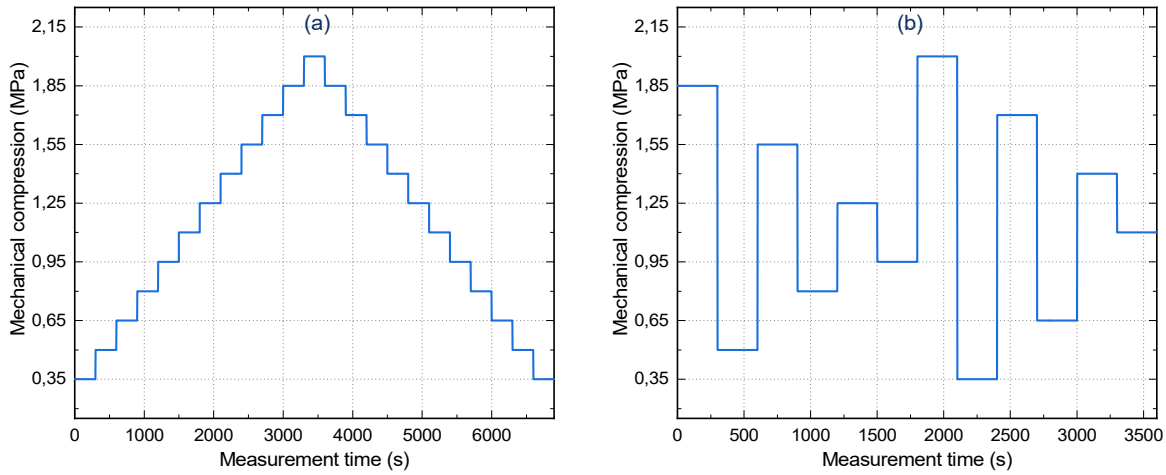

Figure 4.3. Mechanical compression profiles. (a) gradual increase/decrease of mechanical compression; (b) randomised mechanical compression levels.

3 Results and discussion

3.1 Electrochemical measurements results

Testing fuel cells through electrochemical characterisation techniques may take many forms. In this study, three main methods were used, namely cell voltage monitoring, polarisation curve analysis, and electrochemical impedance spectroscopy. These three characterisation techniques were combined to investigate the fuel cell performance using the mechanical compression profiles described in figure 4.3. Table 4.5 shows the corresponding mechanical protocol per each experimental procedure. It has to be mentioned that before conducting each of these characterisation techniques, a first conditioning cycle was systematically applied as depicted in figure 4.2.

Characterisation techniques campaigns	Mechanical compression profile
Cell voltage monitoring	- Gradual increase / decrease - Randomised
Polarisation curves measurements	- Randomised
Electrochemical impedance spectroscopy records	- Gradual increase

Table 4.5. Electrochemical characterisation techniques and their corresponding mechanical compression profiles.

3.1.1 Cell voltage monitoring

The fuel cell voltage was measured for every level of mechanical compression as depicted in figure 4.3 (a) and (b). The use of two different mechanical compression profiles is intended to represent, as close as possible, the mechanical stresses underwent by fuel cells during their lifelong operations. The voltage monitoring was conducted for two current density values, namely 0.6 A.cm^{-2} and 0.9 A.cm^{-2}, and under two levels of anode and cathode relative humidity of 50%RH and 100%RH. Some 150 voltage measurements per mechanical compression cycle were plotted and a second-degree polynomial curve fitting was used to analyse the tendency of the voltage evolution as a function of mechanical compression. The coefficients of determination (i.e. R-squared value) of the fitted curves were higher than 0.9.

i. Gradual increase/decrease of mechanical compression

a. Results at 0.6 A.cm^{-2}

Figure 4.4 shows the voltage measurements as a function of mechanical compression at a current density of 0.6 A. cm^{-2}. The voltage was measured at cathode and anode relative humidity of 50%RH and 100%RH.

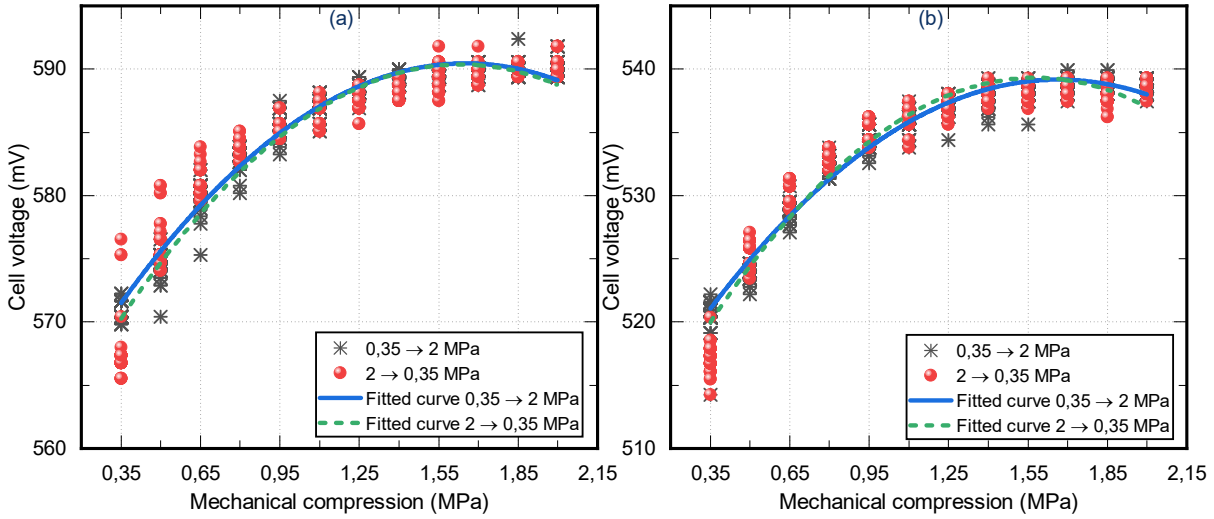

Figure 4.4. Voltage monitoring as a function of mechanical compression at 0.6 A.cm^{-2}. (a) voltage measurements at 50%RH and (b) voltage measurements at 100%RH.

It can be seen from figure 4.4 that the cell voltage measured at all mechanical compression range is lower at 100%RH compared to 50%RH, with an average difference of 51 mV. This voltage difference is attributed to the excessive presence of liquid water at 100%RH compared to 50%RH leading to GDL pores and FFPs channels blockage. This effect induces, therefore, higher mass transport resistances and lower cell voltage at 100%RH compared to 50%RH. With regards to mechanical compression effects, it can be seen that the PEFC voltage was improved with increasing mechanical compression up to 1.55 MPa at both 50%RH and 100%RH. After 1.55MPa, the cell voltage reaches a plateau, meaning that increasing mechanical compression beyond 1.55 MPa would not lead to any further improvement in the PEFC performance, or it may even cause a decay in the PEFC voltage. The cell voltage increased from 0.35 MPa to 1.55 MPa by 3.2% and 3.3% at 50%RH and 100%RH, respectively. These results show that mechanical compression improves the PEFC voltage regardless of the relative humidity level. Thus, considering our operating conditions, the PEFC voltage increase can be solely attributed to the dominance of the decrease in the ohmic resistance of the PEFC components over the increase in mass transport resistance. Comparable results are shown in figure 4.5 for PEFC voltage measurements at a current density of 0.9 A.cm^{-2} using the same experimental procedure.

b. Results at 0.9 A.cm^{-2}

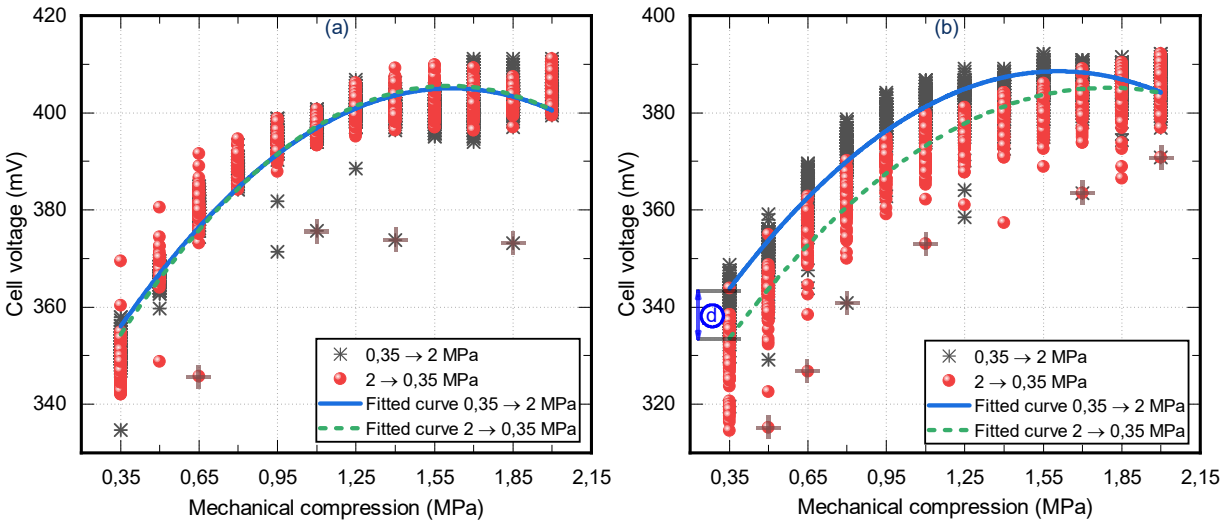

Figure 4.5. Voltage monitoring as a function of mechanical compression at 0.9 A.cm^{-2}. (a) 50%RH and (b) 100%RH. Region (d) shown in figure 4.5 (b) shows the voltage difference after one mechanical compression cycle and (+) symbols depict examples of voltage drops due to water accumulation/reactants starvation.

Similar to the results discussed earlier for current density 0.6 A.cm^{-2}, the measured cell voltage at 50%RH is higher than the one at 100%RH at 0.9 A.cm^{-2}, with a voltage difference value of 14 mV. This voltage difference can be attributed to the liquid water accumulation caused by operating the PEFC at a high relative humidity of 100%RH. This effect led to the formation

of water clusters that clog the GDLs pores and the FFPs channels leading to an increase in the mass transport resistance of the PEFC.

With regards to the voltage evolution with mechanical compression, it can be seen that it increases first with increasing mechanical compression up to 1.55 MPa then it reaches a plateau or even starts to decrease, table 4.6 shows the voltage improvement at this compression range. The increase in the cell voltage from 0.35 MPa to 1.55 MPa is measured to be 48.8% and 44.7% at 50%RH and 100%RH, respectively. A decreasing voltage tendency starting from 1.7 MPa up to 2 MPa can be seen in figure 4.5. In order to confirm the decrease of cell voltage after 1.7 MPa, further investigation needs to be carried out at compression levels above 2 MPa. However, this was not feasible in our study as increasing the mechanical compression beyond this level was not attainable using our apparatus. Nevertheless, this would not be practically recommended in real-life operating PEFCs [5]. As reported in the literature review, the optimum compression to be applied to the PEFC was reported in the literature to be between 1 and 2 MPa [5], which is in good agreement with results reported in this chapter. Thus, increasing the PEFC assembly pressure beyond 2 MPa could lead to a notable increase in the mass transport resistance and also to irreversible damage of the PEFC components [52,80,81] and will not be, therefore, addressed in this study.

Table 4.6 summarises the voltage evolution from 0.35 MPa to 1.55 MPa using the first experimental procedure. The voltage evolution at all mechanical compression range will be addressed at the end of this section.

Current density	**0.6 A.cm^{-2}**		**0.9 A.cm^{-2}**	
Relative humidity	50%RH	100%RH	50%RH	100%RH
Cell voltage evolution (mV)	18.8	18	48.8	44.7

Table 4.6. PEFC voltage evolution from 0.35 to 1.55 MPa using continuous voltage monitoring and increasing/decreasing mechanical compression protocol.

c. Effect of gradual increase/decrease of mechanical compression

It can be observed from figure 4.5 that the cell voltage is less stable at 100%RH compared to 50%RH. This observation is related to the water accumulation leading to voltage drops as depicted by (+) signs in figure 4.5 (b). These voltage drops are more frequent during the backward mechanical compression sweep compared to the forward one. It can also be seen from figure 4.5 (b) that the PEFC presented lower voltage during the backward sweep of mechanical compression. The region depicted by (d) in figure 4.5 (b) shows voltage difference after one cycle of mechanical compression. This voltage difference is also present in figure 4.5 (a) and figure 4.4 and it is caused by the gradual accumulation of water after increasing the mechanical

compression up to 2 MPa. This effect is more discernible (around 10 mV difference) at 0.9 A.cm^{-2} and 100%RH where more water is produced and introduced though fully humidified reactants to the PEFC.

During this experimental procedure, it was shown that the cell voltage was higher in the forward mechanical compression sweep compared to the backward one. This effect is more pronounced at the end of the mechanical compression cycle (see region (d) in figure 4.5 (b)). Since all the operating conditions that contribute to the formation of liquid water were held constant all along the experimentation, this water cluster formation is therefore attributed solely to the effect of increasing mechanical compression, which leads to the GDLs pore blockage and fibres intrusion into the flow fields channels, leading to a formation of water clusters that increase the mass transport resistance and therefore reduce the cell voltage after one cycle of mechanical compression. Although the technique of increasing (and less commonly increasing/decreasing) mechanical load was largely employed in the literature [5–7], this technique may not be fully representative of the stresses endured by PEFC during their lifetime operation. Therefore, in order to reduce the effects of water accumulation due to the gradual increase of mechanical compression, the following subsection employs the same voltage monitoring technique while using a randomised mechanical compression profile as show in figure 4.3 (b).

ii. Randomised mechanical compression profile

In this experimental procedure, randomised mechanical compression levels were applied to the fuel cell as depicted in figure 4.3 (b). As mentioned earlier in this chapter, employing this mechanical compression profile eliminates the effect of gradual water accumulation. Figure 4.6 shows the results from voltage measurement at 0.6 A.cm^{-2} and 0.9 A.cm^{-2} using randomised mechanical compression protocol. These voltage measurements were conducted for both 50%RH and 100%RH.

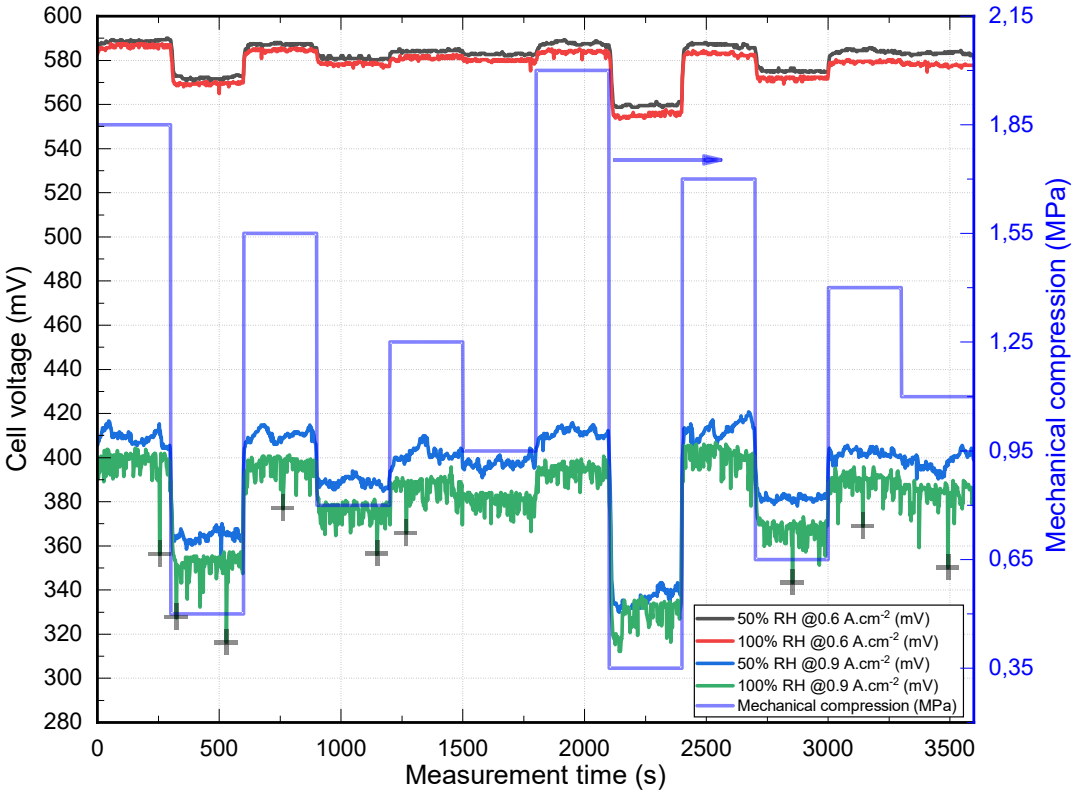

Figure 4.6. Voltage evolution using randomised mechanical compression protocol. (+) signs indicate examples of voltage drops due to liquid water accumulation/reactants starvation. The voltage curves are presented in the same order as the ones in the figure's label (top to bottom).

It can be observed from figure 4.6 that the mechanical compression affects the PEFC voltage at all tested current density and relative humidity ranges. Also, the voltage loss due to the increase in the relative humidity is more important at high current density, where the average voltage difference between tests at 50%RH and 100%RH is measured to be 3.55 mV and 11.22 mV at 0.6 A.cm^{-2} and 0.9 A.cm^{-2} respectively. Figure 4.6 also shows that the fuel cell voltage at 100%RH is substantially unstable compared to 50%RH, which is mainly due to water clusters formation leading to reactants starvation and therefore voltage drops as depicted by the (+) signs in figure 4.6. These voltage drops are more recurrent at the 0.9 A.cm^{-2} and 100%RH where more water is brought to the fuel cell through the humidifiers and also where more water is generated at the cathode side as a product of the cell reaction on the CL. Also, and in line with the results reported using the first experimental procedure, it can be observed from figure 4.6 that mechanical compression affects, with a more pronounced manner, the cell voltage when the PEFC is operating at 0.9 A.cm^{-2} compared to 0.6 A.cm^{-2}. This effect is explained by the important effects of reducing the ohmic resistance at high current density compared to medium current density due to better membrane hydration state, this effect will be addressed in more detail later in this subsection. Data from figure 4.6 are reported in figure 4.7 with average and standard deviation values per each level of mechanical compression. Figure 4.7 shows that the mechanical compression improves the PEFC voltage at all tested

operating conditions, with a major voltage improvement at a mechanical compression up to 1.55 MPa. However, the mechanical compression seems also to have a negative impact on the PEFC performance as it reduces the average pressure of the reactants (especially at the cathode side) within the PEFC (see Appendix E). Nevertheless, this effect is hindered by the positive impacts of mechanical compression on the ohmic resistance, which lead to the improvement of the fuel cell voltage and will be detailed hereafter.

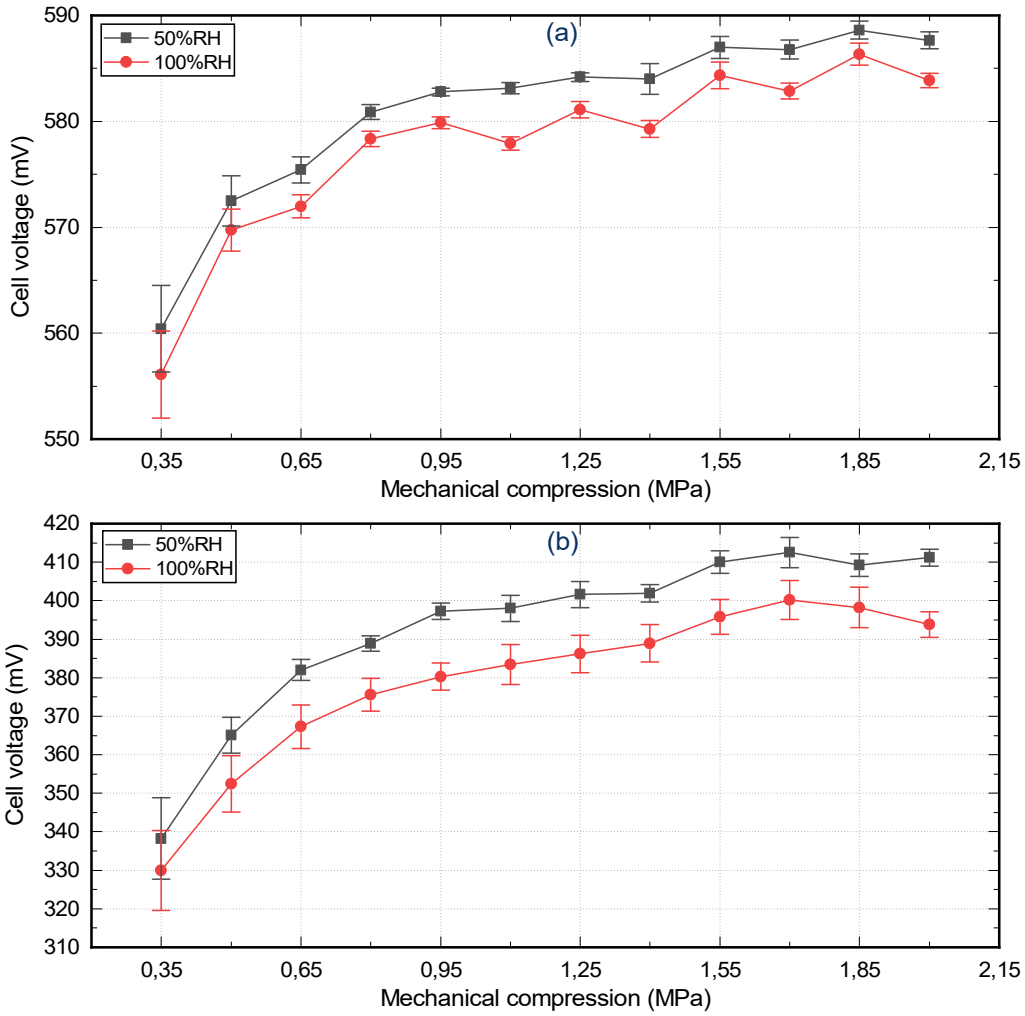

Figure 4.7. Voltage evolution using randomised mechanical compression protocol at 50%RH and 100%RH. (a) at 0.6 A.cm^{-2} and (b) at 0.9 A.cm^{-2}.

Table 4.7 summarises the results reported in figure 4.7.

Current density	0.6 A.cm^{-2}		0.9 A.cm^{-2}	
Relative humidity	50%RH	100%RH	50%RH	100%RH
Cell voltage evolution (mV)	26.6	28.3	71.8	65.8

Table 4.7. PEFC voltage evolution from 0.35 to 1.55 MPa using voltage monitoring and randomised mechanical compression protocol.

From table 4.7, the average voltage improvement from 0.35 MPa to 1.55 MPa at both 50%RH and 100%RH is measured to be 27.5 mV and 68.8 mV at 0.6 A.cm^{-2} and 0.9 A.cm^{-2}, respectively. This difference in voltage increase as a function of mechanical compression is attributed to the higher effect of reducing the ohmic resistance at higher current densities (0.9 A.cm^{-2}) compared to medium current densities (0.6 A.cm^{-2}). This effect can be explained by the fact that since our PEFC was operated at fixed flowrates corresponding to a current density of 0.9 A.cm^{-2}, the membrane endures liquid water evacuation due to the relatively high flowrates at 0.6 A.cm^{-2}, and therefore increasing the protonic resistance of the membrane. These results are in good agreement with the finding of Felix Buchi et al. [188]. These authors measured the ohmic resistance at 60°C of a fuel cell design with forced reactants flowrates to be 11.4% higher than in a design without forced flowrates. This effect seems to be more dominant in our study, as the voltage increase as a function of mechanical compression is 13% higher at 0.9 A.cm^{-2} compared to 0.6 A.cm^{-2}. This effect may be explained by the fact that when the fuel cell is compressed, GDL pores get clogged, which increases the water concentration gradient at the cathode side, leading to a more pronounced back diffusion mechanism of water. Therefore, more water is kept inside the membrane, which in turn improves the voltage of the PEFC through reducing the protonic resistance of the membrane. These results are also in good agreement with the finding of Cha et al. [158]. These authors carried out a study on the effects of assembly pressure on PEFC performance. They reported that the ohmic resistance decreased with increasing the assembly pressure. This result was attributed not only to the decrease in the electronic contact and bulk resistances of the PEFC components but also to the increase in the membrane hydration. This latter was associated with the reduction in the GDL porosity with increasing the assembly pressure leading to a substantial back-diffusion water transport mechanism from the cathode to the anode side, which induces better membrane hydration state and leads to the reduction in the membrane protonic resistance. This effect will be addressed in more detail later in this chapter.

During these first experimental procedures, i.e. fuel cell voltage monitoring using i) gradual increase/decrease and ii) randomised mechanical compression protocols, the PEFC was operated at a fixed electronic load value. These experimental procedures are representative of the effects of mechanical compression on PEFC operating at a fixed electronic load point. The

goal of the following subsection is to investigate the effects of mechanical compression on a fuel cell operating in a dynamic electronic load condition.

3.1.2 Polarisation curve measurements

The polarisation curve analysis is one of the most common techniques used for global PEFC performance assessment. This technique involves an increasing and/or decreasing sweep of electrical load in order to obtain a characteristic of the PEFC voltage as a function of current density (i.e. galvanostatic mode) for specified operating conditions. In our study, the current was controlled using a ramp load profile under specified operating conditions as reported in table 4.4. The electronic load was varied following a smooth ramp sweep with 2.2 mA.cm^{-2} per second (7 minutes on average per each polarisation curve measurement). The mechanical compression was applied following the randomised mechanical compression profile as presented in figure 4.3 (b). The polarisation measurements were conducted at both 50%RH and 100%RH anode and cathode relative humidity.

i. Polarisation measurement at 50%RH

Figure 4.8 shows the polarisation curves of 12 levels of randomised mechanical compression at anode and cathode relative humidity of 50%RH.

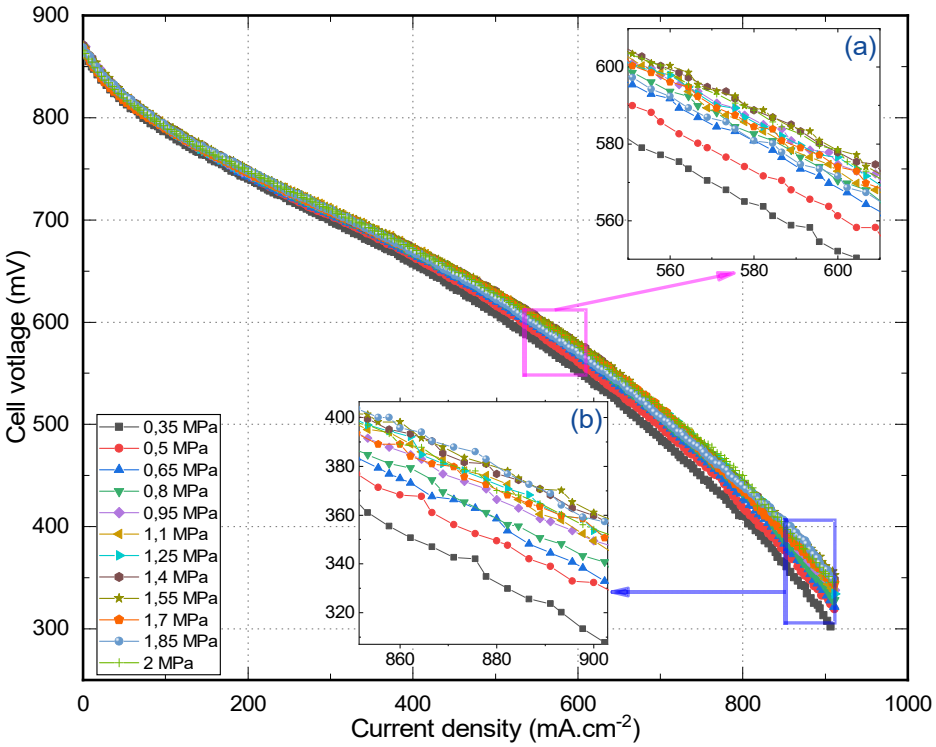

Figure 4.8. Polarisation curves for 12 randomised levels of mechanical compression at 50%RH. Inserts (a) and (b) are zoomed-in regions representative of the ohmic and mass transport losses, respectively.

Results from figure 4.8 show the impact of mechanical compression on PEFC performance. The zoomed-in inserts (a) and (b) correspond to regions where the ohmic and mass transport losses have relatively important values, respectively. It can be observed that the PEFC voltage increases with increasing mechanical compression at all current density ranges, with a substantial increase from 0.35 MPa to 0.95 MPa. For better readability, the results from figure 4.8 corresponding to 0.6 A.cm^{-2} and 0.9 A.cm^{-2} are reported in figure 4.9.

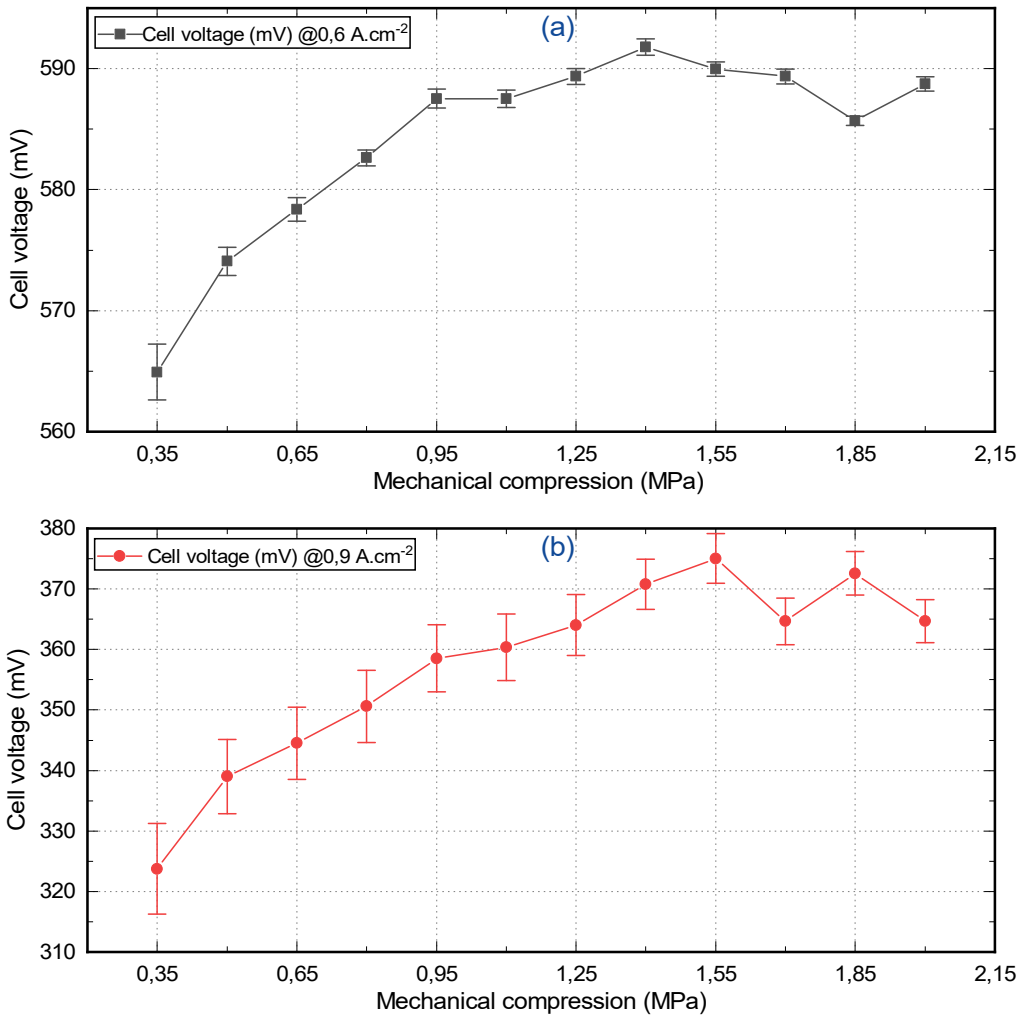

Figure 4.9. Voltage evolution as a function of mechanical compression. (a) at 0.6 A.cm^{-2} and (b) at 0.9 A.cm^{-2}. Data from figure 4.8.

Figure 4.9 shows that as the mechanical compression increased from 0.35 MPa to 1.55 MPa, the cell voltage was improved by 4.3% and 13.7% at current densities of 0.6 A.cm^{-2} and 0.9 A.cm^{-2}, respectively. Therefore, the voltage improvement with mechanical compression at high current density is more pronounced (9.4 % higher) compared to medium current density, which is in good agreement with the results reported using the first two experimental procedures. These results are attributed to the better membrane humidification at high current density compared to medium one. Detailed explanations are given at the end of this subsection.

ii. Polarisation measurement at 100%RH

The same experimental procedure used for tests at 50%RH was conducted at 100%RH, results depicted in figure 4.10 show comparable voltage evolution trend, with a lower overall performance at 100%RH compared to 50%RH.

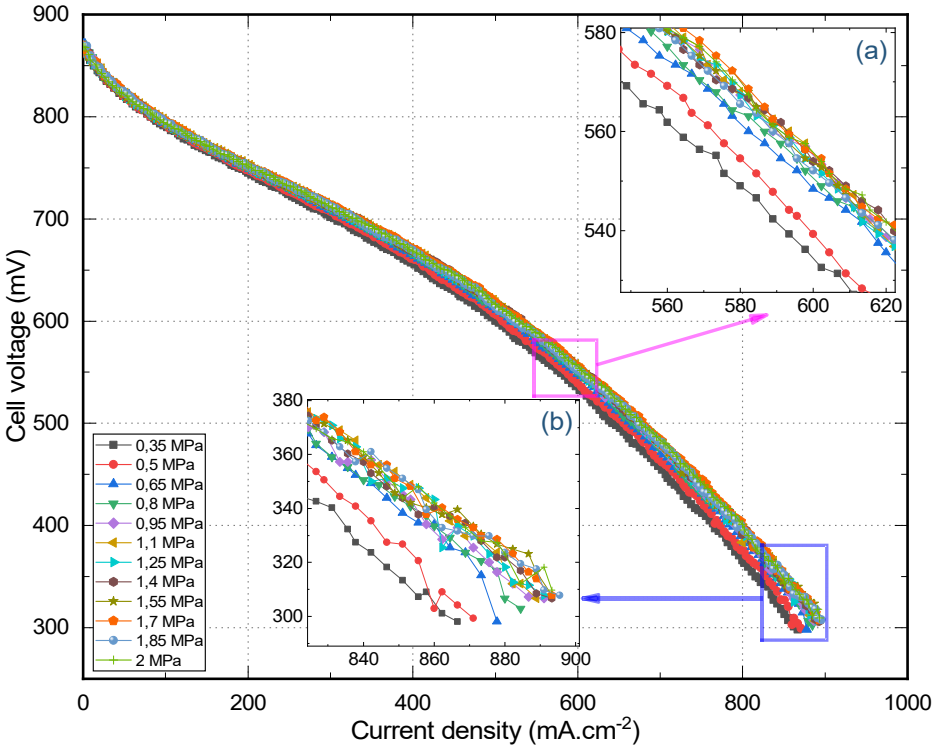

Figure 4.10. Polarisation curves for 12 randomised levels of mechanical compression at 100%RH. Inserts (a) and (b) are zoomed-in regions representative of the ohmic and mass transport losses, respectively.

The ohmic and mass transport regions are shown in figure 4.10 inserts (a) and (b), respectively. Similar to the results at 50%RH, the PEFC voltage at 100%RH becomes higher with increasing mechanical compression at all current density ranges, with a substantial increase from 0.35 MPa to 0.95 MPa. Figure 4.11 shows the results of the voltage evolution as a function of mechanical compression at 0.6 A.cm^{-2} and 0.9 A.cm^{-2}.

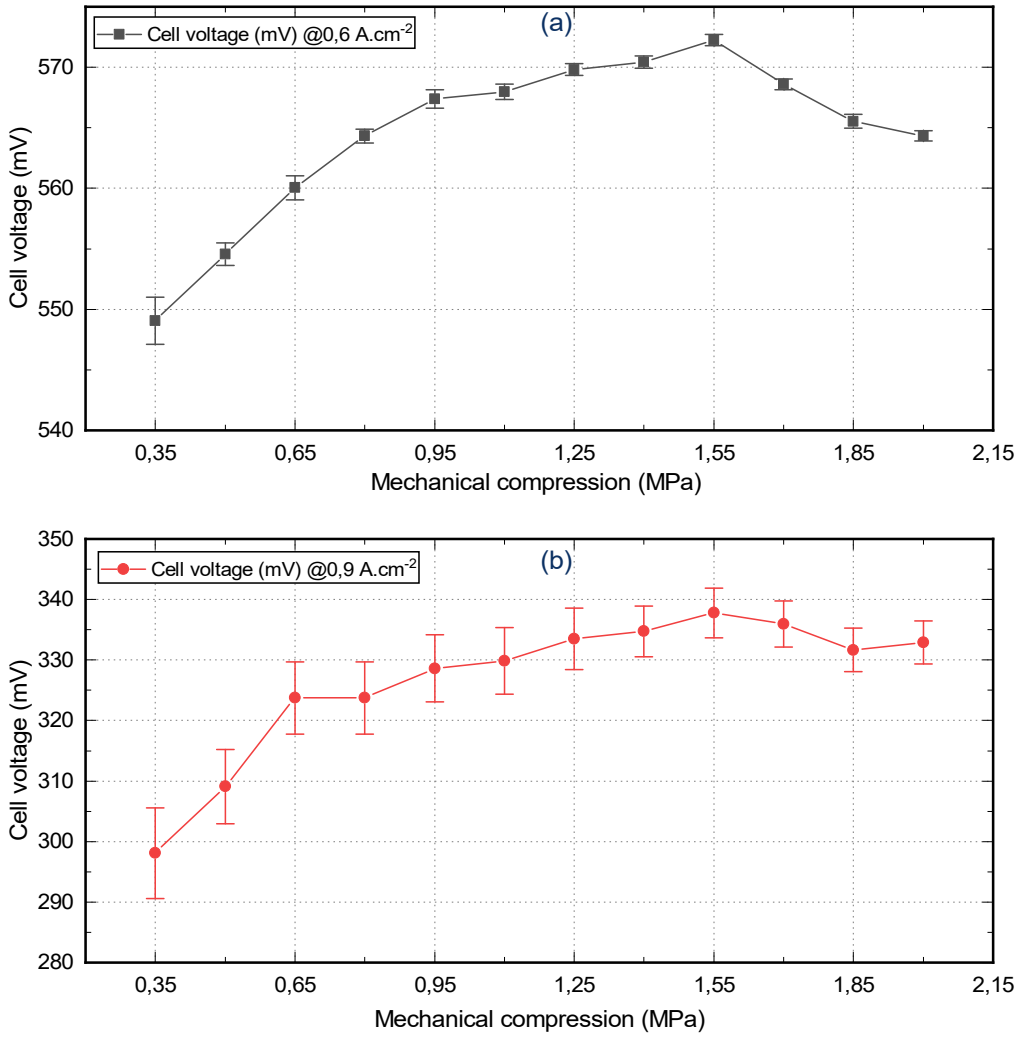

Figure 4.11. Voltage evolution as a function of mechanical compression at 100%RH. (a) at 0.6 A.cm^{-2} and (b) at 0.9 A.cm^{-2}. Data from figure 4.10.

Figure 4.11 shows that the cell voltage was improved in the compression range from 0.35 MPa to 1.55 MPa by 4.1% and 11.8% at current densities of 0.6 A.cm^{-2} and 0.9 A.cm^{-2}, respectively. The voltage increase at high current density is more noticeable (i.e. 7.7% higher) compared to medium current density. This difference in the voltage increase is attributed to the better membrane humidification state when the PEFC is operated at a high current density compared to a medium one. It can be observed from figure 4.11 that cell voltage is less stable at high current density compared to medium one, with an average difference in the voltage standard deviation of 4.3 mV. This voltage instability at 0.9 A.cm^{-2} is mainly attributed to the higher rate of water production at the cathode side, leading to GDLs' pores obstruction with water, which in turn hinders reactants from reaching the catalyst sites and therefore provoking voltage instability as a result of reactants starvation. Table 4.8 summarises the results reported in figure 4.9 and figure 4.11.

Current density	0.6 A.cm^{-2}		0.9 A.cm^{-2}	
Relative humidity	50%RH	100%RH	50%RH	100%RH
Cell voltage evolution (mV)	25.1	23.3	51.3	39.7

Table 4.8. PEFC voltage evolution from 0.35 MPa to 1.55 MPa using polarisation curves measurements and randomised mechanical compression protocol.

3.1.3 Comparison of steady-state experimental procedures results

i. Effect of mechanical compression on fuel cell voltage stability

With regards to voltage stability, results from the first experimental procedure (i.e. cell voltage monitoring) show that mechanical compression reduces the voltage standard deviation at both 50%RH and 100%RH. Figure 4.12 shows the cell voltage standard deviation evolution as a function of mechanical compression at 0.6 A.cm^{-2}. The voltage standard deviation was calculated from 300 measurement points combining forward and backward mechanical compression sweeps as depicted in figure 4.4.

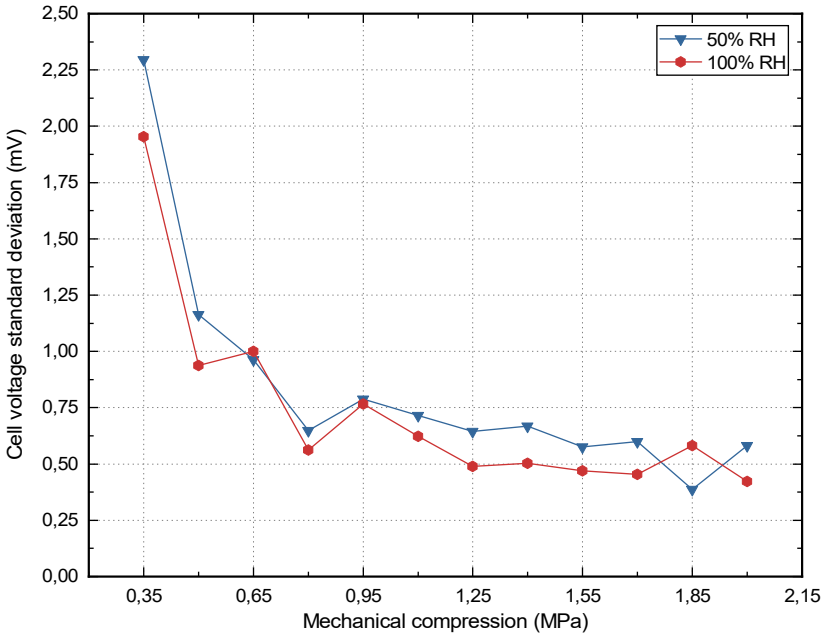

Figure 4.12. Cell voltage standard deviation as a function of mechanical compression at 0.6 A.cm^{-2}.

Although the effect shown in figure 4.12 is complex to describe, two plausible causes may be evoked here. The first is related to the ohmic resistance of the GDL. In fact, since the GDL used in our study was subjected to hundreds of mechanical compression cycles, the GDL fibres

might be crushed [81], and some small GDL fibres fragments (figure 4.13) may get to slightly move with reactants and water flows at mechanical compression below 0.8 MPa. The movements of these GDL fibres fragments modifies the ohmic resistance through changing the electrical contact positions of the GDL fibres and therefore contributing to the cell voltage instability. As the mechanical compression reaches 0.8 MPa (figure 4.12), the GDL material and fibres are settled and the cell voltage reaches its maximum stabilisation level.

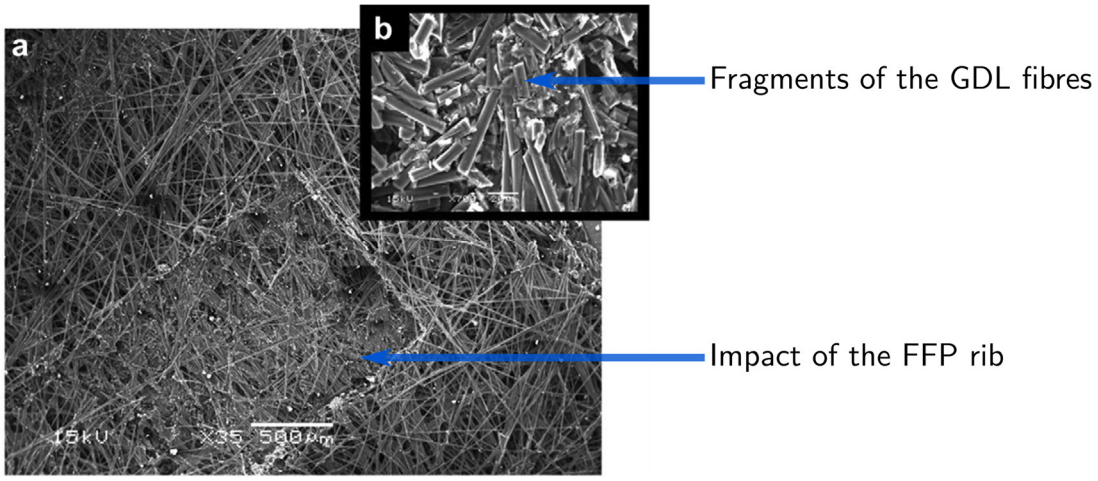

Figure 4.13. SEM image of compressed GDL. (a) mark of the FFP rib and on the GDL and (b) fibres fragments under the rib areas [81].

The second possible cause of the results presented in figure 4.12 may be attributed to the PEFC water management when it is subjected to mechanical stresses, and some related explanations can be found in the literature. Indeed, some studies reported correlations between the water management related issues and the mechanical stresses applied to the PEFC. One of the main subjects of debate is the preferential pathways for liquid water transport within the GDL when subjected to mechanical compression. In fact, some authors reported that water is preferentially transported in the compressed regions beneath the ribs [160,161,164] whereas others reported the areas beneath the channels as preferential pathways for water transport [163,165]. Since mechanical compression was shown to improve the fuel cell voltage stability, it seems that in our case the liquid water is preferentially located in the regions beneath the ribs, where water accumulation is less critical compared to the regions beneath the channels at where water clusters may cause reactants starvation and therefore voltage instability. With this regard, Bazylak et al. [160] investigated the effect of mechanical compression on liquid water transport within the GDL. These authors reported that liquid water is located in the regions beneath the ribs. This finding was attributed to PTFE coating and carbon fibres damage, which led to hydrophobic content degradation in the compressed regions of the GDL. This effect favours water accumulation in the compressed GDL regions (FFPs ribs) compared to the uncompressed ones (FFPs channels). The same effect was reported in an in-situ study by Forner-Cuenca et al. [189]. This water accumulation might be beneficial for fuel cell voltage

stability since water is located beneath the ribs where its accumulation is less critical than regions beneath the channels where reactants are supplied to the reaction sites.

In line with Bazylak et al. [160], Ince et al. [161] investigated the in-plane water transport in both the compressed and the uncompressed regions of the GDLs. These authors emphasised that mechanical compression improves the in-plane water transport in the compressed regions of the GDL. Hartnig et al. [164] employed synchrotron X-ray radiography to visualise water locations in an operating PEFC and reported that water agglomerates mainly beneath the ribs of the FFPs (see figure 2.8 – chapter 2). The experimental findings of [160,161,164] are in good agreement with the results presented in figure 4.12 since the mechanical compression promotes water agglomeration in the regions beneath the FFPs' ribs and improves the in-plane transport of liquid water in the compressed GDL regions. Therefore, these phenomena reduce the voltage fluctuation due to water clusters formation beneath the channels and, as a result, improve the voltage stability.

The results reported in figure 4.12 are only related to a current density of 0.6 $A.cm^{-2}$. The voltage stability evolution at 0.9 $A.cm^{-2}$ does not suggest any discernible trend as a function of mechanical compression. This is attributed mainly to the higher presence of liquid water at the cathode side at 0.9 $A.cm^{-2}$ due to its generation as a result of the cathode reactions, which gives fairly unstable cell voltage independently from the mechanical compression (see figure 4.6). It has to be noted that only possible causes of the effect presented in figure 4.12 are given in this section. However, future studies need to be carried out in order to conduct in-situ investigations on the water clusters location as a function of mechanical compression as this subject was not comprehensively discussed in the literature [5]. Moreover, other phenomena may contribute to the stabilisation of the cell voltage with increasing mechanical compression (e.g. improvement in the electrical and thermal conductivities of the PEFC's components, reduction in the reactants' leak rate) and could be the subject of future research activities.

ii. Effect of mechanical compression on cell voltage evolution

Figure 4.14 shows the average voltage evolution measured using the three experimental procedures reported in this section. The mechanical compression is divided into two ranges: from 0.35 MPa to 1.55 MPa (blue bars) and from 1.55 to 2 MPa (orange bars), hereafter referred to as the first and second compression range, respectively. The goal of gathering the results from all three experimental procedures is to investigate the effect of mechanical compression on the PEFC performance independently from the experimental procedure used.

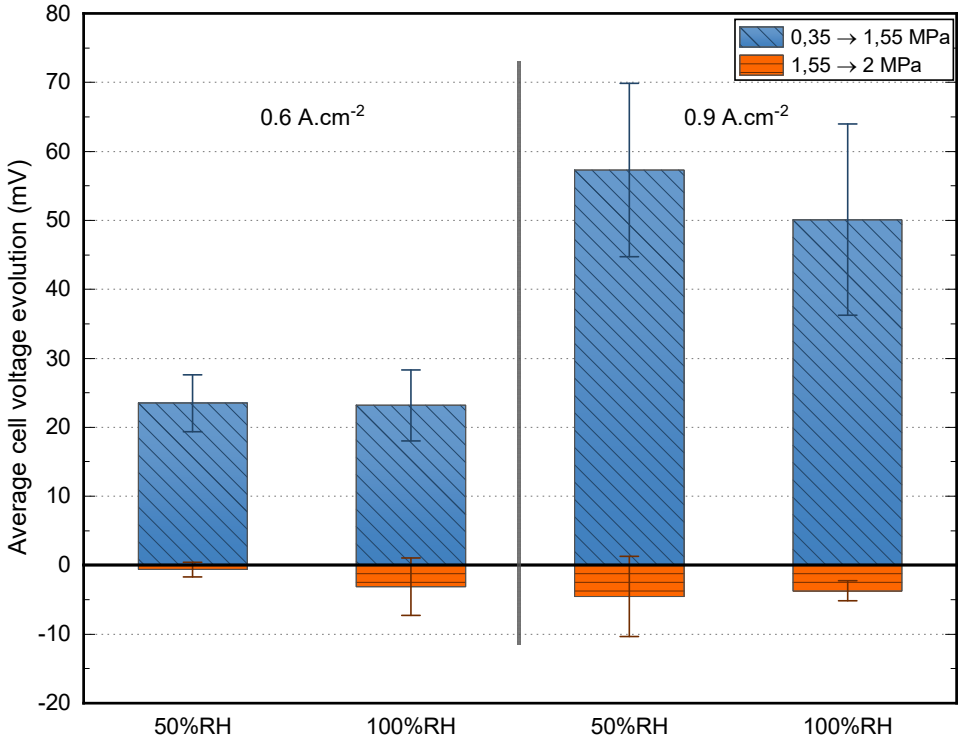

Figure 4.14. Cell voltage evolution over the compression range 0.35 → 2 MPa using the three experimental procedures reported in this section.

It can be observed from figure 4.14 that mechanical compression improves the PEFC voltage during the first compression range (i.e. from 0.35 MPa to 1.55 MPa) at all tested operating conditions. This effect of voltage improvement is preeminent at high current density (0.9 A.cm^{-2}) compared to medium current density (0.6 A.cm^{-2}) at all operating conditions range. The voltage evolution shows a decreasing tendency starting from 1.55 MPa to 2 MPa. The explanations of these effects will be addressed in more detail in the following subsections.

a. Effects of mechanical compression on PEFC voltage at medium current density

The fuel cell voltage evolution at 0.6 A.cm^{-2} over the first and second compression ranges is shown in figure 4.14. It can be observed that the cell voltage increases during the first compression range. This voltage increase is attributed to the dominance of the reduction in the ohmic resistance against the increase in the mass transport resistance. Similar results are observed at both 50%RH and 100%RH at the first compression range and are attributed to the fact that the PEFC was operated at fixed flowrates adapted for 0.9 A.cm^{-2} that are high enough to allow the evacuation of the produced water at 0.6 A.cm^{-2}. Therefore, no substantial mass transport losses were taking place at this compression range. However, as the compression exceeded 1.55 MPa, the cell voltage was further decreased at 100%RH compared to 50%RH. This effect is mainly due to the excess water brought to the PEFC through the fully humidified gases at 100%RH. This effect, added to the fact that the PEFC was further compressed up to 2 MPa, led to a decrease in the GDL porosity that, in turn, induced higher mass transport losses at 100%RH.

As mentioned before, the voltage increase during the first mechanical compression range is caused mainly by the decrease in the ohmic resistance of the PEFC components. This ohmic resistance comprises the protonic resistance of the membrane and the electronic resistance of the PEFC components [190]. This latter includes the bulk resistance of the fuel cell components and also the contact resistance at the interfaces between the MEA, MPL, GDL, and the FFPs [76]. The ohmic resistance is generally attributed to the protonic resistance of the membrane. However, when it comes to mechanical stresses related issues, the electronic resistance, and more importantly the electronic contact resistance, contributes substantially to the total ohmic resistance of the PEFC. This effect was previously reported in the literature, Nitta et al. [191], for instance, reported that uneven assembly pressure may increase the contact resistance, and it may even attain the same order of magnitude as the membrane resistance. This finding is more important to emphasise as the pressure inhomogeneity is a common issue in real-life operating PEFCs assembled using point-load design using typical fastener of bolts and nuts [54,58,94,97].

With this regard, the improvement of the cell voltage during the first compression range at 0.6 $A.cm^{-2}$, as shown in figure 4.14, is attributed up to a certain extent to the reduction in the electronic resistance of the PEFC components. One of the main contributions to this electronic resistance comes from the interfacial contact resistance. Indeed, in a study carried out within the framework of our research project (i.e. MIREPOix project), K. Bouziane et al. [102] conducted an ex-situ investigation on the effects of cyclic mechanical compression (figure 4.15) on the electrical contact resistance between the GDLs and the adjacent PEFC components using a number of commercially available GDLs (more information about the experimental apparatus and process can be found in K. Bouziane's PhD thesis work [192]). In this study, and for in-situ/ex-situ comparison purposes, we have decided to present solely the results of the Sigracet® 24 BC GDL, which has the most similar characteristics (compared to other GDLs used in the ex-situ study) with the Sigracet® 38 BC used in our in-situ investigations, and which is provided by the same company (SGL carbon [193]). The characteristics of the Sigracet® 24 BC GDL are provided in table 4.9.

Characteristic	**Unit**	**Value**
PTFE load	%	5
Porosity	%	40
Area weight	$g\ m^{-2}$	100
Thickness	µm	235
TP gas permeability	$10^{-12}\ m^2$	5.09

Table 4.9. Characteristics of the GDL Sigracet® 24 BC: straight carbon fibre paper with MPL coating [42].

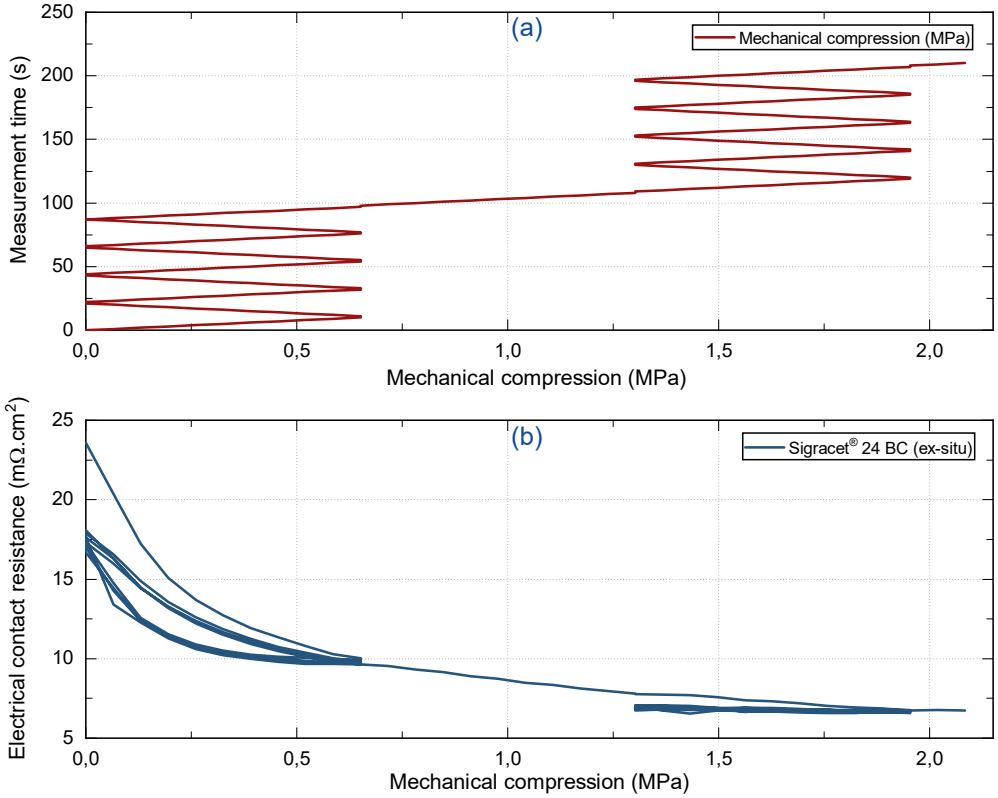

Figure 4.15. Effect of mechanical compression on the contact resistance (a) Mechanical compression profile used in the ex-situ study (b) The electrical contact resistance of the GDL as a function of mechanical compression.

It can be observed from figure 4.15 that the mechanical compression reduces the electrical contact resistance, with a 68% reduction attained at 1.5 MPa over a 71% reduction at 2 MPa. These results show that the major reduction of the contact resistance occurs at 1.5 MPa, which is in good agreement with our in-situ results shown in figure 4.14. The diminution in the contact resistance shown in figure 4.15 (b) is attributed to the improvement in the electrical contact between the GDL and the adjacent components and also to the reduction in the GDLs porosity, which increases carbon fibre electrical connections leading to a reduced electrical resistivity between the GDLs fibres [102]. This effect, which was also reported in an ex-situ study reported by Qiu et al. [194], seems to be dominant over the increase in the mass transport resistance in our in-situ study. Therefore, these combined reductions in the bulk and contact resistances noticeably led to the increase in the fuel cell voltage during the first compression range as shown in figure 4.14.

b. Effect of mechanical compression on PEFC voltage at high current density

It can be observed from figure 4.14 that the fuel cell voltage was improved with increasing mechanical compression at the first compression range. This effect is attributed to the dominance of the decrease in the ohmic resistance against the increase in the mass transport resistance for a compression up to 1.55 MPa. This voltage improvement was measured to be 14.4% higher at 50%RH compared to 100%RH. This voltage improvement difference is

explained by the high mass transport losses that occur when the reactant gases are fully humidified at 100%RH. During the second compression range (i.e. from 1.55 MPa to 2 MPa), the voltage decreased at the same order of magnitude, which is mainly due to the increase in the mass transport resistance as a result of the decrease in the GDLs' porosity with increasing mechanical compression beyond 1.55 MPa.

Figure 4.14 also emphasises an outstanding comparison concerning the voltage improvement at the first compression range, which is ~twice as much higher at 0.9 A.cm^{-2} compared to 0.6 A.cm^{-2}. Considering the operating conditions of the PEFC used in this study, the higher voltage increase at high current density is mainly attributed to the reduction of the protonic resistance of the membrane with increasing mechanical compression. In fact, at 0.9 A.cm^{-2}, more water is formed at the cathode side (compared to 0.6 A.cm^{-2}) as a product of the electrochemical reactions on the CL. Moreover, the GDLs porosity decreases with higher mechanical compression and, therefore, liquid water is kept at the cathode CL side. This water agglomeration creates a concentration gradient that induces the transport of a part of the accumulated water from the cathode to the anode side (i.e. back diffusion process [155,156]) through the membrane, which improves and homogenises the hydration state of the membrane and, in turn, reduces its protonic conductivity as illustrated in figure 4.16. These results are in good agreements with the finding of Cha et al. [158], these authors reported that the ohmic resistance of the PEFC decreased with increasing the current density, which was attributed to the better membrane hydration at high current densities due to the increase in water production rate at the cathode side.

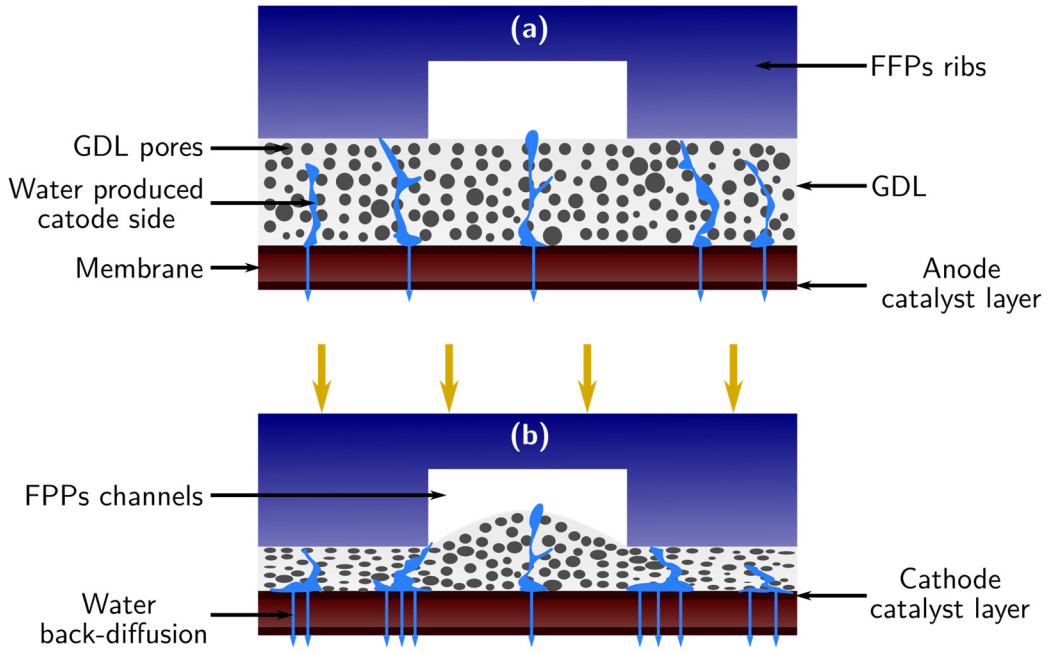

Figure 4.16. Effect of mechanical compression on the back-diffusion process of water (blue arrows). (a) uncompressed GDL and (b) compressed GDL.

The polarisation curve analysis, along with the fuel cell voltage monitoring, reported in this chapter allow a first assessment of the effects of mechanical compression on the global PEFC performance. These techniques are relatively simple to realise experimentally. Nonetheless, for a given operating point, these characterisation techniques do not allow to quantify separately each one of the phenomena occurring within the PEFC. This is made possible by the electrochemical impedance spectroscopy technique.

3.2 Electrochemical impedance spectroscopy

Electrochemical Impedance Spectroscopy (EIS) is a characterisation technique commonly used in electrochemistry. It aims to determine the impedance of a material or a system in response to a low sinusoidal signal with low amplitude (or perturbation, excitation) over a wide frequency range, typically from some mHz to tens of kHz [92]. This technique has been widely used for PEFC performance assessment [38,52,90,90,92,195,196]. In fact, through varying the frequency of the perturbation signal, the dynamics involved within the PEFC can be dissociated. The perturbation signal can be realised on the current, which is referred to as galvanostatic mode, or on the voltage, which corresponds to the potentiostatic mode. For PEFCs, the use of the galvanostatic mode is preferred. This choice is motivated by the fact that fuel cell is usually seen, from a control-command view, as a voltage source. Therefore, it is easier to control its current than its voltage [197]. Moreover, in the case of a fuel cell stack, the elementary cells can operate under different conditions and can possibly have varied performance ranges. Thus, imposing a voltage on a multi-cell stack would lead to the demand of a current that some degraded cells could not provide and would, therefore, operate in the electrolysis mode, which may deteriorate the characterised PEFC stack [197]. For these reasons, the galvanostatic mode is privileged and will be used for the rest of the study presented hereafter.

3.2.1 EIS measurements principle

The EIS is used to determine the electrical impedance of PEFC over a wide range of frequencies throughout the polarisation characteristic. In this technique, a current oscillation input, usually sinusoidal, is generated around an operating point (I_0,V_0) at a given frequency as illustrated in figure 4.17. The total expression of the current is given by. (5.1) which is composed of a continuous part I_0 on which a frequency sinusoidal component is superimposed:

$$i(\omega t)=I_0+i_1 \cdot \sin(\omega t) \qquad (5.1)$$

Where i_1 designates the amplitude of the fundamental perturbation signal, which is a low amplitude excitation signal (5 to 10% of the DC current delivered by the PEFC), and $\omega=2\pi f$ the pulsation ($rad.s^{-1}$). The sinusoidal perturbation of the current induces a sinusoidal voltage v_1 superimposed on the PEFC voltage. Assuming that only the fundamental frequency is present with no other harmonics [197,198], the voltage response of the current single-frequency perturbation is a single-frequency voltage response (figure 4.17) and can be written as :

$$v(\omega t)=V_0+v_1 \cdot \sin(\omega t-\varphi) \tag{5.2}$$

Where φ is the phase shift between current and voltage.

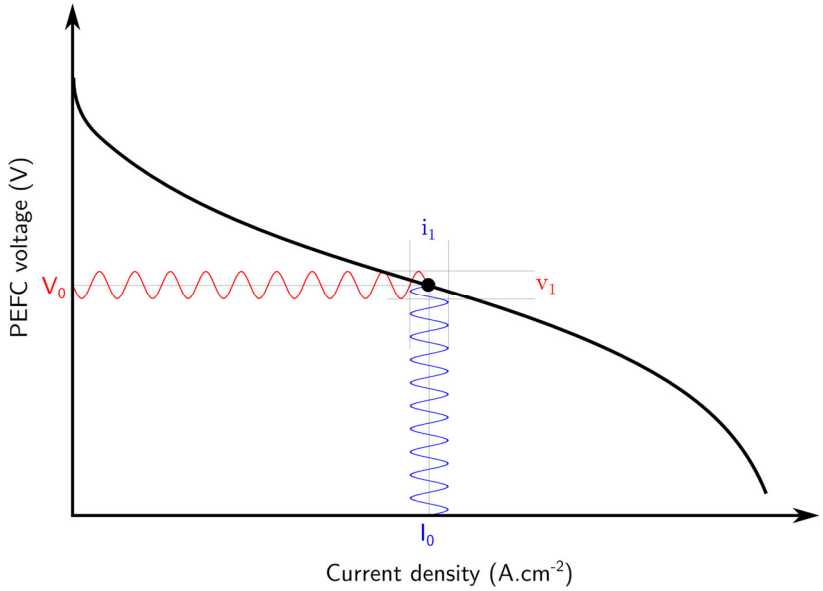

Figure 4.17. EIS characterisation technique operating principle.

The impedance is defined as the ratio between voltage and current in the frequency domain. Therefore, the terms I_0 and V_0 can be removed. Using Euler's formula for (5.1) and (5.2), and considering the response of the system as linear, the impedance $\overline{Z}(\omega)$ of the system can be defined as:

$$\overline{Z}(\omega)=\frac{v_1}{i_1} \cdot e^{j\varphi} \tag{5.3}$$

Equation (5.3) can be, therefore, written as a complex number:

$$\overline{Z}(\omega)=\mathrm{Re}\left(\overline{Z}(\omega)\right)+j \cdot \mathrm{Im}\left(\overline{Z}(\omega)\right) \tag{5.4}$$

With:

$$|\overline{Z}| =\sqrt{\left[\mathrm{Re}\left(\overline{Z}(\omega)\right)\right]^2+\left[\mathrm{Im}\left(\overline{Z}(\omega)\right)\right]^2} \tag{5.5}$$

$$\varphi=\tan^{-1}\left(\frac{\mathrm{Im}\left(\overline{Z}(\omega)\right)}{\mathrm{Re}\left(\overline{Z}(\omega)\right)}\right) \tag{5.6}$$

The impedance $\overline{Z}(\omega)$ can thus be represented either in the Bode diagram by its module $|\overline{Z}|$ and its phase angle φ as a function of frequency, or in the Nyquist diagram where the x-axis corresponds to the real part of the impedance $\overline{Z}(\omega)$ and the y-axis to its imaginary part. This

type of representation is used by electricians while electrochemists prefer to use the ordinate as -Im$\left(\overline{Z}(\omega)\right)$. In our study, all the representations are made in the Nyquist diagram using the notation of the electrochemists.

An illustration of the impedance spectrum represented in the Nyquist diagram using the electrochemists' notation is shown in figure 4.18. In most cases, the impedance of the anode is generally low compared to that of the cathode. Thus, it is difficult to identify its contribution to the overall fuel cell spectrum [1]. As a result, the impedance of a PEFC is often only attributed to the cathode impedance [155,197]. In figure 4.18, two arcs are discernible, these arcs, from left to right, may be representative of the charge transfer and mass transport phenomena, respectively. The combination of these two arcs illustrates the dynamic behaviour of a PEFC (single cell or stack) in response to current excitation over a wide range of frequencies (some mHz to tens of kHz).

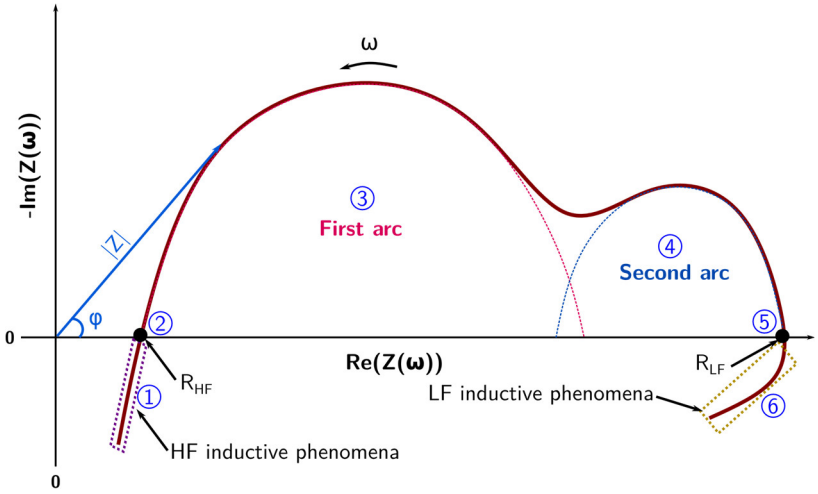

Figure 4.18. Representation of the impedance spectra $\overline{Z}(\omega)$ of a PEFC in the Nyquist diagram.

The physical phenomena that take place within the PEFC and that describe the dynamic behaviour have different time constants. Some phenomena have time constants of the order of a microsecond (e.g. ohmic resistance) whereas others have time constants of the order of several minutes (e.g. phenomena of hydration and humidification of the membrane) [199]. Therefore, the impedance spectrum shown in figure 4.18 can be explained by the following electrochemical processes taking place within the PEFC. Depending on the regions that are presented by blue numbers in figure 4.18, we can observe:

1. The first information that can appear on the spectrum starting from high frequencies (tens of kHz to some kHz) concerns inductive phenomena related to the wires and electrical connections of the test system (neither related to the fuel cell itself nor to its electrochemical phenomena) [198]. This HF inductive phenomenon is represented by a crossing the impedance spectrum towards the positive imaginary axis [200].
2. The high-frequency resistance (R_{HF}) is representative of the ohmic resistance of the fuel cell, which is composed of the protonic resistance of the membrane [92,148], the bulk

electronic resistance of the PEFC components along with their respective electrical contact resistances [83]. The ohmic resistance is determined by the intersection between the impedance spectrum and the real axis at high frequencies range.

3. The first arc is generally representative of the charge transfer phenomena and represents the transfer and accumulation of electric charges at the electrode-electrolyte interfaces.
4. The second arc is generally representative of the mass transport phenomena (i.e. diffusion of species) from the channels to the catalyst layer.
5. The low-frequency resistance (R_{LF}) is referred to as polarisation resistance. As for the ohmic resistance, the polarisation resistance is determined by the intersection of the impedance spectrum with the real axis at low frequencies range.
6. The last region of the spectrum, at low frequencies range, corresponds to the pseudo-inductive loop, which is still a subject of research in the literature. In the review study of Pivac and Barbir [200], two major interpretations have been identified as plausible: water transport characteristics and side reactions with intermediate species. The authors in [200] concluded that further works need to be carried out in order to identify the processes occurring within the fuel cell and therefore explain the LF inductive phenomena. This latter along with the HF inductive phenomenon does not present interest in our study, and will, therefore, not be addressed in our study.

The electrochemical processes described in this section can be modelled using equivalent electric circuits models. These models are based on the analogy that exists between the frequency behaviour of fuel cells and the components of the electrical circuits, meaning that if an electric circuit generates a similar response as the fuel cell does when the same perturbation signal is applied, it is therefore referred to as the equivalent electrical circuit. In these circuits, each phenomenon, or at least the most important ones, of the fuel cell are associated with a single or an association of electrical components.

3.2.2 EIS equivalent circuit

Various electrical models of the fuel cell have been reported in the literature [90,196]. These electrical circuits are intended to be as straightforward as possible to represent the frequency behaviour of the fuel cell. The most common circuit, which also constitutes the basis of more complex models, is the Randles model shown in figure 4.19.

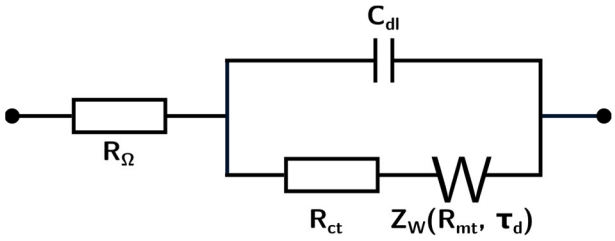

Figure 4.19. The Randles model - electric equivalent circuit.

The impedance of a fuel cell given by the Randles model can be written as follows:

$$\overline{Z}(\omega)=R_{\Omega}+\frac{R_{ct}+Z_W}{1+j\cdot\omega\cdot C_{dl}\cdot(R_{ct}+Z_W)} \tag{5.7}$$

The main interest of this model is that it provides an analytical definition of the impedance of a PEFC that adapts relatively well with most experimental results [201]. Each of the components of the equivalent circuit shown in figure 4.19 represents one of the phenomena occurring within the fuel cell:

- **R_{Ω}:** The total ohmic resistance of the PEFC represents the protonic resistance of the membrane R_m and the electronic resistance R_{e^-} related to electrons' flow. This latter regroups the contributions from the bulk resistances of the electronic conducting components R_{bulk}, and their interfacial contact resistances R_{cr}.

$$R_{\Omega}=R_m+R_{e^-} \tag{5.8}$$
$$R_{e^-}=R_{bulk}+R_{cr} \tag{5.9}$$

  From the EIS plot, the high frequency intersection between the impedance spectrum and the real axis represents the ohmic resistance of the PEFC, which is generally related to R_m [92,148,151]. However, when the fuel cell is subjected to assembly pressure issue, R_{e^-} becomes significant in the electrodes and their interconnections [83]. Therefore, changes in R_{e^-} as a function of mechanical compression will also be considered in this study.
- **R_{ct}:** The charge transfer resistance is associated to the slowness of the kinetics of the electrochemical reaction taking place on the surface of the electrodes. This resistance is generally dominated by the kinetics losses at the cathode [50,151].
- **C_{dl}:** The double layer capacitance represents the charge accumulation e^-/H^+ at the electrode/electrolyte interface [199,202].
- **Z_w:** The Warburg impedance was introduced by the electrochemical community to represent the reactants diffusion process towards the electrodes. The Z_w element can be expressed as a function of the Warburg (or diffusion) time constant τ_d and the mass transport resistance R_{mt} [198,201–203].

$$Z_w(\omega)=R_{mt}\frac{\tanh(\sqrt{j\omega\tau_d})}{(\sqrt{j\omega\tau_d})} \tag{5.10}$$

  The mass transport resistance arises from reactants concentration drop at the active area surfaces and it is preeminent at high current densities where the consumption of the reactants is significant. This type of loss originates more importantly from the limitation in the diffusion of reactants and liquid water accumulation resulting in GDLs pores and FFPs channels blockage.

The resistances shown in the Randles model in figure 4.19, namely R_{Ω}, R_{ct} and R_{mt} will represent the basis of the analysis of our impedance spectra reported in the next section.

3.2.3 Analysis method of the EIS results

The impedance spectrum can be given as depicted in figure 4.20. We opted in our analysis to consider solely the physical phenomena represented by the Randles model as represented in figure 4.19. Therefore, the high and low-frequency impedance inductive phenomena are assumed not to contribute to the changes in the PEFC performance when subjected to mechanical stresses [200] and are, thus, will not be considered in this study.

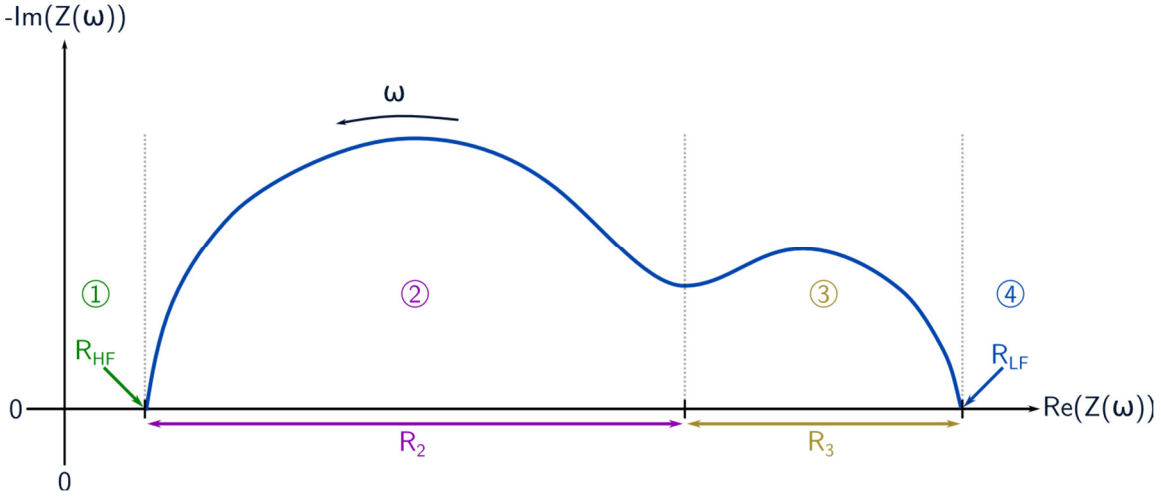

Figure 4.20. Impedance spectrum of the Randles model presented in figure 4.19.

The objective of our study is to separately investigate the impacts of mechanical compression on the ohmic, charge transfer, and mass transport resistances. The R_{HF} in figure 4.20 designates the ohmic resistance of the PEFC components (represented by R_Ω in figure 4.19) and the resistances R_2 and R_3 are related respectively to high frequency phenomena (such as charge transfer) and low frequency phenomena (mass transport). The R_{LF} represents the width of the two arcs and it is defined as $R_{LF}=R_2+R_3$. The analysis of the effects of mechanical compression on PEFC performance in this study will be based on the investigations of the evolution of these resistances, represented by the four regions in figure 4.20, and measured directly from the experimental impedance spectra. The low-frequency intercept with the real axis was not consistently attained during our experimentations. Therefore, the R_{LF} was measured from the corresponding $\mathrm{Re}\left(\overline{Z}(\omega)\right)$ obtained at the nearest point to the real axis. Table 4.10 summarises the investigated resistances and their corresponding significations.

Resistance	Signification
R_{HF}	Region 1: ohmic resistance.
R_2	Region 2: high frequency phenomena including charge transfer.
R_3	Region 3: low frequency phenomena mainly related to mass transport.
R_{LF}	Region 4: sum of R_2 and R_3.

Table 4.10. Significations of the resistances shown in figure 4.20.

3.2.4 EIS results and discussion

EIS characterisation technique has been widely used in in-situ investigations of the behaviour of PEFCs under different mechanical stresses [38,52,92,148]. In our study, the EIS was carried out for 12 levels of mechanical compression using the EIS station (Materials Mates, Italy [204]), as described in chapter 3 of this thesis, and at 50%RH. The current perturbation signal was set at 8% of the DC current delivered by the PEFC and was applied from 1 kHz to 100 mHz at 10 points per decade.

i. Effect of current density on R_{HF} and R_{LF}

Figure 4.21 shows the impedance spectra at different levels of mechanical compression. As in the previous experimental procedures (i.e. steady-state characterisation techniques), EIS measurements were conducted at current densities of 0.6 $A.cm^{-2}$ and 0.9 $A.cm^{-2}$. For clarity purposes, only three levels of mechanical compression are depicted per each current density level. The goal of this subsection is to study the effect of current density on the contribution of the resistances R_{HF} and R_{LF}. The estimation of the separation of the different phenomena taking place within the PEFC as a function of mechanical compression will be detailed in the following subsections.

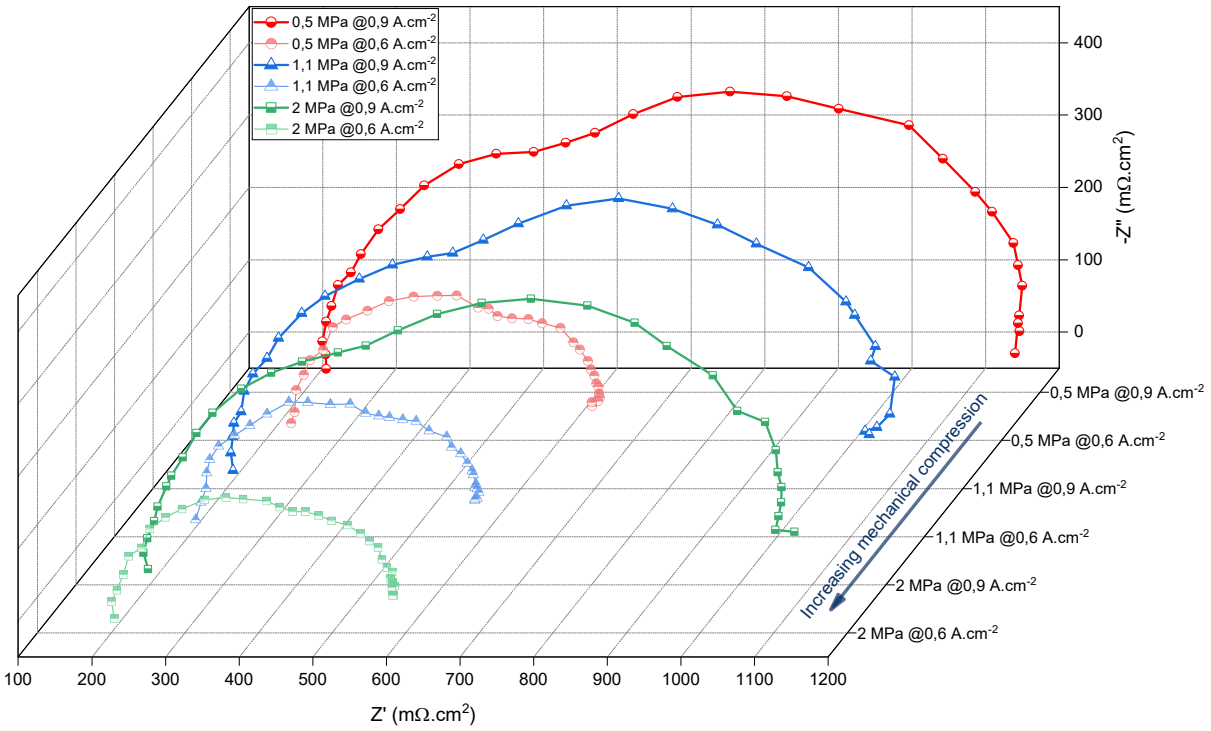

Figure 4.21. Impedance spectra for three levels of mechanical compression at 0.6 A.cm^{-2} and 0.9 A.cm^{-2}.

***a. Effect of current density on* $\mathbf{R_{HF}}$**

Table 4.11 shows the results of the R_{HF} evolution obtained from figure 4.21. It can be observed that the ohmic resistance is low at 0.9 A.cm^{-2} compared to 0.6 A.cm^{-2}. This difference was measured to be 4% and was attributed to the higher presence of water at the cathode side for a current density of 0.9 A.cm^{-2}, which favours the back-diffusion water transport mechanism as previously illustrated in figure 4.16. This effect, in turn, enhances the membrane humidification and leads to a lower ohmic resistance at 0.9 A.cm^{-2} compared to 0.6 A.cm^{-2}. These results, therefore, confirm the explanations given earlier in this chapter (figure 4.14) using the polarisation curves and PEFC voltage monitoring techniques.

R_{HF} / Current density	**0.5 MPa** (mΩ.cm^2)	**1.1 MPa** (mΩ.cm^2)	**2 MPa** (mΩ.cm^2)
0.6 A.cm^{-2}	239.8	217.7	200.7
0.9 A.cm^{-2}	230.2	205.6	191.5

Table 4.11. The evolution of the R_{HF} as a function of the current density at three levels of mechanical compression.

***b. Effect of current density on* R_{LF}**

It can be seen from figure 4.21 that the R_{LF} increases with higher current density. This effect is attributed to the increase in the mass transport resistance as a result of the higher water production rate at 0.9 A.cm^{-2}. Table 4.12 presents the contribution of R_2 and R_3 resistances in the R_{LF}.

R_{LF} / Current density	**0.5 MPa** ($m\Omega.cm^2$)		**1.1 MPa** ($m\Omega.cm^2$)		**2 MPa** ($m\Omega.cm^2$)	
	R_2	R_3	R_2	R_3	R_2	R_3
0.6 $A.cm^{-2}$	295.2 73%	108.4 27%	241.3 65%	130.5 35%	246 64%	135.4 36%
0.9 $A.cm^{-2}$	326 35%	610 65%	301.7 35%	565.4 65%	302.1 34%	582.3 66%

Table 4.12. The contribution of R_2 and R_3 resistances in the R_{LF} as a function of current density.

At medium current density (i.e. 0.6 $A.cm^{-2}$), the R_2 contribute significantly in the R_{LF} (67% on average) compared to the R_3, which is attributed to the dominance of the activation resistance at this current density level. However, at high current density (i.e. 0.9 $A.cm^{-2}$), the R_3 contribution in the R_{LF} becomes substantially high (65% on average). This latter effect is due to the higher liquid water production rate at the cathode side at 0.9 $A.cm^{-2}$ compared to 0.6 $A.cm^{-2}$.

By comparing the results shown in table 4.12 at high and medium current density, it can be observed that the mass transport resistance is about 4.7 times higher at 0.9 $A.cm^{-2}$ compared to 0.6 $A.cm^{-2}$, whereas the activation resistance is about only 1.2 times higher at 0.9 $A.cm^{-2}$ compared to 0.6 $A.cm^{-2}$. These results confirm the dominance of the mass transport resistance at high current density due to the higher water production rate at the cathode CL. The contributions of these resistances as a function of mechanical compression will be detailed hereafter.

ii. The distinction of the different resistances as a function of mechanical compression

a. Results at medium current density

Figure 4.22 depicts the impedance spectra of 12 levels of mechanical compression at 0.6 $A.cm^{-2}$.

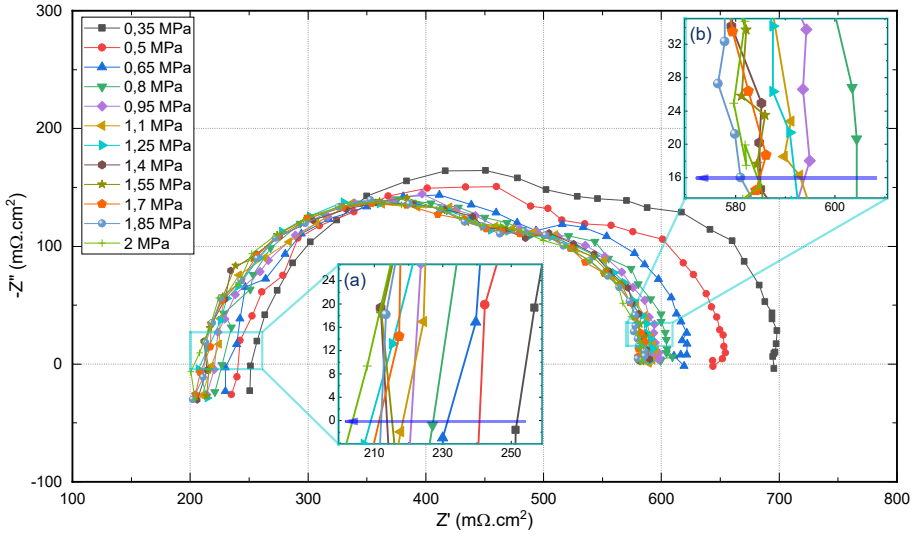

Figure 4.22. Impedance spectra of 12 levels of mechanical compression at 0.6 A.cm^{-2}. Inserts (a) and (b) represent the R_{HF} and R_{LF} regions, respectively. The horizontal arrows represent the increase in the mechanical compression.

It can be observed from insert (a) that the mechanical compression reduces the ohmic resistance of the PEFC, which is in good agreement with the first explanations given using steady-state characterisation techniques (figure 4.14). However, insert (b) shows that mechanical compression also reduces the R_{LF}. This effect, which was not typically reported in the literature [5–7], could be attributed to the decrease in the charge transfer resistance and it will be detailed in the next section.

- ***R_{HF} evolution as a function of mechanical compression***

Figure 4.23 shows the evolution of the R_{HF} as a function of mechanical compression at a current density of 0.6 A.cm^{-2}.

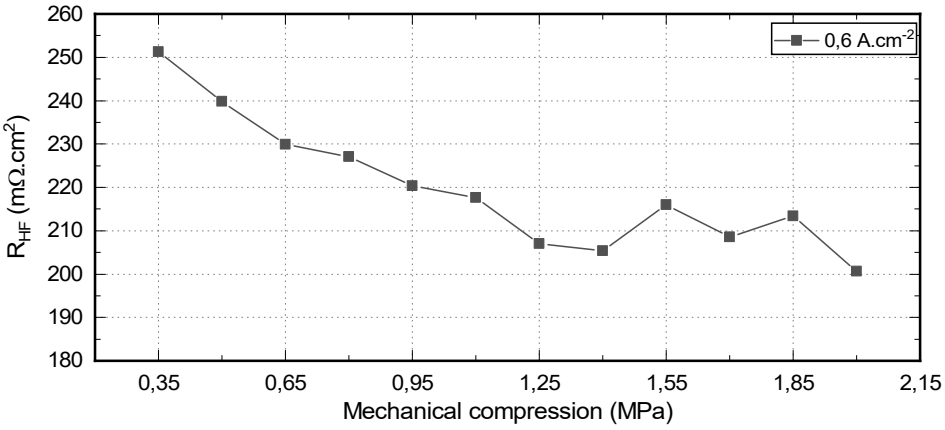

Figure 4.23. The evolution of R_{HF} as a function of mechanical compression at 0.6 A.cm^{-2}.

It can be observed that the ohmic resistance declines with increasing mechanical compression, with an 18.3% decrease attained at 1.4 MPa over a total decrease of 20.1% reached at 2 MPa. This ohmic resistance diminution is attributed to the reduction in the electrical contact and bulk resistances with increasing mechanical compression. Indeed, K. Bouziane [192] conducted, within the framework of our MIREPOIx research project, several ex-situ measurements on the effect of mechanical compression on the through-plane resistance of the same GDL investigated in this in-situ study (i.e. Sigracet® 38 BC). The ex-situ results are reported in figure 4.24.

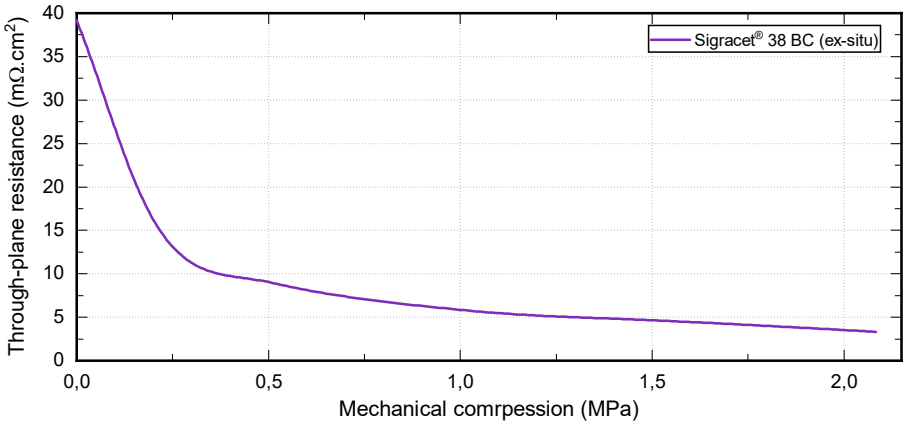

Figure 4.24. Evolution of the through-plane resistance as a function of mechanical compression – ex-situ measurements at 50°C [192].

The through-plane resistance evolution depicted in figure 4.24 shows a nonlinear reduction tendency as a function of mechanical compression. This reduction in the through-plane resistance is explained by the improved electrical carbon fibres' connexions with increasing mechanical compression. Results depicted in figure 4.24 show that 77.8% diminution of the through plane resistance was attained starting from 0.5 MPa. The decrease at 1.5 MPa was measured to be 88.6% over a total decrease of 91.6% at 2 MPa. These results confirm the in-situ investigations' results shown in figure 4.23.

- ***R_{LF} evolution as a function of mechanical compression***

Figure 4.25 shows the evolution of the R_{LF} along with the contributions of R_2 and R_3 as a function of mechanical compression at 0.6 A.cm^{-2}.

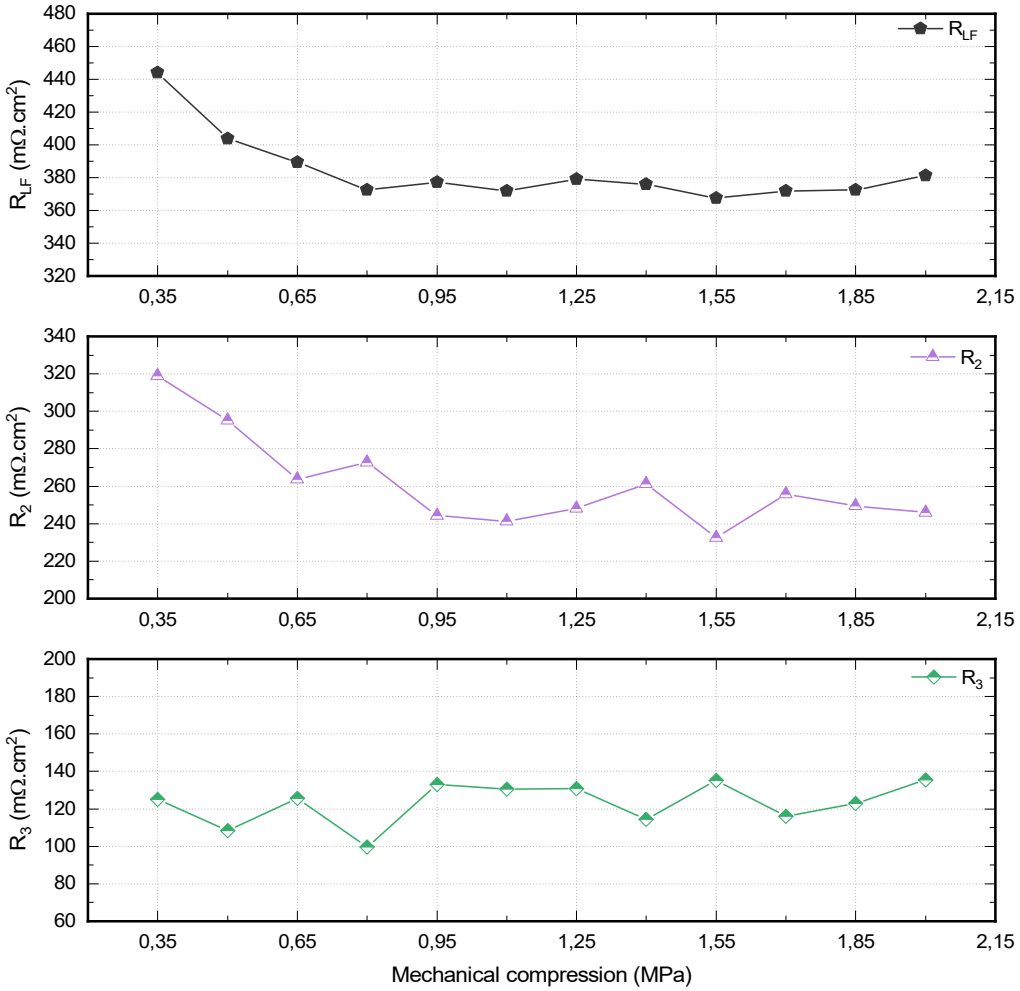

Figure 4.25. The evolution of R_{LF}, R_2, and R_3 as a function of mechanical compression at 0.6 A.cm^{-2} (R_{LF}=R_2+R_3).

It can be observed from figure 4.25 that the R_{LF} decreases with increasing mechanical compression, with a sharp decrease of 16% at 0.8 MPa over a maximum decrease of 17% attained at 1.55 MPa. This R_{LF} decrease at the first compression range (i.e. from 0.35 MPa to 1.55 MPa) is due to the diminution of the charge transfer resistance, represented by R_2, that was reduced by 27%, whereas the mass transport resistance, represented by R_3, augmented by 8% in the same compression range. It can be deduced from figure 4.25 that the R_{LF} decrease with increasing mechanical compression is mainly due to the decrease in R_2, while R_3 evolution represents a barely increasing tendency. The cause of R_2 reduction with mechanical compression will be explained later in this section.

b. Results at high current density

Figure 4.26 shows the impedance spectra of 12 levels of mechanical compression at 0.9 A.cm^{-2}.

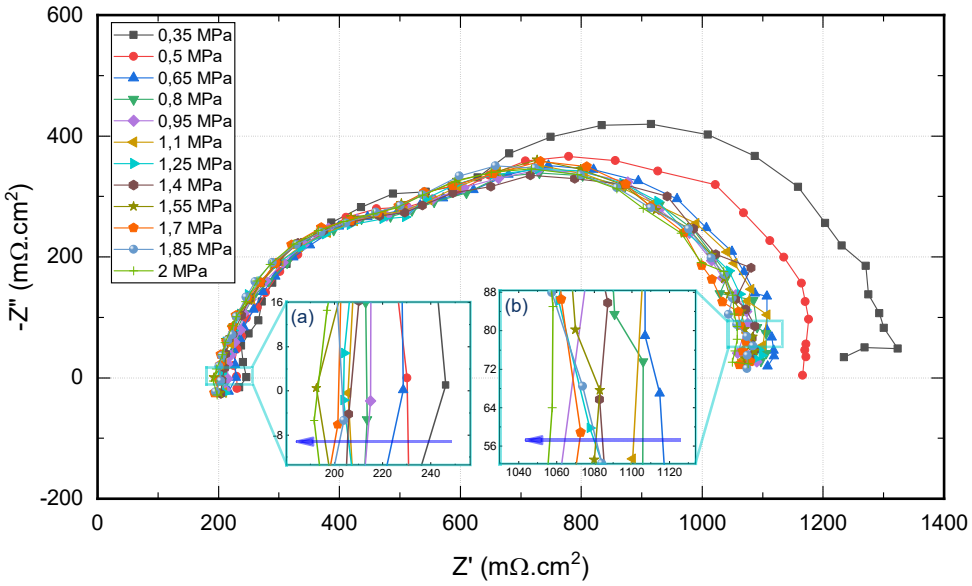

Figure 4.26. Impedance spectra of 12 levels of mechanical compression at 0.9 A.cm^{-2}. Inserts (a) and (b) represent the R_{HF} and R_{LF} regions, respectively. The horizontal arrows represent the increase in the mechanical compression.

Similar to the results reported at medium current density, it can be observed from figure 4.26 that mechanical compression reduces both the R_{HF} and the R_{LF} resistances at 0.9 A.cm^{-2}. Explanations of this effect will be addressed in the following subsections.

- ***R_{HF} evolution as a function of mechanical compression***

The R_{HF} evolution as a function of mechanical compression at 0.9 A.cm^{-2} is depicted in figure 4.27.

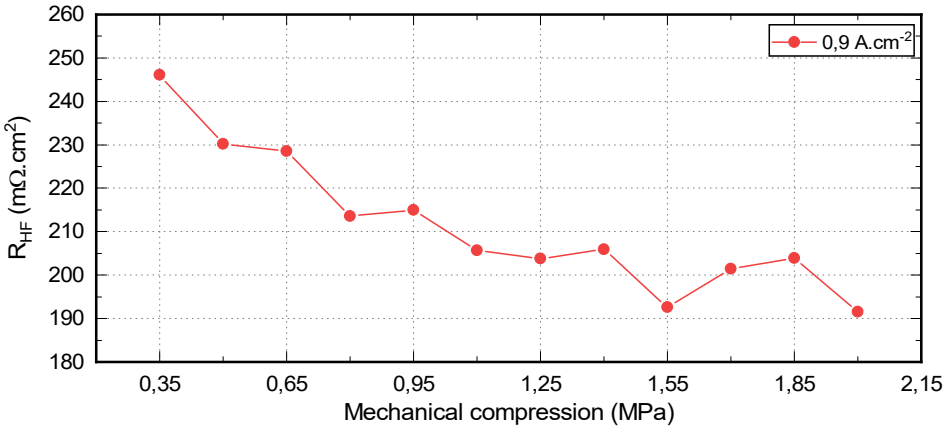

Figure 4.27. R_{HF} evolution as a function of mechanical compression at 0.9 A.cm^{-2}.

Consistently with the results reported at 0.6 A.cm^{-2}, the R_{HF} resistance at 0.9 A.cm^{-2} decreases at higher mechanical compressions, with a 21.8% decrease attained at 1.55 MPa, over a 22.2% decrease at 2 MPa. These results are attributed to the decrease in the ohmic resistance of the PEFC components.

The R_{HF} measured at 0.9 A.cm^{-2} is 4%, on average, lower compared to the R_{HF} obtained at 0.6 A.cm^{-2}. This difference is attributed to the better membrane hydration at high current density due to the higher water production rate at the cathode CL, leading to a substantial water back-diffusion transport mechanism. These results confirm the explanations given previously in this chapter using steady-state techniques and illustrated in figure 4.16.

- ***R_{LF} evolution as a function of mechanical compression***

Figure 4.28 shows the evolution of the R_{LF} along with the contributions of R_2 and R_3 as a function of mechanical compression at 0.9 A.cm^{-2}.

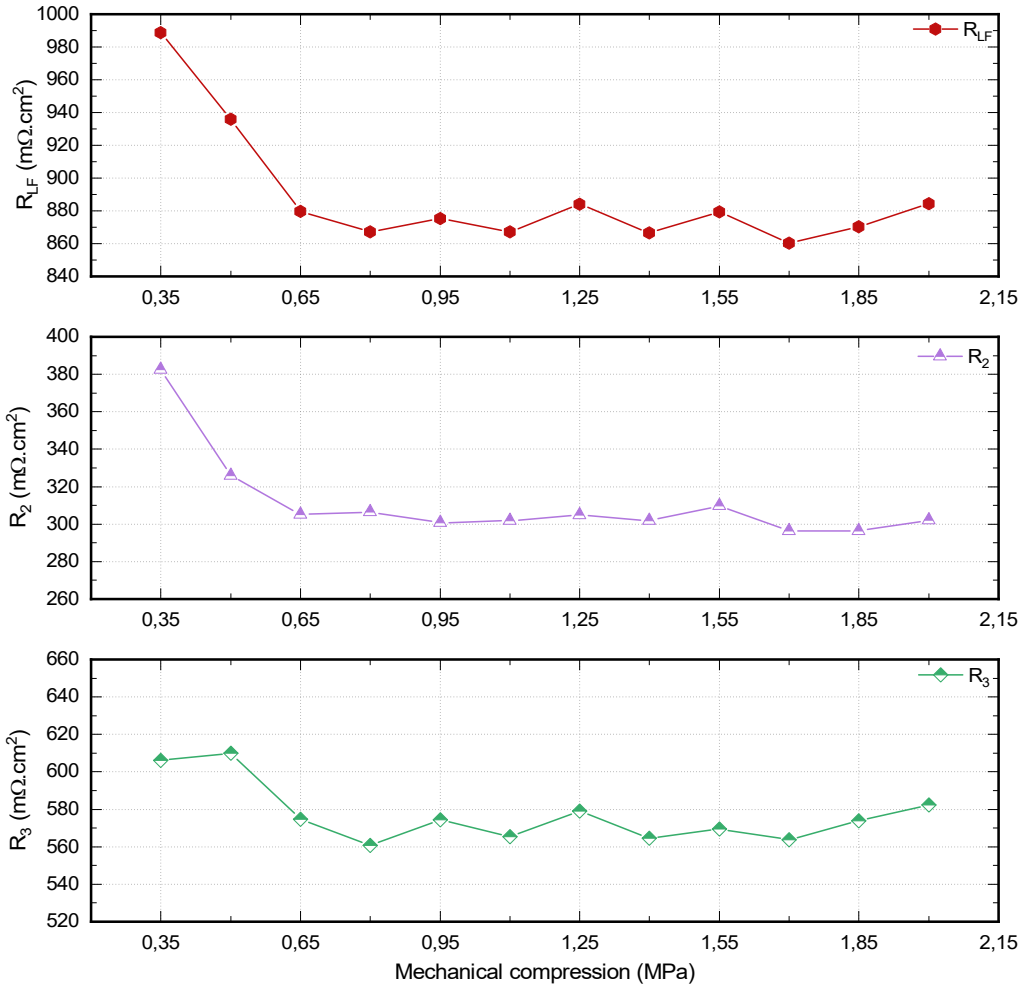

Figure 4.28. The evolution of R_{LF}, R_2, and R_3 as a function of mechanical compression at 0.9 A.cm^{-2} (R_{LF}=R_2+R_3).

It can be observed from figure 4.28 that the R_{LF} decreases with increasing the mechanical compression, which is mainly due to the decrease in the R_2. However, the R_3 does not suggest any discernible trend as a function of mechanical compression, except a small increase from 1.7 MPa to 2 MPa, which may be attributed to the increase in the mass transport resistance at this compression range.

- ***R_2 evolution as a function of mechanical compression***

As shown in figure 4.28 and figure 4.25, the major reduction in R_{LF} with increasing mechanical compression is due to the decline of R_2 (i.e. representative of the activation resistance). Up to the time of writing this thesis, the decrease in the activation resistance with mechanical compression is still not comprehensively addressed in the literature. As a matter of fact, most of the reported studies in this field have focused on mass transport and the ohmic resistances evolution as a function of mechanical compression [5–7]. Therefore, future investigations need to be carried out in order to provide plausible causes that may lead to the reduction of R_2 with increasing mechanical compression and hence it should be subject for future research [205,206,207].

4 Conclusion

This chapter provides a thorough study of the effects of mechanical compression on the global PEFC performance. Investigations were carried out using polarisation measurement analysis, fuel cell voltage monitoring, and electrochemical impedance spectroscopy (EIS). In this study, 12 levels of mechanical compression were investigated, ranging from 0.35 MPa to 2 MPa with steps of 0.15 MPa. These investigations were carried out using gradual increase/decrease and randomised mechanical compression protocols. Results of steady-state characterisation techniques showed that mechanical compression (i.e. up to 1.55 MPa) improves the PEFC performance at all tested operating conditions. This finding was attributed to the dominant reduction of the ohmic resistance against the increase in mass transport resistance. It was also shown that a mechanical compression level higher than 1.55 MPa does not result in any further improvement of the fuel cell voltage, it may even worsen the PEFC performance due to the increase in the mass transport resistance. Therefore, the presented results suggest that compressing the PEFC beyond a specified level (i.e. 1.55 MPa) would not lead to any further improvement of the PEFC performance.

The EIS analysis in this chapter was done by investigating the evolutions of the ohmic, charge transfer, and mass transport resistance as a function of mechanical compression. EIS results confirmed what the polarisation and cell voltage measurement analyses showed earlier in this chapter. The EIS results also emphasised the fact that mechanical compression reduces the activation resistance. However, further investigations need to be provided in order to clarify this effect. Correlations between in-situ results, reported in this chapter, and ex-situ investigations' results, carried out within the framework of this thesis' project, were put forward throughout this chapter.

The following chapter aims to investigate the local phenomena occurring within the operating PEFC through analysing the current density, temperature, and pressure distributions as a function of mechanical compression. Correlations with other ex-situ results will also be provided.

Chapter 5
In-situ assessment of the mechanical compression and its impacts on the local phenomena taking place within the PEFC

The results of the experimental investigations reported in chapter 4 emphasised the impacts of mechanical compression on the global PEFC performance. These investigations were carried out using polarisation measurement analysis, PEFC voltage monitoring, and electrochemical impedance spectroscopy (EIS). It was shown that mechanical compression improves the PEFC performance for a mechanical compression level up to 1.55 MPa. This effect was attributed to the dominant reduction of the ohmic resistance against the increase in mass transport resistance. However, mechanical compressions higher than 1.55 MPa resulted in no further improvement of the fuel cell performance, it was shown that it may even worsen the PEFC performance due to the increase in the mass transport losses. The results of the previous chapter also showed that mechanical compression reduces the charge transfer resistance leading to an improvement of the PEFC voltage.

The present chapter aims to provide a thorough understanding of how mechanical compression quantitively affects the local phenomena taking place within a PEFC with a large active area (i.e. commercial size: 225 cm^2). Investigations are conducted through studying: i) the current distribution, ii) the temperature distribution, and iii) the mechanical pressure distribution. Correlations with the previously reported in-situ results are provided throughout this chapter.

Similar to the preceding chapters, and in order to finely investigate the mechanical compression effects, 12 levels of mechanical compression are considered in this study, ranging from 0.35 MPa to 2 MPa with steps of 0.15 MPa. The experimental results reported in this chapter are intended to provide a comprehensive study on the improvement of the PEFC assembly design. This is carried out by providing guidelines to further understand the effects of mechanical compression in order to improve the PEFC performance and durability.

This chapter proceeds as follows: first, we present the experimental campaigns conducted in this study. Following that, we analyse the results obtained and provide spatial and quantitative analyses regarding the mechanical compression impacts on the local phenomena occurring within the PEFC. Correlations with the ex-situ results are also given throughout this chapter.

1 Presentation of the experimental campaigns

This section aims to provide a brief presentation of the experimental campaigns employed in this chapter. In fact, two experimental campaigns were conducted. The first one is the analysis of the distribution of the current and temperature along with displacement measurement, whereas the second one concerns the study of the pressure distribution on the active area of the PEFC.

1.1 Operating conditions

As mentioned earlier, this chapter aims to obtain correlations with the previously reported results in chapter 4 in which the global PEFC performance was assessed as a function of mechanical compression. To do so, the operating conditions were kept identical to the ones used in the preceding experimental investigations (see table 4.4 - chapter 4). Moreover, it has to be noted that the same PEFC components were used throughout the experimental campaigns of this chapter. Details about the test apparatus along with the used PEFC components are provided in chapter 3.

1.2 Mechanical compression profile

In this chapter, we have employed the same mechanical compression profile as the one depicted in figure 4.3 (a) - chapter 4. This mechanical compression profile is termed as randomised profile and includes the entire mechanical compression range studied here, i.e. from 0.35 MPa to 2 MPa with steps of 0.15 MPa. The reason behind using this mechanical compression profile is the elimination of the materials memory effect, which reduces, for instance, the effects of water accumulation due to the gradual increase of mechanical compression.

1.3 PEFC conditioning protocol

A PEFC conditioning protocol was carried out before conducting each of the experimental campaigns reported in this chapter. The goal is to make sure that the operating conditions are kept sufficiently stable before conducting experiments. This PEFC conditioning protocol was carried out as depicted in figure 4.2 - chapter 4. It has to be noted that the measurements of the local distributions of current and temperatures along with the displacement measurement were performed conjointly with the experimental investigations reported in chapter 4. However, the measurements using the pressure sensitive films were conducted off-line (non-operating PEFC) and an in-house developed mechanical conditioning protocol was developed. Further details will be given later in this subsection.

1.4 Current density distribution measurement

A current and temperature distribution measurement device (S++® simulation services [208], Germany) was installed in the PEFC assembly, namely in between the anode FFP and the current collector. This measurement device, i.e. S++® current scan shunt, was connected to a control station. This allows collecting current and temperature distributions data conjointly using the CurrentVIEW software provided by S++® [208]. This device was designed and assembled in order to have minimum interference with the phenomena taking place within the PEFC (Figure 5.1). More details about the S++® measurement device can be found in chapter 3.

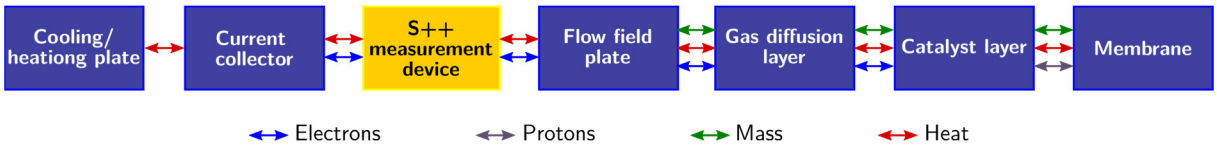

Figure 5.1. Position of the S++® measurement device in the PEFC assembly.

The used current distribution measurement device has the advantage of a good spatial resolution, with 21x21 measurement segments (i.e. 441 in total) per 225 cm^2 active area. Therefore, each segment measures the current passing through a surface of ~ 0.51 cm^2 (i.e. measurements provided in Ampere per segment). In order to obtain units in $A.cm^{-2}$, all the current measurements collected by the S++® device were multiplied by a conversion factor corresponding to $^{441_{segments}}/_{225_{cm^2}}$=1.96.

In this chapter, ten 21×21 current density distribution arrays were collected per each of the 12 randomised levels of mechanical compression. Each of the ten 21×21 arrays was recorded at a frequency of 0.5 Hz (i.e. one reading per two seconds) at the end of a stabilisation period of 5 minutes. Every current density value of the ten arrays was averaged and a new array corresponding to the averaged values was obtained. In order to standardise the scale between the results at 0.6 $A.cm^{-2}$ and 0.9 $A.cm^{-2}$, the averaged arrays were divided by the average current density value. This standardisation process gives a percentage scale depending on the average current density value measured, which means that a standardised current density value of 1 either corresponds to a current density of 0.6 $A.cm^{-2}$ or 0.9 $A.cm^{-2}$ (i.e. 100% of the average tested value), depending on the tested current density levels. Thus, the use of the standardised current density values gives a straightforward interpretation of the current density distributions with a recognised value (i.e. the average current density value) as a reference.

The long-term effects of mechanical compression that impact, for instance, the liquid water management were separated from quick phenomena taking place within the PEFC by taking the average of the ten 21×21 current density distribution arrays. Therefore, changes within the PEFC taking place over a short time scale (i.e. captured by single measurements every 2 seconds), e.g. small liquid water droplets movement inside the FFPs channels, were not considered in this study. Thus, averaging the ten arrays of the current density distribution,

and also the temperature distribution as it will be described hereafter, results in a presentation of the changes taking place within the PEFC over a period of 20 seconds.

1.5 Temperature distribution measurement

The S++® temperature distribution measurement device has 7×7 measurement segments (i.e. 49 in total) per 225 cm^2 active area. Therefore, each segment measures the local temperature over a surface of ~ 4.6 cm^2. Similar to the current density distribution, ten 7×7 arrays of temperature distribution were measured per each level of mechanical compression. The temperature distribution arrays were measured simultaneously with the current density distribution arrays. Each local temperature value of the ten arrays was averaged and a new array corresponding to the average temperature values was calculated.

1.6 Pressure distribution measurement

The achievement of a uniform pressure distribution within the PEFC components is a key factor for improving the current and temperature distributions. In this sense, this chapter explores the possibility of using Prescale® pressure sensitive films (Fujifilm [209], Japan) in order to measure the pressure magnitude and distribution within the PEFC active area. The operating principle of the Prescale® films and their assembly procedure during our experiments will be detailed later in this chapter (figure 5.18). Prescale® films type LLW were used in our experimentations, this choice is based on the pressure measurement range of LLW films (i.e. optimal between 0.5 MPa and 2.5 MPa [209]), which is the most adequate to the mechanical compression range explored in this study (i.e. between 0.35 MPa and 2 MPa).

1.7 Analysis of the local phenomena evolution with mechanical compression

As mentioned earlier, this chapter aims to give a thorough understanding of the effects of mechanical compression on the local phenomena taking place within an operating PEFC. This includes the analysis of the current, temperature, and pressure distributions. As this investigation will be conducted locally, we opted for analysing these phenomena following nine zones as shown in figure 5.2. These zones numbers will be used for the rest of this chapter as conventional locations.

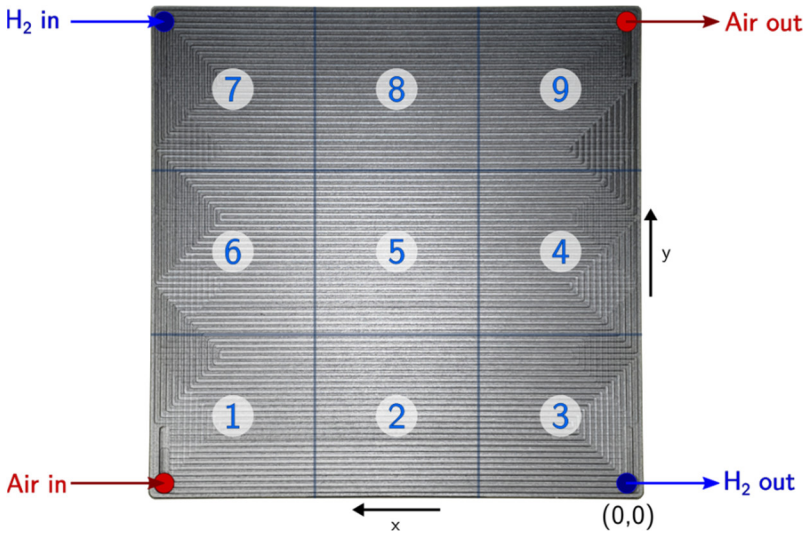

Figure 5.2. Presentation of the locations of the nine regions used in the analysis of the results reported in this chapter. The figure depicts a superimposed image of the anode and cathode FFPs channels.

Figure 5.2 shows the locations of the zones that will be used in the analysis of the results reported in this chapter, figure 5.2 also depicts the reactants inlets/outlets configuration. The position of the origin point (0,0) and the direction of the coordinate system are also shown in figure 5.2. The **x** and **y** arrows represent the horizontal and vertical direction of the measurement points/segments, respectively. The heating/cooling medium (i.e. deionised water in our study) flows at the cathode from the 3rd zone to the 7th zone, whereas it flows at the anode from 1st zone to the 9th zone. This information will be useful for the spatial analysis of the current, temperature, and pressure distributions investigated in this chapter.

2 Analysis of the current and temperature distributions as a function of mechanical compression

Analysing distributions of the current and the temperature is challenging, especially in PEFCs with a large active area, i.e. 225 cm^2 in our study. Using PEFC with a large active area can present a number of issues [210] that can be due for instance to i) the inhomogeneity of electrochemical reaction sites distribution, ii) liquid water management, iii) difference in local electrical and thermal conductivities, iv) manufacturing process issue [211], v) damage occurred during the operational lifetime of the PEFC components, and vi) FFPs design. These effects can lead, in the worst case, to the creation of regions with high current densities leading to the creation of high temperature regions that could potentially damage the PEFC components through the creation of hotspots [91,92,212]. These effects could eventually decrease the fuel cell lifetime or even cause premature failure of the PEFC [213,214]. The objective of our study is not to go through all the plausible effects of the nonhomogeneous distributions of the current

and temperature, as it is not the aim of this research project, but rather to give a thorough analysis of these distributions as a function of mechanical compression.

Similar to the analysis reported preceding experimental campaigns (see chapter 4), the investigations conducted in this chapter are carried out at both current densities of 0.6 A.cm^{-2} and 0.9 A.cm^{-2}, representing the ohmic and the mass transport regions, respectively. Each current density is tested at a relative humidity of 50%RH and 100%RH. Since the goal of this chapter is to find correlations between the local phenomena and the global performance of the PEFC, the procedure followed for the local phenomena analysis is the exact same as the one formerly used in the previous chapter. Results at 0.6 A.cm^{-2} will be further detailed in this chapter, the comparison between results at 0.6 A.cm^{-2} and 0.9 A.cm^{-2} will be addressed in this chapter. In order to avoid redundancy, some figures and results at 0.9 A.cm^{-2} will be provided in Appendix F.

2.1 Analysis of the distributions of current and temperature at 0.6 A.cm^{-2}

This section provides a comprehensive analysis of the distributions of the current and the temperature at a medium current density of 0.6 A.cm^{-2} as a function of mechanical compression. Each distribution of the current and temperature is analysed at both relative humidity levels of 50%RH and 100%RH. First, we present the spatial analysis of the distributions' heterogeneities at six levels of mechanical compression (from 0.5 to 2 MPa with 0.3 MPa steps). Then, each spatial distribution analysis will be followed by a statistical analysis covering all the twelve levels of mechanical compression investigated in this chapter (i.e. from 0.35 MPa to 2 MPa with 0.15 MPa steps).

2.1.1 Current density distribution analysis at 0.6 A.cm^{-2}

i. Results at 50%RH

The measurement results of the standardised current density distribution at six levels of mechanical compression, namely from 0.5 MPa to 2 MPa with 0.3 MPa steps, are depicted in figure 5.3. These results are represented in 2-dimensional contour maps for a PEFC operating at an average current density of 0.6 A.cm^{-2} and relative humidity of 50%RH. The colour bars represent the corresponding colours to each level of the standardised current density.

In this study, we have chosen to represent the standardised current density distribution on a scale from 0 to 2. This scale is intended to include the entire standardised current density values that were measured in all the tested operating conditions. For instance, at 0.9 A.cm^{-2} and 100% (see Appendix F), the maximum standardised current density attained a local value of 2, which corresponds to 200% of the average current density (i.e. 1.8 A.cm^{-2}). This effect is related to assembly pressure issues at low mechanical compression levels, a similar impact was reported in [211]. This effect will be detailed later in this chapter.

The abscissa and ordinate axes in figure 5.3 (and for all the 2-D contour maps in this chapter) represent the and x-axis and y-axis shown in figure 5.2, whereas the axes labels represent the segments' numbers.

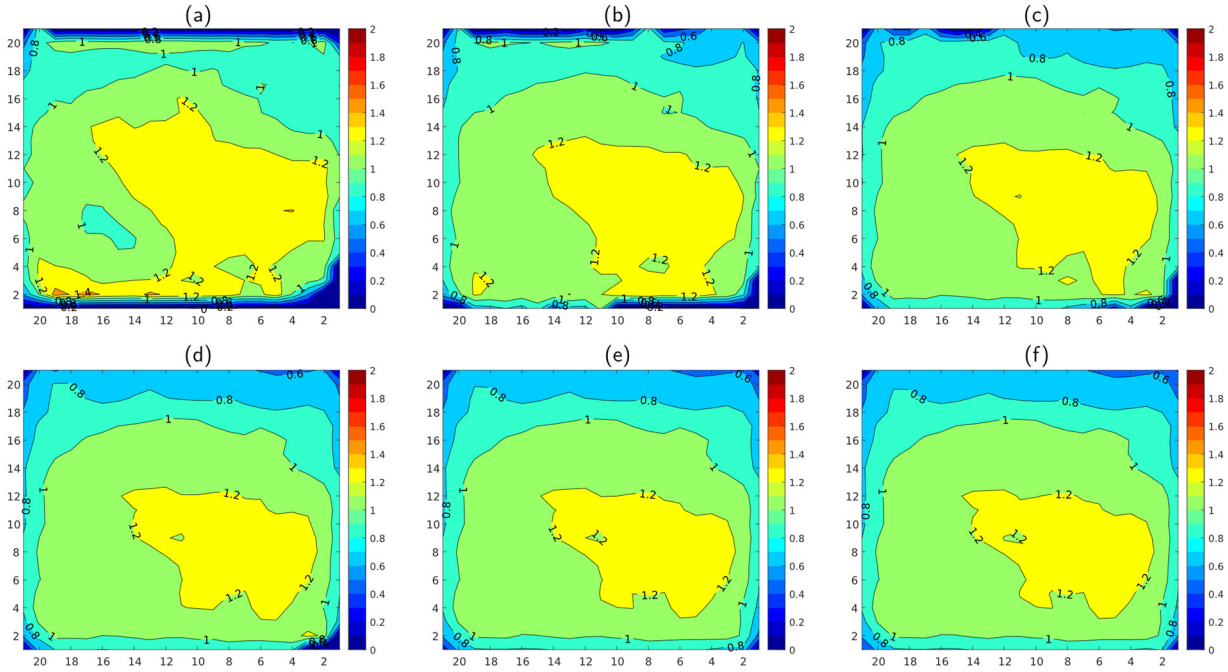

Figure 5.3. Standardised current density distribution 2-D maps at 0.6 A.cm^{-2} and 50%RH. (a) 0.5 MPa, (b) 0.8 MPa, (c) 1.1 MPa, (d) 1.4 MPa, (e) 1.7 MPa, and (f) 2 MPa. Colour bars show the corresponding colours of each level of the standardised current density.

Before going into the analysis of the mechanical compression effects on the current density distributions shown in figure 5.3, it seems important to start first with the analysis of the effects leading to spatial inhomogeneity that are not related to the mechanical compression. Indeed, the inhomogeneity of the current density distribution can be caused by various factors [35] that can be, in some cases, complex to determine depending on the available experimental means (e.g. components manufacturing issues, damage during fuel cell operation, uneven catalyst loading [215]). The explanations provided hereafter intend to explain the plausible effects impacting the current density distribution shown in figure 5.3.

With regards to the spatial current inhomogeneity, the four corners of the current density distribution maps depicted in figure 5.3 show relatively low, or even zero, current density at all mechanical compression range. This observation is mainly due to the presence of the orifices of the reactants' inlets/outlets (depicted in figure 5.2) where no electrical conducting material is present. A similar effect was emphasised by Baumann et al. [211]; these authors created a defect site with no conducting material and reported the same observation as no current was flowing through this defect site.

During our experimentations, hydrogen and air were used as reactants in co-flow mode, meaning that, as shown in figure 5.2, the air was fed from the bottom left to the top right,

whereas the hydrogen was fed from the top left to the bottom right of the FFPs. In fact, this configuration is intended to favour a uniform membrane humidification distribution as the anode inlet is located near the cathode outlet (i.e. top zones 7, 8, and 9) so that water transport mechanisms, namely back-diffusion, helps to homogenise the membrane humidification. However, it can be observed from figure 5.3 that the current distributions present a large spatial inhomogeneity, especially in the horizontal direction. Indeed, the zones from 1 to 6 present relatively higher current density compared to zones from 7 to 9. This relatively low current density at the top region of the active area results from a depletion of the oxygen contained in the air flow near the cathode outlet. Therefore, the remaining oxygen concentration near the outlet is not sufficient enough to reach similar current density levels as in the first locations (i.e. zones from 1 to 6) of the active area of the PEFC. In fact, the available oxygen was progressively consumed while approaching the air outlet. A similar current density distribution was reported by Alaefour et al. [216]. These authors reported that the local current densities are fairly higher in the zones near the reactants' inlet compared to the ones near the reactants' outlet in a co-flow configuration. This effect was attributed to the reactants' depletion at the outlet regions of the active area. Similar observations were also reported in [217] and [218].

Concerning the effects of mechanical compression shown in figure 5.3, it can be observed that the spatial homogeneity of the current density improves with increasing the mechanical compression. This effect is mainly due to the enhancement of the mechanical contact within the PEFC components. Figure 5.3 also shows that the spatial homogenisation effect majorly occurs at mechanical compressions up to 1.4 MPa. This homogenisation effect is mainly visible at the top and bottom regions of the distribution maps, and especially at the 3rd zone. In fact, the contact pressure is insufficient in this zone, which results in high electronic resistance and, therefore, no current flowing through this zone, and most of the current flow through the nearby zones due to relatively low electronic resistance. This effect also explains the high standardised current density levels located nearby the 3rd zone. These results are in good agreement with the observations of Baumann et al. [211]. These authors reported that a nonconducting region of the FFPs led to the increase in the current flowing through their nearby conducting regions.

Compared to other PEFC components, the GDLs are considered to be the components most impacted by structural deformation under mechanical compression due to their soft and brittle structure [52,82]. Therefore, the electro-physical characteristics of the GDLs are highly influenced by compressive loads and play a major role in the current density distributions shown in figure 5.3. In fact, both the bulk and contact resistances of the GDL decrease with increasing mechanical compression. This effect was emphasised by the work of K. Bouziane [102,192] conducted within the research project of this thesis (i.e. MIREPOix project). As the GDL is compressed, its thickness decreases leading to an enhanced fibres connexions, and therefore to a reduced bulk and contact resistances [102,192]. In line with these effects, figure

5.4 depicts in-situ (i.e. measured from our assembled PEFC) and ex-situ (i.e. provided by SGL carbon) displacement measurements using the same GDL employed in this thesis (i.e. Sigracet® 38 BC). Figure 5.4 shows that the in-situ and ex-situ measurements of the displacement have relatively the same trend, with the ex-situ results showing larger displacement but the values are more dispersed so that the in-situ results lie virtually within all the error bars of the ex-situ measurements. This result shows that the major in-situ displacement is due to the GDL compression, leading to a reduced contact and bulk resistances of the GDL as it was emphasised in [102,192].

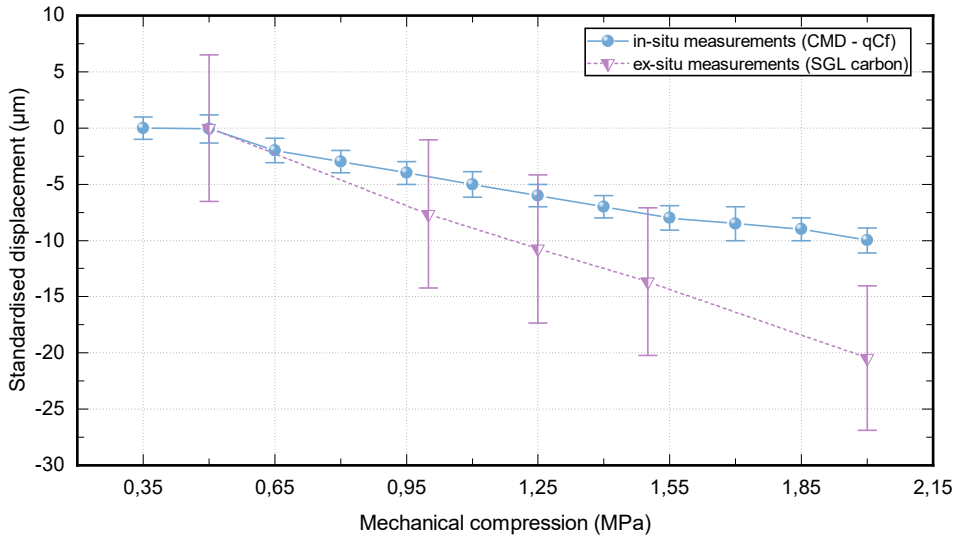

Figure 5.4. Comparison between in-situ measurement using CMD and ex-situ measurement provided by SGL carbon. Both measurements are conducted on a GDL type Sigracet® 38 BC.

Thus, in relation to the results reported in figure 5.3 and figure 5.4, in the regions where the mechanical pressure is higher, the bulk and contact resistances of the GDL are lower, which promotes more current to flow through these low resistance regions. These local resistance variations can, therefore, explain the homogenisation in the current density distributions as a function of mechanical compression shown in figure 5.3. This effect will be further investigated later in this chapter using pressure sensitive films.

In order to statistically analyse the results reported in figure 5.3, we present in figure 5.5 the histograms of the standardised current density distributions. Since we aim here to provide correlations with the results reported previously in this manuscript, the histograms are presented at three levels of mechanical compression, namely 0.5 MPa, 1.4 MPa, and 2 MPa, that are representing as close as possible the first and the second compression ranges as they were defined in chapter 4, i.e. 0.35→1.55 MPa and 1.55→2 MPa, respectively. These three levels of mechanical compression will be used in histogram figures for the rest of this chapter and will be represented by three colours (blue, orange and yellow). However, other colours may be visible due to the superimposition of two of three of these colours.

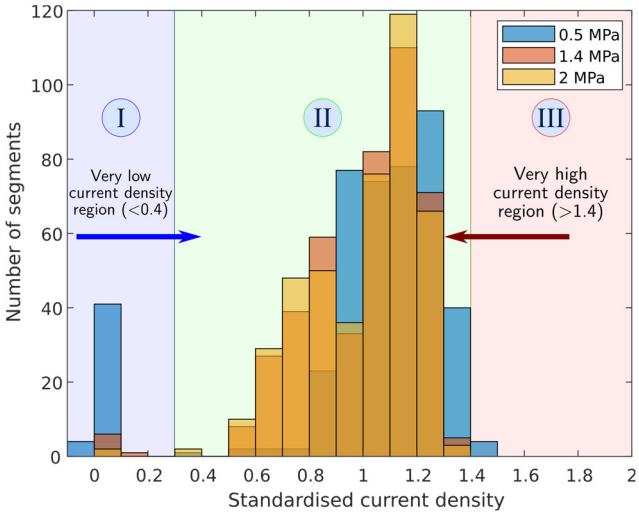

Figure 5.5. Histograms of the standardised current density distribution at three levels of mechanical compression: 0.5 MPa, 1.4 MPa, and 2 MPa. Histograms obtained at 0.6 A.cm^{-2} and 50 %RH. The blue and red arrows represent the ideal effects of mechanical compression on the current density distribution at very low and very high current density regions, respectively.

The histograms shown in figure 5.5 can be analysed following three regions depending on the value of the standardised current density. These regions are coloured in blue, green, and red in figure 5.5 and marked by Latin numerals I, II, and III, respectively. The blue region corresponds to current density levels below 40% of the average current density, whereas the red region corresponds to current density levels higher than 140% of the average current density. These two regions are considered critical since they contain very low and very high current density levels that lead to an uneven current density distribution. Finally, the green region is defined in-between the blue and red regions and defined as the medium current density region.

It can be seen from figure 5.5 that the mechanical compression reduces simultaneously the very low and the very high current density regions. This effect is mainly due to the better mechanical compression distribution and it will be addressed in more detail later in this chapter. These two combined effects increase the medium current density region, which is beneficial for the PEFC as they homogenise the current density distribution as shown in figure 5.4. Through a visual analysis of the histograms shown in figure 5.5, it can be observed that the homogenisation effect majorly occurs at mechanical compressions up to 1.4 MPa. In fact, mechanical compression reduces the standardised current density of 0.1 (i.e.10% of the average current density) by 85,4% at 1.4 MPa over a total reduction of 95,1% at 2 MPa, whereas the 1.4 values were eliminated at 1.4 MPa. Further statistical analyses will be addressed by comparing results at 0.6 A.cm^{-2} and 0.9 A.cm^{-2} at the end of this subsection.

ii. Results at 100%RH

Figure 5.6 shows the 2-D contour maps of the standardised current density distributions at six levels of mechanical compression from 0.5 MPa to 2 MPa. These standardised current density

distributions were measured for the PEFC operating at an average current density of 0.6 A.cm^{-2} and relative humidity of 100%RH.

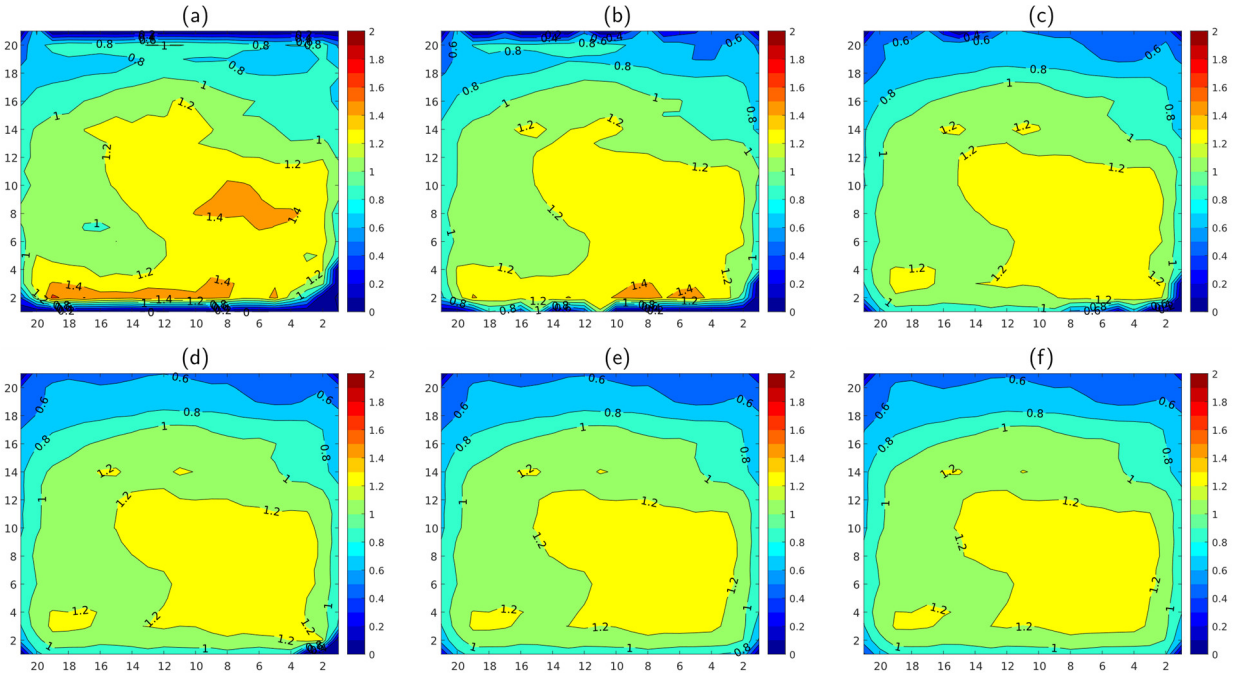

Figure 5.6. Standardised current density distribution 2-D maps at 0.6 A.cm^{-2} and 100%RH. (a) 0.5 MPa, (b) 0.8 MPa, (c) 1.1 MPa, (d) 1.4 MPa, (e) 1.7 MPa, and (f) 2 MPa. Colour bars show the corresponding colours of each level of the standardised current density.

Before discussing the effects of the mechanical compression on the standardised current density distributions shown in figure 5.6, it is important to start first by analysing the current density inhomogeneity causes that are not related to the mechanical compression effects. Similar to the results at 50%RH, it can be observed here that the current density distributions show a large inhomogeneity in the horizontal direction. In fact, figure 5.6 shows that the high current values flow through regions near the air inlet (zones 1, 2, and 3), whereas the upper zones (7, 8, and 9) show relatively low current. This inhomogeneity is mainly attributed to the depletion of the oxygen concentration [216,217] as explained previously in the 50%RH results. This observation is in good agreement with the findings reported by Hakenjos et al. [219].

Through comparing the zones 7, 8, and 9 in figure 5.3 and figure 5.6, it can be observed that the current density is lower at these zones at 100%RH compared to 50%RH, which is due to the oxygen depletion near the air outlet. However, this oxygen depletion effect on the current density distribution seems to be more critical in the case of 100%RH compared to 50%RH. This effect is mainly attributed to the higher presence of water at 100%RH [189] leading to diffusion issues as the water at the cathode side obstructs oxygen transport (e.g. due to clogging of FFPs channels and GDL pores) and therefore leads to oxygen starvation at the zones near the air outlet. The same results were also observed at a current density of 0.9 A.cm^{-2} (See Appendix F). This finding is in good agreement with the results of Iranzo et al. [220] in their

in-situ study on the effects of the PEFC operating conditions on the liquid water distribution. These authors reported that more water is located at the FFPs channels when the PEFC was operated at a high relative humidity (i.e. 90%RH). More importantly, the results in the in-situ study [220] emphasised that liquid water accumulates gradually towards the cathode outlet, which decreased the water removal rate of the PEFC that, in turn, reduces the current flowing through these regions.

Regarding the effects of mechanical compression on the current density distribution, and similar to the results at a relative humidity of 50%RH, the results at 100%RH shown in figure 5.6 emphasise the fact that the mechanical compression improves the homogeneity of the current density distribution. This homogenisation was improved by simultaneously reducing the very low and the very high current density regions, corresponding to the regions with standardised current densities lower than 0.4 and higher than 1.4, respectively. These observations are emphasised in the histograms shown in figure 5.7. This effect is due to the enhanced mechanical contact between the PEFC components, but also to the decrease in the GDLs contact and bulk resistances with increasing mechanical compression as emphasised by the ex-situ results reported by K. Bouziane [102,192]. Therefore, since the electrical resistance of the GDL is highly impacted by mechanical compression, even small variations in the bulk and contact resistances of the GDL will result in various current density levels flowing through some particular regions of the active area of the PEFC. This effect is observed at the bottom and top regions of the current density distributions shown in figure 5.6. In line with these results, Peng et al. [35]. reported an investigation on the effects of the clamping pressure on the distribution of the local current densities using an in-house measurement device. They reported that mechanical compression homogenises the current density distribution and therefore improves the PEFC performance. The authors reported that higher current flows through the regions with large mechanical contact pressure and that the current density is low in the regions with low mechanical contact pressure.

In order to statistically visualise the current density 2-D maps at 100%RH, figure 5.7 depicts the histograms of the standardised current density distribution at three levels of mechanical compression, namely at 0.5 MPa, 1.4 MPa, and 2 MPa.

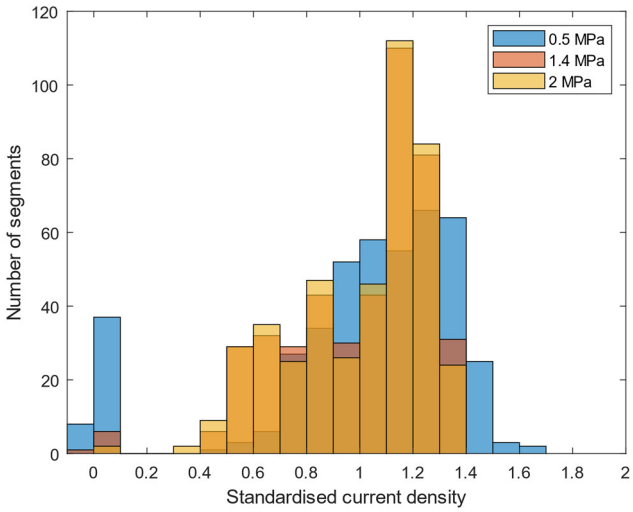

Figure 5.7. Histograms of the standardised current density distribution at three levels of mechanical compression: 0.5 MPa, 1.4 MPa, and 2 MPa. Histograms obtained at 0.6 A.cm^{-2} and 100 %RH.

At first glance, the histograms shown in figure 5.7 confirm that the major current density homogenisation effect occurs for a mechanical compression up to 1.4 MPa. It can be observed that the mechanical compression reduces simultaneously the very high current density region (i.e. higher than 140% of the average current density) and the very low current density region (i.e. lower than 40% of the average current density). Similar to the results at 50%RH, the histograms in figure 5.7 show that mechanical compression reduces the standardised current density of 0.1 (i.e. 10% of the average current density) by 83,8% and 94,6% at 1.4 MPa and 2 MPa, respectively. Also, it can be observed that all the standardised current density values higher than 1.4 (i.e. 150%, 160%, and 170% of the average current density) were completely disappeared starting from mechanical compression of 1.4 MPa. More statistical analyses are given in the following subsections.

iii. Statistical analysis of the standardised current density distributions at 0.6 A.cm^{-2}

A statistical investigation is conducted in this subsection in order to provide a quantitative analysis of the standardised current density distributions measured at 0.6 A.cm^{-2}. This investigation aims to provide thorough comparisons between the results at 50%RH and 100%RH by studying the evolutions of the standard deviation and the maximum standardised current density values as a function of mechanical compression. The analysis given here includes all the 12 levels of mechanical compression from 0.35 MPa to 2 MPa with 0.15 MPa steps. Similar to chapter 4, the first and second compression ranges are defined as 0.35 MPa $\rightarrow$ 1.55 MPa, and 1.55 MPa $\rightarrow$ 2 MPa, respectively.

- Evolution of the standard deviation of the current density distribution at 0.6 A.cm^{-2}

The standard deviations (SD) were measured per each of the 12 averaged arrays of the standardised current density distributions at 0.6 A.cm^{-2}. The evolutions of the SD as a function of mechanical compression at 50%RH and 100%RH are depicted in figure 5.8.

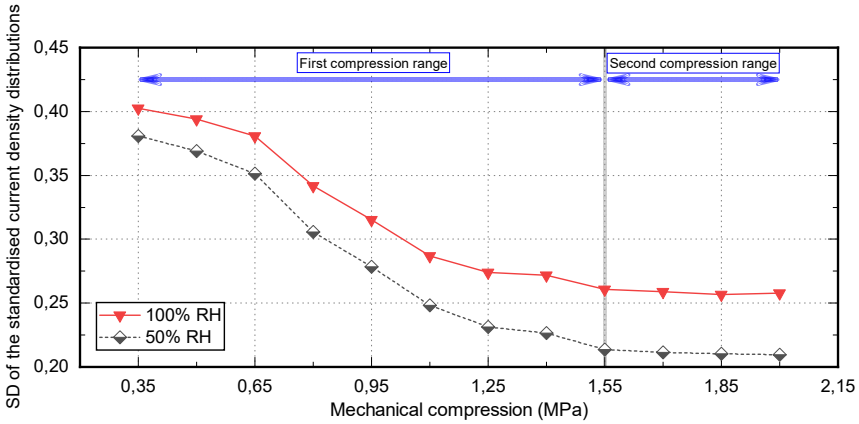

Figure 5.8. SD evolution of the standardised current density distribution as a function of mechanical compression at 0.6 A.cm^{-2}. Results at 50%RH and 100%RH. The horizontal arrays represent the first and the second compression ranges.

Figure 5.8 shows that mechanical compression reduces the SD of the standardised current density distribution at both relative humidity levels, with higher SD values at 100%RH compared to 50%RH. This difference is measured to be 13.4% on average and it is due to the higher presence of water at 100%RH, leading to blockage of reactants pathways [220], which led to uneven current density distribution as detailed in the previous subsection. Table 5.1 summarises the SD reduction as a function of the mechanical compression range and the relative humidity level.

Relative humidity level	50%RH		100%RH	
Mechanical compression range	First range: 0.35 → 1.55 MPa	Second range: 1.55 → 2 MPa	First range: 0.35 → 1.55 MPa	Second range: 1.55 → 2 MPa
SD reduction	43.8 %	1.9 %	35.2 %	1.1 %

Table 5.1. The reduction in the SD of the standardised current density distributions as a function of mechanical compression range at 0.6 A.cm^{-2}. Results at 50%RH and 100%RH.

The reduction in the SD of the current density distribution reaches a plateau starting from 1.55 MPa (Figure 5.8), with a reduction at 50%RH of 43.8% and 1.9% at the first and the second compression range, respectively. This reduction of the SD of the current density distribution was slightly lower at 100%RH, with a reduction of 35.2 % and 1.1% at the first and the second compression range, respectively. These results are in good agreement with the findings reported in chapter 4 using polarisation curves and EIS analyses, where the major performance enhancement of the PEFC was attained at the first compression range.

- ***Evolution of the maximum standardised current density of the current density distribution at 0.6 A.cm^{-2}***

The maximum standardised current density was measured at each of the 12 averaged current density arrays at 0.6 A.cm^{-2}. The results at 50%RH and 100%RH are shown in figure 5.9.

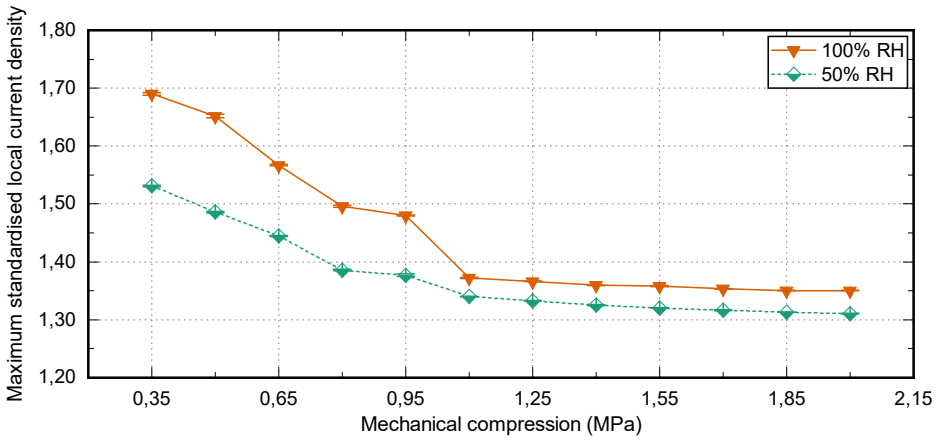

Figure 5.9. Maximum standardised local current density evolution as a function of mechanical compression at 0.6 A.cm^{-2}. Results at 50%RH and 100%RH.

It can be observed from figure 5.9 that the mechanical compression reduces the maximum standardised current density. This reduction was measured at 50%RH to be 12.5% at 1.1 MPa over a total reduction of 14.4% at 2 MPa, whereas the reduction was more important at 100%RH with 18.8% at 1.1 MPa compared to 20.1% at 2 MPa. This reduction in the maximum local current density is beneficial for the PEFC as it reduces the ohmic losses and, therefore, the possible creation of hotspots that may worsen the PEFC performance and durability [91,92,212]. This effect is further detailed in the following subsection that covers the temperature distribution analysis. Table 5.2 summarises the maximum standardised current density reduction as a function of the mechanical compression range and the relative humidity level.

Relative humidity	50%RH		100%RH	
Mechanical compression range	First range: 0.35 → 1.55 MPa	Second range: 1.55 → 2 MPa	First range: 0.35 → 1.55 MPa	Second range: 1.55 → 2 MPa
Maximum current density reduction	13.8 %	0.7 %	19.6 %	0.6 %

Table 5.2. Reduction in the maximum standardised current density as a function of mechanical compression range at 0.6 A.cm^{-2}. Results at 50%RH and 100%RH.

Similar to the results of the SD reduction as a function of mechanical compression, results reported in table 5.2 emphasise the fact that the major reduction in the maximum local current density occurs at the first compression range. These results are also in good agreement with the results reported in chapter 4 regarding the effect of mechanical compression on the global PEFC performance. It has to be mentioned that the results at 0.9 A.cm^{-2} (see Appendix F) showed a comparable trend, with the results at 0.9 A.cm^{-2} and 100%RH showing negative impacts, either in the SD or the maximum current density evolution, at the second compression range. This effect is attributed to the higher presence of liquid water at 0.9 A.cm^{-2} and 100%RH that worsens the water management capability of the PEFC leading to inhomogeneous current density distribution. Comparison between the results at 0.6 A.cm^{-2} and 0.9 A.cm^{-2} will be provided later in this section.

2.1.2 Temperature distribution analysis at 0.6 A.cm^{-2}

The total range of the local temperatures at 0.6 A.cm^{-2} was measured between 63.4°C and 70.4°C. This range was used as a fixed scale to present all the 2-D distribution maps shown in this subsection. The objective behind defining a fixed temperature scale is to compare the temperature distributions at both tested relative humidity levels of 50%RH and 100%RH.

i. Results at 50%RH

The local temperature distributions at 0.6 A.cm^{-2} and 50%RH are shown in figure 5.10. Analogously to the results of the current density distributions, figure 5.10 presents the temperature distribution at six levels of mechanical compression from 0.5 MPa to 2 MPa, with steps of 0.3 MPa. It has to be noted that the temperature measurements have 7×7 segments, meaning that the S++® temperature measurement device has one temperature measurement point per 4.6 cm^2 of the PEFC active area (considering our 225 cm^2 active area PEFC). This resolution is low compared to the current density measurement, which has 21×21 measurement

points, representing one current measurement point per 0.5 cm^2 of the active area of the PEFC. This resolution difference between the current and temperature distributions will be considered for the analysis reported hereafter.

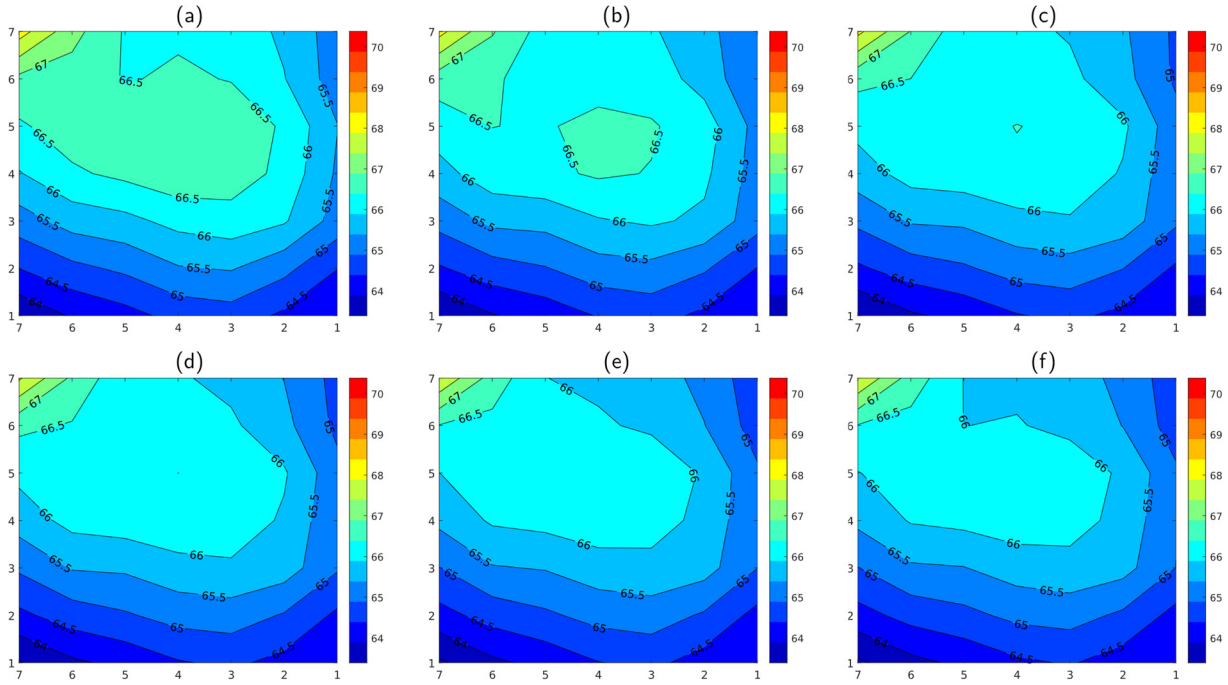

Figure 5.10. Temperature distributions 2-D maps at 0.6 $A.cm^{-2}$ and 50%RH. (a) 0.5 MPa, (b) 0.8 MPa, (c) 1.1 MPa, (d) 1.4 MPa, (e) 1.7 MPa, and (f) 2 MPa. Colour bars show the corresponding colours of each level of the local temperature.

The first observation that can be deduced from figure 5.10, with regards to the operating conditions of the PEFC, is that the measured temperature near the MEA (measured by the S++® device) is higher than the coolant setpoint temperature (i.e. 60°C). This difference is measured to be 5.6°C on average when the PEFC was operated at 0.6 $A.cm^{-2}$ and 50%RH. This temperature difference is explained by the fact that the temperature of the coolant (i.e. deionised water) was controlled by the test bench (Greenlight G7805, see chapter 3 for more details) that uses temperature sensors located outside the PEFC (i.e. located at the test bench) and regulated at 60°C. This temperature setpoint (i.e. 60°C) was kept constant during all the investigations reported in this chapter. Therefore, all the changes in the temperature distributions are considered to be mainly due to the local phenomena taking place within the PEFC.

Even though it was expected that the high current density regions will correspond to the high temperature ones, it seems that the relationship between these two parameters is not so straightforward in our case. The coolant temperature, and especially its pathway inside the PEFC assembly, play an important role as well. In fact, the bottom zones 1 and 3 of the temperature distributions depicted in figure 5.10 show low temperatures compared to the other zones of the PEFC. This low temperature is mainly attributed to the design of the cooling

circuit. In our PEFC assembly, the cooling medium enters from zones 1 and 3, of the anode and cathode sides, respectively. The cooling medium arrives at a relatively low temperature of 60 °C, which cools down the temperature at the bottom of the PEFC as shown in figure 5.10. In addition, the top left region in figure 5.10 shows a relatively high temperature. This temperature increase is explained by the fact that this region corresponds to zone 9 (see figure 5.2) from which the cooling medium at the cathode side is drained from the PEFC. Indeed, the coolant medium at the cathode side is injected from the bottom right region of the PEFC, and it is continuously heated by the heat generated by both the electrochemical reactions and the Joule heating (also referred to as resistive or ohmic heating). Therefore, the cooling medium temperature increases along the direction of the cooling flow, with the maximum temperature measured at the coolant outlet. The temperature difference between the inlet and outlet was measured to be 4.6 °C. Similar observations were also reported by Peng et al. [35].

Analogously to the current density distributions, figure 5.10 shows that mechanical compression homogenises the temperature distribution. This effect is mainly attributed to the reduction in the maximum current density, which decreases the ohmic losses that in turn reduces the temperature through lowering the Joule heating. Moreover, the decrease in the temperature shown in figure 5.10 may also be caused by the reduction in the thermal resistance of the GDL with increasing mechanical compression. As a matter of fact, one of the main functions of the GDL is to conduct the heat generated from the MEA to the cooling plates (via FFPs) that have means for heat removal. Therefore, reducing the thermal resistance of the GDL leads to a better cooling of the MEA and, in turn, to a reduced temperature. This effect was emphasised by Khandelwal and Mench in [145]. These authors provided a correlation between the mechanical compression and the thermal contact resistance of the GDL. It was shown in [145] that the thermal contact resistance between an aluminium bronze material and the GDL was reduced from 6.7×10^{-4} to 2.0×10^{-4} m^2KW^{-1} (i.e. 70.1% reduction) as the mechanical compression was increased from 0.4 MPa to 2.2 MPa.

It can be observed from figure 5.10 that the major evolution of the temperature distribution occurs at mechanical compression up to 1.4 MPa, which is in good agreement with the results of the standardised current density distribution. In order to statistically analyse the temperature distributions depicted in figure 5.10, the histograms of the temperature at three levels of mechanical compression (namely 0.5 MPa, 1.4 MPa, and 2 MPa) are shown in figure 5.11.

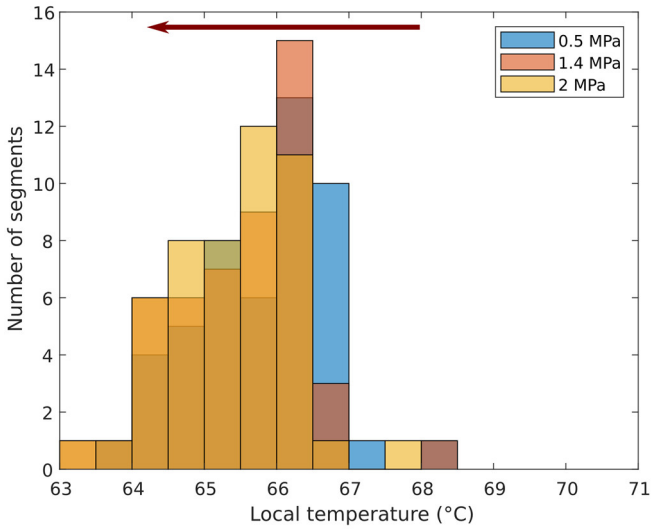

Figure 5.11. Temperature distribution histograms at three levels of mechanical compression: 0.5 MPa, 1.4 MPa, and 2 MPa. Histograms obtained at 0.6 A.cm^{-2} and 50 %RH. The red arrow represents the ideal effect of mechanical compression on the temperature distribution.

As mechanical compression increases, the temperature distribution histograms shift to the left, thus to the low temperature range as shown in figure 5.11. This local temperature reduction is most likely caused by the decrease in the maximum current density, and therefore by the reduction in the heat generated by the electrochemical reaction as well as the Joule heating. It can be observed that the number of segments at a temperature of 65.5°C was reduced by 70% at 1.4 MPa over a total reduction of 90% at 2 MPa. This effect is beneficial for the PEFC as it reduces the possible creation of hotspots that may worsen the performance and the durability of the PEFC [91,92,212]. This observation is in good agreement with the study of Hekenjos et al [219]. These authors reported that high temperature regions correspond to high local current densities' regions. This effect was attributed to the increase in the heat of the electrochemical reactions that occur at the CLs [219]. This effect was also observed at all the tested operating conditions and will be detailed in the following subsection.

ii. Results at 100%RH

Figure 5.12 shows the temperature distribution at 0.6 A.cm^{-2} and 100%RH. The 2-D temperature distribution maps are presented using the same temperature scale as the one used at 50%RH, i.e. from 63.4°C to 70.4°C.

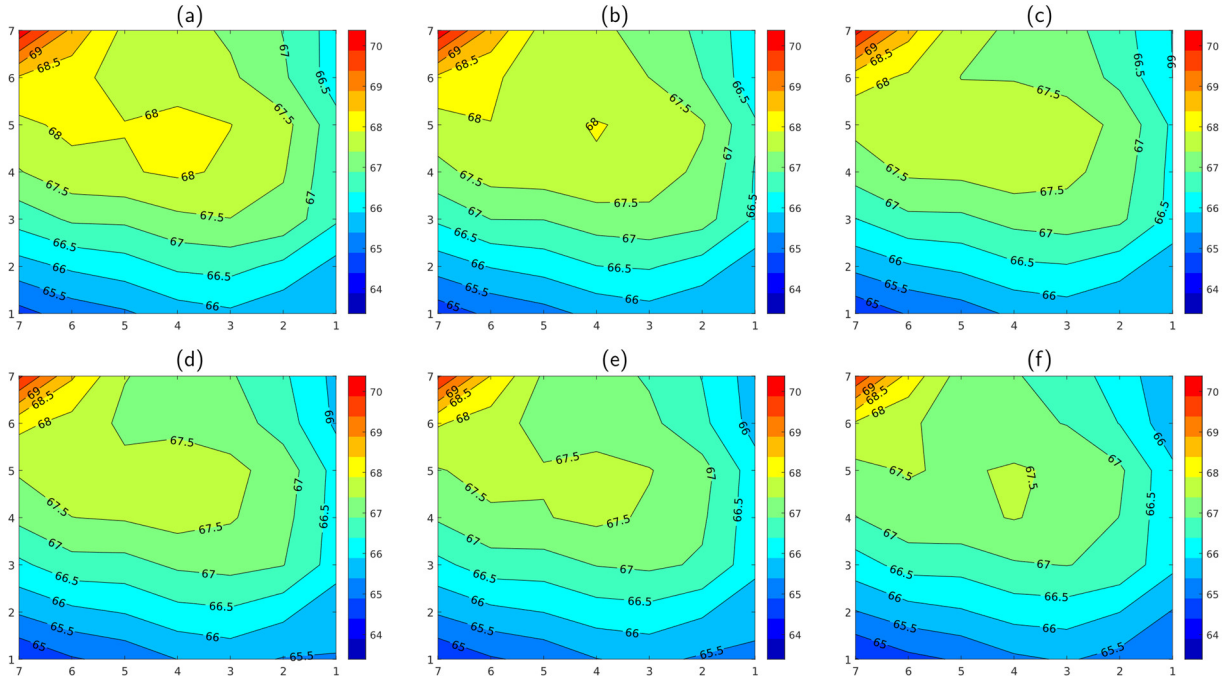

Figure 5.12. Temperature distributions 2-D maps at 0.6 A.cm^{-2} and 100%RH. (a) 0.5 MPa, (b) 0.8 MPa, (c) 1.1 MPa, (d) 1.4 MPa, (e) 1.7 MPa, and (f) 2 MPa. Colour bars show the corresponding colours of each level of the local temperature.

It can be observed from figure 5.12 that the bottom zones 1 and 3 show relatively low temperature compared to the rest of the zones. Similar to the explanations given for the results at 50%RH, this observation is attributed to the fact that the coolant medium enters to the PEFC through the zones 1 and 3 at the anode and cathode side, respectively. Afterwards, the coolant medium is continuously heated, by the heat generated from the electrochemical reactions and the Joule heating, as it flows through the coolant output. Thus, the maximum temperature is measured at the cathode coolant outlet as shown in the 7th zone of figure 5.12. The temperature difference between the coolant inlet and outlet was measured to be 5.5 °C.

The central region (zones 4, 5, and 6) of figure 5.12 shows relatively high local temperatures. This effect is most likely due to the higher local current densities flowing through this region, which leads to a higher local temperature as a result of the heat generated by the electrochemical reactions [219] as well as the Joule heating. Moreover, through comparing the temperature distributions at 50%RH and 100%RH, it can be observed that the PEFC is further heated at 100%RH with the maximum temperature difference between measurements at 100%RH and 50%RH of 1.3 °C on average. Here again, this temperature difference is due to the higher local current densities at 100%RH compared to 50%RH as previously shown in the current density distribution maps.

Regarding the mechanical compression effects, it can be seen from figure 5.12 that the homogenisation of the temperature distribution improves as the mechanical compression

increases. Similar to the results at 50%RH, the high temperature regions, located at the centre of the temperature distribution maps (zones 4, 5, and 6), reduce in size with increasing mechanical compression. This decrease in the high temperature regions is attributed to the decrease in the high current density regions with increasing mechanical compression as previously witnessed in the current density distribution maps. Figure 5.13 depicts the histograms of temperature distribution at three levels of mechanical compression.

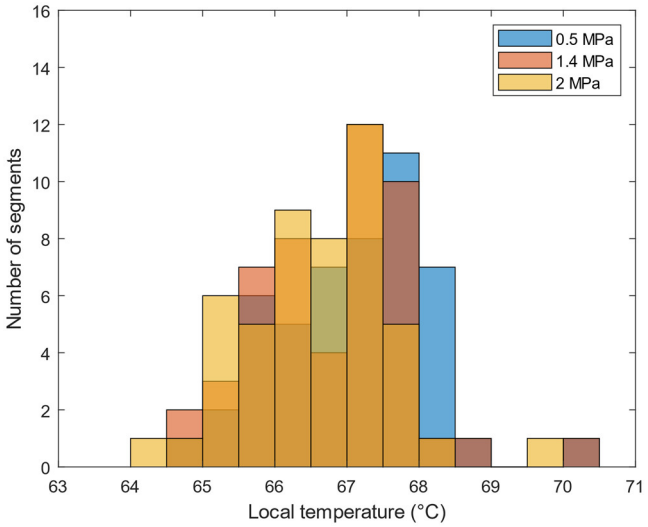

Figure 5.13. Temperature distribution histograms at three levels of mechanical compression: 0.5 MPa, 1.4 MPa, and 2 MPa. Histograms obtained at 0.6 A.cm^{-2} and 100 %RH.

Similar to the results at 50%RH, figure 5.13 shows that mechanical compression shifts the temperature histograms to the left (i.e. to the lower temperature range), which is beneficial for the PEFC as it reduces the creation of hotspots that have detrimental impacts on the PEFC performance and durability [91,92,212]. It can be seen that the number of segments at a temperature of 68°C was reduced by 85.7% starting from mechanical compression of 1.4 MPa. Through comparing the temperature histograms shwon in figure 5.11 and figure 1.13, it can be observed that operating the PEFC at 100%RH increases the PEFC maximum local temperature by 2.1°C on average. This local temperature increase is mainly attributed to the heating effect due to the high local current densities when the PEFC is operating at 100%RH. The following subsection aims to provide further statistical analysis of the temperature distributions at 0.6 A.cm^{-2} via comparing the results obtained at 50%RH and 100%RH.

iii. Statistical analysis of the temperature distributions at 0.6 A.cm^{-2}

This subsection provides a statistical analysis of the temperature distributions at 0.6 A.cm^{-2}. This analysis aims to present a thorough comparison between the results at 50%RH and 100%RH through studying the evolutions of the standard deviation and the maximum values of the temperature distributions as a function of mechanical compression. The results given in this subsection include the entire compression range, from 0.35 MPa to 2 MPa with 0.15 MPa steps.

- Evolution of the standard deviation of the local temperature distributions at 0.6 A.cm^{-2}

The evolution of the standard deviation of the temperature distribution as a function of mechanical compression is shown in Figure 5.14.

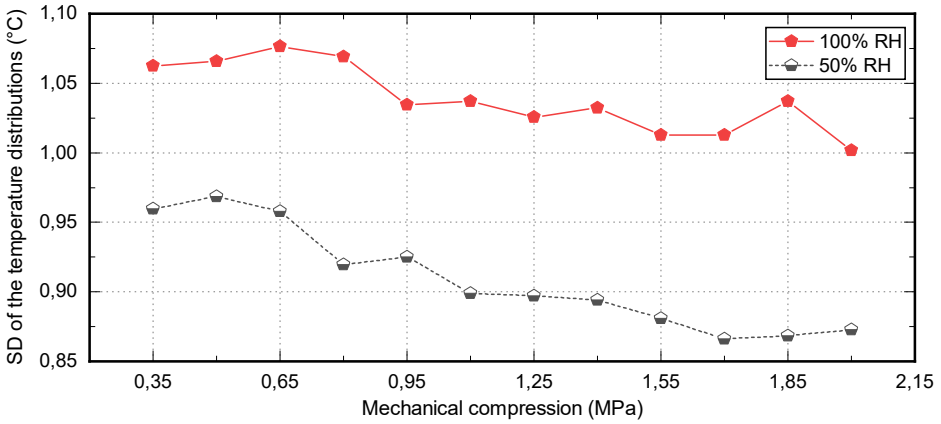

Figure 5.14. SD evolution of the temperature distribution as a function of mechanical compression at 0.6 A.cm^{-2}. Results at 50%RH and 100%RH.

Figure 5.14 shows that the SD of the temperature distributions is 12.5% higher (on average) at 100%RH compared to 50%RH. This difference in the SD of the temperature distributions is in good agreement with the difference in the SD of the standardised current density distribution between 100%RH and 50%RH, which was measured to be 13.5% on average. Thus, the SD difference of the temperature distributions is attributed to the higher local current densities at 100%RH compared to 50%RH caused by diffusion issues as previously evoked in this chapter.

It can be observed from figure 5.14 that mechanical compression improves the homogenisation of the temperature distribution at both relative humidity levels of 50%RH and 100%RH. Table 5.3 lists the percentage of the reduction in the SD of the temperature distribution as a function of the mechanical compression range.

Relative humidity	50%RH		100%RH	
Mechanical compression range	First range: 0.35 → 1.55 MPa	Second range: 1.55 → 2 MPa	First range: 0.35 → 1.55 MPa	Second range: 1.55 → 2 MPa
SD reduction	9 %	0.9 %	4.7 %	1.1 %

Table 5.3. Reduction of the SD of the temperature distributions as a function of mechanical compression range at 0.6 A.cm^{-2}. Results at 50%RH and 100%RH.

The SD reduction results shown in table 5.3 confirms that the major temperature homogenisation effects occur at the first compression range, with relatively higher reduction at 50%RH compared to 100%RH, which is most likely due to the current density inhomogeneity at 100%RH compared to 50%RH. These results are in good agreement with the results of the SD evolution of the standardised current density distribution as a function of mechanical compression (Cf. table 5.1).

- Evolution of the maximum local temperature at 0.6 A.cm^{-2}

Figure 5.15 shows the evolution of the maximum local temperature as a function of mechanical compression at both relative humidity levels of 50%RH and 100%RH.

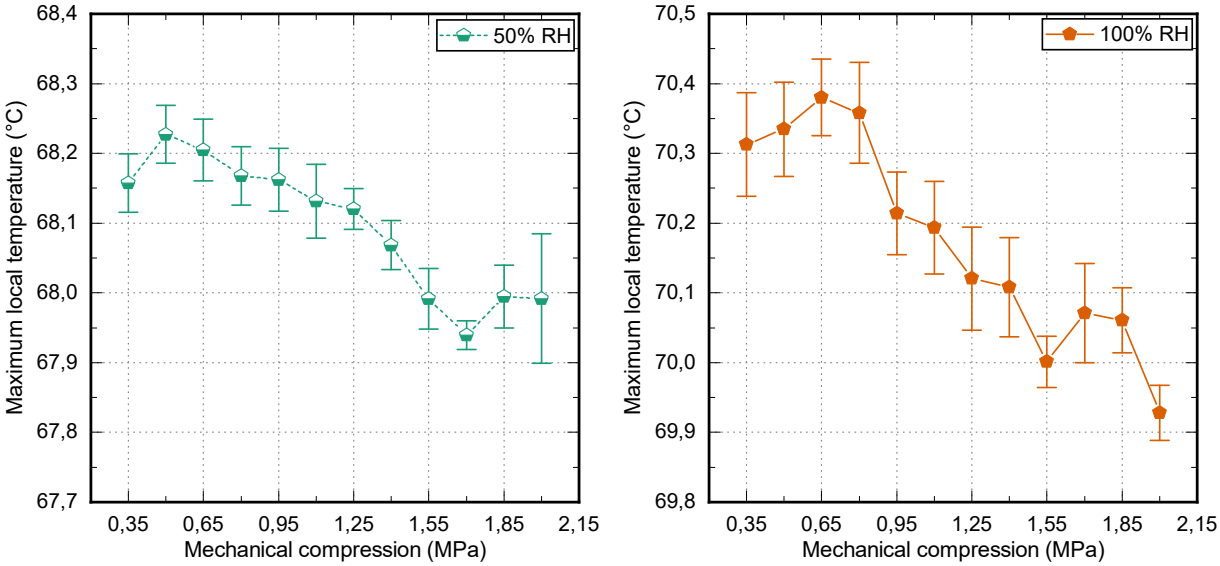

Figure 5.15. Maximum local temperature evolution of the temperature distributions as a function of mechanical compression at 0.6 A.cm^{-2}. Results at 50%RH (left) and 100%RH (right).

It can be observed from figure 5.15 that the mechanical compression reduces the maximum local temperature at both 50%RH and 100%RH relative humidity levels. This effect remains low (i.e. 0.7°C range in figure 5.15) and it is due to the result of two phenomena: the first one is the reduction in the maximal current density and the second one is the enhancement of the thermal conductivity of the GDL as previously explained in this chapter. The maximum temperature at 100%RH is higher than the one at 50%RH. This difference was measured to be 2.1 °C on average and it is explained by the local higher current densities at 100%RH compared to 50%RH as evoked earlier in this section. Table 5.4 lists the percentage of the reduction in the maximum local temperature of the temperature distributions as a function of the mechanical compression range.

Relative humidity	50%RH		100%RH	
Mechanical compression range	First range: 0.35 → 1.55 MPa	Second range: 1.55 → 2 MPa	First range: 0.35 → 1.55 MPa	Second range: 1.55 → 2 MPa
Local max reduction	0.24 %	0 %	0.44 %	0.1 %

Table 5.4. Reduction in the maximum temperature as a function of mechanical compression ranges at 0.6 A.cm^{-2}. Results at 50%RH and 100%RH.

The results reported in table 5.4 show that the effect of mechanical compression on the maximum local temperature is relatively low compared to the other statistical results reported in this section. However, it still represents a desirable effect as it reduces the possible creation of hotspots that have detrimental impacts on the PEFC performance and durability [91,92,212]. Moreover, it is important to note that the major reduction in the maximum local temperature occurs at the first compression range, which is in line with the results regarding the maximum standardised current density evolution as a function of mechanical compression range (Cf. table 5.2). These results, therefore, emphasise the correlations that exist between the current and the temperature distributions.

As it was reported at the beginning of this section, the study of the mechanical compression effects on the current density and temperature distributions was also conducted on the PEFC operating at 0.9 A.cm^{-2}. This study was carried out using the same spatial and statistical analyses. In order to avoid redundancy of the results and their related discussions, the detailed results and figures obtained at 0.9 A.cm^{-2} are reported in Appendix F. Nonetheless, since the objective of this chapter is to investigate the correlations between the current/temperature distributions and the PEFC performance assessed in-situ in chapter 4, the comparison between the results at 0.6 A.cm^{-2} and 0.9 A.cm^{-2} is addressed in the following section.

2.2 Comparison between current and temperature distributions at 0.6 A.cm^{-2} and at 0.9 A.cm^{-2}

This section provides a thorough comparison of the results regarding the distributions of the current and temperature at 0.6 A.cm^{-2} and 0.9 A.cm^{-2}. This comparison is conducted following the same approach reported in chapter 4, i.e. based on the two mechanical compression ranges. For recall, the first compression range is from 0.35 MPa to 1.55 MPa, in which the major PEFC performance enhancement was observed using polarisation curves and EIS analysis techniques, whereas the second compression range is from 1.55 MPa to 2 MPa where only minor PEFC performance enhancement (or even performance worsening) was witnessed.

2.2.1 Mechanical compression impacts on the current density distributions

The reduction (in percentage) of the maximum local value and the SD of the standardised current density distributions, for the various mechanical compression ranges, is shown in figure 5.16.

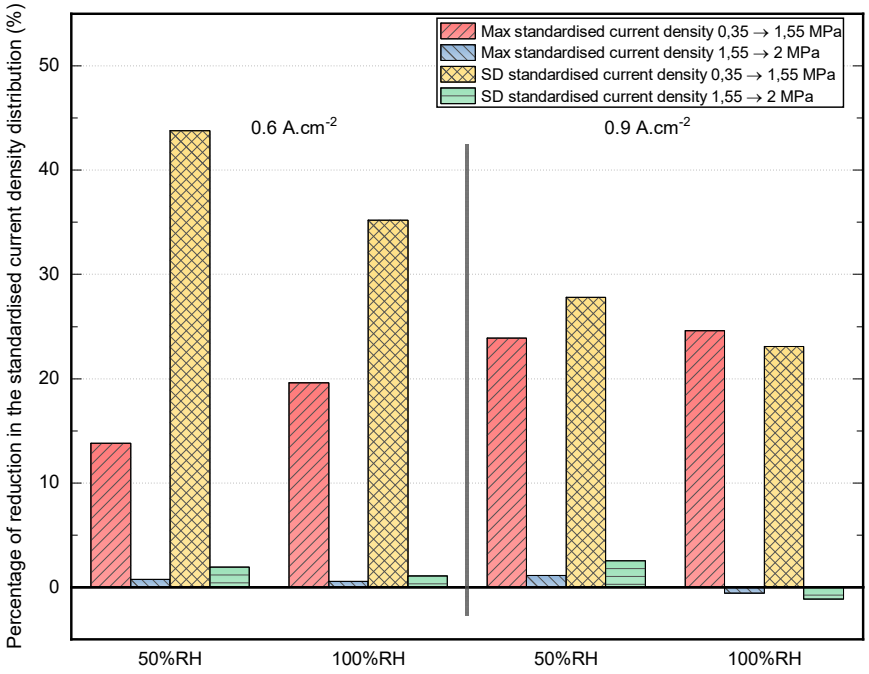

Figure 5.16. Percentage of the reduction in the standardised current density distributions for the mechanical compression ranges. Results at 0.6 A.cm^{-2} (left) and at 0.9 A.cm^{-2} (right).

One important observation that can be made from figure 5.16 is that the major reduction, either in the maximum standardised current density or its standard deviation, occurs at the first compression range. The evolution at the second compression range is far lower (or even in the opposite direction at 0.9 A.cm^{-2} and 100%RH) than the one at the first compression range. This observation is in good agreement with the results reported in chapter 4 regarding the

enhancement of the PEFC performance at the first compression range (see figure 4.14 – chapter 4).

Concerning the SD evolution as a function of the mechanical compression range, it can be observed from figure 5.16 that the SD reduction, at the first compression range, decreases with increasing both the current density and the relative humidity. This effect is mainly attributed to the higher presence of water that leads to GDL pores and FFPs channels blockage and, in turn, tends to cause reactants starvation. These effects cause an uneven current generation that, in turn, increases the SD of the current density distributions. Moreover, when the PEFC has the highest amount of water (i.e. at 0.9 $A.cm^{-2}$ and 100%RH) the mechanical compression increases the SD at the second compression range, showing that mechanical compression starts causing water management issues leading to less homogeneous current density distribution. Therefore, the mechanical compression effect on the homogenisation of the current density distribution is optimal when the PEFC is operating with a relatively low amount of water, otherwise, excessive mechanical compression could lead to water management issues.

Figure 5.16 also shows that the reduction in the maximum local current density rises with increasing the relative humidity and the current density levels. In fact, as these two factors increase, the amount of water within the PEFC becomes important. This high presence of water causes inhomogeneous current density distribution, which leads to high current densities flowing through specific regions of the GDL. Applying mechanical compression, in its first range, reduces the contact and bulk resistance of the GDL. This effect allows the current to be distributed more evenly, leading to a reduction in the maximum local current density. We can assume that this reduction in the maximum local current density has a beneficial impact on the decrease in the ohmic losses [83]. These results are, therefore, in reasonable agreement with the finding of chapter 4 (see figure 4.14 – chapter 4) regarding the higher increase in the PEFC voltage with increasing mechanical compression at the first compression range at 0.9 $A.cm^{-2}$ compared to 0.6 $A.cm^{-2}$. Moreover, it should be noted that this decrease in the maximum current density has also an effect on the decrease in the maximum local temperature and this effect will be addressed in the following subsection.

2.2.2 Mechanical compression impacts on the temperature distributions

The reduction (in percentage) of the maximum local value and the SD of the temperature distributions, as a function of the mechanical compression range, is depicted in figure 5.17.

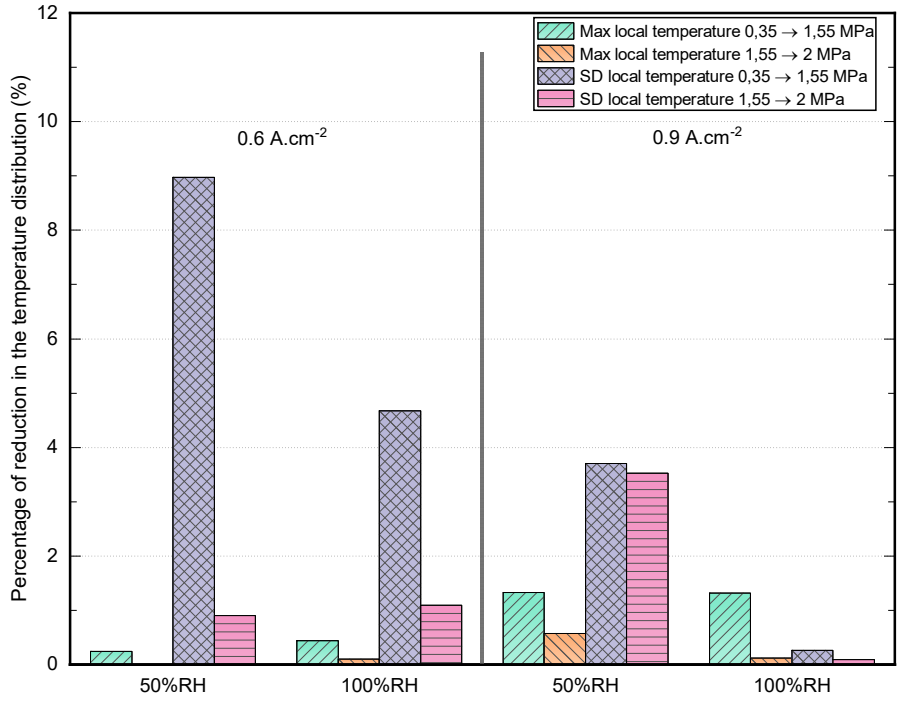

Figure 5.17. Percentage of reduction in the temperature distributions as a function of the various mechanical compression ranges. Results at 0.6 A.cm^{-2} (left) and at 0.9 A.cm^{-2} (right).

It can be observed from figure 5.17 that the SD of the temperature distribution was reduced during the first compression range at 0.6 A.cm^{-2}, which is in good agreement with the results of the reduction in the SD of current density distribution at the same current density. However, at 0.9 A.cm^{-2}, the SD evolution of the temperature distribution as a function of mechanical compression shows no discernible trend at both relative humidity levels of 50%RH and 100%RH. This is mainly due to a number of competing effects that became important at high current densities (e.g. heat of the electrochemical reactions, Joule heating [143], diffusion issues). These effects led to an uneven temperature generation/distribution at 0.9 A.cm^{-2} where mechanical compression has only an effect on the reduction in the maximum local temperature.

Even though the reduction in the temperature distribution values shown in figure 5.17 remains lower compared to the results depicted in figure 5.16, correlation with the results of the current density distributions can be expressed, namely with regards to the maximum temperature reduction during the first mechanical compression range. In this sense, it can be observed from figure 5.17 that the reduction in the maximum temperature, at the first compression range, rises with increasing the relative humidity and the current density levels. These effects are in good agreement with the results regarding the current density distributions reported in figure 5.16. It can be concluded, therefore, that the reduction in the high current density regions corresponds to the reduction in the high temperature regions at all tested operating conditions. This finding confirms the major effect of mechanical compression on the reduction of the hotspots that have detrimental impacts on the PEFC [91,92,212]. These results also show that some arduous development in the performance and durability of fuel cells could be lost due to

inhomogeneous current and temperature distributions. Therefore, the optimisation of the mechanical compression needs to be taken into consideration by manufacturers in order to develop PEFCs with enhanced performance and durability.

3 Analysis of the pressure distribution

The previous findings of this chapter emphasised the fact that mechanical compression, from 0.35 MPa to 1.55 MPa, homogenises the distributions of both the current density and the temperature. This effect has beneficial impacts on the PEFC performance, namely through the reduction of the ohmic losses along with the diminution of the possible creation of hotspots. These effects were assumed to be due to the enhancement of the pressure distribution with increasing mechanical compression. This section aims, therefore, to provide a thorough analysis of the mechanical pressure distribution as a function of mechanical compression. To do so, pressure sensitive films are employed in this section. Henceforth, and in order to avoid any ambiguity all along the rest of this chapter, the mechanical pressure measured by the pressure sensitive films will be referred to as "pressure", whereas the assembly pressure will be referred to as "mechanical compression".

3.1 Presentation of the used pressure sensitive films

Despite the fact that the investigations on the pressure distribution and magnitude using pressure sensitive films (also called pressure indicating films) are typically carried out on off-line PEFCs [57,58,96,99,221], the use of this technique continues to provide valuable analyses regarding the internal pressure distribution across the PEFC components. The pressure sensitive films used in this study were provided by Fujifilm (Prescale® [209]) and they have thicknesses lower than 200 µm for all compression ranges [209]. More importantly, these films were reported to have a negligible effect on the internal pressure distribution of the PEFC [58]. Thus far, their use to investigate pressure distribution across the PEFC components remains suitable and will be, therefore, employed in this study.

In this section, super low pressure Prescale® films are used (LLW, optimal measurements range from 0.5 MPa to 2.5 MPa [209]). This is a two-films type (films A and C) as shown in figure 5.18. The pressure distribution and magnitude measurements are based on the principle that as the mechanical compression is applied, the microcapsules contained in the film A are broken and a colour-forming material is released and absorbed by the film C. The obtained colour intensity indicates the value of the applied compression and it becomes possible to assess the magnitude and the distribution of the pressure by analysing the intensity of the colour obtained: the higher the pressure, the more intense the colour. More specifications about Prescale® films can be found in Appendix F.

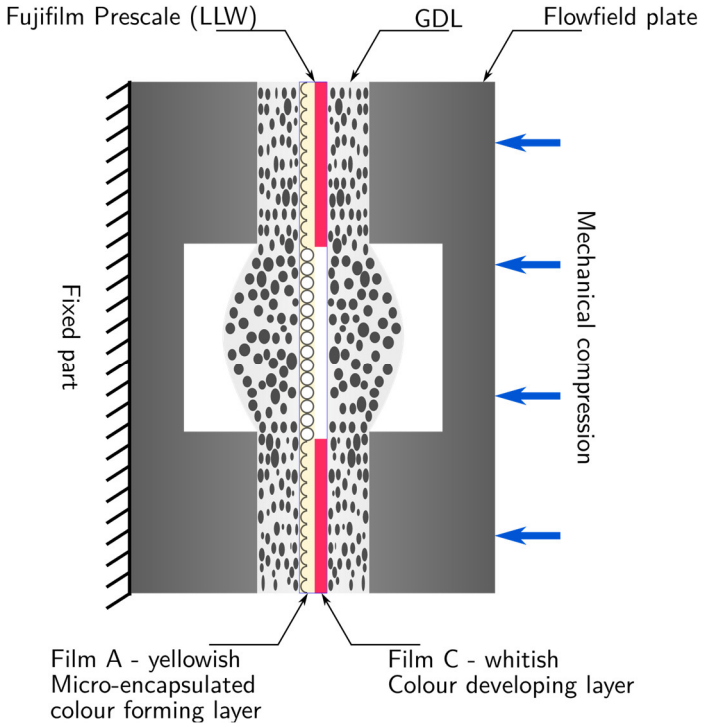

Figure 5.18. Presentation of the location and the measurement principle of the Prescale® LLW. The blue arrows present the mechanical compression application direction.

The pressure distribution investigations were conducted using the same PEFC components employed in the previous investigations (see chapter 5). The Prescale® film was inserted in the place of the MEA as shown in figure 5.18. Similar to the current density and temperature distributions analyses, six levels of mechanical compression were investigated here, ranging from 0.5 MPa to 2 MPa with 0.3 MPa steps. All the tests were conducted within the recommended operating conditions provided by Fujifilm [209], namely at an ambient temperature of 21°C and relative humidity of 54%RH (see Appendix F). The standardised method of applying the mechanical compression preconised by Fujifilm was employed in our investigations. After assembling the qCf with the Prescale® LLW, the mechanical compression was increased during two minutes until reaching the desired compression levels; this latter was maintained for two other minutes. Afterwards, the film A was digitalised and analysed. The investigations reported in this section include first a spatial analysis of the pressure distributions using Prescale® Fujifilm LLW, followed by a quantitative study of the pressure distribution using an image processing protocol. The correlations between the results of the pressure distribution and the current/ temperature distributions are given throughout this section.

3.2 Spatial analysis of the pressure distributions

This subsection aims to provide a spatial analysis of the pressure distribution within the PEFC components and also to find correlations between the current / temperature distributions and

the pressure distribution. The analysis of the pressure sensitive films will be conducted on the same zones depicted in figure 5.2. The digitalised images of the pressure sensitive films are shown in figure 5.19.

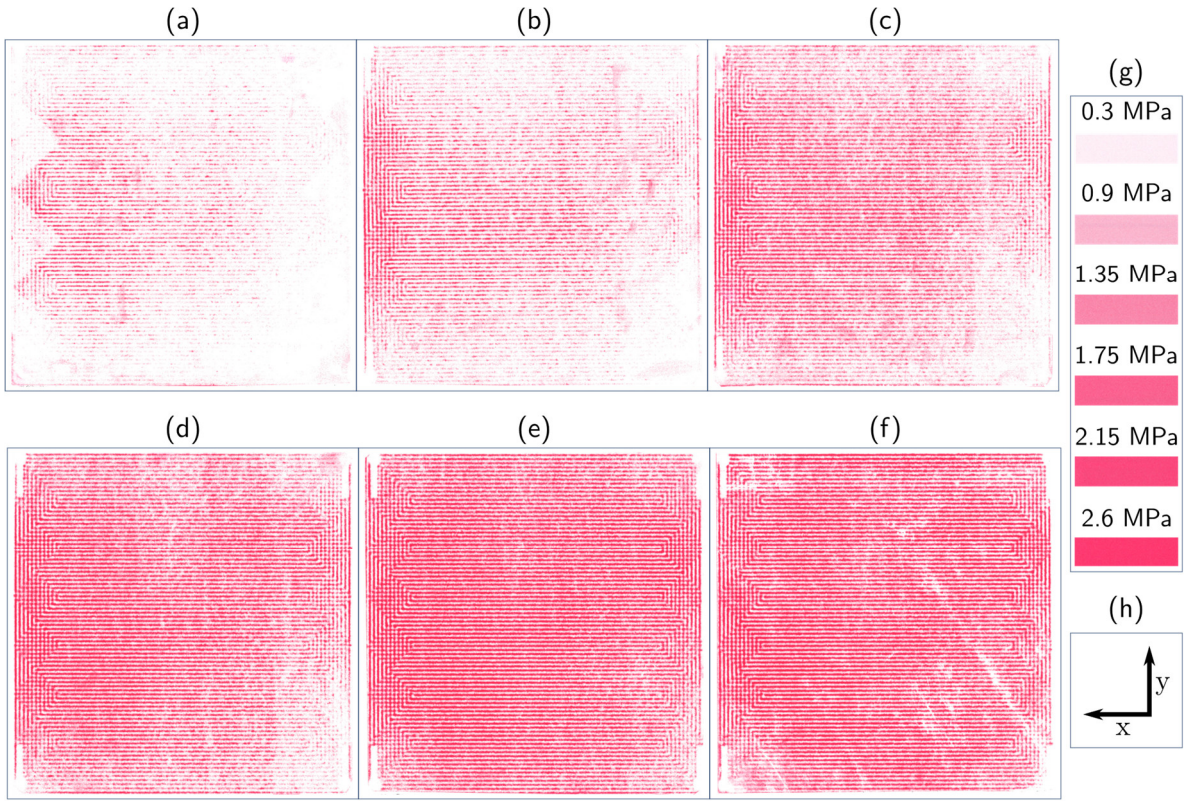

Figure 5.19. Pressure distribution images using Prescale® LLW. (a) 0.5 MPa, (b) 0.8 MPa, (c) 1.1 MPa, (d) 1.4 MPa, (e) 1.7 MPa, and (f) 2 MPa. Colour references shown in (g) are provided by Fujifilm and depict the corresponding colours of each level pressure magnitude. (h) Coordinate system as shown in figure 5.2.

The pressure distribution images shown in figure 5.19 confirm the fact that mechanical compression homogenises the pressure distribution within the PEFC components. In fact, at low mechanical compression (up to 1.1 MPa), the pressure distribution is obviously inhomogeneous and present important gradients between central, top, and bottom regions. For instance, at 0.5 MPa, the imprint marks of the FFPs ribs are sparse and light, and they are mostly concentrated in the 5th and 6th zones, meaning that the pressure magnitude is low and inhomogeneous in general. This pressure inhomogeneity increases the electronic resistance, providing less preferential pathways for electrons to flow through and, therefore, increasing the local current density at the nearby zones (5th and 6th zones). With gradually increasing the mechanical compression, the top and bottom regions get larger pressure. As a result, the pressure distribution gets more uniform (i.e. starting from 1.4 MPa). In this sense, the results

shown in figure 5.19 show that there is a clear correlation between the pressure distribution images and current/temperature distributions. For instance, the four corners show clearly the imprint of the reactants' inlet/outlet orifices with no pressure magnitude. This low pressure magnitude explains the low, or even zero, current flowing through these corners. Moreover, it can be observed that at low mechanical compression, especially at 0.5 MPa and 0.9 MPa, the top and bottom regions present low pressure magnitude compared to the other regions, which is in good agreement with the low current densities flowing through these regions, especially the 3rd zone that presents the lowest pressure magnitude even at relatively high compression levels (up to 1.4 MPa). Thus, this effect explains the lowest current density flowing through the 3rd zone as shown in figure 5.3 and figure 5.6.

With increasing mechanical compression, the colour intensity of the Prescale® films increases showing an improvement of the pressure magnitude and distribution. As the PEFC was operated in galvanostatic mode, the total current must, ideally, flow uniformly through the PEFC active area. However, uneven pressure distribution, as shown at mechanical compressions up to 1.4 MPa, favours more current to flow through the regions with lower electronic resistance and therefore higher pressure magnitudes, whereas very low current flows through the regions with low pressure. This pressure distribution inhomogeneity was reported to increase the ohmic losses of the PEFC [83], and therefore causes a reduced global PEFC performance. These observations are in good agreement with the results reported in chapter 4, where the major PEFC performance enhancement with mechanical compression occurred at first mechanical compression range up to 1.55 MPa, and which was mainly attributed to the reduction in the ohmic resistance. To confirm these observations, we aim in the following subsection to quantify the results of the pressure distribution images shown in figure 5.19.

3.3 Quantitative analysis of the pressure distribution images

In order to quantitively analysis the Prescale® images reported in figure 5.19, an image processing protocol was developed and used in this subsection. This protocol aims to extract the contribution of each one of the pressure magnitudes shown in figure 5.19 (g) from the Prescale® images shown in figure 5.19 (a) to (f). This protocol is briefly described in figure 5.20 for the extraction of the 0.9 MPa pressure contribution of the Prescale® image at a mechanical compression of 1.1 MPa. As a reminder, the mechanical pressure measured by the pressure sensitive films is referred to as "pressure", whereas the assembly pressure is referred to as "mechanical compression".

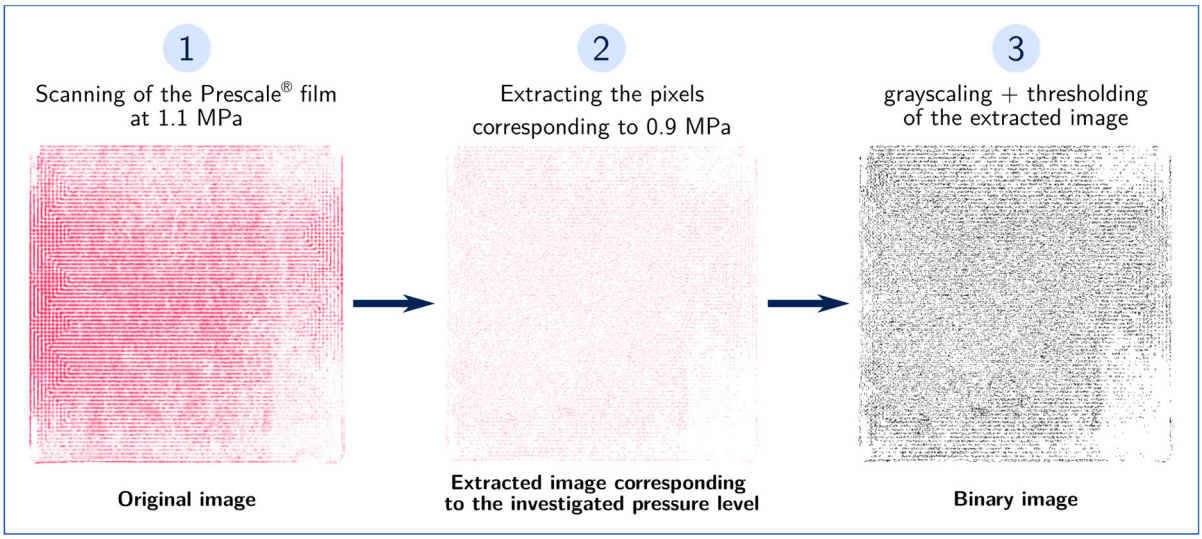

Figure 5.20. Image processing protocol used for the analysis of the Prescale® LLW images. Example for extraction of the 0.9 MPa pressure contribution in the 1.1 MPa mechanical compression image.

The image processing protocol depicted in figure 5.20 was carried out per each level of mechanical compression shown in figure 5.19. The image processing protocol was conducted on MATLAB® using a developed code employing an image processing toolbox [222]. This protocol was carried out as follows:

- *Calculation of the average RGB triplets corresponding to the pressure magnitudes*: the average RGB triplets (i.e. red, green, blue) were first calculated from the colour samples given by Fujifilm and showed in figure 5.19 (g).
- *Extraction of the pixels corresponding to the pressure magnitude*: all the pixels corresponding to the average RGB triplets of the investigated pressure magnitude level are extracted from the Prescale® images and a new image is constructed. This operation was repeated at each level of pressure given in figure 5.19 (g) and per each mechanical compression figure 5.19 (a) to (f). The resolution of the image was identical in all the mechanical compression levels (560×560 pixels).
- *Grayscaling and thresholding*: each of the extracted images is grayscaled and binarised. Afterwards, the sum of the black pixels that correspond to the investigated pressure magnitude is calculated. Then, the percentage of this pixels' sum out of the total image pixels (i.e. including the white ones) is calculated. It has to be noted that the pressure magnitudes lower than 0.3 MPa and higher than 2.6 MPa (i.e. that are not included in figure 5.19 (g)) are not considered in this study, as they cannot be measured by the Prescale® LLW film. The results obtained from this image processing protocol are shown in figure 5.21.

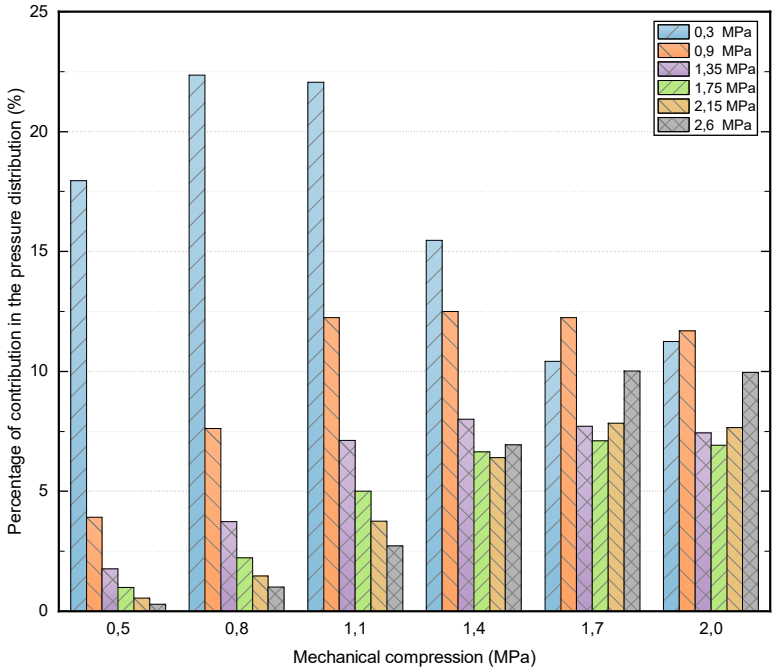

Figure 5.21. Percentage of the contributions of the pressure magnitudes as a function of the mechanical compression level.

A relevant observation that can be deduced from figure 5.21 is that both excessive and insufficient compression magnitude regions exist virtually at all the compression levels, but with different percentages of contribution. It is also shown that the results at 1.7 MPa and 2 MPa are virtually the same, meaning that the pressure distribution has reached its optimal homogenisation within this compression range. These results are in line with the previously reported investigations regarding the current and temperature distributions, emphasising the fact that the major homogenisation effect occurs at the first compression range up to 1.55 MPa. Figure 5.21 also shows that mechanical compression levels below 1.1 MPa present important discrepancies between the measured pressure magnitudes. In order to analyse this pressure discrepancy, figure 5.22 shows the percentage of the combined contributions of all the pressure magnitudes, shown figure 5.19 (g), as a function of mechanical compression.

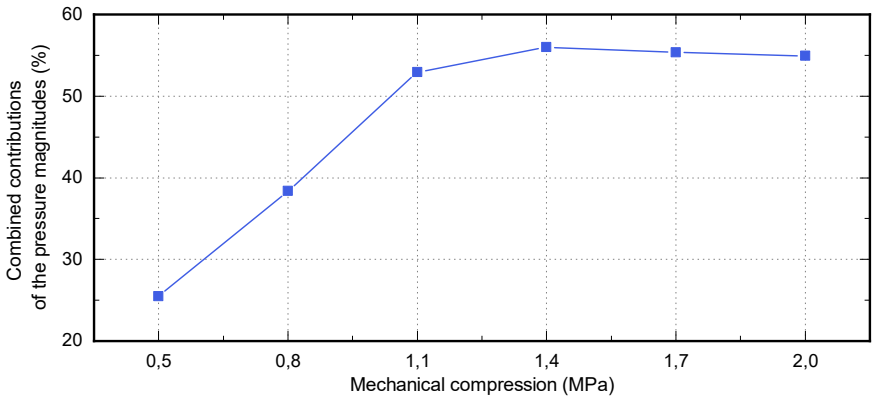

Figure 5.22. Percentage of the combined contributions of all the pressure magnitudes, shown figure 5.19 (g), as a function of mechanical compression.

Through comparing figure 5.22 and figure 5.21, it can be observed that at low mechanical compression levels, i.e. up to 1.1 MPa, the pressure magnitude profile (figure 5.21) shows a large inhomogeneity. For instance, the combined pressure magnitudes at 0.5 MPa represent 25.5% of the total image pixels (figure 5.22). Moreover, the 0.3 MPa pressure magnitude presents 70.5% of the total extracted pixels, whereas the combined 1.75 MPa, 2.15 MPa, and 2.6 MPa pressure magnitudes represent only 7.2%. These results show that at 0.5 MPa the pressure distribution within the PEFC is uneven in general. Concerning the correlations with the previously reported studies, this pressure inhomogeneity shows that the current will preferentially flow through the regions with high pressure magnitude (i.e. low electronic resistance), whereas very low, if no, current will flow through the regions with low pressure magnitude (i.e. high electronic resistance). This effect of pressure inhomogeneity increases the ohmic resistance of the GDL [191] due to the large pressure discrepancy, leading at worsening of the PEFC performance. Similar pressure discrepancies can be observed up to mechanical compression levels below 1.1 MPa. However, starting from 1.4 MPa, figure 5.20 and figure 5.21 show that the pressure magnitudes reach their maximal homogeneity. This effect shows that the impacts of mechanical compression on the reduction of the ohmic resistance reached its plateau, which is in good agreement with the results reported in chapter 4. This quantitative analysis led us, therefore, to confirm the correlation that exists between the mechanical compression, PEFC global performance and the local phenomena taking place within the operating PEFC.

4 Conclusion

This chapter confirms the correlations that exist between the current, temperature, and pressure distributions and the electrochemical performance of the PEFC. The results of this chapter emphasise the fact that that mechanical compression homogenises the current density distribution which, in turn, homogenises the temperature distribution. This latter effect is beneficial as it reduces the development of hotspots that have detrimental impacts on the

performance and durability of the PEFC. This homogenisation effect is mainly due to the better pressure distribution obtained at the first mechanical compression range (i.e. from 0.35 MPa to 1.55 MPa). Furthermore, this homogenisation was also proven to have positive impacts on the PEFC performance due to the reduction of the ohmic resistance. The observations reported in this chapter are in good agreement with the results regarding the global performance enhancement of the PEFC reported in chapter 4 of this thesis.

Investigation of the effect of mechanical compression on the local phenomena is challenging, especially as it combines different phenomena taking place within the PEFC. The results obtained in this chapter will contribute to the knowledge and the understanding of the evolution of the local phenomena occurring within the PEFC when it is subjected to mechanical stresses. This comprehensive study, which includes in-situ characterisation coupled with ex-situ correlations, will assist the manufacturers in developing PEFCs with enhanced performance and durability. Finally, future investigations could be carried on the analysis of the results reported in this chapter using the design of experiment (DOE) approach as done in [223,224]. In fact, we analysed in this chapter the impacts of three factors, i.e. mechanical compression (12 levels from 0.35 MPa to 2 MPa) relative humidity (two levels 50%RH and 100%RH), and current density (two levels 0.6 $A.cm^{-2}$ and 0.9 $A.cm^{-2}$) on three responses: the distributions of the current density, temperature, and pressure. Following a DOE approach, further statistical models could be obtained and the interactions between these three factors analysed in this chapter could be quantified.

Conclusion and future work

1 Conclusion

Fuel cells have gained substantial development momentum recently and could be put on their path to fulfil their role as clean energy conversion devices. Up to now, and among all the fuel cell technologies, the Polymer Electrolyte Fuel Cells (PEFCs) technology was shown to be the most promising one for market penetration. We showed in the first chapter of this thesis that PEFCs may help tackle energy conversion issues as they provide, in more ways than one, solutions to make many sectors more sustainable. This objective could be achieved by accelerating the long-awaited ecological transition. However, the accomplishment of this enthusiastic goal was shown to be dependent on two main factors. The first is the achievement of a hydrogen production and distribution infrastructure based on renewables. The second factor is the development of high performance and durable PEFCs, which starts first by making this technology fairly competitive with other traditional energy conversion devices that present mature technologies so far.

As a result of a relatively recent trend to deploy fuel cells in a wide range of applications, significant efforts have been made to commercialise and scale-up PEFC-based energy conversion systems. To do so, the production of PEFCs needs to be moved from its small-scale level to more established industrial manufacturing processes. As a matter of fact, the final phase of the PEFCs' production process is the assembly of its components. This operation is typically performed using traditional fasteners (i.e. bolts and nuts) and requires the application of mechanical compression. Hence, due to the dependence of the performance of the PEFCs on their internal mechanical stress state, the interest of the scientific community to study the mechanical aspects of the PEFCs has increased. In this sense, we outlined in the first chapter the goal of this thesis, which is to contribute to the thorough understanding of the effect of the mechanical compression on the performance of the PEFCs operating in real-life conditions.

We showed in the second chapter that the PEFC assembly process first requires an accurate control to ensure proper alignment of the stack components as well as an appropriate assembly pressure in order to achieve adequate contacts (i.e. mechanical, thermal, and electrical) between the PEFC components and to ensure gas-tight operation. In fact, the PEFC is a multi-contact structure in which multi-physical phenomena are intercorrelated. Interactions between these phenomena impact the performance of the fuel cell as well as its durability. We showed that these interactions are affected by mechanical stresses endured by the PEFC during its lifelong operation. Indeed, the second chapter presented a comprehensive literature-based analysis on the effect of mechanical compression on the PEFC performance. The objective of this chapter was to provide a thorough overview of the compression mechanisms and their respective impacts on the fuel cell performance and components' properties. Two significant types of

compression mechanisms were shown to take place in a PEFC. The first is due to external forces (e.g. the applied compression during the assembly process, shock and vibrations) and the second is caused by internal forces that are generated inside the fuel cell during its operation (e.g. membrane hydration/dehydration, freeze/thaw cycles). In both cases, components within the PEFC are subjected to compressive forces that may either improve or worsen the fuel cell performance. In this second chapter, the effects of mechanical compression on the properties of the GDLs and their water management capability were also analysed. As a result of this literature review, we showed that mechanical compression has two competing effects on PEFC performance. The first effect is beneficial as it reduces the ohmic resistance of the PEFC components, whereas the second effect is detrimental as excessive assembly pressure was shown to increase the mass transport resistance leading to a decrease in the fuel cell performance. This latter was also shown to possibly cause permanent damage to the PEFC components. This second chapter ended with a number of concluding remarks and perspectives, which allowed us to consider our work with regards to the studies previously reported in the literature. In this sense, the work reported in this thesis presents the novelty of finely studying the PEFC performance as a function of mechanical compression. In fact, 12 levels of mechanical compression were investigated, ranging from 0.35 MPa to 2 MPa with steps of 0.15 MPa. In order to reduce the effects of materials' memory and gradual accumulation of liquid water with increasing mechanical compression, a randomised mechanical compression protocol was proposed. In this study, the mechanical compression levels were investigated on a 225 cm^2 single-cell PEFC. Two current density levels were studied, namely 0.6 $A.cm^{-2}$ and 0.9 $A.cm^{-2}$, that are representative of the ohmic and mass transport loss regions of the polarisation curve, respectively. Moreover, two relative humidity levels were tested, namely 50%RH and 100%RH. The use of these operating conditions at different mechanical compression levels contributed in achieving a better understanding of the effect of the various parameters related to mechanical compression on the PEFC performance. The results were reported and analysed in the fourth and fifth chapters of this thesis.

In parallel with the scientific work presented in this thesis, we have devoted a significant amount of time to the development of a new test facility for the fuel cell platform in Belfort. This new test equipment is dedicated to the study of the mechanical compression effects on the PEFC performance. This experimental development, of a rather technological aspect, was presented in the third chapter of this thesis. Firstly, the test bench used for the control and monitoring of the PEFC operating conditions was described. Then, the operating principle of the mechanical compression unit was presented, including the proportional pressure regulator, the displacement sensor, and the current and temperature distributions' measurement system (i.e. S++® device). All these measurement devices were specifically customised for our application. Since the repeatability of our test protocol was crucial in our study, the third chapter also provided a repeatability study of the mechanical compression and displacement measurements. We first showed that the repeatability of the mechanical compression application process is quite good (i.e. measured standard deviation between tests was lower than the resolution of the pressure sensor of 0.02 MPa). Then, we showed that the repeatability

of the displacement measurements is also satisfactory, especially when using the offset deduction method for displacement measurements as detailed in the third chapter. The results of the proposed method were satisfactory as the measured standard deviations were lower than the measurement resolution of the displacement sensor of 1 µm.

In the fourth chapter, we aimed to investigate the effects of mechanical compression on the PEFC performance through combining the results of our in-situ experimental characterisation campaigns with the ex-situ findings conducted within the framework of the overall research project (i.e. MIREPOIx). Investigations were conducted by combining polarisation measurements analysis, cell voltage monitoring, and Electrochemical Impedance Spectroscopy (EIS). Results of steady-state characterisation techniques showed that a mechanical compression up to 1.55 MPa improves the PEFC performance at all tested operating conditions. This finding was attributed to the dominant reduction of the ohmic resistance against the increase in mass transport resistance with respect to the PEFC operating conditions. We also showed that a mechanical compression level higher than 1.55 MPa does not result in any further improvement of the fuel cell voltage; it may even worsen the PEFC performance due to the higher mass transport losses. Therefore, the presented results suggest that compressing the PEFC beyond a specified level (i.e. 1.55 MPa) would not lead to any further improvement of the PEFC performance. Following the results of these experimental campaigns, we identified two mechanical compression ranges. The first one is between 0.35 MPa and 1.55 MPa, where the PEFC performance was enhanced, whereas the second one ranges from 1.55 MPa to 2 MPa, at which the PEFC performance was either unchanged or even started worsening. The PEFC performance decrease at the second compression range was especially discernible at 0.9 $A.cm^{-2}$ and 100%RH. This effect was mainly attributed to the excess water brought to the PEFC through the fully humidified reactants at 100%RH and also to the higher water production rate at the cathode when the PEFC was operating at relatively high current density (0.9 $A.cm^{-2}$ compared to 0.6 $A.cm^{-2}$). This effect, added to the fact that the PEFC was further compressed up to 2 MPa, led to a decrease in the GDL porosity that, in turn, induced higher mass transport losses. The results of this chapter also emphasised the fact that mechanical compression, at its first range, further improves the PEFC voltage at 0.9 $A.cm^{-2}$ compared to 0.6 $A.cm^{-2}$. This difference in voltage improvement was explained by the better membrane hydration state at 0.9 $A.cm^{-2}$ leading to a reduction in its protonic resistance and, therefore, to a decline in the ohmic resistance of the PEFC. The EIS analysis in this chapter was done by investigating the evolutions of the ohmic, charge transfer, and mass transport losses as a function of mechanical compression. The EIS results confirmed that the major reduction of the ohmic resistance observed by increasing the mechanical compression occurred at the first compression range. The EIS results also confirmed that the ohmic resistance at 0.9 $A.cm^{-2}$ was 4% lower compared to 0.6 $A.cm^{-2}$. Correlations between in-situ results, reported in this chapter, and ex-situ investigations, carried out within the framework of this thesis project (Khadidja Bouziane's PhD Thesis [192]) were put forward throughout this chapter. These correlations mainly emphasised that the evolutions of the ex-situ results of the bulk and contact resistance the GDL and the in-situ results of the ohmic resistance

(measured using the EIS technique) showed a similar reduction tendency with increasing mechanical compression.

The fifth chapter aimed to provide a thorough understanding of how mechanical compression quantitatively affects the local phenomena taking place within an operating PEFC with a large active area (i.e. 225 cm^2 in our study). Investigations were conducted on the distributions of current density, temperature, and mechanical pressure. The results of this chapter emphasised the fact that mechanical compression, at its first range (0.35 →1.55 MPa), homogenises the current density distribution which, in turn, homogenises the temperature distribution. This latter effect was shown to be beneficial as it reduces the high temperature regions and, therefore, the possible creation of hotspots that may have detrimental impacts on the performance and durability of the PEFC [91,92,212]. Through conducting a spatial analysis, we showed that this homogenisation effect is mainly attributed to the better pressure distribution obtained with increasing mechanical compression. The results of this chapter stressed out that the regions with high mechanical pressure correspond to the regions with high local current density which, in turn, correspond to regions with high temperature. Furthermore, through comparing the findings of this chapter with the results of the PEFC performance assessment carried out in the fourth chapter, we emphasised that this pressure homogenisation has positive impacts on the PEFC performance due to the reduction of the ohmic resistance. The results of this chapter confirmed, therefore, the correlations that exist between the enhancement of the current, temperature, pressure distributions and the improvement of the global PEFC performance assessed earlier in the fourth chapter of this thesis.

In conclusion, we believe that we have proposed a significant work that enabled us to respond to the scientific challenges outlined in the introduction of this thesis. The results obtained will contribute to better knowledge and understanding of the phenomena occurring within an operating PEFC when it is subjected to mechanical stresses. This comprehensive study, which included correlations from the results of both in-situ and ex-situ characterisation techniques, will assist the fuel cell manufacturers in developing PEFCs with enhanced performance and durability. In fact, we showed that some hard-won performance enhancement, achieved for instance by onerous materials development, can be lost when applying an inadequate mechanical assembly pressure. We provided results to help achieve the optimal assembly pressure and, therefore, optimise the performance and durability of the PEFCs. Finally, the measurement results reported in this thesis could also be employed as validation parameters for PEFC modellers and designers in order to integrate phenomena that are usually not addressed in model developments (e.g. inhomogeneities of the distributions of current and temperature caused by inadequate assembly pressure). Following the results of this thesis, a number of recommendations for future work can be addressed.

2 Future work

Various research perspectives emerge from the results of this thesis. We will outline hereafter the most important ones to be explored.

In-situ/ex-situ correlations: it was well reckoned by the scientific community that the GDL characteristics play a major role in the PEFC performance. In this sense, we showed in the second chapter that among all the PEFC components, the GDL is the most impacted one by mechanical compression [5]. The work presented in this thesis is a part of the MIREPOIx project aiming to provide correlations between the ex-situ and in-situ results, with a main focus on the GDLs. These correlations were provided throughout this thesis for one GDL type, which is the Sigracet® 38BC. It would be interesting to continue the in-situ characterisation on a number of commercially available GDLs. This could be preferentially done using the GDLs that are already characterised by K. Bouziane [102,192] in the framework of her PhD thesis. This would allow providing more in-situ/ex-situ correlations using other GDL types with different materials, MPL coatings, and PTFE loadings. The objective of this study will be the consideration of the various characteristics of the GDL in the in-situ investigations of the effects of mechanical compression on the PEFC performance. This will allow predicting the in-situ behaviours of the GDLs based on their characterisations carried out ex-situ. The final objective of this study would be to develop a selection criterion for an optimal choice of the type of the GDL depending on the targeted application.

Local phenomena investigations: we emphasised in this manuscript the fact the PEFCs represent a particularly complex system that combines electrochemical, thermal, fluidic, and mechanical phenomena. We also showed in the fourth and fifth chapters how mechanical compression affects the phenomena that take place within an operating PEFC. However, one particular phenomenon remains open for a future in-depth study. This latter is the possible reduction of the activation resistance with increasing mechanical compression. This effect has not been comprehensively addressed in the literature. Therefore, further investigations combining both theoretical model development and local EIS characterisation needs to be carried out in order to provide a comprehensive analysis of this phenomenon.

Further research could also be carried out on the assessment of the local contact resistance R_{cr} based on the mechanical pressure distributions' results as shown in the fifth chapter of this thesis. This could be done by defining a relationship between the local pressure and the contact resistance as reported in the ex-situ study reported by K. Bouziane [102,192]. Then, the R_{Ω} could be measured using spatially resolved EIS measurements as shown in [218,225]. Afterwards, the separation of the R_m (related to the protonic resistance of the membrane) and the R_{e^-} (related to electronic resistance of the PEFC components) could be carried out by employing an approach similar to the one developed in Laplace Laboratory [190], but applied locally. This could allow having a first map combining the effect of mechanical compression on the R_{Ω} with the contributions of R_m and R_{e^-}(including R_{cr}). Afterwards, through comparing this map with the current density distribution maps provided by S++® measurement device,

we could potentially differentiate the local losses that occur due to the ohmic resistance from the other types of resistances (e.g. mass transport resistance). This perspective is quite promising as it would allow to finely deconvolute the different loss sources occurring locally within the PEFC when subjected to mechanical compression.

Durability: The fifth chapter of this thesis provided a spatial analysis of the effects of mechanical compression on the distributions of the current density, temperature, and mechanical pressure. We showed that the regions with high mechanical pressure correspond to the regions with high current density and, in turn, to the regions with high temperature. These high temperature regions may create hotspots that could worsen the PEFC performance and durability [91,92,212]. Moreover, the results of this chapter emphasised the fact that mechanical compression reduces the high temperature regions. Even though this reduction was relatively low, its long-term effect on the PEFCs' performance and durability may be considerable. Therefore, it seems important to propose the integration of the effects of mechanical pressure inhomogeneity in future durability studies, as this subject was not addressed in the literature so far. The aim of this investigation would be to quantify how the optimisation of the mechanical assembly pressure homogenisation improves the durability of the PEFCs.

PEFC stack: The experimental investigations reported in this manuscript were carried out on a single-cell PEFC. Valuable information regarding the effects of mechanical compression on the PEFC performance was put forward throughout this manuscript. These investigations were conducted on a 225 cm^2 active area, which is representative of the active area sizes that are currently used in various fuel cells applications. However, to get closer to real-life operation, it would be interesting to conduct similar in-situ characterisations on PEFC stacks of multiple cells. In fact, the PEFC stacks (e.g. 370 cells in the Toyota Mirai [22]) may have different mechanical behaviour, hence the interest of following a similar approach to the one reported in this thesis but for a PEFC stack.

Stack assembly: we emphasised in the second chapter of this thesis that assembling the PEFCs using the point load design (i.e. using typical fasteners: bolts and nuts) induces an inhomogeneous pressure distribution. We also showed in the fifth chapter that the inhomogeneous pressure distribution creates substantial current and temperature spatial discrepancies. These effects may have detrimental impacts on the fuel cell performance and durability. Therefore, developing new compression methods aiming to reduce pressure distribution inhomogeneity is crucial in order to develop high performance and durable PEFCs. We provided in the second chapter some novel clamping methods that were reported in the patent literature [106–108]. However, the majority of academic studies that investigate the effects of the mechanical pressure distribution have used the typical point-load design. Thus, it seems important to recommend future investigations focusing mainly on the comparison between these new assembly methods following an approach similar to the one proposed in this thesis. This comparative study will guide fuel cell manufacturers to possibly adopt new assembly methods/mechanisms that provide optimal pressure distribution, which may improve both the performance and the durability of the PEFCs as emphasised throughout this thesis.

References

[1] Salameh Z. Chapter 4 - Energy Storage. In: Salameh Z, editor. Renewable Energy System Design, Boston: Academic Press; 2014, p. 201–98. https://doi.org/10.1016/B978-0-12-374991-8.00004-0.

[2] Larminie J, Dicks A. Introduction. Fuel Cell Systems Explained, John Wiley & Sons, Ltd; 2013, p. 1–24. https://doi.org/10.1002/9781118878330.ch1.

[3] Fuel Cell History - Fuel Cell Today. http://www.fuelcelltoday.com/history.

[4] Kalyvas C, Kucernak A, Brett D, Hinds G, Atkins S, Brandon N. Spatially resolved diagnostic methods for polymer electrolyte fuel cells: a review. Wiley Interdisciplinary Reviews: Energy and Environment 2014;3:254–75. https://doi.org/10.1002/wene.86.

[5] Khetabi EM, Bouziane K, Zamel N, François X, Meyer Y, Candusso D. Effects of mechanical compression on the performance of polymer electrolyte fuel cells and analysis through in-situ characterisation techniques - A review. Journal of Power Sources 2019;424:8–26. https://doi.org/10.1016/j.jpowsour.2019.03.071.

[6] Dafalla AM, Jiang F. Stresses and their impacts on proton exchange membrane fuel cells: A review. International Journal of Hydrogen Energy 2018;43:2327–48. https://doi.org/10.1016/j.ijhydene.2017.12.033.

[7] Millichamp J, Mason TJ, Neville TP, Rajalakshmi N, Jervis R, Shearing PR, et al. Mechanisms and effects of mechanical compression and dimensional change in polymer electrolyte fuel cells – A review. Journal of Power Sources 2015;284:305–20. https://doi.org/10.1016/j.jpowsour.2015.02.111.

[8] Simoncini N. Histoire de la recherche sur les piles à combustible en France des années soixante aux années quatre-vingt. phdthesis. Université Bourgogne Franche-Comté, 2018.

[9] Andújar JM, Segura F. Fuel cells: History and updating. A walk along two centuries. Renewable and Sustainable Energy Reviews 2009;13:2309–22. https://doi.org/10.1016/j.rser.2009.03.015.

[10] Dhathathreyan KS, Rajalakshmi N. Polymer Electrolyte Membrane Fuel Cell. In: Basu S, editor. Recent Trends in Fuel Cell Science and Technology, New York, NY: Springer; 2007, p. 40–115. https://doi.org/10.1007/978-0-387-68815-2_3.

[11] The Future of Hydrogen – Analysis. IEA. https://www.iea.org/reports/the-future-of-hydrogen.

[12] Mayé P. Générateurs électrochimiques Piles, accumulateurs et piles à combustible. Paris: Dunod; .

[13] Rosli RE, Sulong AB, Daud WRW, Zulkifley MA, Husaini T, Rosli MI, et al. A review of high-temperature proton exchange membrane fuel cell (HT-PEMFC) system. International Journal of Hydrogen Energy 2017;42:9293–314. https://doi.org/10.1016/j.ijhydene.2016.06.211.

[14] E4tech. The Fuel Cell Industry Review 2019.

[15] COGEN. Japan: A success story in deploying Fuel Cell micro-Cogeneration. PACE 2019. http://www.pace-energy.eu/japan-a-success-story-in-deploying-fuel-cell-micro-cogeneration/.

[16] CI. About PACE. PACE. http://www.pace-energy.eu/about-pace/.

[17] SFC Energy AG - Clean energy everywhere. SFC Energy. https://www.sfc.com/en/.

[18] EFOY-fuel cells have more power than solar systems | EFOY. https://www.efoy-comfort.com/benefits.

[19] Tracking Transport – Analysis. IEA. https://www.iea.org/reports/tracking-transport-2019.

[20] Rajashekara K. Propulsion System Strategies for Fuel Cell Vehicles. Warrendale, PA: SAE International; 2000. https://doi.org/10.4271/2000-01-0369.

[21] Ligen Y, Vrubel H, Girault HH. Mobility from Renewable Electricity: Infrastructure Comparison for Battery and Hydrogen Fuel Cell Vehicles. World Electric Vehicle Journal 2018;9:3. https://doi.org/10.3390/wevj9010003.

[22] Toyota Mirai – The Turning Point. https://www.toyota.com/mirai/fcv.html.

[23] Alternative Fuels Data Center: How Do Fuel Cell Electric Vehicles Work Using Hydrogen? . https://afdc.energy.gov/vehicles/how-do-fuel-cell-electric-cars-work.

[24] HysetCo joint venture to promote hydrogen mobility around Paris. Fuel Cells Bulletin 2019;2019:7. https://doi.org/10.1016/S1464-2859(19)30101-4.

[25] Toyota-Backed Paris Venture Targets 10,000 Hydrogen Taxis by 2024. BloombergCom 2021.

[26] Hyundai NEXO. https://www.hyundai.fr/gamme/vehicules-hybrides-electriques-suv/nexo/decouvrir.

[27] Deployment of Fuel Cell Electric Vehicles as of End 2018. http://ieafuelcell.com/index.php?id=2&tx_news_pi1%5Bnews%5D=8&tx_news_pi1%5Bcontroller%5D=News&tx_news_pi1%5Baction%5D=detail&cHash=2a54d705472343da35e4cd9835734aff .

[28] Zamel N, Li X. Effective transport properties for polymer electrolyte membrane fuel cells – With a focus on the gas diffusion layer. Progress in Energy and Combustion Science 2013;39:111–46. https://doi.org/10.1016/j.pecs.2012.07.002.

[29] Nafion™ Membrane Comparison Table. Fuel Cells Etc 2014. https://fuelcellsetc.com/helpful-tools/nafion-membrane-comparison-table/.

[30] Powering Fuel Cells with Nafion™ Membranes and Dispersions . https://www.nafion.com:443/en/applications/fuel-cells.

[31] Collier A, Wang H, Zi Yuan X, Zhang J, Wilkinson DP. Degradation of polymer electrolyte membranes. International Journal of Hydrogen Energy 2006;31:1838–54. https://doi.org/10.1016/j.ijhydene.2006.05.006.

[32] Boudellal M. La pile à combustible: L'hydrogène et ses applications. 2012.

[33] Wu J, Yuan XZ, Martin JJ, Wang H, Zhang J, Shen J, et al. A review of PEM fuel cell durability: Degradation mechanisms and mitigation strategies. Journal of Power Sources 2008;184:104–19. https://doi.org/10.1016/j.jpowsour.2008.06.006.

[34] Holzer L, Pecho O, Schumacher J, Marmet Ph, Stenzel O, Büchi FN, et al. Microstructure-property relationships in a gas diffusion layer (GDL) for Polymer Electrolyte Fuel Cells, Part I: effect of compression and anisotropy of dry GDL. Electrochimica Acta 2017;227:419–34. https://doi.org/10.1016/j.electacta.2017.01.030.

[35] Peng L, Shao H, Qiu D, Yi P, Lai X. Investigation of the non-uniform distribution of current density in commercial-size proton exchange membrane fuel cells. Journal of Power Sources 2020;453:227836. https://doi.org/10.1016/j.jpowsour.2020.227836.

[36] Zhang F-Y, Advani SG, Prasad AK. Performance of a metallic gas diffusion layer for PEM fuel cells. Journal of Power Sources 2008;176:293–8. https://doi.org/10.1016/j.jpowsour.2007.10.055.

[37] Ozden A, Shahgaldi S, Li X, Hamdullahpur F. A review of gas diffusion layers for proton exchange membrane fuel cells—With a focus on characteristics, characterization techniques, materials and designs. Progress in Energy and Combustion Science 2019;74:50–102. https://doi.org/10.1016/j.pecs.2019.05.002.

[38] Dotelli G, Omati L, Gallo Stampino P, Grassini P, Brivio D. Investigation of gas diffusion layer compression by electrochemical impedance spectroscopy on running polymer electrolyte membrane fuel cells. Journal of Power Sources 2011;196:8955–66. https://doi.org/10.1016/j.jpowsour.2011.01.078.

[39] Qi Z, Kaufman A. Improvement of water management by a microporous sublayer for PEM fuel cells. Journal of Power Sources 2002;109:38–46. https://doi.org/10.1016/S0378-7753(02)00058-7.

[40] Nam JH, Lee K-J, Hwang G-S, Kim C-J, Kaviany M. Microporous layer for water morphology control in PEMFC. International Journal of Heat and Mass Transfer 2009;52:2779–91. https://doi.org/10.1016/j.ijheatmasstransfer.2009.01.002.

[41] Lu Z, Daino MM, Rath C, Kandlikar SG. Water management studies in PEM fuel cells, part III: Dynamic breakthrough and intermittent drainage characteristics from GDLs with and without MPLs. International Journal of Hydrogen Energy 2010;35:4222–33. https://doi.org/10.1016/j.ijhydene.2010.01.012.

[42] El-kharouf A, Mason TJ, Brett DJL, Pollet BG. Ex-situ characterisation of gas diffusion layers for proton exchange membrane fuel cells. Journal of Power Sources 2012;218:393–404. https://doi.org/10.1016/j.jpowsour.2012.06.099.

[43] Wilberforce T, El Hassan Z, Ogungbemi E, Ijaodola O, Khatib FN, Durrant A, et al. A comprehensive study of the effect of bipolar plate (BP) geometry design on the performance of proton exchange membrane (PEM) fuel cells. Renewable and Sustainable Energy Reviews 2019;111:236–60. https://doi.org/10.1016/j.rser.2019.04.081.

[44] Karimi S, Fraser N, Roberts B, Foulkes FR. A Review of Metallic Bipolar Plates for Proton Exchange Membrane Fuel Cells: Materials and Fabrication Methods. Advances in Materials Science and Engineering 2012;2012:e828070. https://doi.org/10.1155/2012/828070.

[45] Tawfik H, Hung Y, Mahajan D. Metal bipolar plates for PEM fuel cell—A review. Journal of Power Sources 2007;163:755–67. https://doi.org/10.1016/j.jpowsour.2006.09.088.

[46] Larminie J, Dicks A. Efficiency and Open Circuit Voltage. Fuel Cell Systems Explained, John Wiley & Sons, Ltd; 2013, p. 25–43. https://doi.org/10.1002/9781118878330.ch2.

[47] Spiegel C. PEM fuel cell modeling and simulation using Matlab. Amsterdam :Boston: Academic Press/Elsevier; 2008.

[48] Baik KD, Kim MS. Characterization of nitrogen gas crossover through the membrane in proton-exchange membrane fuel cells. International Journal of Hydrogen Energy 2011;36:732–9. https://doi.org/10.1016/j.ijhydene.2010.09.046.

[49] Zhang J, Tang Y, Song C, Zhang J, Wang H. PEM fuel cell open circuit voltage (OCV) in the temperature range of 23°C to 120°C. Journal of Power Sources 2006;163:532–7. https://doi.org/10.1016/j.jpowsour.2006.09.026.

[50] Khan MA, Sundén B, Yuan J. Analysis of multi-phase transport phenomena with catalyst reactions in polymer electrolyte membrane fuel cells – A review. Journal of Power Sources 2011;196:7899–916. https://doi.org/10.1016/j.jpowsour.2011.04.040.

[51] Barbir F, GÓMEZ T. EFFCIENCY AND ECONOMICS OF PROTON EXCHANGE MEMBRANE (PEM) FUEL CELLS. International Journal of Hydrogen Energy 1997:1027–37.

[52] Mason TJ, Millichamp J, Shearing PR, Brett DJL. A study of the effect of compression on the performance of polymer electrolyte fuel cells using electrochemical impedance spectroscopy and dimensional change analysis. International Journal of Hydrogen Energy 2013;38:7414–22. https://doi.org/10.1016/j.ijhydene.2013.04.021.

[53] Zhou Y, Lin G, Shih AJ, Hu SJ. Multiphysics Modeling of Assembly Pressure Effects on Proton Exchange Membrane Fuel Cell Performance. J Fuel Cell Sci Technol 2009;6:041005-041005–7. https://doi.org/10.1115/1.3081426.

[54] Lee S-J, Hsu C-D, Huang C-H. Analyses of the fuel cell stack assembly pressure. Journal of Power Sources 2005;145:353–61. https://doi.org/10.1016/j.jpowsour.2005.02.057.

[55] Montanini R, Squadrito G, Giacoppo G. EXPERIMENTAL EVALUATION OF THE CLAMPING PRESSURE DISTRIBUTION IN A PEM FUEL CELL USING MATRIX-BASED PIEZORESISTIVE THIN-FILM SENSORS 2009:6.

[56] Gatto I, Urbani F, Giacoppo G, Barbera O, Passalacqua E. Influence of the bolt torque on PEFC performance with different gasket materials. International Journal of Hydrogen Energy 2011;36:13043–50. https://doi.org/10.1016/j.ijhydene.2011.07.066.

[57] de la Cruz J, Cano U, Romero T. Simulation and in situ measurement of stress distribution in a polymer electrolyte membrane fuel cell stack. Journal of Power Sources 2016;329:273–80. https://doi.org/10.1016/j.jpowsour.2016.08.073.

[58] Wen C-Y, Lin Y-S, Lu C-H. Experimental study of clamping effects on the performances of a single proton exchange membrane fuel cell and a 10-cell stack. Journal of Power Sources 2009;192:475–85. https://doi.org/10.1016/j.jpowsour.2009.03.058.

[59] Chun JH, Park KT, Jo DH, Kim SG, Kim SH. Numerical modeling and experimental study of the influence of GDL properties on performance in a PEMFC. International Journal of Hydrogen Energy 2011;36:1837–45. https://doi.org/10.1016/j.ijhydene.2010.01.036.

[60] Ismail MS, Damjanovic T, Ingham DB, Pourkashanian M, Westwood A. Effect of polytetrafluoroethylene-treatment and microporous layer-coating on the electrical conductivity of

gas diffusion layers used in proton exchange membrane fuel cells. Journal of Power Sources 2010;195:2700–8. https://doi.org/10.1016/j.jpowsour.2009.11.069.

[61] Lim C, Wang CY. Effects of hydrophobic polymer content in GDL on power performance of a PEM fuel cell. Electrochimica Acta 2004;49:4149–56. https://doi.org/10.1016/j.electacta.2004.04.009.

[62] Kong CS, Kim D-Y, Lee H-K, Shul Y-G, Lee T-H. Influence of pore-size distribution of diffusion layer on mass-transport problems of proton exchange membrane fuel cells. Journal of Power Sources 2002;108:185–91. https://doi.org/10.1016/S0378-7753(02)00028-9.

[63] Bultel Y, Wiezell K, Jaouen F, Ozil P, Lindbergh G. Investigation of mass transport in gas diffusion layer at the air cathode of a PEMFC. Electrochimica Acta 2005;51:474–88. https://doi.org/10.1016/j.electacta.2005.05.007.

[64] Park S, Popov BN. Effect of cathode GDL characteristics on mass transport in PEM fuel cells. Fuel 2009;88:2068–73. https://doi.org/10.1016/j.fuel.2009.06.020.

[65] Liu D, Case S. Durability study of proton exchange membrane fuel cells under dynamic testing conditions with cyclic current profile. Journal of Power Sources 2006;162:521–31. https://doi.org/10.1016/j.jpowsour.2006.07.007.

[66] Zhang S, Yuan X, Wang H, Mérida W, Zhu H, Shen J, et al. A review of accelerated stress tests of MEA durability in PEM fuel cells. International Journal of Hydrogen Energy 2009;34:388–404. https://doi.org/10.1016/j.ijhydene.2008.10.012.

[67] Wahdame B, Candusso D, Harel F, François X, Péra M-C, Hissel D, et al. Analysis of a PEMFC durability test under low humidity conditions and stack behaviour modelling using experimental design techniques. Journal of Power Sources 2008;182:429–40. https://doi.org/10.1016/j.jpowsour.2007.12.122.

[68] Tüber K, Pócza D, Hebling C. Visualization of water buildup in the cathode of a transparent PEM fuel cell. Journal of Power Sources 2003;124:403–14. https://doi.org/10.1016/S0378-7753(03)00797-3.

[69] Satija R, Jacobson DL, Arif M, Werner SA. In situ neutron imaging technique for evaluation of water management systems in operating PEM fuel cells. Journal of Power Sources 2004;129:238–45. https://doi.org/10.1016/j.jpowsour.2003.11.068.

[70] Spernjak D, Prasad AK, Advani SG. Experimental investigation of liquid water formation and transport in a transparent single-serpentine PEM fuel cell. Journal of Power Sources 2007;170:334–44. https://doi.org/10.1016/j.jpowsour.2007.04.020.

[71] Wu J, Yuan XZ, Wang H, Blanco M, Martin JJ, Zhang J. Diagnostic tools in PEM fuel cell research: Part I Electrochemical techniques. International Journal of Hydrogen Energy 2008;33:1735–46. https://doi.org/10.1016/j.ijhydene.2008.01.013.

[72] Arvay A, Yli-Rantala E, Liu C-H, Peng X-H, Koski P, Cindrella L, et al. Characterization techniques for gas diffusion layers for proton exchange membrane fuel cells – A review. Journal of Power Sources 2012;213:317–37. https://doi.org/10.1016/j.jpowsour.2012.04.026.

[73] El Oualid S, Lachat R, Candusso D, Meyer Y. Characterization process to measure the electrical contact resistance of Gas Diffusion Layers under mechanical static compressive loads. International Journal of Hydrogen Energy 2017;42:23920–31. https://doi.org/10.1016/j.ijhydene.2017.03.130.

[74] Sadeghifar H, Djilali N, Bahrami M. Thermal conductivity of a graphite bipolar plate (BPP) and its thermal contact resistance with fuel cell gas diffusion layers: Effect of compression, PTFE, micro porous layer (MPL), BPP out-of-flatness and cyclic load. Journal of Power Sources 2015;273:96–104. https://doi.org/10.1016/j.jpowsour.2014.09.062.

[75] Prass S, Hasanpour S, Sow PK, Phillion AB, Mérida W. Microscale X-ray tomographic investigation of the interfacial morphology between the catalyst and micro porous layers in proton exchange membrane fuel cells. Journal of Power Sources 2016;319:82–9. https://doi.org/10.1016/j.jpowsour.2016.04.031.

[76] Sadeghifar H. In-plane and through-plane electrical conductivities and contact resistances of a Mercedes-Benz catalyst-coated membrane, gas diffusion and micro-porous layers and a Ballard graphite bipolar plate: Impact of humidity, compressive load and polytetrafluoroethylene. Energy Conversion and Management 2017;154:191–202. https://doi.org/10.1016/j.enconman.2017.10.060.

[77] Chang WR, Hwang JJ, Weng FB, Chan SH. Effect of clamping pressure on the performance of a PEM fuel cell. Journal of Power Sources 2007;166:149–54. https://doi.org/10.1016/j.jpowsour.2007.01.015.

[78] Lin J-H, Chen W-H, Su Y-J, Ko T-H. Effect of gas diffusion layer compression on the performance in a proton exchange membrane fuel cell. Fuel 2008;87:2420–4. https://doi.org/10.1016/j.fuel.2008.03.001.

[79] Zhang W, Wu C. Effect of Clamping Load on the Performance of Proton Exchange Membrane Fuel Cell Stack and Its Optimization Design: A Review of Modeling and Experimental Research. J Fuel Cell Sci Technol 2013;11:020801-020801–11. https://doi.org/10.1115/1.4026070.

[80] Kandlikar SG, Lu Z, Lin TY, Cooke D, Daino M. Uneven gas diffusion layer intrusion in gas channel arrays of proton exchange membrane fuel cell and its effects on flow distribution. Journal of Power Sources 2009;194:328–37. https://doi.org/10.1016/j.jpowsour.2009.05.019.

[81] Mason TJ, Millichamp J, Neville TP, El-kharouf A, Pollet BG, Brett DJL. Effect of clamping pressure on ohmic resistance and compression of gas diffusion layers for polymer electrolyte fuel cells. Journal of Power Sources 2012;219:52–9. https://doi.org/10.1016/j.jpowsour.2012.07.021.

[82] Lee W, Ho C-H, Van Zee JW, Murthy M. The effects of compression and gas diffusion layers on the performance of a PEM fuel cell. Journal of Power Sources 1999;84:45–51. https://doi.org/10.1016/S0378-7753(99)00298-0.

[83] Nitta I, Hottinen T, Himanen O, Mikkola M. Inhomogeneous compression of PEMFC gas diffusion layer: Part I. Experimental. Journal of Power Sources 2007;171:26–36. https://doi.org/10.1016/j.jpowsour.2006.11.018.

[84] Chi PH, Chan SH, Weng FB, Su A, Sui PC, Djilali N. On the effects of non-uniform property distribution due to compression in the gas diffusion layer of a PEMFC. International Journal of Hydrogen Energy 2010;35:2936–48. https://doi.org/10.1016/j.ijhydene.2009.05.066.

[85] Khajeh-Hosseini-Dalasm N, Sasabe T, Tokumasu T, Pasaogullari U. Effects of polytetrafluoroethylene treatment and compression on gas diffusion layer microstructure using

high-resolution X-ray computed tomography. Journal of Power Sources 2014;266:213–21. https://doi.org/10.1016/j.jpowsour.2014.05.004.

[86] Ge J, Higier A, Liu H. Effect of gas diffusion layer compression on PEM fuel cell performance. Journal of Power Sources 2006;159:922–7. https://doi.org/10.1016/j.jpowsour.2005.11.069.

[87] Senthil Velan V, Velayutham G, Rajalakshmi N, Dhathathreyan KS. Influence of compressive stress on the pore structure of carbon cloth based gas diffusion layer investigated by capillary flow porometry. International Journal of Hydrogen Energy 2014;39:1752–9. https://doi.org/10.1016/j.ijhydene.2013.11.038.

[88] Uzundurukan A, Bilgili M, Devrim Y. Examination of compression effects on PEMFC performance by numerical and experimental analyses. International Journal of Hydrogen Energy 2020. https://doi.org/10.1016/j.ijhydene.2020.04.275.

[89] Wang LP, Zhang LH, Jiang JP. Experimental Study of Assembly Clamping Pressure on Performance of PEM Fuel Cells. Applied Mechanics and Materials 2011. https://doi.org/10.4028/www.scientific.net/AMM.44-47.2399.

[90] Rezaei Niya SM, Hoorfar M. Study of proton exchange membrane fuel cells using electrochemical impedance spectroscopy technique – A review. Journal of Power Sources 2013;240:281–93. https://doi.org/10.1016/j.jpowsour.2013.04.011.

[91] Asghari S, Shahsamandi MH, Ashraf Khorasani MR. Design and manufacturing of end plates of a 5kW PEM fuel cell. International Journal of Hydrogen Energy 2010;35:9291–7. https://doi.org/10.1016/j.ijhydene.2010.02.135.

[92] Asghari S, Mokmeli A, Samavati M. Study of PEM fuel cell performance by electrochemical impedance spectroscopy. International Journal of Hydrogen Energy 2010;35:9283–90. https://doi.org/10.1016/j.ijhydene.2010.03.069.

[93] Yim S-D, Kim B-J, Sohn Y-J, Yoon Y-G, Park G-G, Lee W-Y, et al. The influence of stack clamping pressure on the performance of PEM fuel cell stack. Current Applied Physics 2010;10:S59–61. https://doi.org/10.1016/j.cap.2009.11.042.

[94] Ous T, Arcoumanis C. Effect of compressive force on the performance of a proton exchange membrane fuel cell. Proceedings of the Institution of Mechanical Engineers, Part C: Journal of Mechanical Engineering Science 2007;221:1067–74. https://doi.org/10.1243/09544062JMES654.

[95] Chang HM, Chang MH. Effects of Assembly Pressure on the Gas Diffusion Layer and Performance of a PEM Fuel Cell. Applied Mechanics and Materials 2012. https://doi.org/10.4028/www.scientific.net/AMM.110-116.48.

[96] Hassan NU, Kilic M, Okumus E, Tunaboylu B, Soydan AM. Experimental determination of optimal clamping torque for AB-PEM fuel cell. Journal of Electrochemical Science and Engineering 2016;6:9–16. https://doi.org/10.5599/jese.198.

[97] Carral C, Charvin N, Trouvé H, Mélé P. An experimental analysis of PEMFC stack assembly using strain gage sensors. International Journal of Hydrogen Energy 2014;39:4493–501. https://doi.org/10.1016/j.ijhydene.2014.01.033.

[98] Prescale | Fujifilm Global. http://www.fujifilm.com/products/prescale/prescalefilm/.

[99] Bates A, Mukherjee S, Hwang S, Lee SC, Kwon O, Choi GH, et al. Simulation and experimental analysis of the clamping pressure distribution in a PEM fuel cell stack. International Journal of Hydrogen Energy 2013;38:6481–93. https://doi.org/10.1016/j.ijhydene.2013.03.049.

[100] Debe MK. Electrocatalyst approaches and challenges for automotive fuel cells. Nature 2012;486:43–51. https://doi.org/10.1038/nature11115.

[101] Sadeghifar H, Djilali N, Bahrami M. Effect of Polytetrafluoroethylene (PTFE) and micro porous layer (MPL) on thermal conductivity of fuel cell gas diffusion layers: Modeling and experiments. Journal of Power Sources 2014;248:632–41. https://doi.org/10.1016/j.jpowsour.2013.09.136.

[102] Bouziane K, Khetabi EM, Lachat R, Zamel N, Meyer Y, Candusso D. Impact of cyclic mechanical compression on the electrical contact resistance between the gas diffusion layer and the bipolar plate of a polymer electrolyte membrane fuel cell. Renewable Energy 2020;153:349–61. https://doi.org/10.1016/j.renene.2020.02.033.

[103] Pressure Mapping Sensor 5076. Tekscan. https://www.tekscan.com/products-solutions/pressure-mapping-sensors/5076.

[104] El-Kharouf A, Rees NV, Steinberger-Wilckens R. Gas Diffusion Layer Materials and their Effect on Polymer Electrolyte Fuel Cell Performance – Ex Situ and In Situ Characterization. Fuel Cells 2014;14:735–41. https://doi.org/10.1002/fuce.201300247.

[105] El-kharouf A, Steinberger-Wilckens R. The Effect of Clamping Pressure on Gas Diffusion Layer Performance in Polymer Electrolyte Fuel Cells. Fuel Cells 2015;15:802–12. https://doi.org/10.1002/fuce.201500088.

[106] Bogumil TD, Connor EJ, Chinnici AG, Spacher PF, Keyser MW. Side spring compression retention system. US8012648B2, 2011.

[107] Andreas-Schott B, Fly GW, Rock JA, Jermy IR. Fuel cell stack compression retention system with external springs. US7807316B2, 2010.

[108] Andreas-Schott B, Chinnici A, Lai Y-H, Fly GW. Fuel cell compression retention system using compliant strapping. US20080305380A1, 2008.

[109] Andreas-Schott B, Rock JA, Fly GW, Migliore TP. Fuel cell stack compression retention system using overlapping sheets. US20080311457A1, 2008.

[110] Imen SJ, Shakeri M. Vibration Modeling of PEM Fuel Cell for Prediction of Cell Number Effects by Experimental Data. Fuel Cells 2016;16:193–204. https://doi.org/10.1002/fuce.201500206.

[111] Watts GR, Krylov VV. Ground-borne vibration generated by vehicles crossing road humps and speed control cushions. Applied Acoustics 2000;59:221–36. https://doi.org/10.1016/S0003-682X(99)00026-2.

[112] Rouss V, Lesage P, Bégot S, Candusso D, Charon W, Harel F, et al. Mechanical behaviour of a fuel cell stack under vibrating conditions linked to aircraft applications part I: Experimental. International Journal of Hydrogen Energy 2008;33:6755–65. https://doi.org/10.1016/j.ijhydene.2008.08.032.

[113] Diloyan G, Sobel M, Das K, Hutapea P. Effect of mechanical vibration on platinum particle agglomeration and growth in Polymer Electrolyte Membrane Fuel Cell catalyst layers. Journal of Power Sources 2012;214:59–67. https://doi.org/10.1016/j.jpowsour.2012.04.027.

[114] El-Emam SH, Mousa AA, Awad MM. Effects of stack orientation and vibration on the performance of PEM fuel cell. International Journal of Energy Research 2015;39:75–83. https://doi.org/10.1002/er.3217.

[115] Imen SJ, Shakeri M. Reliability Evaluation of an Open-Cathode PEMFC at Operating State and Longtime Vibration by Mechanical Loads. Fuel Cells 2016;16:126–34. https://doi.org/10.1002/fuce.201500144.

[116] Rajalakshmi N, Pandian S, Dhathathreyan KS. Vibration tests on a PEM fuel cell stack usable in transportation application. International Journal of Hydrogen Energy 2009;34:3833–7. https://doi.org/10.1016/j.ijhydene.2009.03.002.

[117] Hou Y, Zhou W, Shen C. Experimental investigation of gas-tightness and electrical insulation of fuel cell stack under strengthened road vibrating conditions. International Journal of Hydrogen Energy 2011;36:13763–8. https://doi.org/10.1016/j.ijhydene.2011.07.092.

[118] Hou Y, Zhou B, Zhou W, Shen C, He Y. An investigation of characteristic parameter variations of the polarization curve of a proton exchange membrane fuel cell stack under strengthened road vibrating conditions. International Journal of Hydrogen Energy 2012;37:11887–93. https://doi.org/10.1016/j.ijhydene.2012.05.030.

[119] Hou Y, Hao D, Shen C, Shao Z. Experimental investigation of the steady-state efficiency of fuel cell stack under strengthened road vibrating condition. International Journal of Hydrogen Energy 2013;38:3767–72. https://doi.org/10.1016/j.ijhydene.2013.01.037.

[120] Hou Y, Zhang X, Lu X, Hao D, Ma L, Li P. AC impedance characteristics of a vehicle PEM fuel cell stack under strengthened road vibrating conditions. International Journal of Hydrogen Energy 2014;39:18362–8. https://doi.org/10.1016/j.ijhydene.2014.09.054.

[121] Hou Y, Hao D, Shen J, Li P, Zhang T, Wang H. Effect of strengthened road vibration on performance degradation of PEM fuel cell stack. International Journal of Hydrogen Energy 2016;41:5123–34. https://doi.org/10.1016/j.ijhydene.2016.01.072.

[122] Haji Hosseinloo A, Ehteshami MM. Shock and vibration effects on performance reliability and mechanical integrity of proton exchange membrane fuel cells: A critical review and discussion. Journal of Power Sources 2017;364:367–73. https://doi.org/10.1016/j.jpowsour.2017.08.037.

[123] Bétournay MC, Bonnell G, Edwardson E, Paktunc D, Kaufman A, Lomma AT. The effects of mine conditions on the performance of a PEM fuel cell. Journal of Power Sources 2004;134:80–7. https://doi.org/10.1016/j.jpowsour.2004.02.026.

[124] Wang X, Wang S, Chen S, Zhu T, Xie X, Mao Z. Dynamic response of proton exchange membrane fuel cell under mechanical vibration. International Journal of Hydrogen Energy 2016;41:16287–95. https://doi.org/10.1016/j.ijhydene.2016.06.082.

[125] Palan V, Shepard WS. Enhanced water removal in a fuel cell stack by droplet atomization using structural and acoustic excitation. Journal of Power Sources 2006;159:1061–70. https://doi.org/10.1016/j.jpowsour.2005.12.020.

[126] Palan V, Shepard WS, Williams KA. Removal of excess product water in a PEM fuel cell stack by vibrational and acoustical methods. Journal of Power Sources 2006;161:1116–25. https://doi.org/10.1016/j.jpowsour.2006.06.021.

[127] Ma HK, Huang SH, Kuo YZ. A novel ribbed cathode polar plate design in piezoelectric proton exchange membrane fuel cells. Journal of Power Sources 2008;185:1154–61. https://doi.org/10.1016/j.jpowsour.2008.07.019.

[128] Ma H-K, Huang S-H, Wang J-S, Hou C-G, Yu C-C, Chen B-R. Experimental study of a novel piezoelectric proton exchange membrane fuel cell with nozzle and diffuser. Journal of Power Sources 2010;195:1393–400. https://doi.org/10.1016/j.jpowsour.2009.09.033.

[129] Ma H-K, Wang J-S, Chang Y-T. Development of a novel pseudo bipolar piezoelectric proton exchange membrane fuel cell with nozzle and diffuser. Journal of Power Sources 2011;196:3766–72. https://doi.org/10.1016/j.jpowsour.2010.12.093.

[130] Ma HK, Cheng HM, Cheng WY, Fang FM, Luo WF. Development of a piezoelectric proton exchange membrane fuel cell stack (PZT-Stack). Journal of Power Sources 2013;240:314–22. https://doi.org/10.1016/j.jpowsour.2013.03.161.

[131] Bussayajarn N, Ming H, Hoong KK, Ming Stephen WY, Hwa CS. Planar air breathing PEMFC with self-humidifying MEA and open cathode geometry design for portable applications. International Journal of Hydrogen Energy 2009;34:7761–7. https://doi.org/10.1016/j.ijhydene.2009.07.077.

[132] Santa Rosa DT, Pinto DG, Silva VS, Silva RA, Rangel CM. High performance PEMFC stack with open-cathode at ambient pressure and temperature conditions. International Journal of Hydrogen Energy 2007;32:4350–7. https://doi.org/10.1016/j.ijhydene.2007.05.042.

[133] Jeong SU, Cho EA, Kim H-J, Lim T-H, Oh I-H, Kim SH. Effects of cathode open area and relative humidity on the performance of air-breathing polymer electrolyte membrane fuel cells. Journal of Power Sources 2006;158:348–53. https://doi.org/10.1016/j.jpowsour.2005.09.044.

[134] Fuel Cell Technologies Office Multi-Year Research, Development, and Demonstration Plan | Department of Energy 2016. https://www.energy.gov/eere/fuelcells/downloads/fuel-cell-technologies-office-multi-year-research-development-and-22.

[135] Chen Y, Jiang C, Cho C. Effects of Freeze–Thaw Thermal Cycles on the Mechanical Degradation of the Gas Diffusion Layer in Polymer Electrolyte Membrane Fuel Cells. Polymers 2019;11:428. https://doi.org/10.3390/polym11030428.

[136] Gavello G, Zeng J, Francia C, Icardi UA, Graizzaro A, Specchia S. Experimental studies on Nafion® 112 single PEM-FCs exposed to freezing conditions. International Journal of Hydrogen Energy 2011;36:8070–81. https://doi.org/10.1016/j.ijhydene.2011.01.182.

[137] Alink R, Gerteisen D, Oszcipok M. Degradation effects in polymer electrolyte membrane fuel cell stacks by sub-zero operation—An in situ and ex situ analysis. Journal of Power Sources 2008;182:175–87. https://doi.org/10.1016/j.jpowsour.2008.03.074.

[138] Guo Q, Qi Z. Effect of freeze-thaw cycles on the properties and performance of membrane-electrode assemblies. Journal of Power Sources 2006;160:1269–74. https://doi.org/10.1016/j.jpowsour.2006.02.093.

[139] Lee Y, Kim B, Kim Y, Li X. Effects of a microporous layer on the performance degradation of proton exchange membrane fuel cells through repetitive freezing. Journal of Power Sources 2011;196:1940–7. https://doi.org/10.1016/j.jpowsour.2010.10.028.

[140] Hou J, Song W, Yu H, Fu Y, Shao Z, Yi B. Electrochemical impedance investigation of proton exchange membrane fuel cells experienced subzero temperature. Journal of Power Sources 2007;171:610–6. https://doi.org/10.1016/j.jpowsour.2007.07.015.

[141] Lee S-Y, Kim H-J, Cho E, Lee K-S, Lim T-H, Hwang IC, et al. Performance degradation and microstructure changes in freeze–thaw cycling for PEMFC MEAs with various initial microstructures. International Journal of Hydrogen Energy 2010;35:12888–96. https://doi.org/10.1016/j.ijhydene.2010.08.070.

[142] Islam MR, Shabani B, Rosengarten G, Andrews J. The potential of using nanofluids in PEM fuel cell cooling systems: A review. Renewable and Sustainable Energy Reviews 2015;48:523–39. https://doi.org/10.1016/j.rser.2015.04.018.

[143] Ju H, Meng H, Wang C-Y. A single-phase, non-isothermal model for PEM fuel cells. International Journal of Heat and Mass Transfer 2005;48:1303–15. https://doi.org/10.1016/j.ijheatmasstransfer.2004.10.004.

[144] Chen Y, Jiang C, Cho C. An Investigation of the Compressive Behavior of Polymer Electrode Membrane Fuel Cell's Gas Diffusion Layers under Different Temperatures. Polymers 2018;10:971. https://doi.org/10.3390/polym10090971.

[145] Khandelwal M, Mench MM. Direct measurement of through-plane thermal conductivity and contact resistance in fuel cell materials. Journal of Power Sources 2006;161:1106–15. https://doi.org/10.1016/j.jpowsour.2006.06.092.

[146] Cui T, Chao YJ, Zee JWV, Chien C-H. Effect of Temperature on Mechanical Property Degradation of Polymeric Materials. Challenges in Mechanics of Time-Dependent Materials, Volume 2, Springer, Cham; 2015, p. 41–7. https://doi.org/10.1007/978-3-319-06980-7_5.

[147] Lai Y-H, Mittelsteadt CK, Gittleman CS, Dillard DA. Viscoelastic Stress Analysis of Constrained Proton Exchange Membranes Under Humidity Cycling. J Fuel Cell Sci Technol 2009;6:021002-021002–13. https://doi.org/10.1115/1.2971045.

[148] Mason TJ, Millichamp J, Neville TP, Shearing PR, Simons S, Brett DJL. A study of the effect of water management and electrode flooding on the dimensional change of polymer electrolyte fuel cells. Journal of Power Sources 2013;242:70–7. https://doi.org/10.1016/j.jpowsour.2013.05.045.

[149] Huang G-M, Chang M-H. Effect of Gas Diffusion Layer With Double-Side Microporous Layer Coating on Proton Exchange Membrane Fuel Cell Performance Under Different Air Inlet Relative Humidity. Int J Electrochem Sci 2014;9:13.

[150] Tötzke C, Gaiselmann G, Osenberg M, Arlt T, Markötter H, Hilger A, et al. Influence of hydrophobic treatment on the structure of compressed gas diffusion layers. Journal of Power Sources 2016;324:625–36. https://doi.org/10.1016/j.jpowsour.2016.05.118.

[151] Ferreira RB, Falcão DS, Oliveira VB, Pinto AMFR. Experimental study on the membrane electrode assembly of a proton exchange membrane fuel cell: effects of microporous layer, membrane thickness and gas diffusion layer hydrophobic treatment. Electrochimica Acta 2017;224:337–45. https://doi.org/10.1016/j.electacta.2016.12.074.

[152] Biesdorf J, Forner-Cuenca A, Schmidt TJ, Boillat P. Impact of Hydrophobic Coating on Mass Transport Losses in PEFCs. J Electrochem Soc 2015;162:F1243–52. https://doi.org/10.1149/2.0861510jes.

[153] Simon C, Hasché F, Gasteiger HA. Influence of the Gas Diffusion Layer Compression on the Oxygen Transport in PEM Fuel Cells at High Water Saturation Levels. J Electrochem Soc 2017;164:F591–9. https://doi.org/10.1149/2.0691706jes.

[154] Jiao K, Li X. Water transport in polymer electrolyte membrane fuel cells. Progress in Energy and Combustion Science 2011;37:221–91. https://doi.org/10.1016/j.pecs.2010.06.002.

[155] Barbir F. PEM Fuel Cells, Second Edition: Theory and Practice. 2 edition. Amsterdam: Academic Press; 2012.

[156] Iranzo A, Boillat P. Liquid water distribution patterns featuring back-diffusion transport in a PEM fuel cell with neutron imaging. International Journal of Hydrogen Energy 2014;39:17240–5. https://doi.org/10.1016/j.ijhydene.2014.08.042.

[157] Zawodzinski TA, Springer TE, Davey J, Jestel R, Lopez C, Valerio J, et al. A Comparative Study of Water Uptake By and Transport Through Ionomeric Fuel Cell Membranes. J Electrochem Soc 1993;140:1981–5. https://doi.org/10.1149/1.2220749.

[158] Cha D, Ahn JH, Kim HS, Kim Y. Effects of clamping force on the water transport and performance of a PEM (proton electrolyte membrane) fuel cell with relative humidity and current density. Energy 2015;93:1338–44. https://doi.org/10.1016/j.energy.2015.10.045.

[159] Bazylak A. Liquid water visualization in PEM fuel cells: A review. International Journal of Hydrogen Energy 2009;34:3845–57. https://doi.org/10.1016/j.ijhydene.2009.02.084.

[160] Bazylak A, Sinton D, Liu Z-S, Djilali N. Effect of compression on liquid water transport and microstructure of PEMFC gas diffusion layers. Journal of Power Sources 2007;163:784–92. https://doi.org/10.1016/j.jpowsour.2006.09.045.

[161] Ince UU, Markötter H, George MG, Liu H, Ge N, Lee J, et al. Effects of compression on water distribution in gas diffusion layer materials of PEMFC in a point injection device by means of synchrotron X-ray imaging. International Journal of Hydrogen Energy 2018;43:391–406. https://doi.org/10.1016/j.ijhydene.2017.11.047.

[162] Mortazavi M, Santamaria AD, Chauhan V, Benner JZ, Heidari M, Médici EF. Effect of PEM fuel cell porous media compression on in-plane transport phenomena. Journal of Power Sources Advances 2020;1:100001. https://doi.org/10.1016/j.powera.2020.100001.

[163] Zenyuk IV, Parkinson DY, Hwang G, Weber AZ. Probing water distribution in compressed fuel-cell gas-diffusion layers using X-ray computed tomography. Electrochemistry Communications 2015;53:24–8. https://doi.org/10.1016/j.elecom.2015.02.005.

[164] Hartnig C, Manke I, Kuhn R, Kleinau S, Goebbels J, Banhart J. High-resolution in-plane investigation of the water evolution and transport in PEM fuel cells. Journal of Power Sources 2009;188:468–74. https://doi.org/10.1016/j.jpowsour.2008.12.023.

[165] Manke I, Hartnig Ch, Grünerbel M, Lehnert W, Kardjilov N, Haibel A, et al. Investigation of water evolution and transport in fuel cells with high resolution synchrotron x-ray radiography. Appl Phys Lett 2007;90:174105. https://doi.org/10.1063/1.2731440.

[166] Turhan A, Heller K, Brenizer JS, Mench MM. Passive control of liquid water storage and distribution in a PEFC through flow-field design. Journal of Power Sources 2008;180:773–83. https://doi.org/10.1016/j.jpowsour.2008.02.028.

[167] Owejan JP, Gagliardo JJ, Sergi JM, Kandlikar SG, Trabold TA. Water management studies in PEM fuel cells, Part I: Fuel cell design and in situ water distributions. International Journal of Hydrogen Energy 2009;34:3436–44. https://doi.org/10.1016/j.ijhydene.2008.12.100.

[168] Boillat P, Lehmann EH, Trtik P, Cochet M. Neutron imaging of fuel cells – Recent trends and future prospects. Current Opinion in Electrochemistry 2017;5:3–10. https://doi.org/10.1016/j.coelec.2017.07.012.

[169] Wu Y, Cho JIS, Lu X, Rasha L, Neville TP, Millichamp J, et al. Effect of compression on the water management of polymer electrolyte fuel cells: An in-operando neutron radiography study. Journal of Power Sources 2019;412:597–605. https://doi.org/10.1016/j.jpowsour.2018.11.048.

[170] Pragma Industries – Fuel cells – Hydrogen Energy. Pragma Industries. https://www.pragma-industries.com/.

[171] FCW2500T Chiller | JULABO GmbH. https://www.julabo.com/en/products/recirculating-coolers/fc-chiller/fcw2500t.

[172] Fuel Cell and Battery Test Equipment | Greenlight Innovation. https://www.greenlightinnovation.com/.

[173] The electronic load - Höcherl & Hackl. Höcherl & Hackl En. https://www.hoecherl-hackl.com/.

[174]: : balticFuelCells GmbH :: Innovation in fuel cell technologies. https://www.balticfuelcells.de/defaultE.html.

[175] FESTO. https://www.festo.com/net/en-gb_gb/SupportPortal/Default.aspx?q=554044.

[176] D5 & D6 LVDT Displacement Transducer. https://www.rdpe.com/ex/d5-d6.htm.

[177] S++ Simulation Services. http://www.splusplus.com/measurement/en/csshunt.html.

[178] National Institute of Standards and Technology. NIST TN 1297: Appendix D1. Terminology. NIST 2015. https://www.nist.gov/pml/nist-technical-note-1297/nist-tn-1297-appendix-d1-terminology.

[179] Nafion™ XL. https://www.fuelcellstore.com/nafion-xl.

[180] Robert M, El Kaddouri A, Perrin J-C, Mozet K, Daoudi M, Dillet J, et al. Effects of conjoint mechanical and chemical stress on perfluorosulfonic-acid membranes for fuel cells. Journal of Power Sources 2020;476:228662. https://doi.org/10.1016/j.jpowsour.2020.228662.

[181] DOE Technical Targets for Polymer Electrolyte Membrane Fuel Cell Components. EnergyGov. https://www.energy.gov/eere/fuelcells/doe-technical-targets-polymer-electrolyte-membrane-fuel-cell-components.

[182] Fuel Cells on the Rise. SGL Carbon. https://www.sglcarbon.com/en/for-a-smarter-world/fuel-cells-on-the-rise/.

[183] (PDF) SIGRACET® Gas Diffusion Layers for PEM Fuel Cells, Electrolyzers and Batteries (White Paper). https://www.researchgate.net/publication/295859224_SIGRACETR_Gas_Diffusion_Layers_for_PEM_Fuel_Cells_Electrolyzers_and_Batteries_White_Paper.

[184] Bi-polar Plates. https://www.schunk-carbontechnology.com/en/products/produkte-detail/bipolar-plates.

[185] EU HARMONISED TEST PROTOCOLS FOR PEMFC MEA TESTING IN SINGLE CELL CONFIGURATION FOR AUTOMOTIVE APPLICATIONS | EU Science Hub. https://ec.europa.eu/jrc/en/publication/eur-scientific-and-technical-research-reports/eu-harmonised-test-protocols-pemfc-mea-testing-single-cell-configuration-automotive.

[186] Bezmalinović D, Radošević J, Barbir F. Initial conditioning of Polymer Eelectrolyte Membrane fuel cell by temperature and potential cycling. Acta Chimica Slovenica 2014;62:83–7. https://doi.org/10.17344/acsi.2014.730.

[187] Gaz spéciaux - Messer France SAS. https://www.messer.fr/gaz-purs-et-melanges.

[188] Büchi FN, Scherer GG. In-situ resistance measurements of Nafion® 117 membranes in polymer electrolyte fuel cells. Journal of Electroanalytical Chemistry 1996;404:37–43. https://doi.org/10.1016/0022-0728(95)04321-7.

[189] Forner-Cuenca A, Biesdorf J, Manzi-Orezzoli V, Gubler L, Schmidt TJ, Boillat P. Advanced Water Management in PEFCs: Diffusion Layers with Patterned Wettability III. Operando Characterization with Neutron Imaging. J Electrochem Soc 2016;163:F1389. https://doi.org/10.1149/2.0891613jes.

[190] Mrozewski KJ. Diagnosis of mechanical tightening of a single polymer electrolyte membrane fuel cell (LT-PEM and HT-PEM) in aeronautical applications. PhD thesis supervisors: Christophe Turpin and Antoine Picot. Toulouse, INPT, 2019.

[191] Hottinen T, Himanen O, Karvonen S, Nitta I. Inhomogeneous compression of PEMFC gas diffusion layer: Part II. Modeling the effect. Journal of Power Sources 2007;171:113–21. https://doi.org/10.1016/j.jpowsour.2006.10.076.

[192] Bouziane K. Etude des liens entre les performances de composants de pile à combustible PEM et leurs comportements à l'intérieur de la pile observés en fonctionnement. Développement de caractérisations électriques et mécaniques in–situ et ex-situ. These en préparation. université Paris-Saclay, 2017.

[193] Smart Solutions in Graphites & Fiber Composites. SGL Carbon . https://www.sglcarbon.com/en/.

[194] Qiu D, Janßen H, Peng L, Irmscher P, Lai X, Lehnert W. Electrical resistance and microstructure of typical gas diffusion layers for proton exchange membrane fuel cell under compression. Applied Energy 2018;231:127–37. https://doi.org/10.1016/j.apenergy.2018.09.117.

[195] Pérez-Page M, Pérez-Herranz V. Study of the electrochemical behaviour of a 300 W PEM fuel cell stack by Electrochemical Impedance Spectroscopy. International Journal of Hydrogen Energy 2014;39:4009–15. https://doi.org/10.1016/j.ijhydene.2013.05.121.

[196] Tang Z, Huang Q-A, Wang Y-J, Zhang F, Li W, Li A, et al. Recent progress in the use of electrochemical impedance spectroscopy for the measurement, monitoring, diagnosis and optimization of proton exchange membrane fuel cell performance. Journal of Power Sources 2020;468:228361. https://doi.org/10.1016/j.jpowsour.2020.228361.

[197] Wasterlain S. approches expérimentales et analyse probabiliste pour le diagnostic de piles à combustible de type PEM. PhD thesis. Université de Franche-Comté, 2010.

[198] Petrone R. Electrochemical Impedance Spectroscopy for the on-board diagnosis of PEMFC via on-line identification of Equivalent Circuit Model parameters. These en préparation. Besançon, 2012.

[199] Candusso D. Hybridation du groupe électrogène à pile à combustible pour l'alimantation d'un véhicule électrique. These de doctorat. Grenoble INPG, 2002.

[200] Pivac I, Barbir F. Inductive phenomena at low frequencies in impedance spectra of proton exchange membrane fuel cells – A review. Journal of Power Sources 2016;326:112–9. https://doi.org/10.1016/j.jpowsour.2016.06.119.

[201] Chevalier S. Modélisation multiphysique de l'impédance des piles à combustible PEM. : application au diagnostic de stack par spectroscopie : application au diagnostic de stack par spectroscopie. These de doctorat. Nantes, 2013.

[202] Sadli I. Modélisation par impédance d'une pile à combustible PEM pour utilisation en électronique de puissance. These de doctorat. Vandoeuvre-les-Nancy, INPL, 2006.

[203] Yuan X-Z, Song C, Wang H, Zhang J, editors. EIS Equivalent Circuits. Electrochemical Impedance Spectroscopy in PEM Fuel Cells: Fundamentals and Applications, London: Springer; 2010, p. 139–92. https://doi.org/10.1007/978-1-84882-846-9_4.

[204] Material Mates Italia Srl. Material Mates Italia Srl. https://www.mmates.it/.

[205] Zhang J, Song C, Zhang J, Baker R, Zhang L. Understanding the effects of backpressure on PEM fuel cell reactions and performance. Journal of Electroanalytical Chemistry 2013;688:130–6. https://doi.org/10.1016/j.jelechem.2012.09.033.

[206] Iftikhar MU, Riu D, Druart F, Rosini S, Bultel Y, Retière N. Dynamic modeling of proton exchange membrane fuel cell using non-integer derivatives. Journal of Power Sources 2006;160:1170–82. https://doi.org/10.1016/j.jpowsour.2006.03.044.

[207] Kongkanand A, Gu W, Mathias MF. Proton-Exchange Membrane Fuel Cells with Low-Pt Content. In: Meyers RA, editor. Encyclopedia of Sustainability Science and Technology, New York, NY: Springer; 2017, p. 1–20. https://doi.org/10.1007/978-1-4939-2493-6_1022-1.

[208] S++ Simulation Services. http://www.splusplus.com/measurement/en/CurrentVIEW.html.

[209] Pressure measurement film "Prescale": Specifications | Fujifilm Global. http://www.fujifilm.com/products/measurement_film/en/prescale/product/.

[210] Wang J. Barriers of scaling-up fuel cells: Cost, durability and reliability. Energy 2015;80:509–21. https://doi.org/10.1016/j.energy.2014.12.007.

[211] Baumann N, Blankenship A, Dorn M, Cremers C. Evaluating Current Distribution and Influence of Defect Sites for Graphitic Compound Bipolar Plate Materials. Fuel Cells 2020;20:40–7. https://doi.org/10.1002/fuce.201900138.

[212] Bender G, Felt W, Ulsh M. Detecting and localizing failure points in proton exchange membrane fuel cells using IR thermography. Journal of Power Sources 2014;253:224–9. https://doi.org/10.1016/j.jpowsour.2013.12.045.

[213] Lü W, Liu Z, Wang C, Mao Z, Zhang M. The effects of pinholes on proton exchange membrane fuel cell performance. International Journal of Energy Research 2011;35:24–30. https://doi.org/10.1002/er.1728.

[214] Wu B, Parkes MA, de Benedetti L, Marquis AJ, Offer GJ, Brandon NP. Real-time monitoring of proton exchange membrane fuel cell stack failure. J Appl Electrochem 2016;46:1157–62. https://doi.org/10.1007/s10800-016-0995-4.

[215] Siegel C, Bandlamudi G, Filusch F, Heinzel A. Locally Resolved Measurements in a Segmented HTPEM Fuel Cell with Straight Flow-Fields. Fuel Cells 2011;11:489–500. https://doi.org/10.1002/fuce.201000101.

[216] Alaefour I, Karimi G, Jiao K, Li X. Measurement of current distribution in a proton exchange membrane fuel cell with various flow arrangements – A parametric study. Applied Energy 2012;93:80–9. https://doi.org/10.1016/j.apenergy.2011.05.033.

[217] Hwnag JJ, Chang WR, Peng RG, Chen PY, Su A. Experimental and numerical studies of local current mapping on a PEM fuel cell. International Journal of Hydrogen Energy 2008;33:5718–27. https://doi.org/10.1016/j.ijhydene.2008.07.035.

[218] Gerteisen D, Zamel N, Sadeler C, Geiger F, Ludwig V, Hebling C. Effect of operating conditions on current density distribution and high frequency resistance in a segmented PEM fuel cell. International Journal of Hydrogen Energy 2012;37:7736–44. https://doi.org/10.1016/j.ijhydene.2012.02.024.

[219] Hakenjos A, Muenter H, Wittstadt U, Hebling C. A PEM fuel cell for combined measurement of current and temperature distribution, and flow field flooding. Journal of Power Sources 2004;131:213–6. https://doi.org/10.1016/j.jpowsour.2003.11.081.

[220] Iranzo A, Boillat P, Biesdorf J, Salva A. Investigation of the liquid water distributions in a 50 cm2 PEM fuel cell: Effects of reactants relative humidity, current density, and cathode stoichiometry. Energy 2015;82:914–21. https://doi.org/10.1016/j.energy.2015.01.101.

[221] Verdin B, Fouda-Onana F, Germe S, Serre G, Jacques PA, Millet P. Operando current mapping on PEM water electrolysis cells. Influence of mechanical stress. International Journal of Hydrogen Energy 2017;42:25848–59. https://doi.org/10.1016/j.ijhydene.2017.08.189.

[222] Image Processing Toolbox. https://www.mathworks.com/products/image.html.

[223] Ouaidat G, Cherouat A, Kouta R, Chamoret D. Numerical modeling of the mechanical behavior of proton exchange membrane fuel cell performance: Design of experiment study and optimization. International Journal of Hydrogen Energy 2020. https://doi.org/10.1016/j.ijhydene.2020.06.015.

[224] Noguer N, Candusso D, Kouta R, Harel F, Charon W, Coquery G. A framework for the probabilistic analysis of PEMFC performance based on multi-physical modelling, stochastic method, and design of numerical experiments. International Journal of Hydrogen Energy 2017;42:459–77. https://doi.org/10.1016/j.ijhydene.2016.11.074.

[225] Gerteisen D, Mérida W, Kurz T, Lupotto P, Schwager M, Hebling C. Spatially Resolved Voltage, Current and Electrochemical Impedance Spectroscopy Measurements. Fuel Cells 2011;11:339–49. https://doi.org/10.1002/fuce.201000181.

Appendix A
Résumé étendu en français

1 Introduction

Une pile à combustible (PàC) est un dispositif électrochimique qui convertit l'énergie chimique d'un combustible (le plus souvent du dihydrogène ou bien un mélange riche en dihydrogène) et d'un comburant (oxygène ou air) directement en énergie électrique, en chaleur et en eau par une réaction électrochimique d'oxydoréduction. La volonté récente de développer et de commercialiser des PàCs s'explique par leurs nombreux avantages, notamment leur rendement élevé, leurs sous-produits respectueux de l'environnement (de l'eau lorsque du dihydrogène pur est utilisé, de la chaleur) et leur fonctionnement silencieux. Parmi les différents types de PàCs, les piles à combustible à membrane échangeuse de protons (Polymer Electrolyte Fuel Cells en anglais, acronyme PEFC) ont particulièrement montré un potentiel important pour les applications mobiles (telles que l'automobile et les véhicules lourds, l'aérospatiale, les applications nomades) et stationnaires (e.g. la micro-cogénération de chaleur et d'électricité) en raison de leur poids réduit, de leur compacité et de leur faible température de fonctionnement (entre 60 et 80°C pour les PEFCs basse température [1]).

L'empilement des PàCs (ou stack) nécessite l'introduction d'une compression mécanique pendant le processus d'assemblage, ce qui implique d'abord un contrôle précis pour assurer un alignement approprié des composants. Ensuite, une compression d'assemblage adaptée est appliquée afin d'obtenir des contacts (mécaniques, thermiques et électriques) adéquats entre les composants de la PàC et d'assurer un fonctionnement étanche vis-à-vis des gaz. Une PEFC est en effet une structure multi-contact dans laquelle interviennent des phénomènes multi-physiques fortement couplés. Les interactions entre ces phénomènes affectent la performance de la PEFC et sa durée de vie. Il est donc essentiel d'étudier les effets mécaniques en détail pour mieux comprendre les interactions présentes au niveau des composants de la PEFC.

Une PEFC est concernée par deux principaux types de mécanismes de compression. Le premier est dû à des forces externes (e.g. la compression appliquée pendant le processus d'assemblage, les chocs et les vibrations) ; le second est engendré par des forces internes qui sont générées à l'intérieur de la PEFC pendant son fonctionnement (e.g. l'hydratation/la déshydratation de la membrane, la variation de température, les cycles de gel/dégel). Dans les deux cas, les composants au sein de la PEFC sont soumis à des forces de compression qui peuvent soit améliorer, soit détériorer les performances de la PàC [2–4].

Dans les PEFCs en fonctionnement, la compression mécanique joue un rôle essentiel pour assurer une étanchéité aux gaz efficace ainsi que pour obtenir des conductivités (électrique et thermique) optimisées. Une pression mécanique excessive peut détériorer les performances de la PàC en réduisant la porosité et la capacité de transport des espèces (réactifs et produits) des

composants de la PEFC (GDLs). Certains effets négatifs de la compression mécanique peuvent même, à long terme, causer des pertes de performance irréversibles, affectant donc la durée de vie des piles. Il est par conséquent essentiel d'approfondir la connaissance des effets des contraintes mécaniques sur les performances des PEFCs. C'est dans ce contexte que cette thèse est menée en suivant une approche fortement expérimentale. Les investigations menées dans le cadre de ce travail combinent en effet différentes techniques de caractérisation, à savoir (1) l'analyse des performances électriques par des courbes de polarisation, (2) le suivi de la tension de PàC, (3) les mesures de déplacement mécanique, (4) l'analyse de la distribution locale des densités de courant, (5) l'analyse de la répartition locale des températures, (6) la spectroscopie d'impédance électrochimique et (7) l'analyse de la distribution de la pression mécanique. Les principaux défis scientifiques sont les suivants :

- L'approfondissement de la compréhension des phénomènes qui se déroulent dans la PEFC lorsqu'elle est soumise à des contraintes mécaniques.
- Le développement des techniques de caractérisation et d'analyse in-situ pour étudier finement les effets de la compression mécanique sur les performances de la PEFC.
- La déconvolution des différentes origines de pertes observées dans les performances électriques de la PEFC par rapport à la compression mécanique.
- La définition des corrélations entre les résultats des caractérisations in-situ et ex-situ.

Ce résumé a été rédigé dans l'objectif de présenter un aperçu général des résultats d'essais obtenus dans le cadre de cette thèse. S'il souhaite plus de détails sur ces résultats et sur les analyses réalisées, le lecteur est invité à consulter la version complète du mémoire, rédigée en anglais.

2 Présentation du projet de recherche

Les travaux présentés dans cette thèse s'inscrivent dans le cadre du projet **MIREPOIx**, qui est l'acronyme de "Study of the influence of internal **M**echan**I**cal comp**R**ession on the **E**lectrical **P**erf**O**rmance of a PEFC". L'objectif principal de ce projet est d'étudier les effets de la compression mécanique sur les composants des PEFCs en combinant des techniques de caractérisation et de modélisation électrique, électrochimique et mécanique. L'un des principaux défis scientifiques de ce projet est de développer des méthodes permettant la déconvolution des différentes sources de pertes de performance au sein de la PEFC lorsqu'elle est soumise à des contraintes mécaniques. Les travaux présentés dans cette thèse sont menés dans le cadre du développement de nouvelles procédures expérimentales permettant une compréhension approfondie des phénomènes qui se produisent dans une PEFC en fonctionnement et soumise à diverses contraintes mécaniques (i.e. caractérisation in-situ). Les investigations ex-situ sont menées par Khadidja BOUZIANE dans le cadre de sa thèse de doctorat [5]. L'objectif final des travaux de ces deux thèses est de trouver des corrélations pertinentes entre les résultats in-situ et ex-situ.

Cette thèse de doctorat de l'Université Paris-Saclay (ENS Paris-Saclay) a été financée par la Région Bourgogne-Franche-Comté (Convention N° 2017 Y_07529) et l'Université Gustave Eiffel (anciennement IFSTTAR). D'autres partenaires sont impliqués dans ce projet, en

particulier l'Université de Technologie de Belfort Montbéliard où toutes les expérimentations ont été menées, et le Fraunhofer ISE (Allemagne). Les recherches menées dans le cadre du projet MIREPOix ont également intéressé la société Plastic Omnium.

3 Expérimentations

Une partie substantielle du temps dévolu à la thèse a été consacrée au développement d'un nouvel environnement expérimental venant s'intégrer dans la plateforme hydrogène-énergie de Belfort (figure A.1). Ce nouveau moyen d'essai est principalement dédié à l'étude des effets de la compression mécanique sur les performances électriques des PEFCs. Cette phase du travail de thèse, à fort contenu technologique, a été présentée dans le troisième chapitre de ce rapport. Le banc d'essai utilisé pour le contrôle et le suivi des conditions de fonctionnement de la PEFC y a d'abord été décrit (G7805 de Greenlight Innovation® [6], donné par la société 3M à l'UTBM). Nous avons ensuite présenté le principe de fonctionnement de l'unité de compression mécanique (quickCONNECT FC225 de batlticFuelCells [7]) comprenant un régulateur de pression proportionnel, un capteur de déplacement, ainsi qu'un système de mesure des distributions locales du courant et de la température (current scan shunt de S++® [8]). Tous les appareils de mesure mis en œuvre dans le nouvel environnement expérimental ont été spécialement adaptés à nos besoins. Étant donné que la répétabilité de notre protocole d'essai était cruciale dans notre démarche, nous avons également fourni une étude de répétabilité des mesures de compression mécanique et de déplacement.

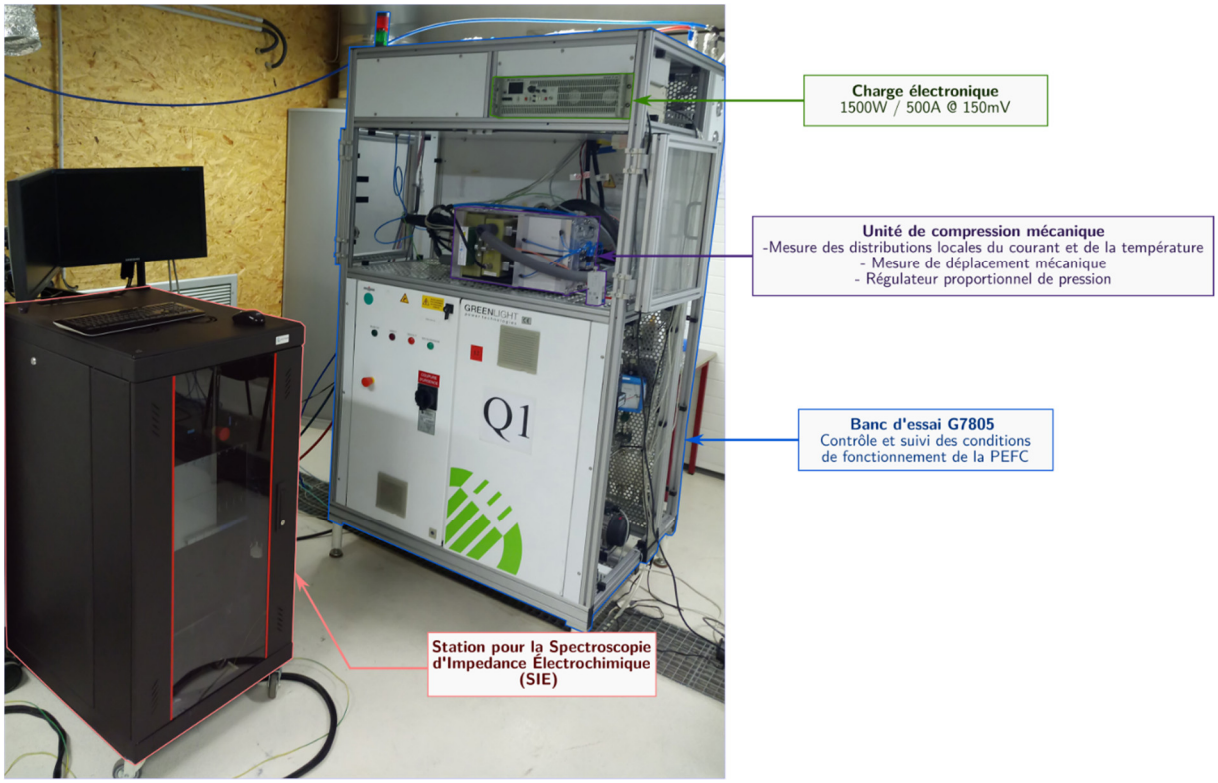

Figure A.1. Photographie du nouveau moyen d'essai dédié à l'étude des effets de la compression mécanique sur les performances électriques des PEFCs.

Les travaux menés dans cette thèse présentent l'originalité d'étudier finement les performances de la PEFC en fonction de la compression mécanique. En effet, 12 niveaux de compression mécanique « standard » ont été étudiés, allant de 0.35 MPa à 2 MPa avec des incréments de 0.15 MPa. Afin de réduire les effets de la mémoire des matériaux et de l'accumulation progressive d'eau liquide liée à une compression mécanique croissante, un protocole de compression « randomisé » a été proposé en introduisant un profil de contrainte aléatoire. Dans cette thèse, les niveaux de compression mécanique ont été étudiés sur une PEFC mono-cellule de 225 cm^2. Deux niveaux de densité de courant ont plus particulièrement été étudiés, 0.6 $A.cm^{-2}$ et 0.9 $A.cm^{-2}$, qui sont représentatifs des régions de la courbe de polarisation relatives respectivement aux pertes ohmiques et au transport des espèces. De plus, deux niveaux d'humidité relative des réactifs ont été considérés, à savoir 50 %HR et 100 %HR.

La PEFC était alimentée en Air/H_2 à des débits cathodiques et anodiques constants. Le tableau A.1 indique les conditions de fonctionnement considérées comme optimales pour notre PEFC. Ces conditions ont été maintenues tout au long des campagnes expérimentales présentées dans cette thèse.

Facteur	**Valeur**
Débit H_2	2.4 $Nl.min^{-1}$
Débit Air	19.1 $Nl.min^{-1}$
Température du fluide caloporteur de la PàC	60 °C
Contrepression à la cathode	50 kPa rel.
Contrepression à l'anode	50 kPa rel.

Tableau A.1. Conditions de fonctionnement de la PEFC investiguée.

Comme indiqué dans l'introduction, l'objectif de ce résumé est de fournir un aperçu général des résultats obtenus dans cette thèse. Nous avons choisi de présenter ici uniquement les résultats à 50%RH et 0.6 $A.cm^{-2}$. Nous avons en effet montré par nos expérimentations que ces résultats sont représentatifs des conditions optimales de la PàC mise en œuvre. Le reste des résultats et des analyses est détaillé dans la version complète du manuscrit en anglais.

4 Résultats et discussions

4.1 Courbes de polarisation

L'analyse de la courbe de polarisation est l'une des techniques les plus utilisées pour l'évaluation des performances électriques de la PEFC. Cette technique implique un balayage croissant et/ou décroissant du courant de la charge électrique afin d'obtenir une caractéristique de la tension de la PEFC en fonction de la densité de courant (i.e. mode galvanostatique). Dans notre étude, le courant a été contrôlé en utilisant un profil de charge en rampe à 2.2 $mA.cm^{-2}$ par seconde (7 minutes en moyenne pour une mesure de courbe de polarisation). La compression mécanique a été appliquée en suivant un profil de compression mécanique « randomisé ». Les courbes de polarisation obtenues pour 12 niveaux de compression mécanique, pour une humidité relative anodique et cathodique de 50%RH, sont affichées sur la figure A.2.

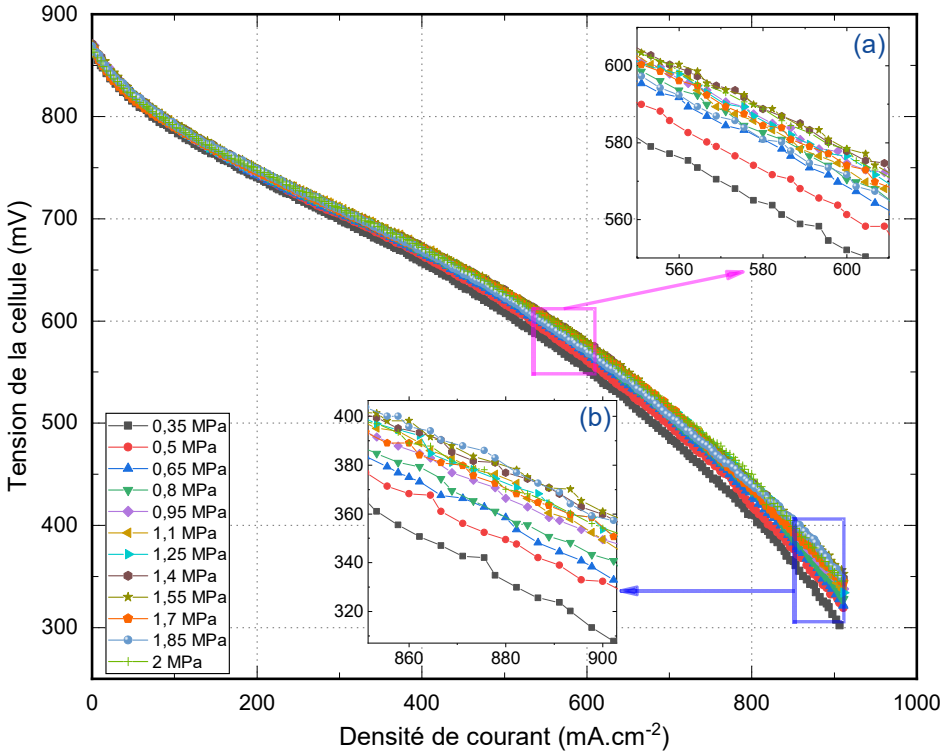

Figure A.2. Courbes de polarisation pour 12 niveaux « randomisés » de compression mécanique à 50 %RH. Les inserts (a) et (b) représentent respectivement les zones liées aux pertes ohmiques (0.6 A.cm^{-2}) et au transport des espèces (0.9 A.cm^{-2}).

L'impact de la compression mécanique sur les performances de la PEFC apparaît sur la figure A.2. Les inserts (a) et (b) correspondent respectivement aux régions en lien avec les pertes ohmiques et le transport des espèces. La figure A.2 indique que la tension de la PEFC augmente avec la compression mécanique. L'analyse des résultats de la figure A.2 montre qu'en augmentant la compression mécanique de 0.35 MPa à 1.55 MPa, la tension de la cellule s'est améliorée de 4.3 % et de 13.7 % pour des densités de courant respectives de 0.6 A.cm^{-2} et 0.9 A.cm^{-2}. Par conséquent, l'amélioration de la tension de la PàC avec la compression mécanique à haute densité de courant (i.e. 0.9 A.cm^{-2}) est plus prononcée (9.4 % de plus) par rapport à une densité de courant moyenne (i.e. 0.6 A.cm^{-2}). Ces résultats sont attribués à une meilleure humidification de la membrane à densité de courant élevée (i.e. 0.9 A.cm^{-2}).

4.2 Spectroscopie d'impédance électrochimique (SIE)

L'analyse des performances de la PEFC par SIE a été faite en étudiant les évolutions des résistances ohmiques, du transfert de charges et du transport des espèces en fonction de la compression mécanique. Les spectres d'impédance enregistrés aux 12 niveaux de compression mécanique, à 0.6 A.cm^{-2} et 50%RH, sont affichés dans la figure A.3.

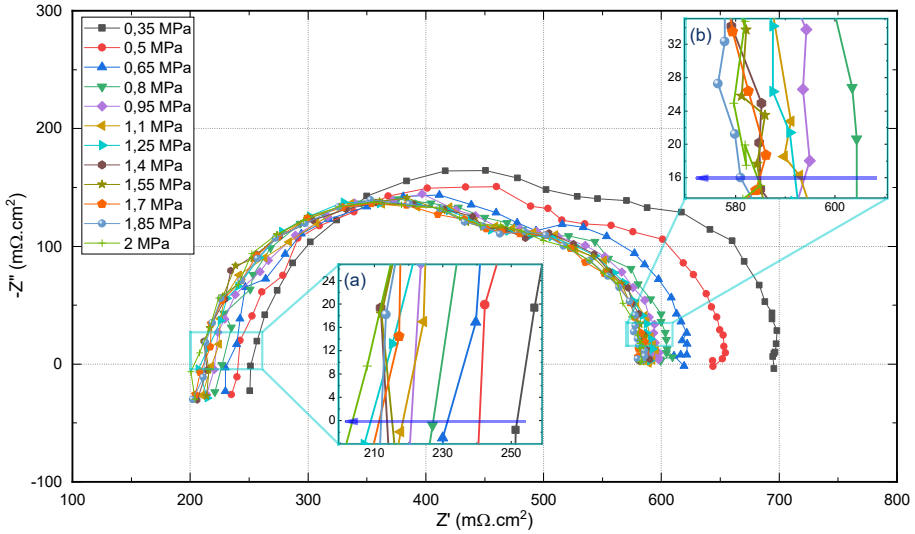

Figure A.3. Spectres d'impédance mesurés à 12 niveaux de compression mécanique à 0.6 A.cm^{-2}. Les inserts (a) et (b) représentent respectivement les régions des basses et hautes fréquences. Les flèches horizontales indiquent le sens de l'augmentation de la compression mécanique.

L'analyse des résultats de la SIE a confirmé que la réduction majeure de la résistance ohmique avec l'augmentation de la compression mécanique s'est produite entre 0.35 MPa et 1.55 MPa. A la suite de ces campagnes expérimentales, nous avons identifié deux gammes de compression mécanique. La première, correspondant à l'amélioration des performances de la PEFC, se situe entre 0.35 MPa et 1.55 MPa. La seconde plage, qui a vu les performances de la PEFC inchangées ou même commencer à se détériorer, se situe entre 1.55 MPa et 2 MPa. Les résultats de la SIE ont également confirmé que la résistance ohmique mesurée à 0.9 A.cm^{-2} est inférieure de 4 %, en moyenne, à celle mesurée à 0.6 A.cm^{-2}. Par ailleurs, il faut noter que des corrélations entre les résultats in-situ et les investigations ex-situ ont été précisées tout au long de cette thèse. Ces corrélations ont principalement mis en évidence les relations qui existent entre les évolutions des résultats ex-situ (mesurée dans le cadre du projet MIREPOIx), de la résistance de masse (épaisseur) et de contact de la GDL, et les résultats in-situ de la résistance ohmique (mesurée par la SIE). Une tendance similaire, à la baisse avec l'augmentation de la compression mécanique, a été observée pour les différentes résistances.

4.3 Mesures des densités de courant locales

Afin d'étudier les phénomènes locaux qui se produisent au sein de la PEFC lorsqu'elle est soumise à des contraintes mécaniques, les distributions locales de la densité de courant et de la température ont été analysées avec un système dédié. Celui-ci (développé par S++® Simulation Services [8]) a été spécialement conçu pour notre PEFC de 225 cm^2 avec respectivement 21×21 et 7×7 zones (ou segments) de mesure des densités du courant et des températures. Nous allons présenter dans ce résumé uniquement les résultats de la distribution locale des densités de courant. Néanmoins, l'analyse de la distribution locale des températures est détaillée dans la version complète de cette thèse.

Dans notre étude, dix matrices de distribution de densité de courant ont été collectées pour chacun des 12 niveaux de compression mécanique. Chaque valeur de densité de courant de ces

dix matrices a été moyennée et une nouvelle matrice relative aux valeurs moyennes a ainsi été obtenue. Afin de standardiser l'échelle d'affichage des résultats entre les mesures à 0.6 A.cm^{-2} et 0.9 A.cm^{-2}, les matrices moyennées ont été divisées par la valeur moyenne de la densité de courant. Ce processus de standardisation donne lieu à une échelle exprimée en pourcentage de la valeur moyenne de la densité de courant mesurée. Une valeur standardisée de 1 (soit 100 % de la valeur moyenne) correspond alors à une densité de courant de 0.6 A.cm^{-2} ou de 0.9 A.cm^{-2} selon le niveau de la densité de courant analysée. Les distributions standardisées obtenues pour la densité de courant de 0.6 A.cm^{-2} (à 50 %RH) sont représentées dans la figure A.4 pour six niveaux de compression mécanique (de 0.5 MPa à 2 MPa avec des pas de 0.3 MPa).

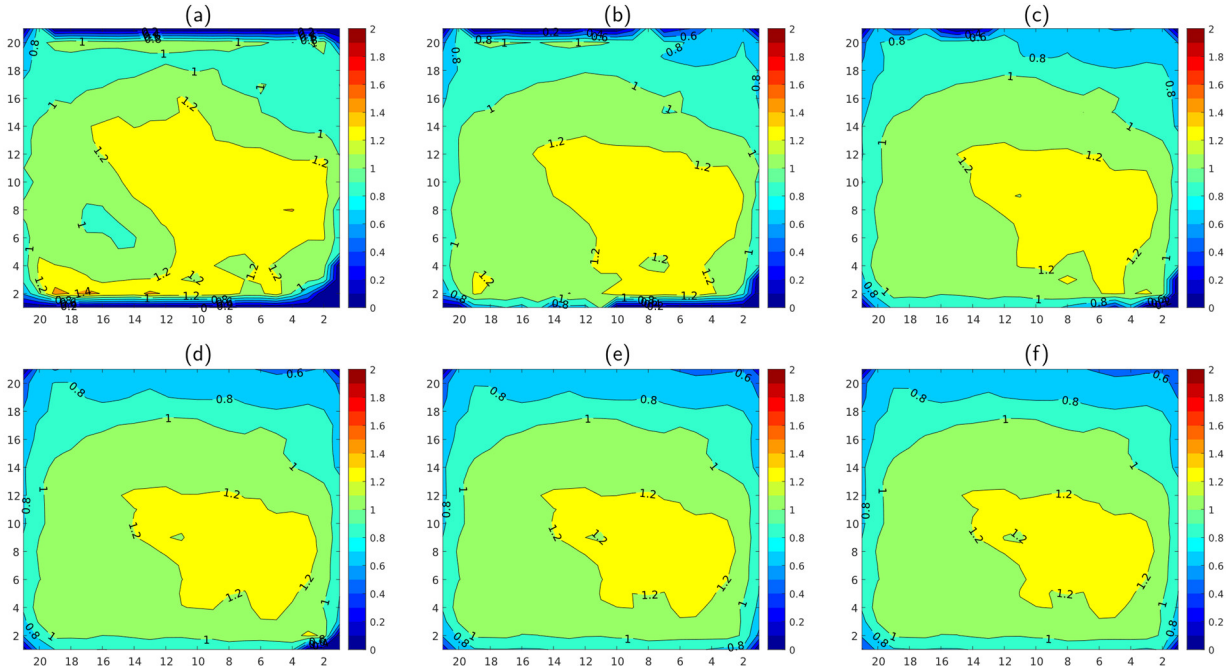

Figure A.4. Cartographies standardisées de la distribution de la densité de courant en 2-D à 0.6 A.cm^{-2} et 50 %RH. (a) 0.5 MPa, (b) 0.8 MPa, (c) 1.1 MPa, (d) 1.4 MPa, (e) 1.7 MPa, et (f) 2 MPa.

A partir de la figure A.4, nous pouvons observer que l'homogénéité spatiale de la distribution des densités locales du courant s'améliore avec l'augmentation de la compression mécanique. Cela est principalement dû à l'amélioration du contact mécanique entre les composants de la PEFC. La figure A.4 montre également que cet effet d'homogénéisation se produit principalement à des compressions mécaniques allant jusqu'à 1.4 MPa. Il est principalement visible dans les régions hautes et basses des cartographies affichées dans la figure A.4, et substantiellement dans la zone en bas à droite. En effet, la compression mécanique est insuffisante dans cette zone, ce qui entraîne une résistance électronique élevée et, par conséquent, entrave le courant à cet endroit. La majeure partie du courant passe par les zones voisines en raison de leur résistance électronique relativement plus faible. Cet effet explique également les niveaux élevés des densités locales du courant situés à proximité de la zone en bas à droite. Dans le rapport complet, les cartographies des densités de courant locales ont été analysées de manière plus détaillée, grâce à des outils statistiques et des représentations graphiques adaptées (histogrammes par exemple, voir figure A.5). Les résultats de ces analyses ont été confirmés en utilisant des films sensibles à la compression.

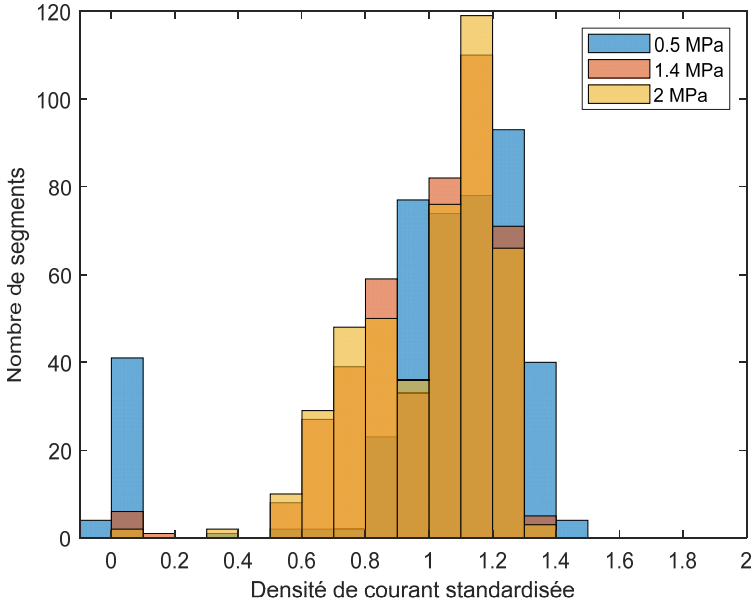

Figure A.5. Histogrammes des distributions des densités de courant standardisées. Mesures à 0.6 A.cm^{-2} et 50%RH.

4.4 Mesures de la distribution de la compression mécanique

L'obtention d'une répartition uniforme de la compression mécanique entre les composants de la PEFC est un facteur clé pour homogénéiser la distribution du courant et de la température. Dans ce sens, nous avons exploré la possibilité d'utiliser des films sensibles à la compression (Prescale® de Fujifilm [9]) afin de mesurer l'amplitude et la distribution de la compression mécanique dans la PEFC. Ce sont les films Prescale® de type LLW qui ont été utilisés dans nos expérimentations. Ce choix a été fait en considérant la gamme de mesure de pression des films LLW (i.e. optimale entre 0.5 MPa et 2.5 MPa [9]), qui est la plus adéquate avec la plage de compression mécanique explorée dans notre étude (i.e. entre 0.35 MPa et 2 MPa). Le film Prescale® de type LLW utilisé contient deux films (i.e. film A et film C). La mesure de la distribution et de l'amplitude de la compression est basée sur le principe suivant : lorsque la compression mécanique est appliquée, les microcapsules contenues dans le film A sont brisées et un matériau chromogène est libéré puis absorbé par le film C. L'intensité de la couleur obtenue indique la valeur de la compression mécanique appliquée et il devient alors possible d'évaluer l'amplitude et la distribution de la compression mécanique en analysant l'intensité de la couleur obtenue : plus la pression est élevée, plus la couleur est intense. Les images numérisées des films sensibles à la compression (i.e. films C), obtenues à six niveaux de compression mécanique (de 0.5 MPa à 2 MPa avec des pas de 0.3 MPa), sont présentées dans la figure A.6.

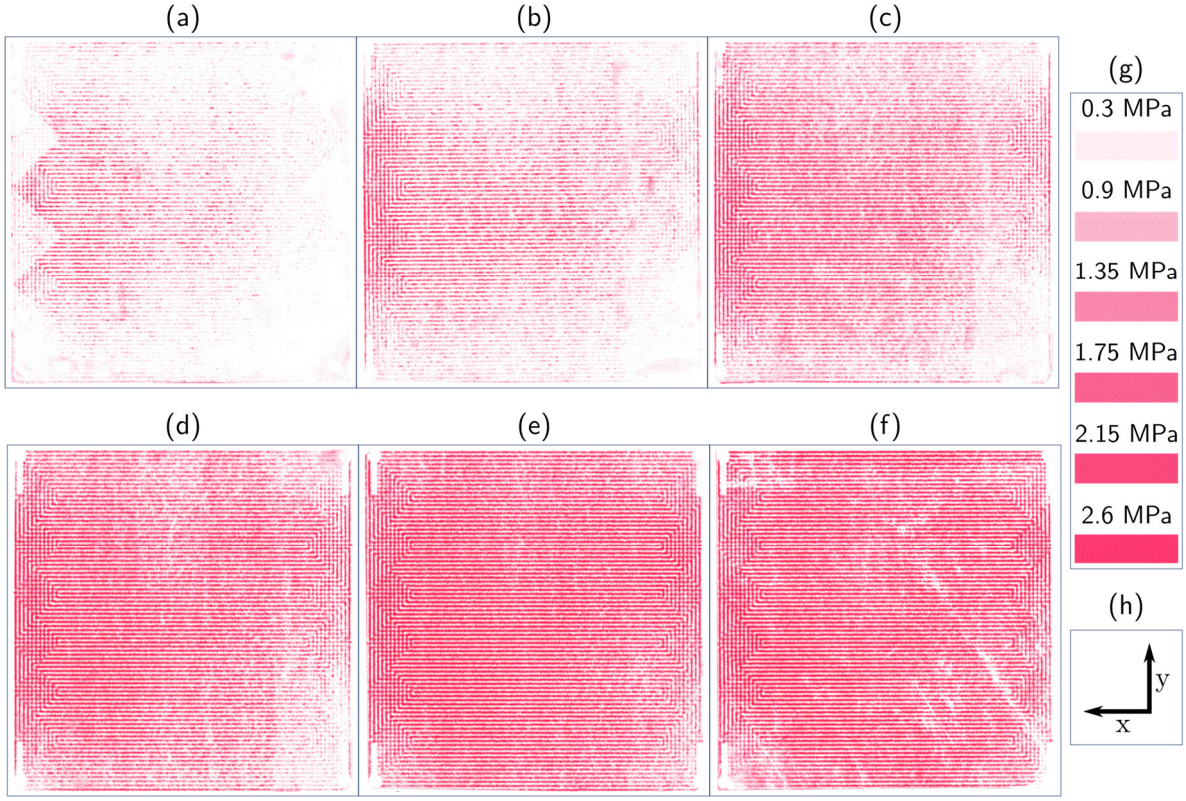

Figure A.6. Images numérisées de la distribution de la compression mécanique en fonction de la compression d'assemblage. (a) 0.5 MPa, (b) 0.8 MPa, (c) 1.1 MPa, (d) 1.4 MPa, (e) 1.7 MPa et (f) 2 MPa. Les références des couleurs indiquées en (g) sont fournies par Fujifilm et représentent les couleurs correspondant à chaque niveau de compression. (h) Système de coordonnées comme indiqué sur la figure A.4.

La figure A.6 montre que la distribution de la compression mécanique s'est améliorée avec l'augmentation de la compression d'assemblage. Cet effet d'homogénéisation est visible jusqu'à une compression d'assemblage de 1.4 MPa. Les résultats et des analyses quantitatives (basés sur du traitement des images ; détaillés dans le mémoire) ont indiqué que les régions à forte compression mécanique correspondent aux régions à fortes densités de courant locales qui, à leur tour, correspondent aux régions aux températures élevées. Par ailleurs, en comparant les résultats de cette étude avec ceux issus de l'évaluation des performances électriques de la PEFC, nous avons observé que cette homogénéisation de la compression mécanique a des effets positifs sur les performances de la PEFC en raison de la réduction de la résistance ohmique. Les résultats de cette étude menée avec les films sensibles nous ont permis de confirmer les corrélations qui existent entre l'homogénéisation des distributions de courant, de température, de la contrainte mécanique et l'amélioration des performances globales de la PEFC.

5 Conclusion

En conclusion, nous pensons avoir proposé un ensemble de travaux qui nous a permis de répondre aux défis scientifiques exposés dans l'introduction de cette thèse. En effet, les résultats de cette thèse indiquent qu'une compression mécanique allant jusqu'à 1.55 MPa améliore les

performances électriques de la PEFC dans les conditions opératoires considérées. Ces résultats ont été attribués à la réduction de la résistance ohmique, dominante par rapport à l'augmentation de la résistance au transport des espèces. Par ailleurs, nous avons montré que l'augmentation de la compression mécanique homogénéise les répartitions des densités de courant et des températures jusqu'à 1.55 MPa. Cette homogénéisation a été attribuée à une meilleure distribution de la contrainte mécanique obtenue avec une compression d'assemblage croissante. Les résultats de notre étude suggèrent que le fait de comprimer la PEFC au-delà d'un niveau spécifié (i.e. 1.55 MPa) n'entraînera pas d'amélioration significative des performances électriques. Elle pourrait même les détériorer en raison de l'augmentation de la résistance au transport des espèces. Enfin, des corrélations entre les résultats des techniques de caractérisation in-situ et ex-situ ont été fournies et analysées tout au long de la thèse.

Les résultats obtenus dans cette thèse contribuent au développement de la connaissance et de la compréhension de l'évolution des phénomènes qui se déroulent au sein d'une PEFC en fonctionnement et soumise à des contraintes mécaniques. Cette étude, qui inclut des corrélations entre des résultats de techniques de caractérisation in-situ et ex-situ, pourra aider les fabricants de PàC à développer des PEFCs aux performances et à la durabilité accrues. En effet, nous avons mis en exergue que certaines améliorations de performances, obtenues par exemple par le développement de matériaux et composants onéreux, peuvent être perdues lorsqu'une compression d'assemblage mécanique inadéquate est appliquée. Nous avons fourni dans cette thèse des résultats et des outils pour aider à atteindre une compression d'assemblage optimale et, par conséquent, optimiser la performance et la durée de vie des PEFCs. Enfin, les résultats de mesure présentés dans cette thèse pourraient également être utilisés comme paramètres d'entrée et de validation pour des modèles de PEFC intégrant des phénomènes qui ne sont généralement pas abordés en modélisation (par exemple, les inhomogénéités des distributions locales de courant et de température causées par une compression d'assemblage inadéquate). Suite aux résultats obtenus dans cette thèse, nous avons pu établir un certain nombre de recommandations et de perspectives pour des travaux futurs (notamment en termes de : corrélations in-situ/ex-situ, étude des phénomènes locaux, durée de vie, investigations sur des stacks PEFCs, étude comparative des méthodes d'assemblage des PEFCs). Ces perspectives sont détaillées dans la version complète du rapport.

6 Références

[1] C. Kalyvas, A. Kucernak, D. Brett, G. Hinds, S. Atkins, N. Brandon, Spatially resolved diagnostic methods for polymer electrolyte fuel cells: a review, Wiley Interdisciplinary Reviews: Energy and Environment. 3 (2014) 254–275. https://doi.org/10.1002/wene.86.

[2] A.M. Dafalla, F. Jiang, Stresses and their impacts on proton exchange membrane fuel cells: A review, International Journal of Hydrogen Energy. 43 (2018) 2327–2348. https://doi.org/10.1016/j.ijhydene.2017.12.033.

[3] J. Millichamp, T.J. Mason, T.P. Neville, N. Rajalakshmi, R. Jervis, P.R. Shearing, D.J.L. Brett, Mechanisms and effects of mechanical compression and dimensional change in polymer electrolyte fuel cells – A review, Journal of Power Sources. 284 (2015) 305–320. https://doi.org/10.1016/j.jpowsour.2015.02.111.

[4] E.M. Khetabi, K. Bouziane, N. Zamel, X. François, Y. Meyer, D. Candusso, Effects of mechanical compression on the performance of polymer electrolyte fuel cells and analysis through in-situ characterisation techniques - A review, Journal of Power Sources. 424 (2019) 8–26. https://doi.org/10.1016/j.jpowsour.2019.03.071.

[5] K. Bouziane, Etude des liens entre les performances de composants de pile à combustible PEM et leurs comportements à l'intérieur de la pile observés en fonctionnement. Développement de caractérisations électriques et mécaniques in–situ et ex-situ., Thèse en préparation, Université Paris-Saclay, 2017. http://www.theses.fr/s185891.

[6] Fuel Cell and Battery Test Equipment | Greenlight Innovation. https://www.greenlightinnovation.com/.

[7] balticFuelCells GmbH :: Innovation in fuel cell technologies. https://www.balticfuelcells.de/defaultE.html.

[8] S++ Simulation Services. http://www.splusplus.com/measurement/en/csshunt.html.

[9] Pressure measurement film "Prescale": Specifications | Fujifilm Global. http://www.fujifilm.com/products/measurement_film/en/prescale/product/.

Appendix B
Synthesis of the literature review

Table B.1 summarises the previously reported studies concerning the effects of mechanical compression on both the fuel cell performance and the components properties by way of in-situ electrochemical and mechanical characterisation technique

Used technique	Investigation	Compression method	Compression measurement	Active area (cm^2)	Single cell/stack	GDL Type	GDL initial thickness (µm)	GDL initial thickness measurement	Membrane / MEA used	Pt loading	FPP	Compression range MPa	Other compression data	Year of study	Ref
Polarisation curves Pressure-sensitive films	-Effect of stack clamping pressure -Optimal clamping torque determination with regard to the GDL type	Clamping torque on four bolts	Pressure-sensitive films	10	Single-cell	Toray, ELAT, and CARBEL series 100 combined with Toray	Toray: 203, ELAT:508, and CARBEL series 100 combined with Toray:279	Measured at nine points on the GDL surface	Gore ™ PRIMEA® Series 5000	0.3 mg cm^{-2} for both anode and cathode	Serpentine flow channels	Toray: 1.61, 1.8, and 2.08 MPa ELAT: 8.37, 9.3, and > 9.35 MPa CARBEL – Toray:7.34, 8.6, and 8.75 MPa	Clamping torque of 11.3, 14.12, and 16.94 N.m	1999	[1]
Polarisation curves	-Effect of GDL compression on the PEFC performance	Clamping torque on eight bolts plus a large central screw	Two gauges on both cell sides	50	Single-cell	ELAT carbon cloth with a double-sided MPL Toray carbon fibre paper with an MPL	N/A	N/A	Nafion ® 115	0.4 mg cm^{-2} for both anode and cathode	Single serpentine flow channels	N/A	Compression ratios[2] ranging from 10% to 45%	2006	[2]
Polarisation curves Measurement of electro-physical properties of the GDL	-Effect of stack clamping pressure -Optimal clamping torque determination	N/A	N/A	25	Single-cell	Toray	120	Measured with a thickness gauge	N/A	N/A	Serpentine graphite of five uniformly spaced channels and bends	Clamping pressure of 0.2, 1, and 2 MPa	N/A	2007	[3]
Polarisation curves Pressure-sensitive films	-Effect of stack clamping pressure -Pressure distribution analysis	Compression unit using a torque wrench on central bolt pushing a flat metal plate	Clamping torque from a torque wrench	25	Single-cell	Toray H-060	N/A	N/A	N/A	3.5 mg m^{-3}	Single serpentine with ribs and channels width of 1.5 mm.	Clamping pressure from 0.8 to 5 MPa	N/A	2007	[4]

Polarisation curves Electrical conductivity, gas permeability measurements SEM images	-Effect of GDL compression and material properties	N/A	N/A	25	Single-cell	Carbon fibre cloth OC14 and NC14	OC14: 510 NC14: 430	N/A	Nafion® NRE212	N/A	Serpentine graphite plate	N/A	Compression ratio ranging from 3% to 90%.	2008	[5]
Polarisation curves Pressure-sensitive films	-Effects of clamping torque and bolt configuration -Pressure distribution analysis	2, 4, and 6 clamping blots torque (according to USFCC[1])	Clamping torque from torque wrench Post-processing of pressure-sensitive films' images	100	Single & 10 cell stack	Toray carbon paper (TGP-H-090)	N/A	N/A	Nafion® 212	Anode and cathode Pt/Ru 0.5 mg cm^{-2} and Pt 0.65 mg cm^{-2}, respectively	Pelcan® graphite BPP, 155 x 85 x4 mm, three-parallel-channel serpentine flow fields, cathode and anode channel width 1 and 0.6 mm, respectively	N/A	Clamping torque values of 8, 12, and 16 Nm	2009	[6]
Piezoresistive pressure-sensitive film	-Assembly pressure distribution	Torque bolts	Directly from a calibrated torque wrench	50	Single-cell	N/A	N/A	N/A	N/A	N/A	N/A	N/A	Torque bolts of 2, 4, 6, 8, 10, and 11 Nm	2009	[7]
Polarisation curves	-Effect of stack clamping pressure -Performance stability under anode reformate gas condition	Clamping torque on six bolts	N/A	N/A	5 cell stack	Sigracet® 10BC carbon-fibre felt with MPL	380	Manufacturer data from SGL	Gore™ PRIMEA® series 57	N/A	N/A	N/A	Compression ratios of 15% and 30%	2010	[8]
Polarisation curves EIS analysis	-Effect of endplate thickness (through numerical simulations) and bolt torques (experimental)	Clamping torque on six bolts	N/A	225	Single & 50 cell stack	N/A	N/A	N/A	N/A	N/A	Graphite plates	N/A	Clamping torque ranging from 5 to 30 Nm	2010	[9]
Polarisation curves EIS analysis	-Effect of clamping pressure uniformity and clamping torque	Clamping torque on six bolts	N/A	225	Single & three-	MPL coated Sigracet®	N/A	N/A	Nafion® 112	0.4 mg cm^{-2} for both	Parallel serpentine	N/A	Clamping torque ranging	2010	[10]

	-Optimal clamping torque determination				cell stack	carbon cloth				anode and cathode			from 5 to 30 Nm		
Polarisation curves Piezoresistive pressure-sensitive film	-Effect of bolt torques and gasket materials -Pressure distribution analysis	Clamping torque on four bolts	N/A	25	Single-cell	Textron Carbon cloth GDL	350	Measured with a thickness gauge	Nafion ® 115	0.1 mg cm^{-2} for both anode and cathode	Graphite plates	N/A	Clamping torque ranging from 7 to 13 Nm	2011	[11]
Polarisation and power curves measurements EIS analysis SEM images	-Effect of GDL compression and MPL coating	Clamping torque	N/A	25	Single-cell	MPL coated and uncoated carbon cloth (SAATI SpA)	-MPL Coated GDLs: ~420 - 450 -Uncoated GDL: ~400	Measured from SEM images	Nafion ® 212	0.3 mg cm^{-2} at the anode and 0.6 mg cm^{-2} for the cathode	Anode: Single serpentine Cathode: triple parallel serpentine	N/A	Compression ratios of 30 and 50 %	2011	[12]
EIS analysis Dimensional change analysis Electrolyte membrane resistance measurement	-Effect of membrane hydration and electrodes flooding on the dimensional change and the PEFC performance	Cell Compression Unit (CCU)	Directly from the CCU	5	Single-cell	Toray H-060	N/A	N/A	Nafion ® 117	N/A	Single serpentine with land and channel width of 1.2 mm and 1.1 mm respectively.	Clamping pressure from 0.2 to 1.2 MPa	N/A	2013	[13]
Polarisation curves EIS analysis Dimensional change analysis	-Effect of assembly pressure	Cell Compression Unit (CCU)	Directly from the CCU	5	Single-cell	Toray H-060	190	Manufacturer data from Toray	Nafion ® 212	N/A	Single serpentine with land and channel width of 1.2 mm and 1.1 mm respectively.	Clamping pressure from 0.5 to 2.5 MPa	N/A	2013	[14]
Pressure-sensitive films	-Effects of: clamping pressure, clamping duration, central compressive load, and GDL type	Torque wrench on the bolts and hydraulic press on the centre region of the stack	Clamping torque from a torque wrench	N/A	16 cell stack	- MPL coated GDL - uncoated GDL	- MPL Coated GDL: 254 - Uncoated GDL: 140	Measured using a digital calliper	N/A	N/A	N/A	Ranging from 0.5 to 2.5 MPa with an increment of 0.5 MPa	Clamping torque: 10.17 N.m Hydraulic press: 59.16 N, 11.12 kN, 15.57 kN	2013	[15]

Polarisation curves EIS analysis SEM images Electrical resistivity measurement Capillary flow porometry	-Effect of compressive loads on the pore structure of the GDLs -Determination of optimal clamping pressure and pore structure	GDLs compressed ex-situ using a hydraulic press	Pressures from the hydraulic press	6.25	Single-cell	Carbon cloth GDL	N/A	N/A	Nafion ® 212	0.9 mg cm^{-2} (total) for both anode and cathode	N/A	19.61, 58,8, and 98 MPa	Compression ratios of 16.6, 22.2, and 30.55%	2014	[16]
Polarisation curves EIS analysis	-Effect of assembly pressure on PEFC performance and water management	Clamping torque	N/A	25	Single-cell	Toray TGP-H-120	N/A	N/A	Gore ™ M815 series	N/A	Three lines modified serpentine with ribs and channels width of 1.2 mm.	N/A	Clamping torque ranging from 5.9 to 8.9 Nm	2015	[17]
Pressure distribution analysis Polarisation curves	-Optimal clamping torque determination	Clamping torque on eight bolts	N/A	20	Single-cell	N/A	N/A	N/A	Nafion ® 212	0.6 mg cm^{-2} for both anode and cathode	Graphite, double serpentine flow channels for anode and parallel flow channels for cathode	0.5 to 3 MPa (only for ex-situ measurement of the contact resistance)	Clamping torque values 0.5, 1.0, 1.5, 2.0, and 2.5 Nm	2016	[18]
Polarisation curves EIS analysis Pressure-sensitive films SEM images	-Effect of GDL compression on oxygen transport -Pressure distribution analysis	Clamping torque on eight bolts	Calculated from the measured variation in the thickness of the gaskets	5	Single-cell	MPL coated GDL: Sigracet 25BC Uncoated GDL: Sigracet 25BA	25BC: 220 ± 10 24BA: 153 ± 14	Measured with a thickness gauge and SEM images	Gore ™ A510.1 /M715 .18/C5 80.4	0.1 mg cm^{-2} at the anode and 0.4 mg cm^{-2} for the cathode	Serpentine graphite plates with ribs and channels width of 0.5 mm.	N/A	Compression ratios ranging from 8 to 53%	2017	[19]
Polarisation curves EIS analysis Neutron radiography	-Effect of GDL compression on the water management of the PEFC and its performance.	Clamping torque on bolts	Measured using a pressure transducer	25	Single-cell	ELE00162 Johnson Matthey MPL coated	210 ± 5 µm	Measured with a micrometre	Nafion ® 212	0.4 mg cm^{-2} at the anode and the cathode	Serpentine flow channels with ribs and channels width of 1 mm.	1.0 MPa, 1.8 MPa, and 2.3 MPa	Compression ratios of 16.7, 26.2, and 31%	2019	[20]

Polarisation curves	-Effect of assembly pressure and method on PEFC performance	hydraulic press and clamping torque on eight bolts	Measured from torque wrench and hydraulic press	25	Single-cell	Freudenberg-H23C3	N/A	N/A	From 3M ™	N/A	Graphite three parallel serpentine flow channels	N/A	Clamping torque from 0.4 to 1.9 Nm (torque wrench); Clamping force from 1341 to 6340 N	2020	[21]
Current and temperature distribution Pressure-sensitive films	-Effect of stack clamping pressure and method -Optimal clamping torque determination	Clamping torque on fourteen bolts	N/A	250	20-cell stack	MPL coated GDL	N/A	N/A	From Gore ™	0.1 mg cm^{-2} at the anode and 0.4 mg cm^{-2} for the cathode	laser-welded metallic plates. 40 parallel channels with ribs and channels width of 1 mm.	N/A	Clamping torques of 4, 6, and 8 N.m	2020	[22]

Table B.1. Summary of literature studies on the effects of mechanical compression on PEFC performance.

[1]United State Fuel Cell Council.

[2]The ratio of the operating thickness of the GDL to its original thickness.

References

[1] Lee W, Ho C-H, Van Zee JW, Murthy M. The effects of compression and gas diffusion layers on the performance of a PEM fuel cell. Journal of Power Sources 1999;84:45–51. https://doi.org/10.1016/S0378-7753(99)00298-0.

[2] Ge J, Higier A, Liu H. Effect of gas diffusion layer compression on PEM fuel cell performance. Journal of Power Sources 2006;159:922–7. https://doi.org/10.1016/j.jpowsour.2005.11.069.

[3] Chang WR, Hwang JJ, Weng FB, Chan SH. Effect of clamping pressure on the performance of a PEM fuel cell. Journal of Power Sources 2007;166:149–54. https://doi.org/10.1016/j.jpowsour.2007.01.015.

[4] Ous T, Arcoumanis C. Effect of compressive force on the performance of a proton exchange membrane fuel cell. Proceedings of the Institution of Mechanical Engineers, Part C: Journal of Mechanical Engineering Science 2007;221:1067–74. https://doi.org/10.1243/09544062JMES654.

[5] Lin J-H, Chen W-H, Su Y-J, Ko T-H. Effect of gas diffusion layer compression on the performance in a proton exchange membrane fuel cell. Fuel 2008;87:2420–4. https://doi.org/10.1016/j.fuel.2008.03.001.

[6] Wen C-Y, Lin Y-S, Lu C-H. Experimental study of clamping effects on the performances of a single proton exchange membrane fuel cell and a 10-cell stack. Journal of Power Sources 2009;192:475–85. https://doi.org/10.1016/j.jpowsour.2009.03.058.

[7] Montanini R, Squadrito G, Giacoppo G. EXPERIMENTAL EVALUATION OF THE CLAMPING PRESSURE DISTRIBUTION IN A PEM FUEL CELL USING MATRIX-BASED PIEZORESISTIVE THIN-FILM SENSORS 2009:6.

[8] Yim S-D, Kim B-J, Sohn Y-J, Yoon Y-G, Park G-G, Lee W-Y, et al. The influence of stack clamping pressure on the performance of PEM fuel cell stack. Current Applied Physics 2010;10:S59–61. https://doi.org/10.1016/j.cap.2009.11.042.

[9] Asghari S, Shahsamandi MH, Ashraf Khorasani MR. Design and manufacturing of end plates of a 5kW PEM fuel cell. International Journal of Hydrogen Energy 2010;35:9291–7. https://doi.org/10.1016/j.ijhydene.2010.02.135.

[10] Asghari S, Mokmeli A, Samavati M. Study of PEM fuel cell performance by electrochemical impedance spectroscopy. International Journal of Hydrogen Energy 2010;35:9283–90. https://doi.org/10.1016/j.ijhydene.2010.03.069.

[11] Gatto I, Urbani F, Giacoppo G, Barbera O, Passalacqua E. Influence of the bolt torque on PEFC performance with different gasket materials. International Journal of Hydrogen Energy 2011;36:13043–50. https://doi.org/10.1016/j.ijhydene.2011.07.066.

[12] Dotelli G, Omati L, Gallo Stampino P, Grassini P, Brivio D. Investigation of gas diffusion layer compression by electrochemical impedance spectroscopy on running polymer electrolyte membrane fuel cells. Journal of Power Sources 2011;196:8955–66. https://doi.org/10.1016/j.jpowsour.2011.01.078.

[13] Mason TJ, Millichamp J, Neville TP, Shearing PR, Simons S, Brett DJL. A study of the effect of water management and electrode flooding on the dimensional change of polymer electrolyte fuel cells. Journal of Power Sources 2013;242:70–7. https://doi.org/10.1016/j.jpowsour.2013.05.045.

[14] Mason TJ, Millichamp J, Shearing PR, Brett DJL. A study of the effect of compression on the performance of polymer electrolyte fuel cells using electrochemical impedance spectroscopy and dimensional change analysis. International Journal of Hydrogen Energy 2013;38:7414–22. https://doi.org/10.1016/j.ijhydene.2013.04.021.

[15] Bates A, Mukherjee S, Hwang S, Lee SC, Kwon O, Choi GH, et al. Simulation and experimental analysis of the clamping pressure distribution in a PEM fuel cell stack. International Journal of Hydrogen Energy 2013;38:6481–93. https://doi.org/10.1016/j.ijhydene.2013.03.049.

[16] Senthil Velan V, Velayutham G, Rajalakshmi N, Dhathathreyan KS. Influence of compressive stress on the pore structure of carbon cloth based gas diffusion layer investigated by capillary flow porometry. International Journal of Hydrogen Energy 2014;39:1752–9. https://doi.org/10.1016/j.ijhydene.2013.11.038.

[17] Cha D, Ahn JH, Kim HS, Kim Y. Effects of clamping force on the water transport and performance of a PEM (proton electrolyte membrane) fuel cell with relative humidity and current density. Energy 2015;93:1338–44. https://doi.org/10.1016/j.energy.2015.10.045.

[18] Hassan NU, Kilic M, Okumus E, Tunaboylu B, Soydan AM. Experimental determination of optimal clamping torque for AB-PEM fuel cell. Journal of Electrochemical Science and Engineering 2016;6:9–16. https://doi.org/10.5599/jese.198.

[19] Simon C, Hasché F, Gasteiger HA. Influence of the Gas Diffusion Layer Compression on the Oxygen Transport in PEM Fuel Cells at High Water Saturation Levels. J Electrochem Soc 2017;164:F591–9. https://doi.org/10.1149/2.0691706jes.

[20] Wu Y, Cho JIS, Lu X, Rasha L, Neville TP, Millichamp J, et al. Effect of compression on the water management of polymer electrolyte fuel cells: An in-operando neutron radiography study. Journal of Power Sources 2019;412:597–605. https://doi.org/10.1016/j.jpowsour.2018.11.048.

[21] Uzundurukan A, Bilgili M, Devrim Y. Examination of compression effects on PEMFC performance by numerical and experimental analyses. International Journal of Hydrogen Energy 2020. https://doi.org/10.1016/j.ijhydene.2020.04.275.

[22] Peng L, Shao H, Qiu D, Yi P, Lai X. Investigation of the non-uniform distribution of current density in commercial-size proton exchange membrane fuel cells. Journal of Power Sources 2020;453:227836. https://doi.org/10.1016/j.jpowsour.2020.227836.

Appendix C
Specifications of the test bench G7805

Equipment	Range	Accuracy	Reference
Air mass flow meter /controller	0-50 Nl.min^{-1}	±0.5% Rd [1] ±0.1% FS [2]	Bronkhorst F-201AC
H_2 mass flow meter /controller	0-15 Nl.min^{-1}	±0.5% Rd [1] ±0.1% FS [2]	Bronkhorst EL-FLOW F-201C
N_2 mass flow meter /controller	0-15 Nl.min^{-1}	±0.5% Rd [1] ±0.1% FS [2]	Bronkhorst EL-FLOW F-201C
Cathode and anode compartments pressure regulator	0-4 barg	± 0.25% FS [2]	Fairchild TDEI 7800-415
Cathode and anode inlet pressure transducer	0-6 bara	± 1% FS [2]	WIKA ECO-1
Cathode and anode outlet pressure transducer	0-4 bara	± 1% FS [2]	WIKA ECO-1

Table C.1. Overview of the technical specifications of the main sensors and actuators used in the test bench - Greenlight G7805.

[1] Percentage of Full Scale

[2] Percentage of Reading

Appendix D
Repeatability study – displacement measurements

Displacement measurements at atm:

Average standard deviation (µm)	0.6
Median standard deviation (µm)	0.58
Average first cycle offset (µm)	5.7

Displacement measurements at 12.5 kPa:

Average standard deviation (µm)	0.08
Median standard deviation (µm)	0
Average first cycle offset (µm)	5

Displacement measurements at 25 kPa:

Average standard deviation (µm)	0.16
Median standard deviation (µm)	0
Average first cycle offset (µm)	6

Appendix E
Cathode backpressure measurements as a function of mechanical compression

The cathode outlet backpressure variations, at both 0.6 A.cm^{-2} and 0.9 A.cm^{-2}, with changing mechanical compression using the randomised protocol are shown in figure B.1. It has to be noted that the test bench used (i.e. Greenlight G7805, see chapter 3 for more information) regulates the backpressure at the inlet of the fuel cell reactants whereas the outlet is only used for backpressure measurement, and therefore is kept variable.

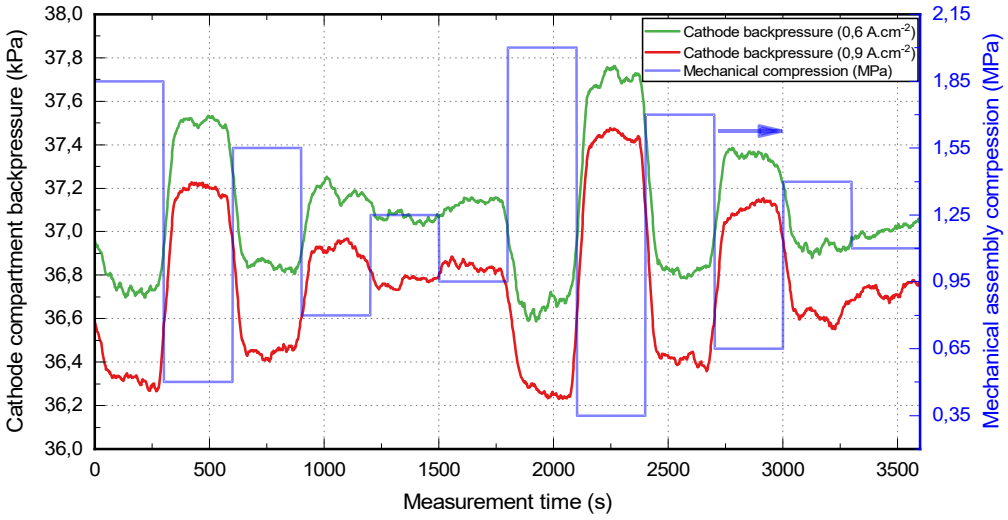

Figure E.1. Variation of the cathode backpressure (i.e. 50 kPa) as a function of mechanical compression at 0.6 A.cm^{-2} and 0.9 A.cm^{-2}. Plotted values correspond to the moving average of 15 measured points per 150 measurements per mechanical compression level.

It can be observed from figure E.1 that mechanical compression impacts the reactants backpressure at the cathode outlet, which is mainly due to both the reduction of the GDL porosity and the GDL fibres intrusion into the FFPs channels. In fact, significant gas pressure losses occur when the GDLs are compressed, which reduces the backpressure at the cathode outlet. This effect was not discernible at the anode outlet due to the low anode flowrate compared to the cathode one (2.4 Nl.min^{-1} at the anode compared to 19.1 Nl.min^{-1} at the cathode). Figure E.1 also shows that the backpressure value is lower at 0.9 A.cm^{-2} compared to 0.6 A.cm^{-2}. This difference is mainly attributed to the substantial water production rate at high current density (i.e. 0.9 A.cm^{-2}) compared to medium one (i.e. 0.6 A.cm^{-2}) leading to gas

pressure decrease due to friction losses. For better readability, figure E.2 shows the average backpressure values, of 150 measured points, as a function of mechanical compression.

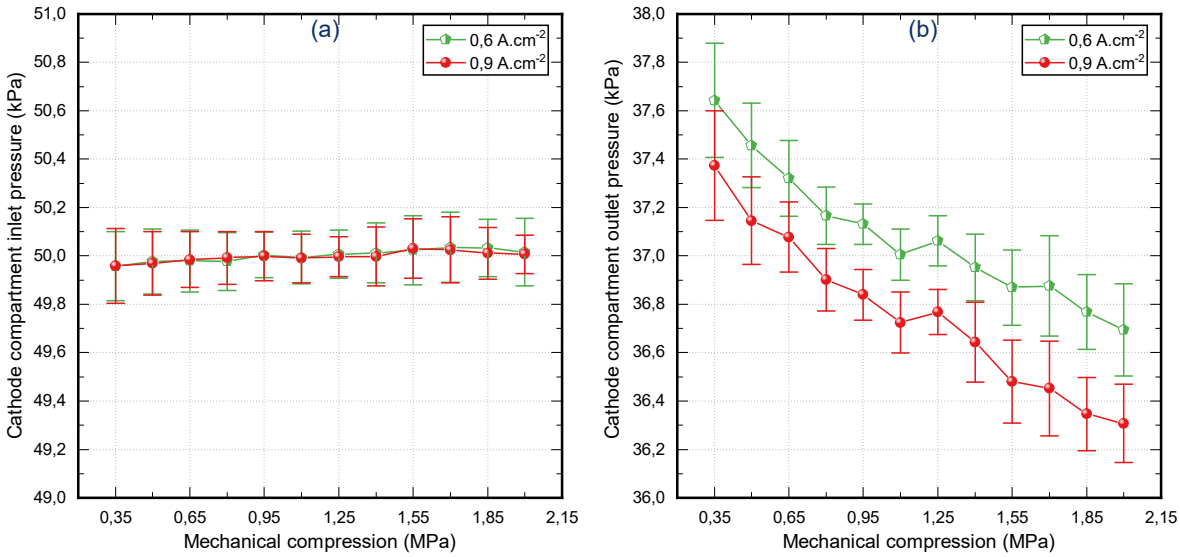

Figure E.2. Variation of the cathode compartment inlet (a) and outlet (b) pressure as a function of mechanical compression at 0.6 and 0.9 A.cm^{-2} using randomised mechanical compression protocol. Data (b) from figure 5.30.

It can be observed from figure E.2 that the mechanical compression reduces the pressure measured at the cathode outlet, whereas the inlet pressure remains constant. Since the cathode backpressure was regulated using the inlet pressure, the outlet pressure was mainly affected by both the reduction of the GDL porosity and GDL fibres intrusion into the FFPs channels with increasing mechanical compression. This effect was reported to cause PEFC voltage decrease [1] and, therefore, emphasises the fact that the mechanical compression has a negative impact on the PEFC performance as it reduces the pressure of the reactants within the PEFC. However, this impact was hindered by the relatively higher increase in the cell voltage by reducing the ohmic resistance of the PEFC as reported in chapter 5 of this thesis.

Reference

[1] J. Zhang, C. Song, J. Zhang, R. Baker, L. Zhang, Understanding the effects of backpressure on PEM fuel cell reactions and performance, Journal of Electroanalytical Chemistry. 688 (2013) 130–136. https://doi.org/10.1016/j.jelechem.2012.09.033.

Appendix F
Local current and temperature distributions – additional data

Current density distribution analysis at 0.9 A.cm^{-2}

Results at 50%RH

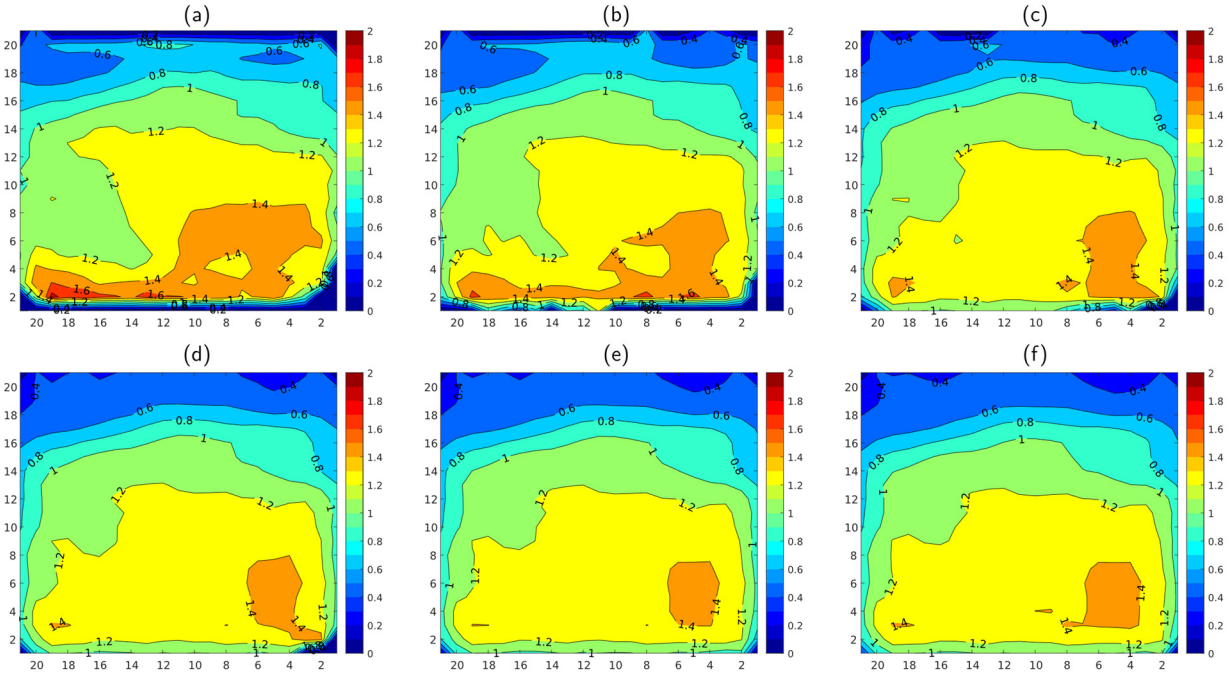

Figure F.1. Standardised current density distribution 2-D maps at 0.9 A.cm^{-2} and 50%RH. (a) 0.5 MPa, (b) 0.8 MPa, (c) 1.1 MPa, (d) 1.4 MPa, (e) 1.7 MPa, and (f) 2 MPa. Colour bars show the corresponding colours of each level of the standardised current density.

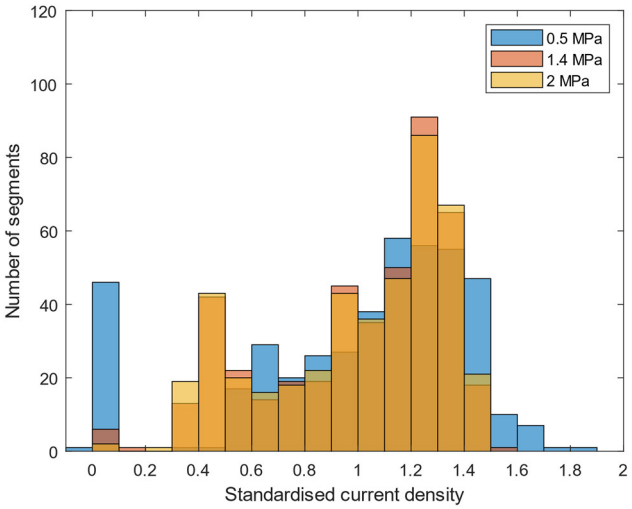

Figure F.2. Histograms of the standardised current density distribution at three levels of mechanical compression: 0.5 MPa, 1.4 MPa, and 2 MPa. Histograms obtained at 0.9 A.cm^{-2} and 50 %RH.

Results at 100%RH

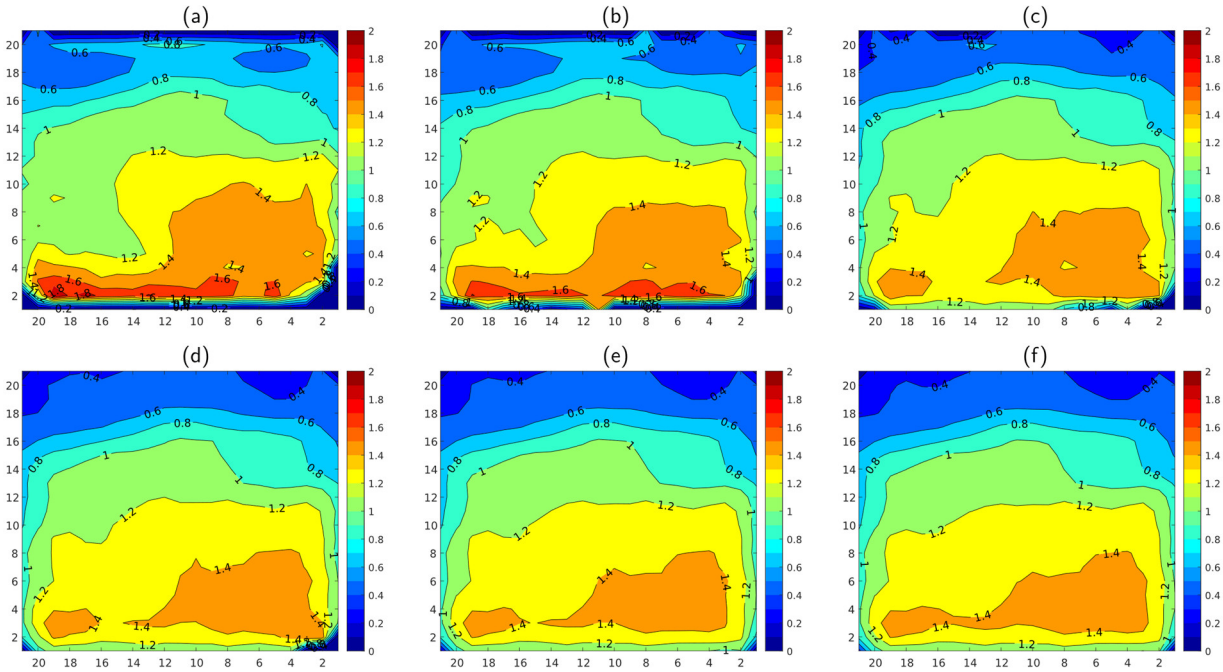

Figure F.3. Standardised current density distribution 2-D maps at 0.9 cm^{-2} and 100%RH. (a) 0.5 MPa, (b) 0.8 MPa, (c) 1.1 MPa, (d) 1.4 MPa, (e) 1.7 MPa, and (f) 2 MPa. Colour bars show the corresponding colours of each level of the standardised current density.

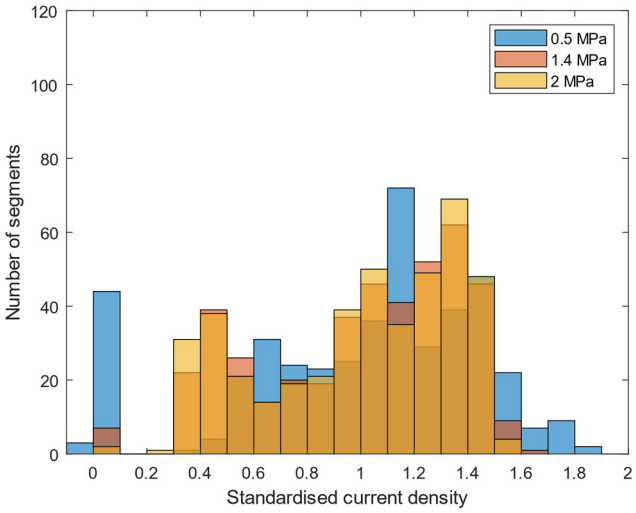

Figure F.4. Histograms of the standardised current density distribution at three levels of mechanical compression: 0.5 MPa, 1.4 MPa, and 2 MPa. Histograms obtained at 0.9 A.cm^{-2} and 100 %RH.

Statistical analysis of the standardised current density distributions at 0.9 A.cm^{-2}

- Evolution of the standard deviation of the current density distribution at 0.9 A.cm^{-2}

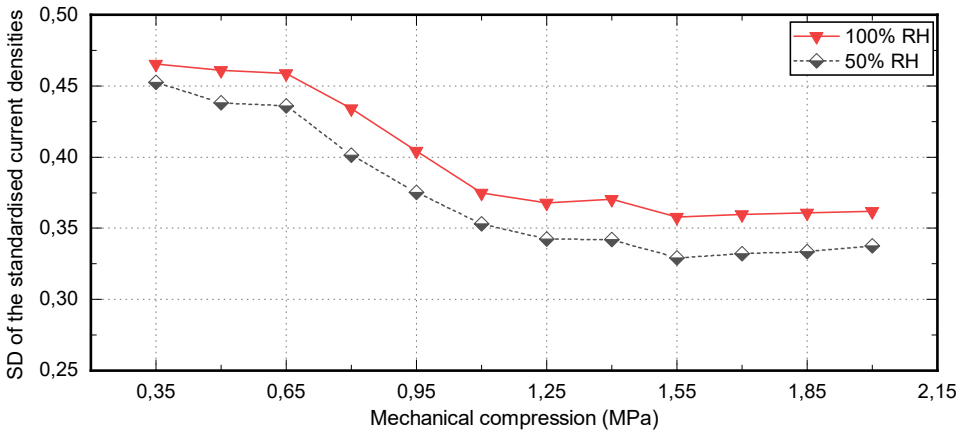

Figure F.5. SD evolution of the standardised current density distribution as a function of mechanical compression at 0.9 A.cm^{-2}. Results at 50%RH and 100%RH.

Relative humidity	50%RH		100%RH	
Mechanical compression range	First range: 0.35 → 1.55 MPa	Second range: 1.55 → 2 MPa	First range: 0.35 → 1.55 MPa	Second range: 1.55 → 2 MPa
SD reduction	27.2 %	2.6 %	23.1 %	-1.1 %

Table F.1. The reduction in the SD of the standardised current density distributions as a function of mechanical compression range at 0.9 A.cm^{-2}. Results at 50%RH and 100%RH.

- Evolution of the maximum standardised current density of the current density distribution at 0.9 A.cm^{-2}

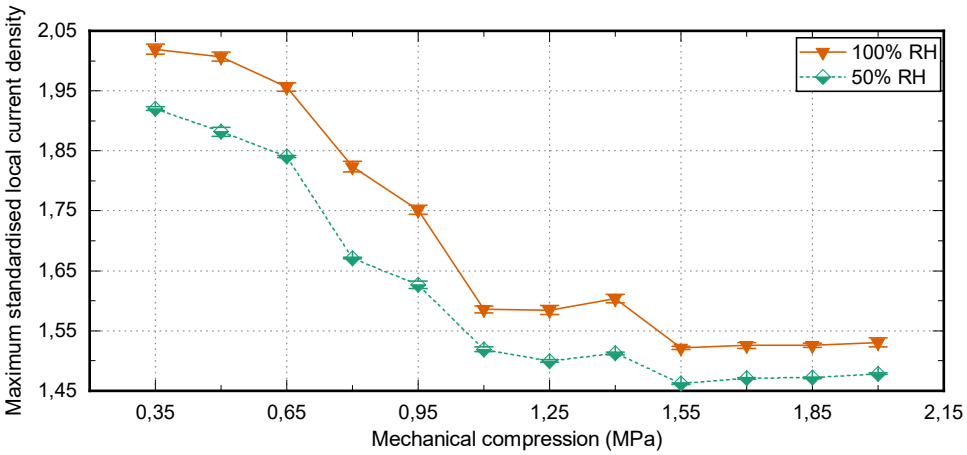

Figure F.6. Maximum standardised local current density evolution as a function of mechanical compression at 0.9 A.cm^{-2}. Results at 50%RH and 100%RH.

Relative humidity	50%RH		100%RH	
Mechanical compression range	First range: 0.35 → 1.55 MPa	Second range: 1.55 → 2 MPa	First range: 0.35 → 1.55 MPa	Second range: 1.55 → 2 MPa
Maximum current density reduction	23.9 %	1.1 %	24.6 %	-0.6 %

Table F.2. Reduction in the maximum standardised current density as a function of mechanical compression range at 0.9 A.cm^{-2}. Results at 50%RH and 100%RH.

Temperature distribution analysis at 0.9 A.cm^{-2}

Results at 50%RH

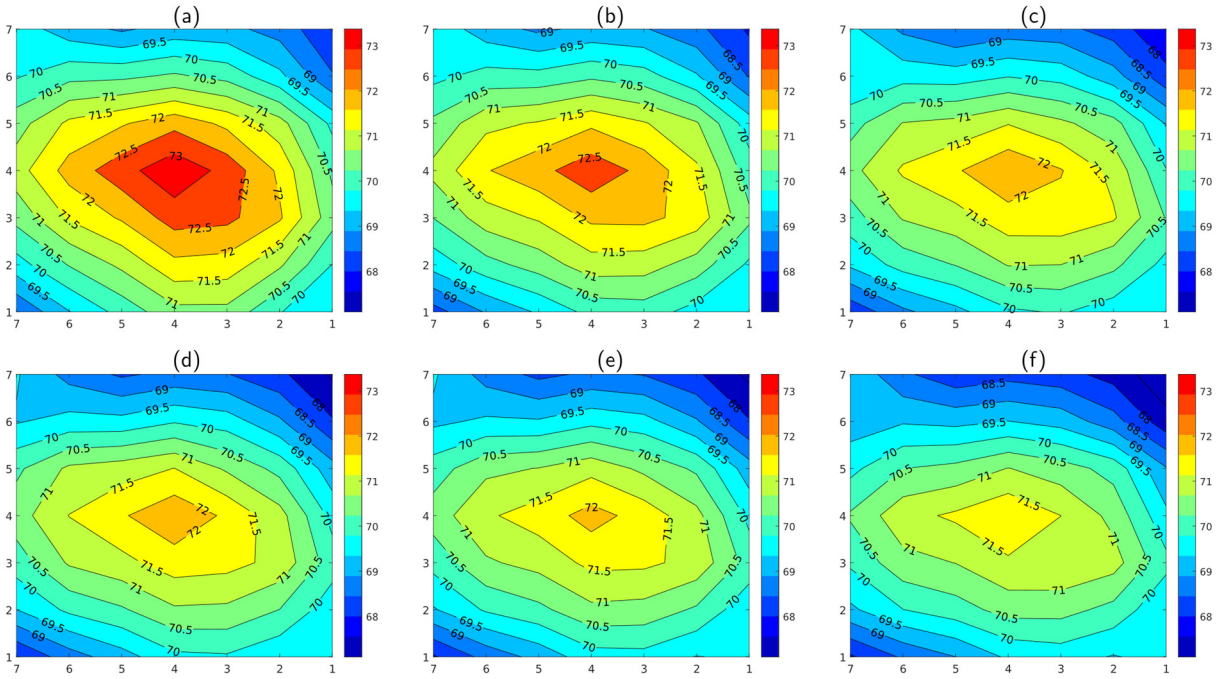

Figure F.7. Temperature distributions 2-D maps at 0.9 A.cm^{-2} and 50%RH. (a) 0.5 MPa, (b) 0.8 MPa, (c) 1.1 MPa, (d) 1.4 MPa, (e) 1.7 MPa, and (f) 2 MPa. Colour bars show the corresponding colours of each level of the local temperature.

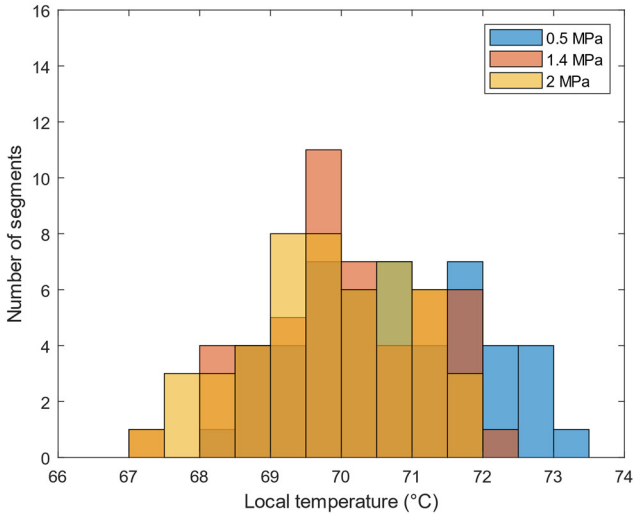

Figure F.8. Temperature distribution histograms at three levels of mechanical compression, 0.5 MPa, 1.4 MPa, and 2 MPa. Histograms obtained at 0.9 A.cm^{-2} and 50 %RH.

Results at 100%RH

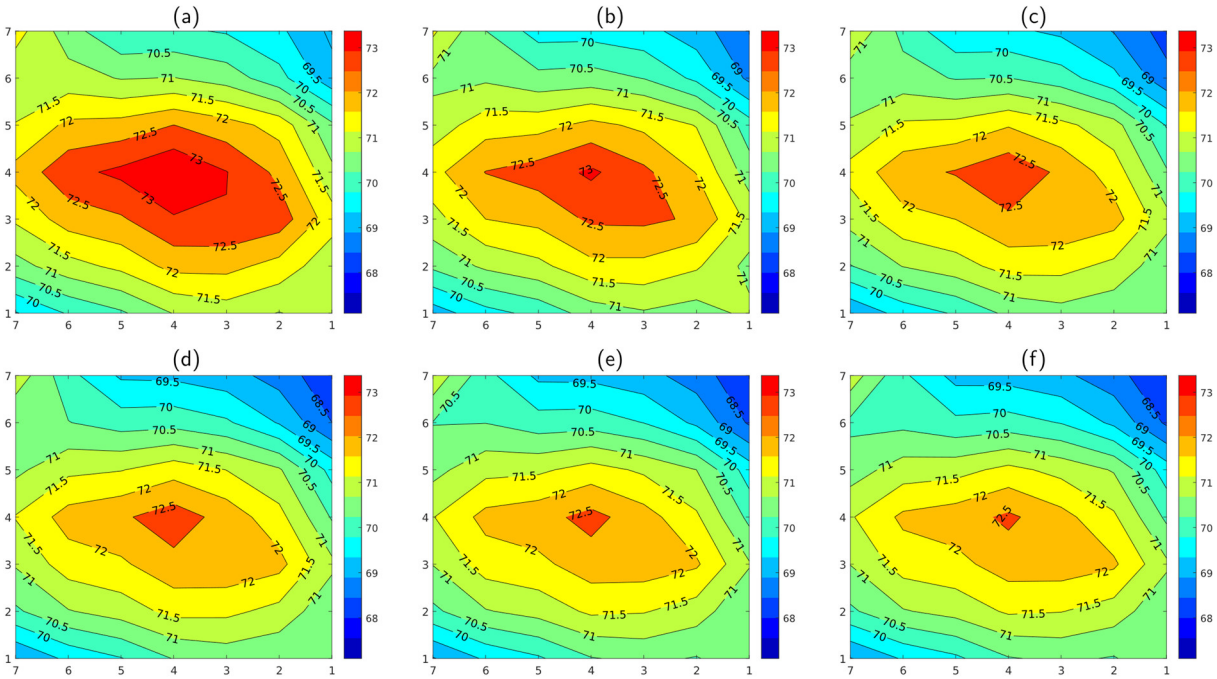

Figure F.9. Temperature distributions 2-D maps at 0.9 A.cm^{-2} and 100%RH. (a) 0.5 MPa, (b) 0.8 MPa, (c) 1.1 MPa, (d) 1.4 MPa, (e) 1.7 MPa, and (f) 2 MPa. Colour bars show the corresponding colours of each level of the local temperature.

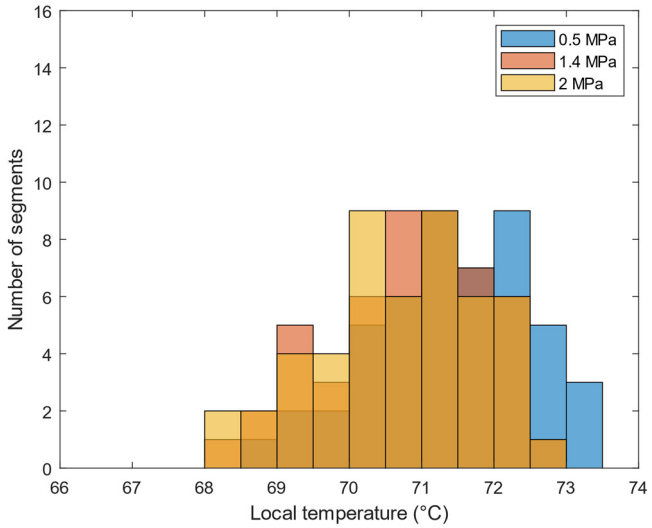

Figure F.10. Temperature distribution histograms at three levels of mechanical compression: 0.5 MPa, 1.4 MPa, and 2 MPa. Histograms obtained at 0.9 A.cm^{-2} and 100 %RH.

Statistical analysis of the temperature distributions at 0.9 A.cm^{-2}

- Evolution of the standard deviation of the local temperature distributions at 0.9 A.cm^{-2}

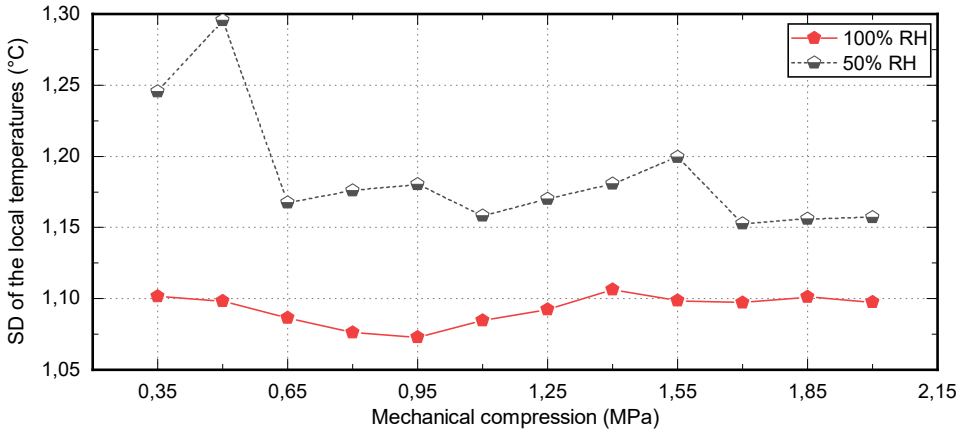

Figure F.11. SD evolution of the temperature distribution as a function of mechanical compression at 0.9 A.cm^{-2}. Results at 50%RH and 100%RH.

Relative humidity	50%RH		100%RH	
Mechanical compression range	First range: 0.35 → 1.55 MPa	Second range: 1.55 → 2 MPa	First range: 0.35 → 1.55 MPa	Second range: 1.55 → 2 MPa
SD reduction	3.7 %	3.5 %	0.3 %	0.1 %

Table F.3. Reduction of the SD of the temperature distributions as a function of mechanical compression range at 0.9 A.cm^{-2}. Results at 50%RH and 100%RH.

- Evolution of the maximum local temperature at 0.9 A.cm^{-2}

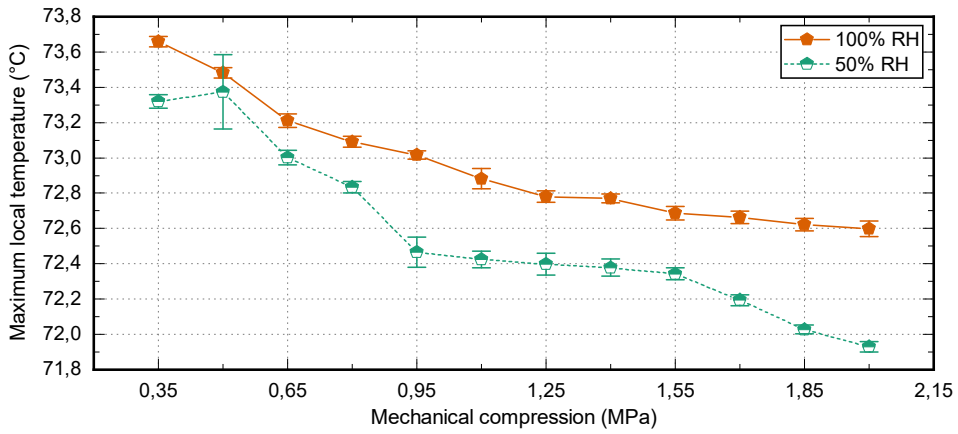

Figure F.12. Maximum local temperature evolution of the temperature distributions as a function of mechanical compression at 0.9 A.cm^{-2}. Results at 50%RH and 100%RH.

Relative humidity	50%RH		100%RH	
Mechanical compression range	First range: 0.35 → 1.55 MPa	Second range: 1.55 → 2 MPa	First range: 0.35 → 1.55 MPa	Second range: 1.55 → 2 MPa
Local max reduction	1.3 %	0.6 %	1.3 %	0.1 %

Table F.4. Reduction in the maximum temperature as a function of mechanical compression ranges at 0.9 A.cm^{-2}. Results at 50%RH and 100%RH.

Fujifilm Prescale® LLW additional data

Accuracy	±10%* or less
Recommended temperature	20°C → 35°C
Recommended relative humidity	35%RH → 80%RH

*measured by a densitometer at 23°C and 65%RH

Table F.5. Technical specifications of the Fujifilm Prescale® LLW pressure sensitive films [1].

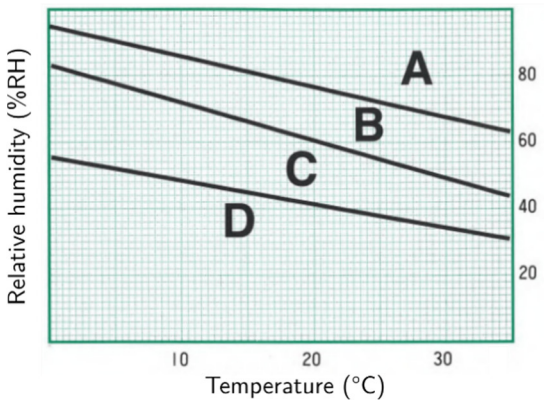

Figure F.13. Graph of the relative humidity/ temperature conditions. Regions A to D represent the graph to be used in figure F.14. In our study, the tests were conducted at a temperature of 21°C and relative humidity of 54%RH → graph C.

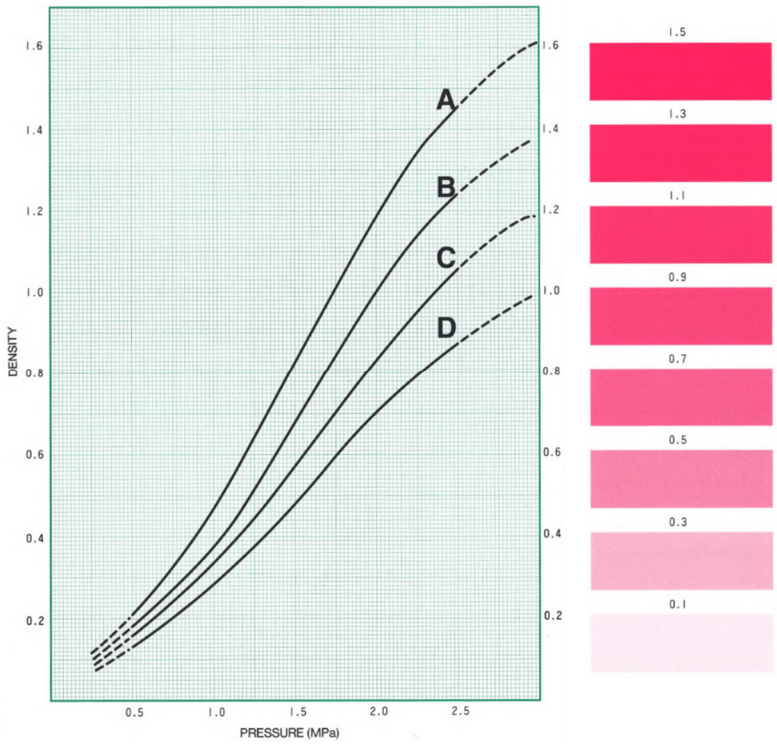

Figure F.14. Graph of the colour density as a function of mechanical compression (graph C).

Reference

[1] Pressure measurement film “Prescale”: Specifications | Fujifilm Global. http://www.fujifilm.com/products/measurement_film/en/prescale/product/.

Titre : Analyse comportementale de composants de pile à combustible de type PEM et recherche d'un lien causal entre les performances observées de manière in-situ et ex-situ.

Mots clés : Pile à combustible ; Caractérisation expérimentale in-situ ; Compression mécanique.

Résumé : Les piles à combustible à membrane échangeuse de protons (sigle PEFC en anglais) ont déjà montré un potentiel important dans des applications mobiles et stationnaires. L'empilement des PEFCs (stack) nécessite, à l'assemblage, l'introduction d'une compression mécanique afin d'obtenir des contacts (mécaniques, thermiques, électriques) adéquats entre les composants et pour assurer une étanchéité vis-à-vis des réactifs. Cependant, une contrainte mécanique excessive peut détériorer les performances de la PEFC en réduisant notamment la porosité des couches de diffusion (GDLs) et leur capacité à transporter les espèces (réactifs et produits). Les travaux présentés dans cette thèse visent à étudier les effets d'une compression mécanique (variant de 0.35 à 2 MPa suivant 12 niveaux) sur les performances in-situ d'une PEFC à la surface active de 225 cm^2. Les travaux menés présentent la particularité de combiner plusieurs techniques de caractérisation et d'analyse (courbes de polarisation et Spectroscopie d'Impédance Électrochimique - SIE ; distributions locales de courant, de température et de pression ; mesures de déplacement mécanique) tout en fournissant des corrélations avec les résultats d'essais ex-situ obtenus dans le cadre du projet de recherche MIREPOIx.

Les observations réalisées ici indiquent qu'une compression mécanique allant jusqu'à 1.55 MPa améliore les performances électriques de la PEFC dans les conditions opératoires considérées. Ce résultat est attribué à la réduction dominante de la résistance ohmique par rapport à l'augmentation de la résistance au transport des espèces. Par ailleurs, l'augmentation de la compression mécanique homogénéise les répartitions des densités de courant et des températures jusqu'à 1.55 MPa. Cette homogénéisation est attribuée à une meilleure distribution de la pression mécanique obtenue avec la compression croissante. Les essais suggèrent que la compression de la PEFC au-delà d'un niveau spécifié (1.55 MPa) n'entraînerait pas d'amélioration significative des performances électriques. Elle pourrait même les détériorer en raison de l'augmentation de la résistance au transport des espèces. Enfin, des corrélations entre les résultats des techniques de caractérisation in-situ et ex-situ sont fournies et analysées tout au long de la thèse.

Title: Behavioural analysis of PEM fuel cell components and research of causal relationships between in-situ and ex-situ observed performances.

Keywords: Fuel cell; In-situ experimental characterisation; Mechanical compression.

Abstract: Polymer Electrolyte Fuel Cells (PEFCs) have shown their potential for both mobile and stationary applications. Assembling the PEFC stacks requires an appropriate mechanical compression in order to achieve adequate contacts (i.e. mechanical, thermal, and electrical) between the fuel cell components and to ensure gas-tight operation. However, an excessive mechanical compression may worsen the fuel cell performance as a result of the reduction in the porosity and mass transport ability of the Gas Diffusion Layers (GDLs). The work presented in this thesis aims to investigate the effects of 12 levels of mechanical compression, ranging from 0.35 to 2 MPa, on the in-situ performance of a 225 cm^2 PEFC. The experimental investigations present the novelty of combining various characterisation techniques (i.e. polarisation measurement; Electrochemical Impedance Spectroscopy - EIS; local current/temperature and pressure distributions analysis; displacement measurement) while providing correlations with ex-situ results obtained within the MIREPOIx research project.

The results show that a mechanical compression up to 1.55 MPa improves the PEFC performance at all tested operating conditions. This finding was attributed to the dominant reduction of the ohmic resistance against the increase in mass transport resistance. The results also emphasise the fact that mechanical compression up to 1.55 MPa improves the distributions of current and temperature. This effect was attributed to the enhanced pressure distribution achieved with increasing mechanical compression. The results obtained in this thesis suggest that compressing the PEFC beyond a specified level (1.55 MPa) would not lead to any further improvement of the PEFC performance. It may even worsen this performance due to the increase in the mass transport resistance. Finally, valuable correlations between the results from in-situ and ex-situ characterisation techniques are provided and analysed throughout the thesis.